# Graphène pour la nanoélectronique : de la croissance CVD jusqu'à la suparconductivité de proximité à deux dimensions

Zheng Han

UNIVERSITÉ DE GRENOBLE

# THÈSE

Pour obtenir le grade de

## DOCTEUR DE L'UNIVERSITÉ DE GRENOBLE

Spécialité : **Nano-électronique et Nanotechnologies**

Arrêté ministériel : 7 août 2006


Présentée par

## Zheng (Vitto) HAN

Thèse dirigée par **Vincent BOUCHIAT** et
codirigée par **Irina IONICA**

préparée au sein du **Département Nanosciences de l'Institut Néel**
dans **l'École Doctorale « Electronique, Electrotechnique, Automatique, Télécommunications, Signal » (EEATS)**


# Macroscopic CVD Graphene for Nano-electronics: from growth to proximity-induced 2D superconductivity.

# Graphène macroscopique pour la nanoélectronique : de la croissance CVD à la supraconductivité de proximité à deux dimensions.

Thèse soutenue publiquement le **26 Septembre 2013**
devant le jury composé de :

**Prof. Christoph STRUNK**
Professeur à l'Université de Ratisbonne, Regensburg (Allemagne) Rapporteur.
**Dr. Annick LOISEAU**
Directeur de recherche à L'ONERA, Chatillon, Rapporteur.
**Dr. Claude CHAPELIER**
Chercheur au CEA-INAC, Grenoble, Examinateur.
**Dr. Marek POTEMSKI**
Directeur de recherche au LNCMI, CNRS, Grenoble, Examinateur.
**Dr. Ali MADOURI**
Ingénieur de recherche à LPN-CNRS, Marcoussis, Examinateur.
**Dr. Jean DIJON**
Chercheur au CEA-LITEN, Grenoble, Invité.
**Dr. Irina IONICA**
Maitre de Conférence à l'INP-Grenoble Invité, Co-Encadrant de thèse.
**Dr. Vincent BOUCHIAT**
Directeur de recherche à l'Institut Néel, Grenoble, Directeur de thèse.

# MACROSCOPIC CVD GRAPHENE FOR NANOELECTRONICS: FROM GROWTH TO PROXIMITY-INDUCED 2D SUPERCONDUCTIVITY

ZHENG HAN

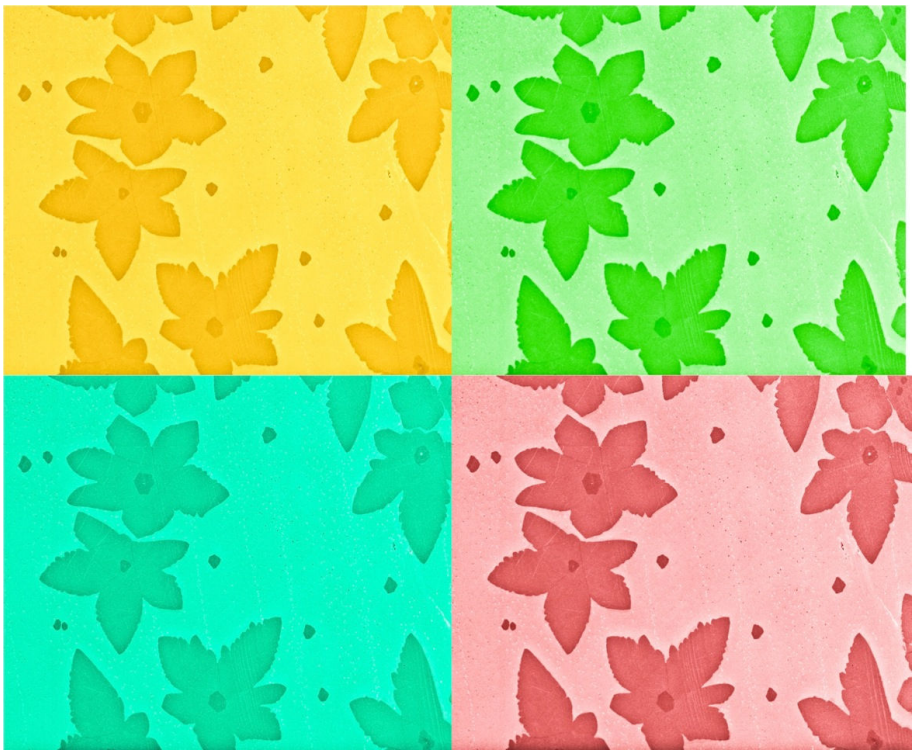

Flower power: graphene crystals on Cu

Zheng HAN: *Macroscopic CVD Graphene for Nanoelectronics: From Growth to Proximity-induced 2D Superconductivity,*
Cover image: Flower power: graphene crystals on Cu, © 2013.

# CONTENTS

## Résumé en français de la thèse

Cette thèse présente un travail expérimental sur le graphène. Le graphène est un cristal bidimensionnel atomiquement fin d'atomes de carbone liés dans un réseau covalent de symétrie hexagonale. Les propriétés nouvelles et les applications potentielles de ce matériau sont nombreuses, grâce à la combinaison de propriétés optiques, mécaniques et électroniques exceptionnelles. C'est un semi-conducteur à gap nul, qui présente tout à la fois une excellente mobilité électronique et une faible absorbance optique [1, 2]. Son épaisseur monoatomique le rend tout à fait compatible avec une électronique à très haute fréquence ainsi que pour des capteurs. En effet, le graphène rentre déjà dans la réalisation de composants innovants pour l'électronique sur substrat flexible et transparent [3, 4], des transistors analogiques fonctionnant à 100 GHz [5], des détecteurs photoniques pour l'imagerie Terahertz [6], des composants pour le photovoltaïque [7], des resonateurs nano-mécaniques [8], des étalons de résistance basés sur l'effet Hall Quantique [9, 10], etc.

Du point de vue de la physique fondamentale, le graphène est un système électronique vraiment unique, implémentant un gaz bidimensionnel « exotique » car peuplé de fermions de Dirac à masse nulle. De plus son épaisseur ultimement fine supprime tout écrantage des charges et autorise l'ajustement du signe et de la densité de porteurs via une tension électrique appliquée sur une électrode de grille [11]. Par conséquent, le graphène est un objet d'étude idéal pour la physique de la matière condensée de basse dimensionnalité. De plus, de part l'absence de liaisons pendantes, le graphène est chimiquement et physiquement stable, ce qui offre une possibilité originale de le coupler à d'autres matériaux pour réaliser des systèmes hybrides. Comme on le montrera plus tard dans ce manuscrit, le graphène décoré par des nano-particules supraconductrices s'est révélé être un système 2D supraconducteur tout à fait original [12, 13, 14].

Dans ce travail de thèse, nous cherchons à fabriquer puis à mesurer le transport électronique à très basse température dans des dispositifs quantiques à base de graphène, entièrement fonctionnalisés et intégrés sur puce. Pour atteindre cet objectif, nous avons mis en place un protocole expérimental complet permettant de synthétiser du graphène à haute mobilité électronique, de le transférer sur des supports compatibles avec les applications, tout en contrôlant le désordre électronique et enfin, de l'intégrer dans des dispositifs quantiques hybrides présentant des propriétés inédites.

**Les questions au centre de cette thèse**

A ce jour, la technique de dépôt par vapeur chimique réactive (CVD) du graphène sur feuille de cuivre [15] est sans aucun doute la meilleure technique pour une monocouche polycristalline de taille macroscopique, qui peut être par la suite transposée sur un substrat isolant de taille et de composition arbitraires (silicium, verre, films plastiques, etc.). Cependant, cette technique présentent une série d'inconvénients : le graphène réalisé présente des défauts structurels, tels que des lacunes, des joints de grains, des zones multicouches etc.. Avant d'envisager une production de masse de dispositifs électroniques à base de graphène, il faut adresser ces problèmes et trouver des solutions. Par exemple, est-il possible de faire croître par CVD des couches continues de graphène présentant une mobilité électronique comparable à celles des petits échantillons obtenus par la technique traditionnelle d'exfoliation du graphite ? Pour une intégration du graphène dans des applications à grande échelle, le but ultime serait la production d'un monocristal de graphène à l'échelle d'une galette (wafer) entière de silicium de 300mm. Est-il déjà possible d'améliorer la CVD sur Cu pour se débarrasser de ces défauts et d'obtenir une monocouche de graphène homogène ? Ces questions sont examinées dans le premier chapitre de cette thèse, dans lequel on abordera des détails sur notre nouvelle méthode de croissance CVD pulsée permettant de supprimer complètement les zones multicouches.

D'autre part, le graphène déposé sur le métal doit être transféré sur des substrats isolants pour applications en nanoélectronique. Comment cela peut t-il être réalisé ? Si nous visons les applications à plus court terme du graphène, le transfert sur des substrats transparents flexibles est également un point critique. Dans quelle mesure est-t-il possible d'obtenir un graphène sur ces substrats d'aussi bonne qualité que celle présentés dans les résultats à l'état de l'art ? Nous aborderons ces sujets dans le chapitre 2. Nous discuterons des procédés de transfert secs et humides sur substrats variés et nous examinerons les performances de conduction d'électrodes de graphène transparentes et flexibles. Le graphène est essentiellement un matériau constitué de deux interfaces, sans aucun volume propre, par conséquent l'influence de l'environnement (tant physico-chimique qu'électromagnétique) sur ce matériau est considérable. De plus, de part sa structure carbonée des adsorbats peuvent se lier facilement physiquement ou chimiquement sur la surface. Ceci pose des questions importantes concernant la pureté du

graphène. Est-il possible de produire du graphène véritablement "neutre" c'est à dire présentant de très faibles niveaux de dopage (c'est à dire moins de $10^{11}$ electron/$cm^{-2}$) ? Comment peut-on obtenir le graphène le plus propre possible, avec une surface sans contamination visible et ainsi compatible avec des études de surfaces aussi exigeantes que sont les techniques de microscopies à sonde locale telle que le STM ? Pour y répondre, nous allons explorer dans le chapitre 4 une série de méthodes de nettoyage optimisées, et notamment détailler la mise au point d'une méthode basée sur des traitements acides, permettant l'élimination des résidus de polymère.

Une autre problématique, importante pour l'utilisation du graphène en tant que matériau pour la nanoélectronique, concerne le contrôle des défauts à l'échelle de la maille cristalline (tels que des trous, la rugosité, les joints de grains).

En effet, la présence de désordre à cette échelle dans un tel système de basse dimension affecte considérablement le libre parcours moyen des électrons, générant de la diffusion visible dans la conductance électronique. Parmis ceux-ci on peut citer la localisation faible ou forte qui, associés au contrôle de la densité de porteurs, permet d'induire une transition métal-isolant contrôlée par la tension de grille. Dans ce cadre, il est intéressant de savoir s'il est possible de concevoir des méthodes qui permettent d'adapter précisément le niveau du désordre, en induisant une quantité bien contrôlée de défauts à l'échelle atomique ? Le chapitre 5 de cette thèse va traiter de ce problème. Nous allons présenter les méthodes classiques pour induire des défauts basés sur des plasmas réactifs puis nous allons montrer nos résultats basés sur une voie chimique induisant des lacunes.

Le graphène est le premier gaz d'électrons bidimensionnel entièrement nu, ce qui représente un énorme intérêt de ce matériau pour l'élaboration de systèmes hybrides à 2D. Par exemple, si ce tapis électronique est décoré par des nanoparticules supraconductrices, celle-ci vont induire localement des fluctuations supraconductrices par effet de proximité et le graphène peut devenir par percolation de ces fluctuations un supraconducteur macroscopique à 2D. Quelle sera la physique dominante dans un tel système et comment cette physique dépendra-t-elle de paramètres intrinsèques présents dans le graphène tels que le niveau du désordre structural, le signe et la densité des porteurs de charge ?

Dans le dernier chapitre, nous allons montrer nos expériences sur la transition supraconducteur – isolant dans le graphène décoré par des

nanoparticules d'étain. Dans ce système hybride, du graphène synthétisé par les techniques CVD présentés au début du manuscrit est décoré d'un réseau de nanoparticules d'étain supraconductrices. Suivant la densité de particules et sa superstructure spatiale (réseau aléatoire ou triangulaire), de nombreuses phases distinctes peuvent être obtenues et étudiées, notamment la présence d'une phase métallique exotique entre les phases isolantes et supraconductrices. Nous allons comparer ces résultats avec des prédictions théoriques récentes.
Je présente dans ce qui suit les principaux résultats obtenus dans cette thèse en détaillant chaque chapitre.

## 1. Croissance d'une monocouche homogène de graphène sur cuivre par une technique innovante de CVD pulsée.

*Après un état de l'art rapide sur les progrès récentes dans la fabrication du graphène sur cuivre, nous allons décrire notre technique innovante basée sur de la CVD pulsée. Cette technique nous a permis d'obtenir pour la première fois des monocouches de graphène exemptes de zones multicouches habituellement présentes lors de la croissance sur cuivre.*

Les techniques CVD (dépôt chimique en phase vapeur) sont maintenant devenues les méthodes parmi les plus efficaces et prometteuses pour produire du graphène de haute qualité et de grande taille [15]. C'est un domaine de recherche en plein essor pour le graphène; on note par exemple que plus de 1600 articles ont été publiés au cours des trois dernières années contenant dans leur titre les mots « Graphène » et « CVD ».

Le meilleur substrat pour le dépôt catalytique du graphène est inconstestablement une feuille laminée de cuivre, principalement parce qu'elle fournit un substrat sacrificiel soluble qui permet ensuite la libération de la couche macroscopique de graphène et son report sur substrat isolant. Les mécanismes de croissance du graphène sur cuivre sont complexes et ont fait l'objet d'une fraction importante des 1600 articles sus-cités. Certains points font encore débats : par exemple, une seule monocouche de graphène est censée croître sur Cu en raison de l'auto-limitation du procédé lié à la très faible solubilité du carbone dans le volume de cuivre [16]. Cependant, les observations expérimentales montrent lors du procédé CVD du graphène sur feuille de cuivre, des multicouches sont toujours présentes et peuvent couvrir une fraction importante de la surface (de 5% jusqu'à 30%), en recouvrant notamment les sites de défauts de surface du métal. Ces multicouches

apparaissent quelles que soient les conditions de croissance. Jusqu'à présent, seuls les substrats monocristallins (incompatibles avec un caractère sacrificiel et peu adaptées pour une utilisation industrielle) permettaient de s'en affranchir. La croissance de zones multicouches dans le graphène sur Cu semble a priori en contradiction avec le mécanisme d'auto-limitation, qui suppose en effet que toute zone recouverte d'une monocouche de carbone devient inerte vis à vis d'une croissance supplémentaire.

Ces zones multicouches constituent pourtant des défauts considérables en ce qui concerne les applications potentielles du graphène. Nous montrons en effet que ces multicouches sont néfastes pour les propriétés optiques et électroniques du graphène, et doivent donc être éliminées. En comparant nos observations expérimentales avec d'autres résultats rapportés dans la littérature [17], nous avons compris que la formation des multicouches pendant le processus CVD est due à la ségrégation dans les sites de défauts de la surface de Cu, où le carbone peut être piégé, et puis relargué durant la phase de ségrégation. Ainsi, des multicouches de graphène se forment sous la monocouche macroscopique aux points du nucléations des grains de graphène, comme le montre la Figure 1.

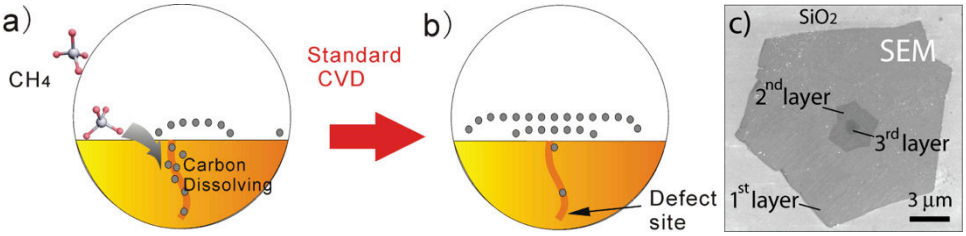


*Figure 1: a) et b) Représentation schématique en coupe des mécanismes de croissance du graphène à la proximité d'un site de défaut sur le cuivre pour le processus standard sur Cu (CVD continue). La ségrégation conduit à la formation d'un multicouche sous la couche macroscopique de . c) Image MEB d'un grain héxagonal de graphène après transfert sur silicium oxydé. Notez que les multicouches apparaissent dans le centre de l'hexagone, ce qui coïncide avec la position du site de nucléation.*

Par conséquent, on peut tester plusieurs stratégies pour d'éviter la formation de multicouches:

(a) Soit supprimer entièrement tous les défauts possibles sur la surface du Cu, ce qui a été effectivement prouvé pour le Cu monocristalin ou pour des films minces épitaxiés [18];

(b) Soit interdire aux atomes de carbone d'être pris au piège dans les sites de défauts en limitant leur présence.

Le premier choix est tout à fait abordable dans un laboratoire de recherche, mais se servir des couches sacrificielles epitaxiées ou de substrats monocristallines reste trop coûteux si des applications industrielles sont envisagées.

Dans un premier temps, nous avons construit un prototype « fait maison » de réacteur CVD optimisé pour la croissance de graphène par méthane sur cuivre, que nous avons entièrement automatisé. L'automate permet le contrôle en temps réel du flux des gaz réactifs et diluants ainsi que de la température et la pression de l'enceinte comme le montre la Figure 2. Un tube en quartz de diamètre de 80 mm de diamètre et de 1 m de long sert de réacteur de croissance autorisant la production d'échantillons de grande taille (typiquement 2 pouces et jusqu'à 20×20 cm pour des feuilles de cuivre enroulées en cylindre). Il est équipé d'un four à trois zones de chauffage/contrôle, autorisant des températures jusqu'à 1050°C sur une zone homogène de 0,3 m de longueur. La pression de la chambre de croissance est réglable par ajustement de la vitesse de la pompe indépendamment du flux des gaz. Quatre contrôleurs de débit massique sont utilisés pour régler avec précision et en temps réel l'injection de chaque gaz (en de diffusion).

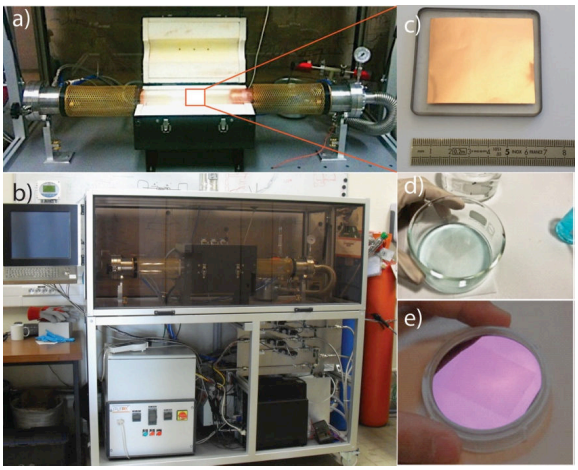


*Figure 2: Réacteur CVD automatisé pour la fabrication du graphène par technique CVD continue et pulsée. A) vue de la partie du four ouverte c) Substrat de Cu typique chargé pour la croissance de graphène. d) et e) Transfert de graphène CVD sur une plaquette de silicium oxydée de 2 pouces de diamètre.*

Grace à la flexibilité apportée par notre réacteur prototype, nous avons pu développer une nouvelle technique de synthèse basée sur une croissance non continue obtenue par injection d'impulsion de gaz précurseur, que nous avons appelée 'CVD pulsée', et pour laquelle nous avons déposé un brevet et soumis une publication (arXiv : 1205.1337) à paraître dans la revue « Advanced Functional materials » . Le procédé revient donc à exposer le substrat catalytique à une vapeur de carbone de manière intermittente, tout en gardant l'hydrogène présent. Le procédé global est basé sur une succession de plusieurs centaines de cycles, chaque cycle étant caractérisé par la répétition de deux étapes respectivement de durée $t_1$ (présence de carbone) et $t_2$ (absence de carbone), comme le montre la Figure 3a. Ce procédé tire profit du caractère réducteur de l'hydrogène pur, présent durant la phase $t_2$, au cours de laquelle le gaz précurseur du carbone est retiré, comme indiqué sur la Figure 3. La Figure 3 montre également des résultats des structures obtenues avec notre procédé CVD pulsé, pour un échantillon obtenu pour deux régimes de croissance distincts, le premier effectué à basse pression conduisant à des grains de morphologie dendritique et le deuxième effectué à haute pression et à faible teneur en carbone, conduisant à des grains hexagonaux. Pour ces deux régimes de croissance très distincts, on note l'absence totale de multicouche sur l'ensemble du substrat de plusieurs dizaines de centimètres carrés.

Lorsque le nombre de cycles est suffisamment grand (typiquement plusieurs centaines), une couche continue et homogène à l'échelle macroscopique de graphène peut être atteinte, comme l'illustre la Figure 4. Le mécanisme de croissance pulsée est le suivant: l'absence intermittente de méthane permet d'éviter que les défauts du cuivre se saturent en carbone, limitant ainsi davantage la ségrégation et la production de zones multicouches. Lors de la première étape de la croissance (durée $t_1$), seule une quantité faible de carbone peut arriver à s'adsorber sur la surface puis à diffuser. Cette quantité est cependant suffisamment élevée pour déclancher la nucléation, mais suffisamment faible pour éviter qu'une quantité massive de C vienne se dissoudre dans les défauts. Lors de l'étape suivante (deuxième partie du cycle, ou seul l'hydrogène est présent), les atomes de carbone libres sont évacués, et seuls ceux liés aux liaisons $sp^2$ de surface subsistent car ils sont beaucoup plus stables énergétiquement. Si cette procédure est repétée d'une manière contrôlée, les îlots de graphène obtenus s'élargissent à 2D, mais sans carbone dissous dans les défauts, jusqu'à ce

qu'une couverture complète de la surface soit obtenue par percolation des grains.

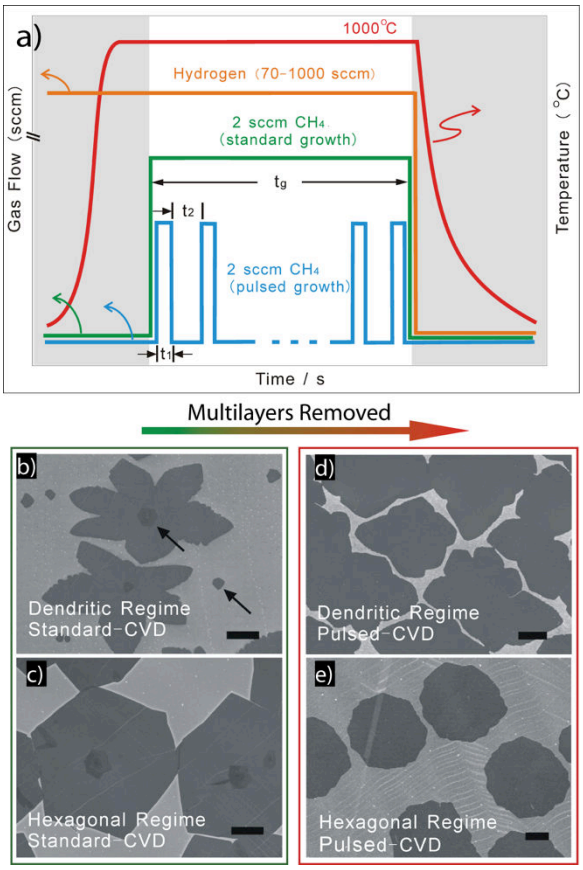


*Figure 3: a) « Process-flow » montrant le chronogramme du flux des gaz lors d'une CVD standard (ligne verte) et d'une CVD pulsée (ligne bleue). b) à e) micrographies MEB (microscope électronique à balayage) du graphène sur Cu; la croissance a été interrompue avant d'atteindre une couverture sur toute la surface, pour montreer la morphologie de croissance dans la CVD standard (colonne de gauche) et dans la CVD pulsée (colonne de droite). Les flèches en b) indiquent les différentes formes de multicouches. Les barres d'échelle sont de 10 µm.*

Les cartographies Raman (Figure 5) d'un grain de graphène typiquement obtenu par cette méthode CVD pulsée montre des intensités homogènes des bandes G et 2D, avec une intensité de bande D négligeable, ce qui suggère la bonne qualité cristalline du graphène obtenu. En outre, nous avons réalisé des statistiques de mesures à effet de champ sur 20 dispositifs fabriqués à partir de la technique CVD standard et de la technique CVD

pulsée, respectiveme`t. Comme le mo`tre la Figure 6, la mobilité électro`ique des porteurs da`s les tra`sistors de graphè`e obte`us par la méthode pulsée est supérieure à celle de tra`sistors obte`us par la méthode sta`dard. La meilleure mobilité obte`ue da`s le graphè`e par CVD-pulsée est 6781 $cm^2V^{-1}s^{-1}$ ce qui se rapproche de la valeur maximale obte`ue à l'état de l'art pour du graphè`e CVD.

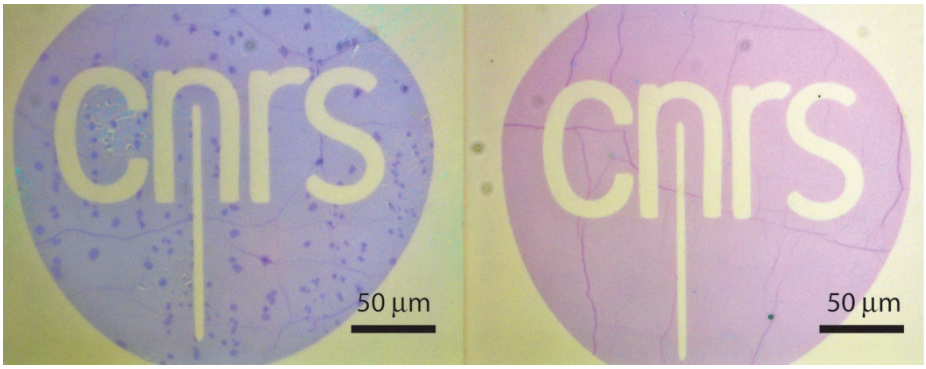


*Figure 4: Micrographies optiques de couches continues de graphène après report sur substrat de silicium oxydé, obtenues par la CVD classique (à gauche) et pulsée (à droite). Les multicouches créent des distorsions optiques sur la gauche, tandis qu'à droite, seules les ridules sont présentes. Le logo CNRS a été obtenu par lithographie optique suivi par une gravure plasma oxygène.*

La tech`ique CVD pulsée que `ous avo`s développée évite do`c la formatio` des multicouches, grâce à la faible solubilité du carbo`e sur certai`s métaux comme le cuivre. E` plus d'éviter l'apparitio` des multicouches, ce qui est u` des problèmes majeurs du graphè`e, cette tech`ique est facileme`t impla`table da`s u` milieu i`dustriel.

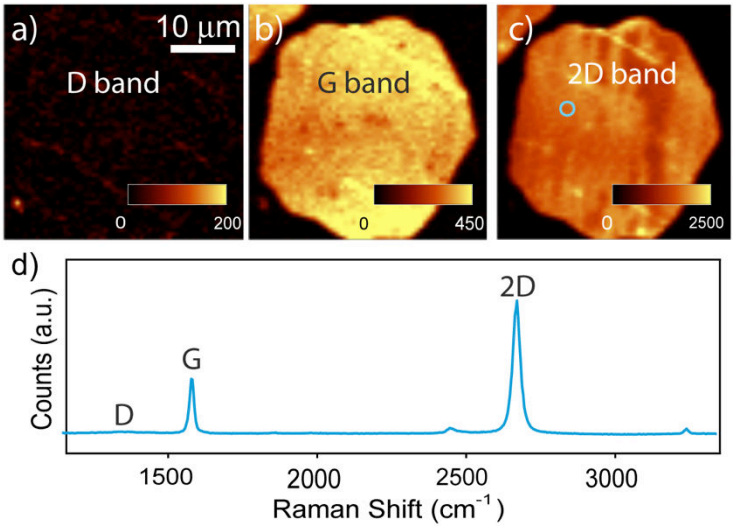


*Figure 5: Cartographie Raman sur un grain de graphène hexagonal (fixé par les paramètres de croissance); les bandes D (a), G (b) et 2D (c). d) Unique spectre pris dans la zone bleue dans l'image (c). La faible intensité de la bande D, qui indique les défauts, suggère la bonne qualité du graphène obtenu.*

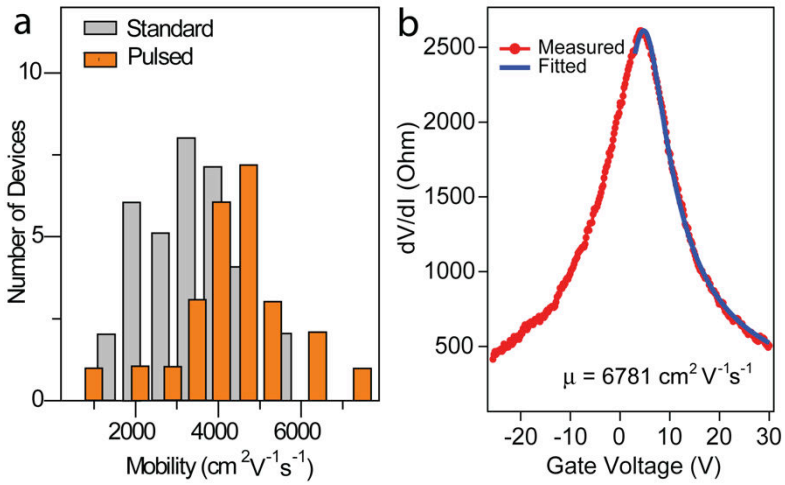


*Figure 6: a) Distribution statistique de la mobilité électronique extraite dans des transistors à canal de graphène déposé sur 285nm de $SiO_2$ (10µm de longueur, 5µm de largeur). Des dispositifs obtenus pas la CVD standard et pulsée ont été réalisés et testés. La meilleure mobilité obtenue à température ambiante (6781 $cm^2V^{-1}s^{-1}$) a été relevée pour un dispositif en configuration 4 pointes, obtenu par CVD pulsée.*

## 2. Graphène de haute mobilité reporté sur substrat souple et transparent

*Pour valoriser les couches de graphène obtenues par croissance CVD pour des applications, nous devons être en mesure de les transférer sur les substrats adaptés. Dans cette partie, nous évaluons la performance des couches de graphène transférées sur substrat transparent souple, ainsi que la possibilité de les transférer sur des supports non classiques tels que des grilles pour l'observation en microscopie électronique à transmission.*

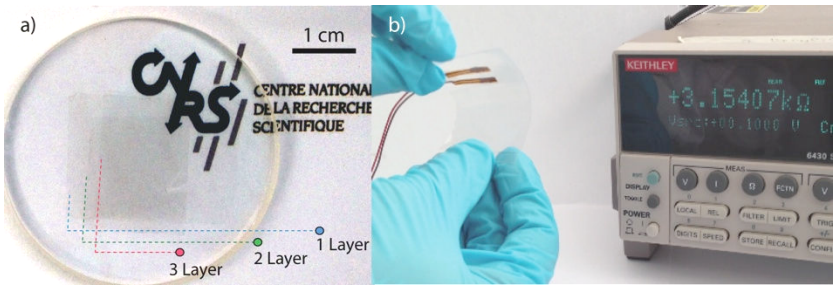


Figure 7: *a) Substrat de verre recouvert de graphène transféré couche par couche, jusqu'à trois empilements successifs au centre du disque. b) Graphène transféré sur un film plastique présentant de bonnes propriétés de conductions sous contrainte mécanique. Les caractéristiques de ces couches sont présentées dans le graphique suivant.*

Pour toutes les applications, de la physique fondamentale à l'industrie, le graphène doit être transféré sur un substrat isolant, soit rigide (plaquettes de silicium, de saphir, plaques de verre, etc) soit souples (sur la surface de films polymère ou bien laminé entre deux couches plastiques). Même si les équipes de recherche tentent actuellement d'obtenir une croissance de graphène directement sur les isolants, les films de graphène qui en résultent sont encore loin de montrer une bonne cristallinité [19, 20], ou une grande taille [21]. Par conséquence, la plupart des applications de graphène sur isolant sont réalisées en détachant le graphène à partir de la surface du métal (essentiellement à base de cuivre comme décrit dans la partie 1).

Dans ce chapitre, nous allons évaluer le transfert de graphène sur des substrats souples et transparents, comme le montre la Figure 7. Des caractérisations électriques complètes indiquent que la résistance de notre couche de graphène transférée sur film de polyéthylène descend jusqu'à 200Ω/carré pour un sandwich de 4 monocouches empilées et en l'absence de tout dopage intentionel. Ces performances sont à l'état de l'art, comme le montrent les données rapportées dans la Figure 8.

Outre le transfert réussi sur des films plastiques, nous démontrons également le transfert de graphène sur des grilles de microscopie électronique à transmission (TEM). Deux types de réseaux TEM ont été testés: le Lacey-carbone et le $Si_4N_3$. Il s'est avéré que le graphène est capable de coller sur les deux types de surface de grilles de TEM, et entièrement suspendu au-dessus des zones de plusieurs $\mu$m carrés. Cela nous a donné l'occasion d'introduire des structures sur graphène pour l'observation au TEM. De plus, la grille de TEM à base de graphène représente une plate-forme prometteuse [23] pour des analyses TEM d'échantillon biologiques (ADN, proteines, etc…) grâce à la possibilité d'éliminer le signal cristallin du support de graphène par analyse des données informatiques.

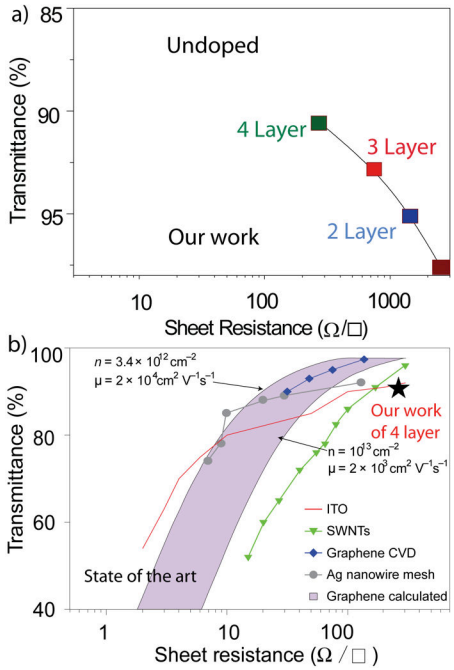


Figure 8: *a) Figure de mérite pour l'utilisation du graphène en tant qu'électrode transparente. Le graphe montre la transmitance optique pour des multicouches en fonction du nombre de couches de graphène produit par notre technique de CVD pulsée puis transféré sur film plastique. b) Evaluation de notre echantillon par rapport à l'état de l'art (figure adaptée de la ref. [22]). L'étoile noire montre les données correspondantes à notre graphène à 4-couches et se trouve sur la courbe de performance de l'oxyde d'indium et d'étain (ITO), matériau standard pour la réalisation d'électrodes transparentes.*

De plus, comme le graphène forme une membrane étanche aux liquides et aux gaz [24], il peut servir de membrane utile pour des études de « matière molle » permettant de séparer des liquides, des molécules ou des nanoparticules. Un exemple de nanoparticules de Sn déposées sur le graphène a été testé sur une grille $Si_4N_3$ TEM avec des trous de 4 $mm^2$ (voir Figure 9b).

La facilité de transfert qu'offre le graphène réalisé par CVD présentée dans ce chapitre ouvre la voie pour des usages polyvalents et des nombreuses futures applications tel que des heterostructures empilées avec du graphène. Les parties suivantes de cette thèse sont réalisées sur du graphène réalisée par CVD et transféré sur les plaques avec oxydes de silicium.

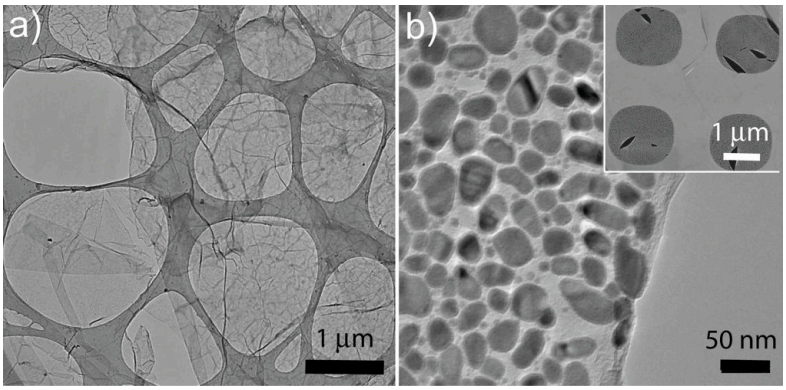


Figure 9: *a) Image TEM du graphène réalisée par notre procédé CVD et transféré sur une grille en carbone (tension d'accélération de 80 kV). b) Graphène décoré par de l'étain, transféré sur grille de TEM en $Si_4N_3$. Les nanoparticules d'étain sont déposées sur le graphène par évaporation thermique et présentent un parfait démouillage. Encart de b) est une image large champ de la grille $Si_4N_3$ avec le graphène transféré par-dessus.*

## 3 Contrôle par voie chimique de la contamination de surface et du désordre électronique dans le graphène

*Les parties précédentes démontrent que nous sommes en mesure de fabriquer et de transférer des monocouches de graphène macroscopique présentant une haute mobilité électronique. Dans cette partie, nous discutons d'abord plusieurs techniques de nettoyage de la surface du graphène et nous montrons que par un traitement*

*chimique, on peut générer une densité controlée de lacunes dans le graphène donnant des propriétés électroniques bien spécifiques.*

Le graphène est connu pour être un matériau facilement dopé ou contaminé, à cause de l'absence de volume et par le fait que ses surfaces supérieure et/ou inférieure qui sont dans la plupart des cas exposées à l'environnement. Le nettoyage du graphène par des techniques non invasives constitue une tâche délicate mais incontournable pour les études de transport électronique dans du graphène ultra-propre, telles que l'effet de Hall quantique, transport balistique mais également les études par microcopie à sonde locale (AFM, STM) . Il existe plusieurs voies pour parvenir à ce nettoyage faisant appel à trois phases de la matière: par chimie humide (solvants, acides faibles), par chimie sèche (gaz réactifs chauds, tels que le recuit à haute température dans de l'hydrogène dilué) et par attaque plasma (plasma réactif en présence d'hydrogène ou oxygène).

Nous avons étudié l'effet de plusieurs traitements sur des dispositifs à base de graphène, conduisant notamment à la suppression du PMMA présent en surface. Nous montrons par exemple que le traitement à l'acide acétique [25], permet d'obtenir une surface plutôt propre, ce qui est compatible avec des études STM, comme le montre la Figure 10.

Le contrôle des défauts dans le réseau cristallin (comme des trous, la rugosité des bords, les lacunes, les joints de grains) constitue un enjeu important dans la nanoélectronique à base du graphène.

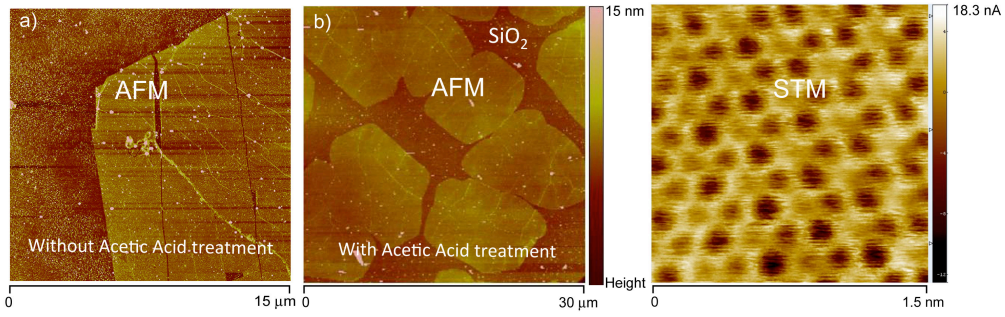


*Figure 10: Image AFM en mode tapping sur des surfaces de graphène réalisées par CVD et transférées sur $SiO_2$ avec une méthode assistée par PMMA. a) Le PMMA est éliminé par l'acétone. b) Le PMMA est éliminé par l'acide acétique pur pendant 48 heures. Par rapport au traitement à l'acétone, la rugosité de la surface est beaucoup plus faible avec le traitement par l'acide acétique. c) image STM du graphène de l'image b). (Remerciements à C. Tonnoir et C. Chapellier du CEA-INAC pour cette image).*

Pour le transport des électrons, la présence d'un défaut conduit à la diffusion puis à la localisation des ondes électroniques. La corrélation entre le désordre induit par un traitement physico-chimique et l'observation de signatures de localisation faible ou forte ont été étudiées [26]. De plus, les défauts dans le graphène peuvent jouer le rôle de moments magnétiques effectifs, donnant lieu à un effet Kondo contrôlable par une grille [27]. Par conséquent, il est important d'adapter précisément le niveau de désordre dans le graphène pour les études de transport.

Normalement, pour créer des défauts dans le graphène, un bombardement ionique ou une irradiation par plasma sont utilisés [26]. Ici, nous montrons que lorsque le graphène est plongé dans un bain d'acide $Na_2S_2O_8$ (0.1 g/ml), on crée des défauts dont la densité augmente avec le temps du traitement, comme le montre la Figure 11. Une nette augmentation de l'intensité du pic D Raman avec la durée de séjour dans la solution de gravure peut être observée dans la Figure 11a, ce qui est la caractéristique de la densité croissante de défauts dans le graphène. On remarque que, à droite du pic G, il y a un petit pic dont l'intensité augmente également (bande D'), ce qui constitue une autre signature de la présence de défauts structuraux. Il a été démontré que le rapport d'intensité D/D' reflète la nature du type de défaut [28]. Dans le cas du graphène mesuré après 19 heures de traitement chimique, le ratio d'intensité D/D' est d'environ 13, ce qui est compatible avec un défaut de type $sp^3$ [28]. La résistance surfacique de ces mêmes échantillons a été également mesurée en fonction du temps d'attaque. Une augmentation quasi-linéaire de la résistivité avec le temps de traitement peut être observée dans la Figure 11b. L'augmentation de la résistivité est connue pour être directement liée à la diffusion des électrons par le désordre. Ce résultat, compatible avec l'apparition du pic D dans les spectres Raman, prouve que par simple trempage dans un solvant chimique, des défauts peuvent être induits dans le graphène. Qu'elle est la nature réelle et la taille typique de ces défauts ?

Pour vérifier la structure de ces défauts à l'échelle microscopique, nous avons procédé à l'observation TEM du graphène traité pour différents temps de gravure. Le graphène sans traitement montre une bonne cristallinité (Figure 12a), tandis qu'au bout de 14 heures de gravure (Figure 12b), des lacunes de taille atomique apparaissent sur l'échantillon.

La méthode chimique ($Na_2S_2O_8$ - solvant) permet donc de contrôler facilement le niveau des défauts sur une échelle et une densité tout à fait interessantes pour le transport électronique. Une dépendance quasi linéaire des défauts est visible dans la mesure de résistance carrée des échantillons. Cette méthode a déjà été mise à profit par notre équipe pour des études fondamentale basées sur le graphène désordonné, telles que la transition quantique de phase supraconducteur-isolant [13].

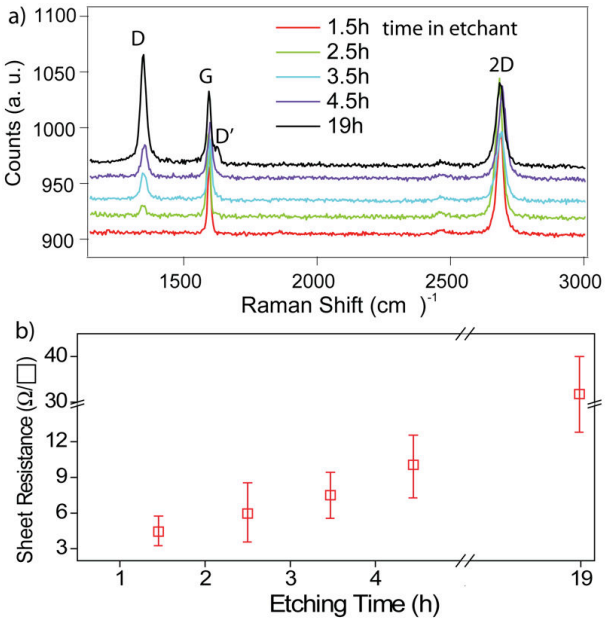


*Figure 11 : a) Spectres Raman du graphène traité dans 0.1 g/ml $Na_2S_2O_8$ pour des différentes durées, et leur résistances carré (b) correspondante. Une augmentation presque linéaire de la résistivité à température ambiante est obtenue avec le temps de gravure dans le solvant $Na_2S_2O_8$.*

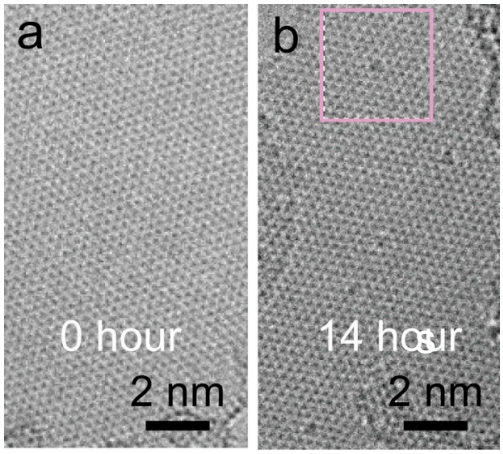


*Figure 12: a) Image TEM du graphène sans défauts sur grille de carbone dentelée. Le graphène a été réalisée par CVD pulsée, nettoyé par l'acétone et recuit à 120 °C sous vide pendant 2 heures. Les images TEM ont été prises par Hanako OKUNO de CEA-INAC. b) Image TEM du graphène après immersion dans 0.1 g/ml $Na_2S_2O_8$ pendant 14 heures. La zone entourée souligne le site d'une lacune probablement induite par une réaction avec solution.*

## 4. Phase métallique quantique dans le graphène décoré par un réseau régulier de nanoparticules supraconductrices d'étain.

*Dans le dernier chapitre, nous abordons enfin la clé de voûte de cette thèse : l'étude plus fondamentale du transport à basse température d'un réseau triangulaire régulier des îlots supraconducteurs sur graphène. A basse température, nous montrons une transition de phase quantique supraconducteur – métal, contrôlée par la grille ; cette transition est induite par des fluctuations de phase quantique de la phase supraconductrice et peut être expliquée par un modèle théorique.*

Dans les métaux usuels à 2D, l'état métallique est rendu instable par la localisation électronique par les défauts structuraux [29]. Toutefois, un état métallique intermédiaire est souvent observé expérimentalement dans la région proche de la transition supraconducteur-isolant (SIT) dans des films minces désordonnés [30, 31, 32, 33]. Pour comprendre la physique présente derrière cet état quantique métallique, un modèle basé sur une transition de phase quantique (TPQ) a été proposé dans un réseau d'îlots supraconducteurs couplés par effet de proximité via un métal « sale » [34, 35,

14]. Ce modèle prédit que les fluctuations de phase quantique à l'intérieur de chaque îlot provoqueront une disparition progressive de la cohérence de phase, qui diminue l'intensité du couplage supraconducteur, et qui donc conduit à un état métallique à température nulle.

Des études récentes [36] sur des réseaux de pastilles de niobium déposés sur un film mince d'or ont démontré que la température critique de ces réseaux de proximité couplés diminue lorsqu'on augmente la distance inter-îlots ; elle arrive à zéro pour une distance inter-îlots finie. Ceci indique une transition de phase quantique vers un état métallique à 2D [37]. Toutefois, en raison de l'absence de modulation de la densité de porteurs dans les films d'Au, ce système expérimental ne permet pas d'obtenir des résultats expérimentaux compatibles avec la théorie complète décrite ci-dessus.

Or le graphène offre une plate-forme idéale pour les études de la supraconductivité de proximité à 2D, notamment parce que sa faible densité de porteur permet d'éviter l'appauvrissement des particules supraconductrices par effet de proximité inverse. Par exemple il est prédit que le graphène décoré avec 1% de sa surface par des îlots supraconducteurs peut devenir facilement supraconducteur à l'échelle macroscopique [14].

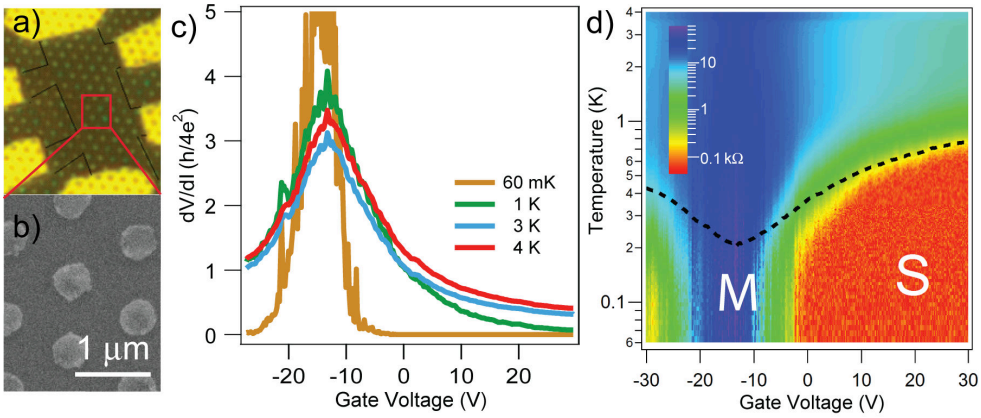


*Figure 13 : Imagerie optique (a) et au MEB (b) des réseaux ordonnés d'étain sur graphène. c) dépendance de la résistance à polarisation nulle avec la tension de grille, pour plusieurs températures. d) Cartographie de la résistance à polarisation nulle en fonction de la température et de la tension de grille. La ligne en pointillés est la température de transition BKT calculée à partir de la théorie [14]. Les lettres "S" et "M" représentent les états respectivement supraconducteurs et métalliques.*

Dans ce cadre, nous avons conçu un réseau triangulaire d'îlots supraconducteurs déposés sur graphène pour étudier l'influence du couplage supraconducteur par effet de proximité. Les couches de graphène obtenues par CVD sont transférées sur une plaque de silicium recouverte de 285 nm d'oxyde servant de diélectrique de grille. La couche de graphène ainsi obtenue sert de métal 2D à résistance variable. La surface du graphène entière a été décorée par lithographie avec un réseau de nanodisques de Sn de 50 nm d'épaisseur. Ces nanodisques d'étain ont un diamètre de 400 nm et sont séparées par 1$\mu$m entre leurs centres (Figure 13a) (soit 16% de couverture). Ce type de réseaux supraconducteur régulier sur le graphène est un système modèle pour étudier les fluctuations quantiques de la phase supraconductrice ; il se prête parfaitement à des comparaisons quantitatives avec la théorie. En effet, le couplage de proximité à travers le métal désordonné 2D est longue portée (décroissance en $1/r^2$), et est donc idéal pour un traitement théorique dans l'approximation des champs moyens.

Trois caractéristiques principales sont observées:

1) la très bonne concordance de la température de transition supraconductrice à 2D (de type Berezinski-Kosterlitz-Thouless) entre les données expérimentales et les prédictions théoriques (Figure 13.d)

2) la saturation de la résistance à basse température pour des tensions de grille voisines du point de neutralité de charge, ce qui est un signe de l'état métallique,

3) l'apparition d'un effet de ré-entrance de la phase supraconductrice aux plus basses températures et en présence de champ magnétique, en accord avec les prédictions théoriques [38].

## 5 Conclusions

Après avoir rattrapé l'état de l'art de la croissance CVD et du transfert du graphène sur substrat isolant, nous avons développé une nouvelle méthode de CVD pulsée, qui est capable d'éliminer totalement les multicouches présentes dans ce matériau. Cette méthode réduit considérablement les défauts sur le graphène CVD et conduit à la réalisation du graphène avec des propriétés optiques et électriques supérieures. Nous avons examiné les questions techniques relatives à la fabrication de dispositifs de graphène, comme le processus de transfert et du nettoyage. Des électrodes transparentes et flexibles avec des propriétés de transport à l'état de l'art ont été démontrées. En outre, diverses méthodes pour la purification du graphène ont été introduites.

Que ce soit en termes de fabrication ou de la caractérisation du matériau, nous avons pu faire contrôler la densité de défauts aussi bien sur la surface qu'au sein du matériau ceci d'une manière contrôlée par des traitement par voie humide. Nous avons découvert une nouvelle façon chimique d'introduire des défauts dans le graphène par simple immersion dans du $Na_2S_2O_8$. Cette méthode ouvre la possibilité d'obtenir une large variété d'échantillons présentant des propriétés physiques différentes et de faire le lien entre structure et propriétés électroniques. Cela nous permet d'avoir un paramètre supplémentaire pour contrôler les caractéristiques du graphène, et dont nous avons profité pour nos études du transport électronique à basse température.

Grâce l'usage du graphène obtenu par CVD suivi du contrôle du désordre, de la densité et de la symétrie des réseau de grains, nous avons réussi à obtenir un dispositif quantique macroscopique, montrant une transition supraconducteur-isolant contrôlée en tension de grille avec dans certains cas, une phase métallique intermédiaire. Cette expérience a deux conséquences importantes: la démonstration d'un supraconducteur 2D de taille illimitée, et la manifestation d'un switch quantique.

Pour compléter davantage notre étude, nous avons réussi à décorer notre graphène avec un réseau triangulaire régulier de nanodisques de Sn, qui est un système prototype pour l'étude des transitions de phase quantique. Nous avons compris le comportement en comparant à des travaux théoriques et constaté l'existence d'un état métallique induit par la fluctuation des phases quantique et qui est contrôlable par une grille électrostatique.

En conclusion, le point clé de cette thèse consiste en une étude générale du graphène, allant de la mise au point d'une technique de synthèse innovante par CVD pulsée, jusqu'aux mesures de transport électronique à très basse température sur des dispositifs quantiques hybrides.

## SYNOPSIS OF THIS THESIS

This experimental work deals with graphene. Graphene is a monolayer of graphite, and thus can be considered as a bi-dimensional crystal of carbon atoms organized in a honeycomb lattice. It is a promising material for future electronic applications due to a unique combination of optical, mechanical and electrical properties. It is almost transparent [1, 2], a zero-gap semiconducting, and its atomic thickness is compatible with ultra-high frequency analogue electronics. Consequently, it could be widely used in fields such as transparent flexible electronics [3, 4], 100 GHz transistors [5], THz imaging systems [6], photovoltaics [7], nano-mechanical systems [8], quantum resistance standards [9, 10], etc.

From the fundamental physics point of view, graphene exhibits the unique characteristics of 2D massless Dirac fermions, combined with gate tunability of the charge carrier density [11]. Therefore, it is of great importance for low dimension condensed matter physics. Furthermore, graphene offers physically and chemically stable 2D electron gas exposed to air, which can be coupled to other materials, thus leading to hybrid systems. For example, as we will see in this dissertation, graphene combined with superconducting nanoparticles has been reported to be able to serve as an ideal media for implementing tunable 2D superconductivity [12, 13, 14].

In this thesis work, we indeed aim at measuring very low temperature electronic transports of fully functionalized and integrated graphene quantum devices. To achieve this goal, we have built an experimental protocol allowing us to grow high mobility graphene, transfer it on substrates, and control the amount of electronic disorder and integrate it in quantum devices.

### THE QUESTIONS ADDRESSED IN THIS WORK

Today, CVD of graphene on Copper [15] is undoubtedly the best technique to grow macroscopic monolayers that can be further transposed on arbitrary substrates. However, this technique is still plagued with a series of flaws and drawbacks: the produced graphene still show structural defects such as wrinkles, mosaic of multi-grains, multilayers patches, etc. Therefore, many challenges remain before one could use this technique for mass production of electronic devices. For example, is it possible to grow continuous layers of graphene with mobility comparable to exfoliated devices? For production of graphene useful for large scale integration, the ultimate goal would be the production of a pure single crystal of graphene at the wafer scale. Is it possible to improve the CVD on Cu to get rid of these defects, for example, to have absolute monolayer graphene? These issues are reviewed in the first chapter of this thesis, in which details of the CVD growth methods will be introduced, as well as a novel method to fully suppress the multilayers patches which is known to cover a significant surface amount of CVD graphene.

Graphene grown on metal has to be transferred onto insulator substrates for nanoelectronics applications. How can this be realized? And how can the graphene we produce compare with state-of-the-art, since the most promising short-term application prospect of graphene concerns transparent electrodes? We address these issues in chapter 2. Graphene dry/wet transfer processes are discussed, and we will also show our demonstration of flexible transparent electrodes made of CVD graphene.

Graphene consists of basically two surfaces and no bulk, therefore it is easily influenced by the environment, such as adsorbates (physically or chemically bound to the surface). This raises another question of whether it is possible to produce really "neutral" graphene with a very low doping level (i.e., below $10^{11} cm^{-2}$)? How can one get it as clean as possible, with a surface free from contaminations and compatible with STM studies? To answer this, we will explore a series of cleaning methods in chapter 4, with emphasis on the method of acetic acid removal of PMMA residues.

Another important issue in graphene nanoelectronics is the control of lattice disorder (such as hole, edge roughness, vacancies, grain boundaries). As disorder in a low dimensional system drastically affects the electron mean free path, phenomena such as weak- or strong-localization will appear while cooling or tuning the carrier density. This could also lead to a metal-to-insulator transition. Is it possible to devise methods which allow tailoring precisely the level of disorder by inducing well-controlled amount of atomic scale defects? Chapter 5 in this dissertation will deal with this problem. We will introduce the background of conventional plasma methods of inducing disorder, and will show our results using a chemical route.

The discovery of graphene has produced for the first time, a fully naked 2D electron gas, which is of great interest for the investigation of graphene hybrid systems. For example, when decorated with superconducting nanoparticles, graphene is able to extend a tunable 2D superconductivity to a macro scale by percolation of the local superconducting proximity effect. What kind of physics will dominate when superconductor-decorated onto CVD graphene is coupled to another physical parameter, such as the level of disorder?

In the final chapter, we will show our experiments on superconductor-to-insulator quantum phase transition when a disordered CVD graphene is decorated with random network of tightly-packed non-percolating superconducting nanoparticles. Moreover, we will also discuss the new generation of graphene hybrid devices, i.e., sparsely-distributed regular triangle arrays of superconducting nanoparticles decorated CVD graphene. In this kind of device, due to the quantum phase fluctuations inside each superconducting island, global phase coherence is broken, and a new metallic state is established.

In the following sections, I will detail one after another the main results for each chapter of my thesis.

# 1 GROWTH OF HOMOGENEOUS MONOLAYER GRAPHENE ON COPPER BY INNOVATIVE PULSED-CVD.

*In this part, we introduce the mechanism and recent progresses of graphene grown on Cu foils. We were the first to conceive a new method based on the pulsed-CVD technique to completely suppress the parasitic multilayers of graphene during growth on normal Cu foil.*

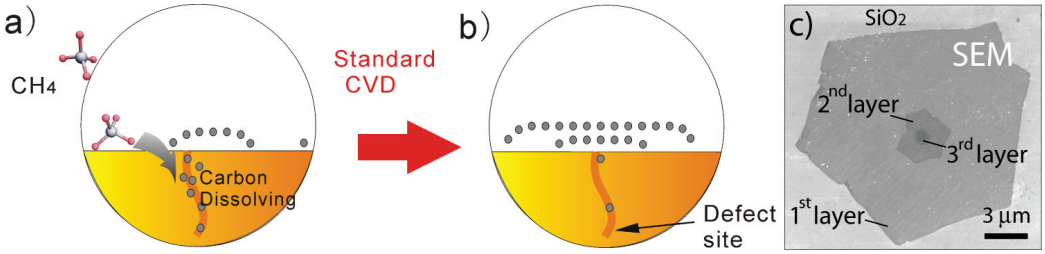


Figure 0.1: a) and b) Schematics highlighting the growth mechanisms near a defect site on copper for standard process on Cu (continuous CVD), leading to a real graphene flake with multi-layers in c) SEM picture of a graphene grain after transfer on oxidized silicon. Notice that the multilayers appear in the center, which indicates the site of nucleation.

CVD, in full terms "Chemical Vapour Deposition", has become one of the most efficient way to produce large-size, high-quality graphene [15]. It is a booming research area for graphene as more than 1600 papers have been published during the last three years.

Copper foil is chosen to grow graphene mainly because it provides a sacrificial catalytic substrate. Moreover, a strictly monolayer graphene is believed to grow on Cu due to the self-limiting process due to the low carbon solid solubility in Cu [16]. However, experimental observations show that, so far, in CVD process of graphene on Cu foils, multilayers are often covering a significant fraction of the surface, preferentially at the defect sites on Cu surface, regardless of the growth conditions. The occurrence of multilayer patches in graphene grown on Cu seems in contradiction with the above mentioned "self-limiting" mechanism. Most importantly, we found that those multilayers are detrimental for optical and electronic properties in graphene, and therefore has to be removed by some means.

By comparing our experimental observations with other results reported in the literature [17], we understood that multilayers formation during CVD process is due to the segregation at the Cu foil defect sites, such as grains boundaries, grooves, where carbon can be trapped, and then released, leading to carbon segregation.

Thus graphene multilayers form below the macroscopic layer, as shown in Figure 0.1. Consequently, one has two choices in order to avoid multilayers formation:

(a) to remove all possible defects in Cu foil, which is indeed proven to be true for single crystal Cu or epitaxial thin films [18];

(b) to prohibit the carbon atoms from being trapped at the defect sites. The first choice is affordable in a laboratory-scale, but too costly to serve as sacrificial layers, especially if industrial applications are envisioned.

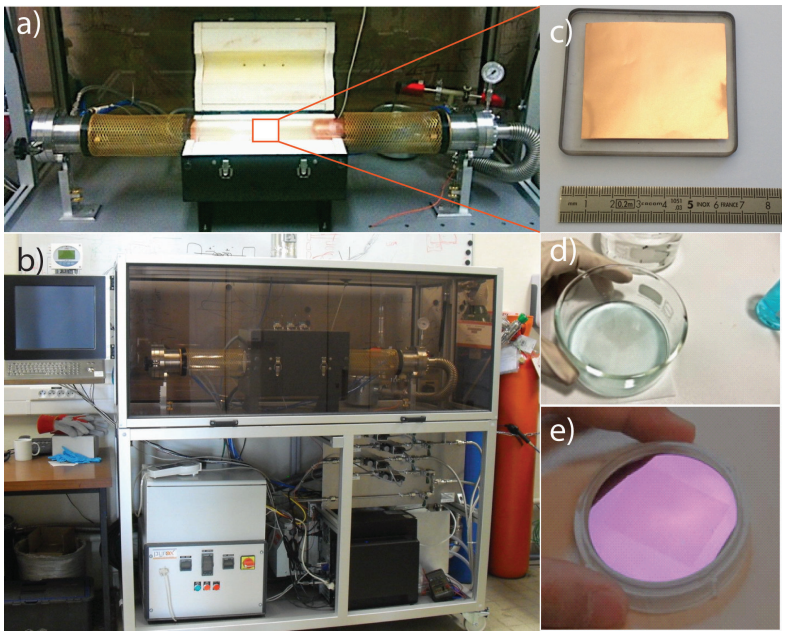


Figure 0.2: a) and b) Our home-designed and home-assembled fully-automatized setup for graphene CVD growth, built up from separate parts. c) a typical Cu foil loaded for graphene growth. d) and e) transfer of CVD graphene onto 2" $SiO_2$ wafer.

As a start, we built a home-made automatized CVD prototype, as shown in Figure 0.2. A 80-mm diameter quartz tube serves as the growth chamber for large size graphene growth. A three-zone furnace with PID-controlled temperatures allows processes up to 1050 °C, with a heating zone of about 0.5 m in length. Pressure of the growth chamber is tunable by adjusting the pump speed. Four mass flow controllers are used to precisely tune in real time the injection of each reacting and dilution gases.

With our home-made CVD prototype, we were able to develop a new method for which we have filed for a patent application, called "pulsed-CVD". The method consists in exposing the catalytic substrate to the carbon precursor in an intermittent fashion of short time periods of alternative durations $t_1$ and $t_2$ Figure 0.3a. This method takes advantage of the etching nature of hydrogen gas separated by duration $t_2$, during which the carbon precursor gas is removed, as indicated in Figure 0.3. Neither graphene obtained by the pulsed-CVD method with parameters for dendritic ($t_1$=10 s, $t_2$=50 s) and hexagonal ($t_1$=5 s, $t_2$=55 s) graphene growth show multilayers (Figure 0.3). When making the number of pulses large enough, continuous and homogeneous layer of large scale graphene, with macroscopically homogeneous one layer can be achieved, as illustrated in Figure 0.4.

The pulsed growth mechanism is proposed as follows: the intermittent absence of methane avoids the defect sites to be saturated with carbon, therefore limiting further segregation and production of multilayer patches. When the

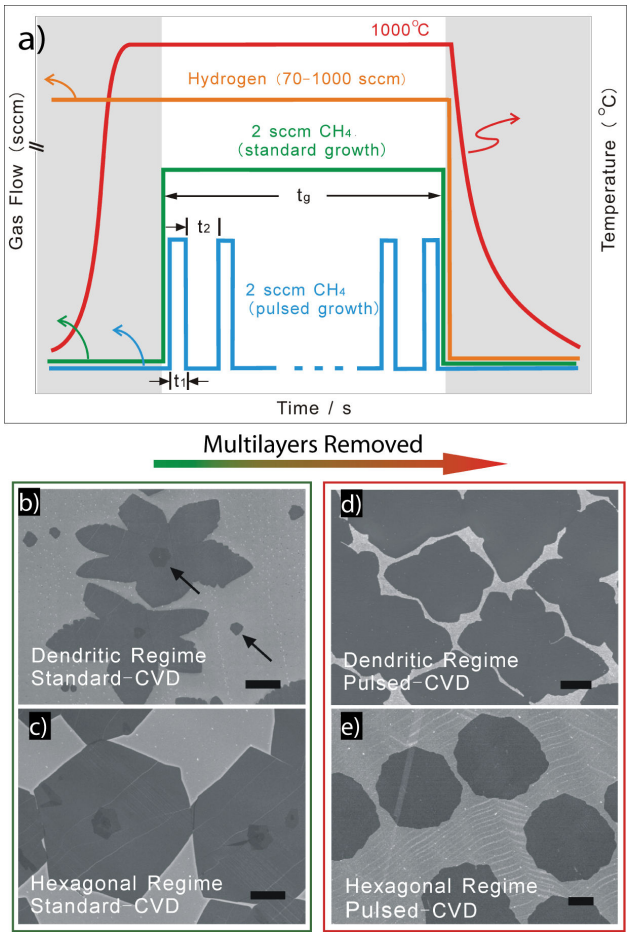


Figure 0.3: a) Work flow of standard and pulsed-CVD. b)-e) Scanning electron Micrograph (SEM) of graphene on Cu for which growth was interrupted before reaching full surface coverage, showing morphology for standard-CVD growth (left column) and pulsed-CVD growth (right column). Arrows in b) indicate the different shapes of small multilayers. Scale bars are 10 µm.

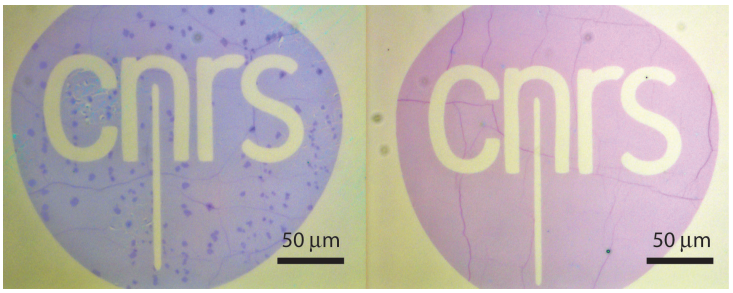


Figure 0.4: Optical micrograph of patterned continuous sheets of graphene grown by conventional (left) and pulsed (right) CVD methods. The multilayer patches create optical distortions on the left, while on the right only wrinkles remain. The CNRS logo was made by lithography and oxygen plasma etch.

first growth step is triggered, a very small amount of carbon can become surface adatoms and diffuse on the Cu surface, whose amount is high enough to trigger some nucleation, but small enough to avoid massive dissolution into defects. The

following idle step thus evacuates free carbon atoms, except for the as-nucleated $sp^2$ bondings, as they are much more stable energetically. If this procedure is repeated in a controlled manner, graphene islands will get expanded in 2D, but without any dissolved carbon underneath, until a complete coverage is fulfilled.

Raman maps (Figure 0.5) of a typical graphene grain grown by the pulsed-CVD method exhibit homogeneous G and 2D band intensity, with negligible D band intensity, suggesting good quality of graphene obtained by this method. Moreover, statistics of field effect measurements were carried out over 20 devices made from standard- and pulsed-CVD techniques, respectively. As shown in (Figure 0.6), charge mobility of graphene obtained by pulsed-CVD method is superior to the one grown by standard method. The best mobility obtained in pulsed-CVD graphene is 6781 $cm^2V^{-1}s^{-1}$.

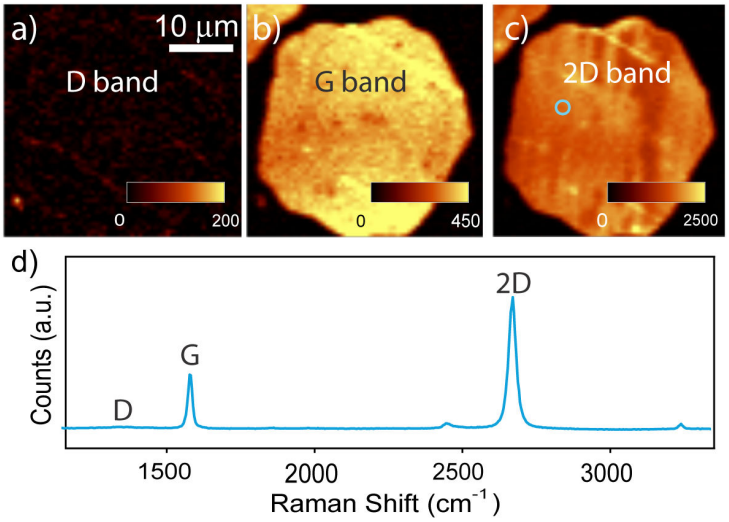


Figure 0.5: Raman map of a) D, b) G, and c) 2D bands for a transferred graphene grain grown using parameters leading to hexagonal grains. d) is a single spectrum taken at the blue-dotted area. The weak intensity of D band (denotes for defects) intensity suggests good quality of graphene.

The pulsed-CVD technique we developed is based on the formation mechanism of multilayers on low carbon solid solubility metals, and it provides an easy and industrially affordable way of obtaining strictly monolayer graphene. So far, the main sources of defects in CVD graphene are 1) wrinkles, 2) grain boundaries, and 3) multilayers. Our pulsed-CVD method ultimately solves the third one.

## 2 FLEXIBLE AND TRANSPARENT HIGH MOBILITY GRAPHENE.

*In order to use graphene layers obtained by CVD growth for applications, we must be able to transfer them on substrates. In this part, we are assessing the performance of graphene sheets transferred on flexible transparent substrate, and the possibility of transferring them onto non-classical substrates such as a TEM grid.*

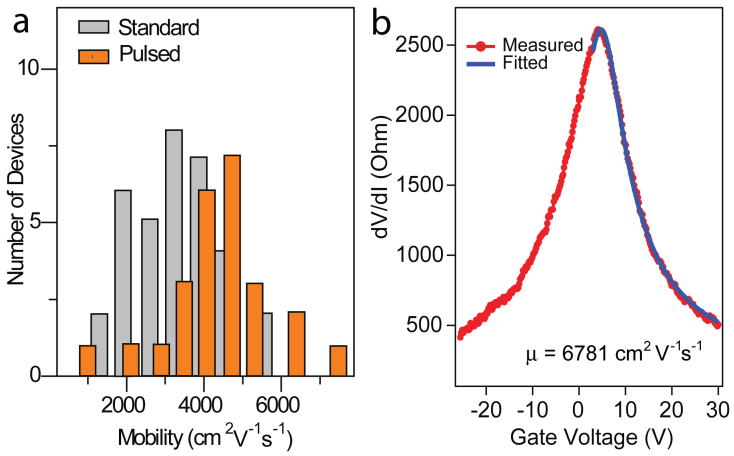


Figure 0.6: a) Distribution of electronic mobility extracted by a semiconducting like fit (see b) of graphene transistor (10 $\mu$mlength$\times$ 5 $\mu$m width) on 285 nm $SiO_2$, grown by standard and pulsed-CVD, respectively. b) the best room-temperature mobility was obtained in a four-probe device made of pulsed-CVD graphene, which is 6781 $cm^2V^{-1}s^{-1}$.

For all industrial and fundamental physics applications, graphene has to be supported on a substrate, either solid (silicon or sapphire wafers, glass plates, etc.) or flexible (laminated inside or at the surface of polymer films). Even though research teams are currently trying hard to get graphene directly grown on insulators, their resultant graphene films are still far from showing good crystallinity [19, 20], or from large size [21]. And therefore, most of the applications are realized by detaching graphene from metal surface such as Cu, as described in part I.

Here we will show the transfer of graphene onto flexible and transparent substrates, as shown in Figure 0.7. Full characterizations indicate that sheet resistance of our CVD graphene transferred onto plastic film (polyethylene) scales down to 200 $\Omega$/square for 4 monolayer stack, whose performance is state-of-the-art, as compared to other reported data Figure 0.8.

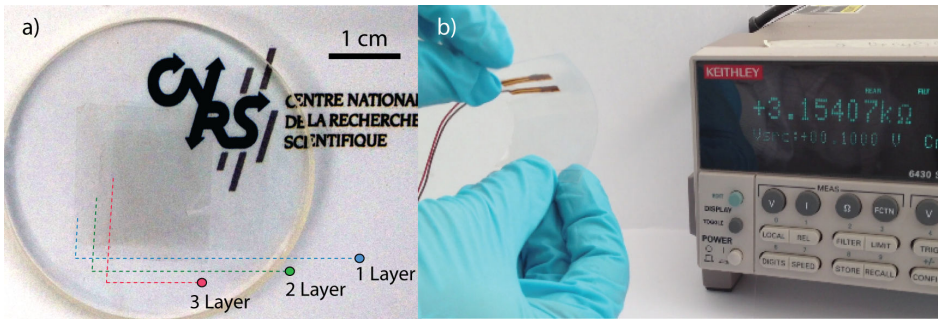


Figure 0.7: a) A glass window covered with CVD graphene transferred layer by layer, up to three layer stack. b) CVD graphene transferred onto a plastic film. Figure of merit of these layers are presented in next graph.

Besides the successful transfer on plastic films, we also demonstrate the transfer of CVD graphene onto transmission electron microscopy (TEM) grids. Two

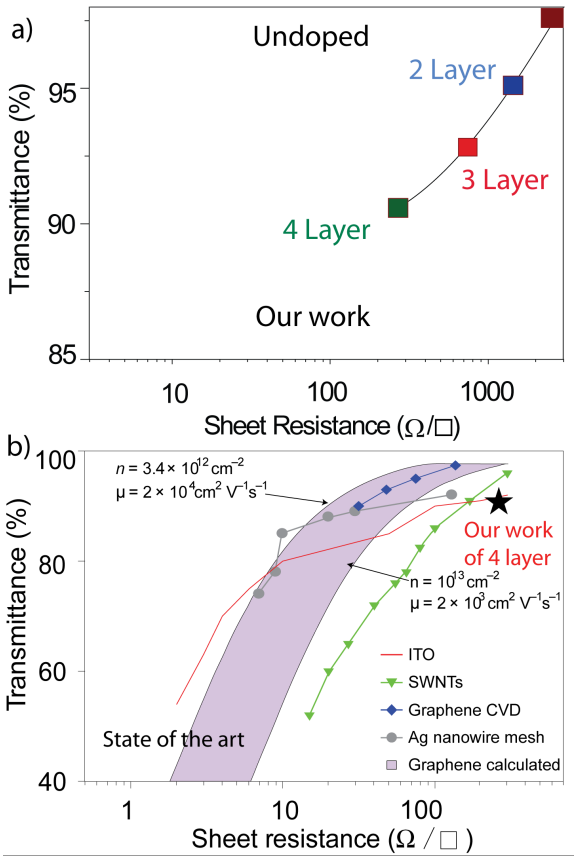


Figure 0.8: a) Sheet resistance versus number of layers of our CVD graphene transferred onto plastic film.Solid line is guide to the eye. b) Performance of transparent conductive electrodes [22]. The data point of our 4-layer transferred CVD graphene is indicated by the black star.

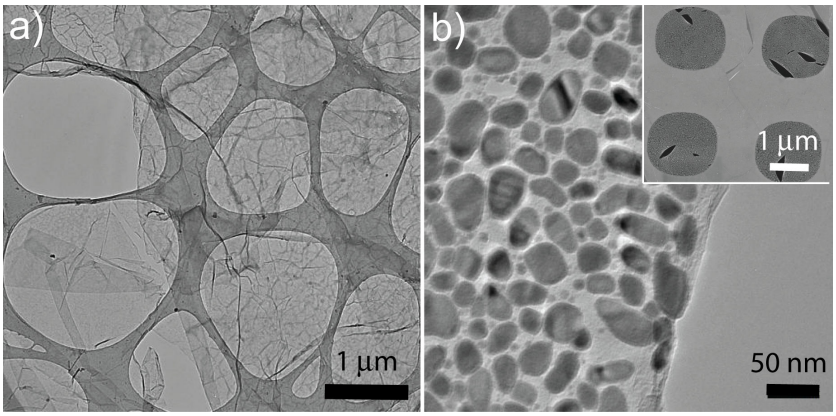


Figure 0.9: a) TEM micrograph of CVD graphene transferred onto a lacey carbon TEM grid, imaged with 80 kV acceleration voltage. b) CVD graphene transferred onto a $Si_4N_3$ TEM grid. Sn nanoparticles are deposited onto graphene by thermal evaporation. Inset of b) is a picture of the zoomed-out $Si_4N_3$ TEM grid with CVD graphene transferred on it.

kinds of TEM grids were tested, the lacey-carbon one, and the $Si_4N_3$ one. It turned out that graphene is able to stick on both kind of surfaces of TEM grids,

and fully suspended over areas up to several μm. This provides us an opportunity to introduce materials on graphene for TEM observation, and the produced graphene-based TEM grid is a promising platform [23] for biological studies, as the deterministic light carbon background can be removed by computer analysis. Moreover, since graphene is penetration-proof (actually almost no molecules can penetrate the graphene lattice [24]), it can serve as a load membrane of microliquid, molecular, or nanoparticles. An example of Sn nanoparticles deposited onto graphene was tested on a $Si_4N_3$ TEM grid with 4 $\mu m^2$ holes, is shown in Figure 0.9b.

The easy-transferable nature of CVD graphene is shown in this chapter to be of versatile uses. And it is of interest for many future applications, such as graphene stacked hetero-structures. The following parts of this thesis is based on the transferred CVD graphene on silicon oxide wafers.

## 3 CHEMICAL CONTROL OF GRAPHENE SURFACE CONTAMINATION AND INTERNAL DISORDER.

*The previous parts demonstrate that we are able to fabricate and transfer high mobility monolayer graphene. We are also able to make the crossover from "clean" graphene to "dirty" graphene, in a controlled manner. In this part, we discuss first several ways of cleaning graphene, and we show that by chemical treatment, one can control the density of vacancies in graphene.*

It is known that graphene is easily doped or contaminated, since its top (and/or bottom) surface is in most cases exposed to the environment. Non-invasive cleaning of graphene is a challenging but mandatory task for transport studies of ultra-clean graphene, such as fractional quantum Hall effect, ballistic graphene junction, etc. There are several routes to achieve that: wet chemistry (solvent, weak acids), dry chemistry (hot reactive gases, such as annealing in hydrogen gas), plasma chemistry (hydrogen, oxygen).

We investigated the field effect of graphene devices by several means, i.e., the acetone removal of PMMA, and thermal annealing. And we show that by acetic acid treatment [25], one can get rather clean surface, which is compatible with STM studies, as shown in Figure 0.10.

Control of lattice disorder (such as hole, edge roughness, vacancies, grain boundaries) is an important issue in graphene nanoelectronics. For electron transport, the presence of disorder scatters the propagation of electron waves, and makes the electrons less mobile (localized). Weak- or strong-localization while cooling or tuning the carrier density in disordered graphene has been studied [26]. Moreover, defects in graphene can play the role of effective magnetic moments, giving rise to the gate-tunable Kondo effect [27]. Therefore, it is of importance to precisely tailor the level of disorder in graphene for transport studies.

Normally, to create defects in graphene, ion bombardment or plasma irradiation is used [26]. Here, we show that when CVD graphene is dipped into a $Na_2S_2O_8$ acid solvent (0.1 g/ml), it becomes defective by increasing the dipped time, as shown in Figure 0.11. A clear increase of the D-peak intensity with in-

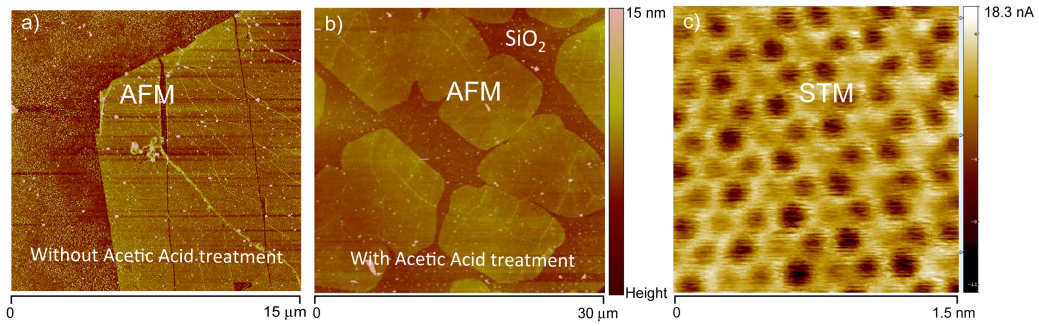


Figure 0.10: AFM tapping mode scan of surfaces of CVD graphene transferred with PMMA assisted method on $SiO_2$. a) PMMA is removed by acetone, and b) PMMA is removed by pure acetic acid for 48 hours. Compared to the acetone treatment, surface roughness is much lower with the treatment of acetic acid. c) STM image of the graphene in b). Image a) is measured by Dipankar Kalita in our group, and image c) is measured by C. Toonoir and C. Chapellier, from CEA-INAC.

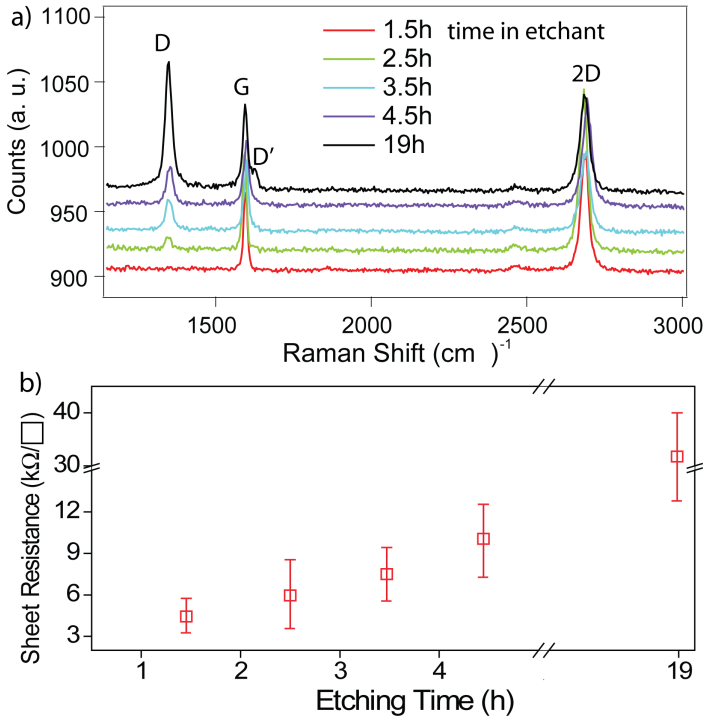


Figure 0.11: a) Raman spectra of graphene treated in 0.1 g/ml $Na_2S_2O_8$ for different durations, and b) their corresponding sheet resistance, showing an almost linear increase of room temperature sheet resistivity with etching time in $Na_2S_2O_8$ solvent.

creasing etching time can be seen in Figure 0.11a, which is characteristic of the increasing amount of defects in graphene. It is noticed that at the right shoulder of the G-peak, there is an increasing small peak called D′, which is also related to defects. It is reported that the ratio of D/D′ intensity reflects the nature of the defect type [28]. In the case of graphene etched for 19 hours, the ratio is about 13, which is believed to be the $sp^3$ type [28].

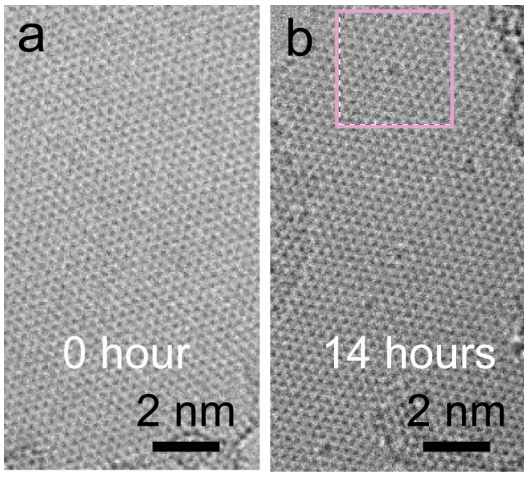


Figure 0.12: a) TEM image of a non-defected graphene membrane transferred on lacey carbon grid. The graphene was grown by pulsed-CVD, cleaned by normal acetone and annealed at 120 °C in vacuum for 2 hours. TEM images taken by Hanako OKUNO from CEA-INAC. b) TEM image of the CVD graphene after dipped in 0.1 g/ml $Na_2S_2O_8$ for 14 hours. Boxed area highlights the defect site.

Sheet resistivity for samples dipped into 0.1 g/ml $Na_2S_2O_8$ for different durations (same set of samples used for the Raman measurement) were also measured. An almost linear increase of room temperature sheet resistivity with etching time can be seen in Figure 0.11b. The resistivity is known to be directly related to the electron scattering by disorder. The increasing sheet resistance and Raman D-peak intensity proves the fact that by simply dipping in a chemical solvent, defects can be induced in graphene.

To check the defects microscopically, we have performed the TEM observation of graphene sheets treated by $Na_2S_2O_8$ for different etching time. As shown in Figure 0.12a, graphene without treatment shows good crystallinity, while the one after 14 hours etching in $Na_2S_2O_8$, in Figure 0.12b, exhibits defect sites throughout the sample.

The chemical method ($Na_2S_2O_8$ solvent) enables easy control of defect level. Almost linear dependence of disorder against time is found in the sheet-resistance of the samples. This method provides opportunities in studies such as superconducting-to-insulating quantum phase transitions [13].

## 4 GATE CONTROLLED QUANTUM METALLIC STATE IN SUPERCONDUCTING TIN ARRAY DECORATED GRAPHENE .

*In the last chapter, we finally address the main course of this thesis, which is devoted to a more fundamental study of low temperature transport of a regular triangle array of superconducting islands on CVD graphene. We demonstrate a gate-controlled quantum phase transition from superconductor to a low-temperature metal state which is induced by quantum phase fluctuations.*

In usual 2D metals, the metallic state is unstable with respect to localization in the presence of disorder [29]. However, an intervening metallic state is often observed experimentally in the region close to superconductor-insulator transitions (SIT) in disordered thin films [30, 31, 32, 33]. To understand the physics behind this quantum metallic state, a model of a quantum phase transition (QPT) in an array of superconducting islands coupled by proximity effect through a dirty metal [34, 35, 14] has been proposed. It predicts that quantum phase fluctuations inside each island will cause a phase de-coherence, which gives rise to the failure of superconducting coupling, leading to a zero-temperature metallic state.

Recent studies [36] of proximity arrays made of Au thin film covered with Nb nano-islands have demonstrated that the critical temperature of such proximity coupled arrays decreases upon increasing the inter-island distance and extrapolates to zero for a finite inter-island distance. It indicates a quantum phase transition to a non-superconducting, 2D metallic ground state [37]. However, due to the lack of carrier density in Au film, they did not have the opportunity to relate experimental results with the above mentioned theory.

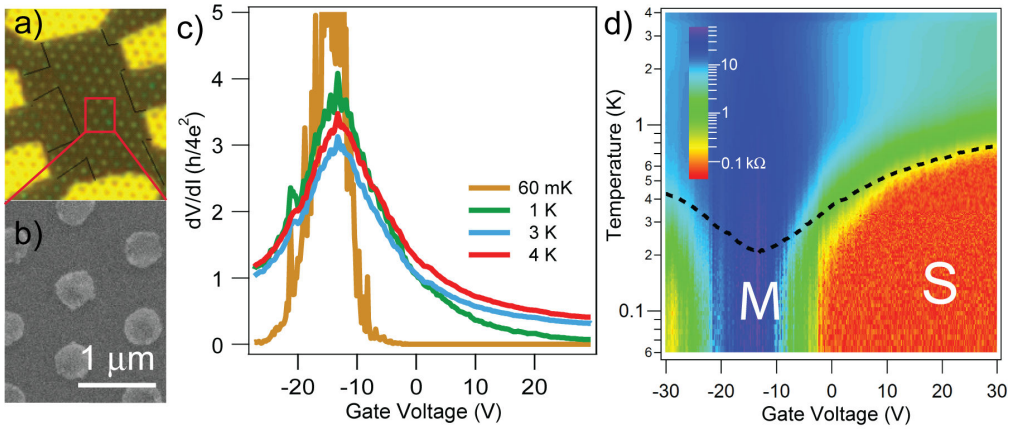


Figure 0.13: a) Optical micrograph and b) zoomed-in SEM image of the Sn arrays of superconducting dots on graphene sample. c) Gate dependence of zero-bias resistance at several temperatures. d) Colour-scaled map of zero-bias resistance versus temperature and gate voltage. Dashed line is the BKT temperature calculated from theory [14]. The letters "S" and "M" denote superconducting and metallic states.

Graphene is an ideal platform for 2D superconductivity studies. Amazingly it is predicted that graphene decorated with 1% of superconducting dots can be easily made macroscopically superconducting [14].

Here, we designed a proximity-induced array, which consists in a triangular lattice of circular superconducting islands on CVD graphene. The CVD-grown graphene sheets transferred onto 285 nm oxidized silicon wafer serves as 2D diffusive metal. The entire graphene surface was decorated with lithography by an array of 50 nm thick Sn nanodisks. These Sn nanodisks have a diameter of 400 nm and are separated by 1 µm between their centres (Figure 0.13a). This kind of regular superconducting arrays on graphene is a model system to study quantum fluctuations of phases, and it is convenient for quantitative comparison with theory. Indeed, proximity coupling through 2D disordered metal is long-range

(decays as $1/r^2$), and thus is amenable to quantitative mean field approximation theoretical descriptions.

Three main features are observed:

1) the good match of superconducting transition temperature between experimental data and theoretical predictions (Figure 0.13.d),

2) the low temperature saturation of resistance at gate voltages close to the Dirac point, which is a sign of metallic state,

3) the formation of a re-entrant superconducting glass state at the lowest temperatures, in agreement with expectations [38].

With the above three experimental observations, we conclude that by studying low density ordered arrays of superconducting islands coupled through graphene, we realized macroscopic superconducting state at high gate voltages. Its transition temperature and critical current are in good agreement with a recently developed theory. We demonstrate a gate-controlled quantum phase transition from superconductor to a low-temperature metallic state with quantum phase fluctuation enhanced conductivity, and discovered a re-entrant superconducting state induced by magnetic frustration.

# 1 SUPPRESSING MULTILAYERS IN CVD GRAPHENE ON CU

*The aim of this chapter is to find a solution for the challenge in suppressing the parasitic multi-layers during CVD growth of graphene on Cu. We will first briefly introduce the recent progress on CVD growth of graphene on Cu. Then we will describe a novel pulsed-CVD process which allows for the growing of fully homogeneous and continuous single-layer graphene up to the macroscale. Graphene grown by this method is then used for further studies in the next chapters.*

CVD, in full terms "Chemical Vapor Deposition", has become in the last few years the most efficient way to produce large-size, high-quality graphene. It is a booming research area for graphene, more than 1600 papers can be found in literature in just 2 or 3 years [39, 40]. However, this field is not really new as systematic studies of graphene growth can be traced back to 1980's. For example, Gall *et al.* [41] tried graphene growth on Ni, Pt, Au, Ru, Rd, It, *etc.*, characterized by Auger spectroscopy, revealing that graphene can grow on many kinds of metals. Among those metals, graphene can have totally different growth kinetics, crystal shape, number of layers, and different coupling with the underneath substrates.

## 1.1 BRIEF INTRODUCTION TO CVD OF GRAPHENE

In general, graphene preparation can be classified into two opposite and complementary classes: bottom-up, and top-down routes.

Top-down means thinning or isolating graphene layer from bulk graphite, for example, by means of the legendary scotch tape technique [42]. Other ways to produce graphene can be found in chemical liquid-phase exfoliation of graphite, known also as a top-down method [43]. Even though presenting the best quality among all kinds of ways of preparing graphene, top-down method gives micrometer size flakes, which is not compatible with the batch-producing of large size graphene. Therefore, this method is rather popular in laboratories, but not compatible with the scaling up required for industrial applications.

Meanwhile, bottom-up is rather a complementary approach aiming at building nano-devices from elemental components, which uses a template substrate to let one deposit or epitaxially grow the target materials. CVD belongs to the family of bottom-up techniques as it makes possible the growth of a material by local reaction and deposition on a surface of precursors present in a gaseous phase.

Principle of CVD graphene is quite simple. One can imagine that in our three dimensional world, a solid can sublimate into the gas phase, with the driving force consisting of thermal fluctuations at the phase boundaries. For example, ice can turn into water molecules and vice-versa. This is very similar to the case of CVD growth of graphene. Only that in the latter case, the "gas" phase is actu-

ally chemisorbed carbon atoms, while the "solid" phase are graphene domains. We call it "chemisorbed", because in general, carbon precursors ($CH_4$, for example) will be trapped onto the catalytic surface and hence de-associate, leaving carbon atoms covalently bonded with the surface. The binding energy of this chemisorption can be as high as 6 eV on Iridium [41]. More than that, those chemisorbed atoms are mobile, behaving like a two dimensional gas. If one continues to inject the precursors, the concentration of carbon atom gas will reach a critical value, and trigger nucleations. It has long been debated in the case of graphene growth, that before nucleation into the initial state of graphene $sp^2$ bonds, carbon atoms tend to form some dimers, trimers, or even 5-atom clusters [44, 45]. It is only for sure that once $sp^2$ bonding starts to form, the chemisorbed carbon atoms will get unbound from the metal surface, instead rearranging into $sp^2$ lattices. This can be simply understood by the fact that graphene is valence saturated and cannot have extra bonding with the underneath substrate [46]. However, it is believed that in Ni or Co, the case is different, because carbon adatoms are actually strongly bonded to the metal. Even though they still form a hexagonal array, strictly, it is not graphene since $sp^3$ hybridizations exist [47].

## 1.2 CVD GROWTH OF GRAPHENE ON CU

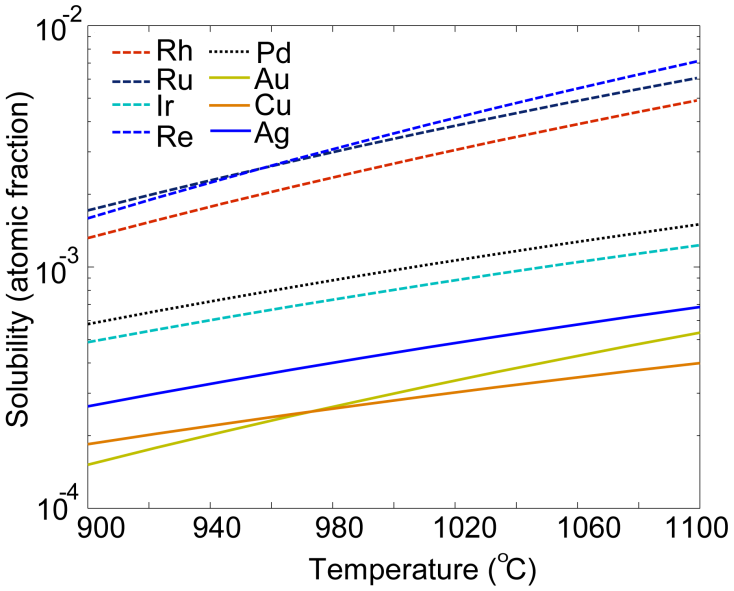


Figure 1.1: Carbon solubility in some metals for high temperatures. Adapted from [48]. Cu has the lowest carbon solid solubility at around 1000°C among these metals.

Carbon solubility varies a lot in different metals, ranging from $10^{-4}$ to $10^{-2}$ atomic fraction [48]. Therefore, the picture of a 2-dimensional chemisorbed carbon atom gas introduced in the previous section is partially true for many kinds of metals. Carbon atoms can not only "swim" on the metal surface, but also "dive" into the bulk via diffusion. The activation energy of such bulk diffusion is of the order of sub-mili-electron-volts [41]. Therefore, the exchange of surface

carbon adatoms and bulk carbon atoms can take place, namely, some of those dissolved carbon atoms will come out to the surface. When they come out from the bulk in a large amount, they start to nucleate at the surface. This behaviour is called segregation. And segregation can happen as long as the nucleation condition is met, regardless of whether there is already a first layer grown there or not. This can actually give rise to the formation of patches of multilayers. The segregation process repeats as the self limiting factor as surface diffusion is no longer active, and eventually thick graphite can form, similar to the case of Ni [49].

As described above, to achieve the growth of graphene with *strictly* one monolayer on the full surface, one needs a metal with low carbon solubility. Cu, Au, Ir, Ag are good candidates. Among all kinds of CVD growth of graphene demonstrated so far, huge progress has been made so far in the topic of CVD growth of graphene on Cu. For example, the 30-inches wide graphene sheets laminated on polymer, largest size ever reported, were grown on Cu. It opens the doors of mass production of graphene and unleashing its uses for flexible electronics [4]. A modification of this process by SONY also resulted in a 100 m long graphene laminated film [50].

Morphology control of graphene has also been extensively studied (as discussed in Section 1.2.1). According to different growth conditions, graphene domains vary from dendritic to hexagonal shapes, with different edge roughness. The consequence of those domains is the eventual formation of multi-grain mosaicity when growing continuous layers by percolation and stitching [51]. And the detrimental effect of the grain boundaries on electron transport is now well known [52]. Therefore, single crystal graphene with large size is the ultimate goal of CVD graphene. So far, several methods have been tried to achieve large single crystal graphene domain, for example, Prof. James Tour's group at Rice University reported a 2.3 mm wide single crystal graphene on Cu by reducing Cu surface roughness [53]. These methods will be discussed in section Section 1.2.2.

Here, our study focuses on Cu, for several reasons:

1. Cu foil is a low cost material and fully accessible industrially, with arbitrary size and thickness.

2. Cu can be easily etched by some standard etchants, such as $Na_2S_2O_8$, $(NH_4)_2S_2O_8$, etc., which makes the transfer of graphene onto arbitrary surfaces a routine task in many labs.

3. Great amount of work can be found in the literature, with all kinds of recipes. This is like cooking guides, which helps to find a set of good parameters according to specific set-ups.

### 1.2.1 *Controlling the shape of graphene domains*

The very first paper of graphene growth on Cu was published in 2009 by the group of Prof. Rodney S. Ruoff at the University of Texas at Austin [15]. It was shown that after being transferred onto $SiO_2$ wafer, electronic mobility of

graphene can reach 4000 $cm^2V^{-1}s^{-1}$. The dominantly monolayer and easy transfer nature of this work instantly triggered a race of growing graphene on Cu all around the world.

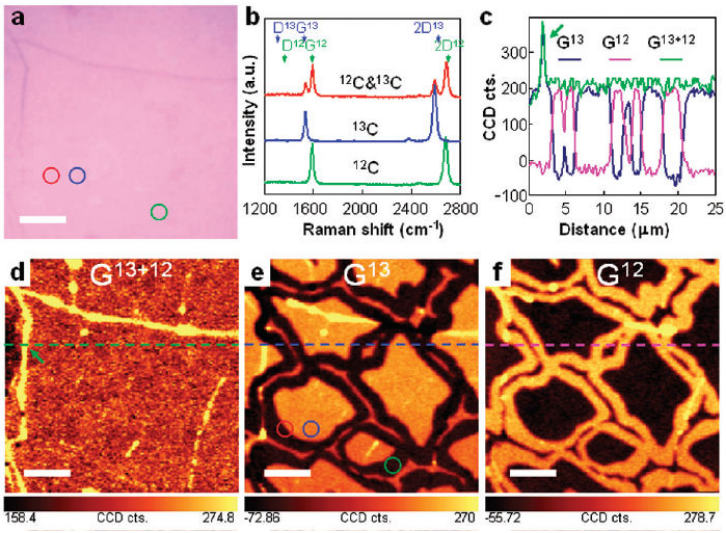


Figure 1.2: The 2D surface limited growth of graphene on Cu evidenced using isotopic labelling of carbon followed by Raman spectroscopy. The growth was made using a succession of $^{13}C$ and $^{12}C$ gases. Picture taken from [16].

Shortly after, Ruoff's group released another work on CVD growth of graphene on Cu [16], in order to discriminate between different growth mechanisms using methane enriched in $^{13}C$. Instead of a constant $^{12}C$ precursor, they used consecutive injections of $^{12}C$ and $^{13}C$ isotope precursors. Those carbon isotopes appeared in a form of contour rings according to the injection sequence, as shown in Figure 1.2. This means carbon atoms do not dissolve into Cu bulk (and therefore became a mix, which is the case for Ni, where no clear contour ring of isotopes can be seen). This is a first and direct proof that indeed on a Cu surface the growth of graphene is confined in a 2D manner. Note that in Figure 1.2, there are wrinkles in the upper-left panel, which does not have any relation to grain boundaries of graphene, since the grain boundaries are indicated by the star-like rings in the Raman mapping (Introduction of Raman will be given in Chapter 2).

It was soon realized that when doing CVD growth of graphene on Cu, different growth conditions lead to totally different shapes: either dendritic [54, 57, 56], or hexagonal [52, 58], as shown in Figure 1.3. In fact, given the dendritic shape of graphene islands, one would immediately think of the very popular theory of fractal growth of crystal developed in 1981 by Witten and Sander, the so-called Diffusion Limited Aggregation (DLA) model [59]. The algorithm begins with fixing one particle at the center of coordinates in d-dimensions, and follows the creation of a cluster by releasing random walkers from infinity, allowing them to walk around until they hit any particle belonging to the cluster. In existing literature, the crystallinity of the dendritic graphene flower is still debated, mainly focusing on whether they are single crystal or not [60, 56].

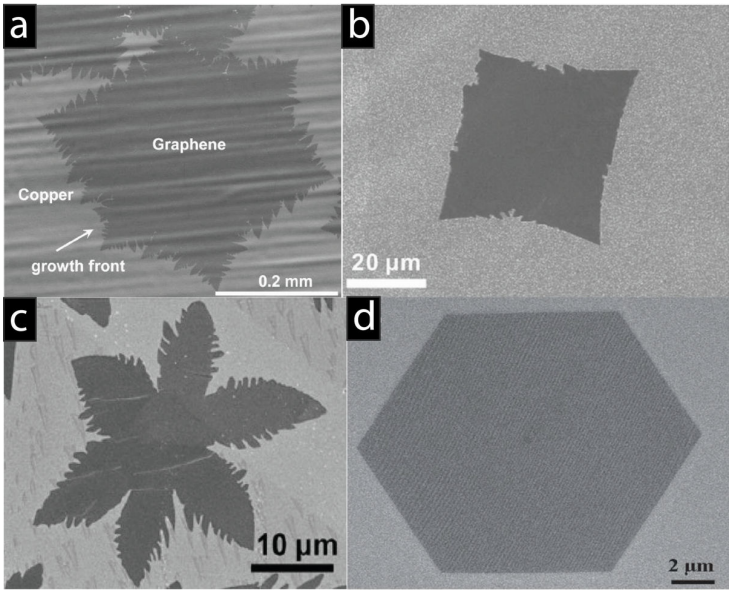


Figure 1.3: Various grain morphologies of graphene domains under different growth conditions. a) taken from [54], b) taken from [55], c) taken from [56], d) taken from [52]. Growth conditions of each can be found in Table 1.

Dendritic graphene islands are always found in a condition of either low total pressure or low hydrogen concentration [54, 57, 56]. Table 1 lists a summary of data, which shows the parameters for obtaining either dendritic or hexagonal shaped graphene islands. All pressures are normalized to the partial pressure of each reacting gases. If neglecting the effect of temperature (suppose the variation of temperature around 1000°C has a negligible effect on growth), then partial pressure $p_i$ and the ratios between gases $\Gamma_{i,j}$ are the only parameters. One can see from this table that, to get hexagonal graphene, there must be two conditions:

1. a low carbon concentration should be achieved, for example, $P_{CH_4}$ <0.1 mbar, for example.

2. when the first condition is fulfilled, the ratio of $\Gamma_{H,C}$ should be large (larger than 200, for example).

An example of pressure dependence of graphene island morphology is given in Figure 1.4. The word "Hexagonality" is a measure of how much the graphene grain is close to a hexagonal shape. As can be seen, hexagonality increases with increasing total pressure, while keeping all other growth parameters the same, except that the growth durations are different. Higher pressure gives much faster growth speed than lower pressure growth.

The above empirical growth conditions are extracted from part of the data existing in the literature. One can see that, to some extent, the dendritic growth requires more chemisorbed carbon atom concentration, or relatively low $\Gamma_{H,C}$. The fact that Cu pocket growth gives fractal growth will then indicate qualitative diffusion rates of carbon and hydrogen in polycrystalline Cu foils. It therefore resembles a lot to the so-called vapor-trapped CVD growth of graphene on Cu, in which the Cu foil is either sandwiched by two quartz plates, or domed with a

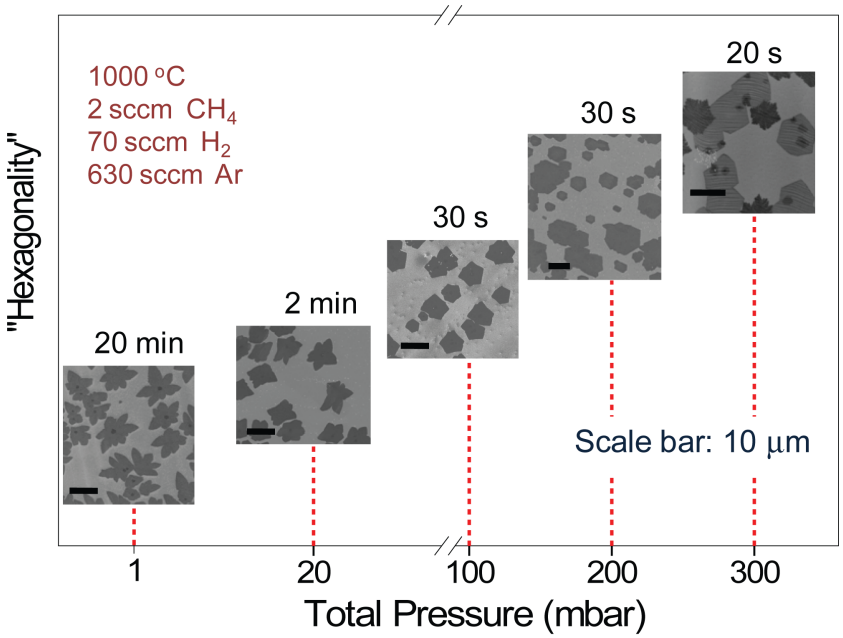


Figure 1.4: Dependence of the morphology of our CVD graphene islands on total pressure for standard growth.

quartz tube [56]. However, this way of growing graphene is not so controllable in terms of growth parameters, as the concentration of gases in the confined zone is unknown, and can vary from sample to sample.

*However, this diffusion method of growing graphene directly on insulator can not produce well controlled continuity and number of layer of graphene, so far.*

Low total pressure is sometimes realized by extracting graphene from the inner wall of an enclosure [56]. In other words, the process is such that there is no direct exposure to gas precursors of the Cu surface. All nucleations can only happen through diffusion of carbon atoms from the outer surface of Cu foil into the inner surface. Grain boundaries will play an important role here, since they can serve as a "speedway" for carbon/hydrogen atoms. Carbon atoms travel through the whole thickness (25 µm) of the Cu foil, while some of them gain mobility and become surface adatoms in the inner wall.

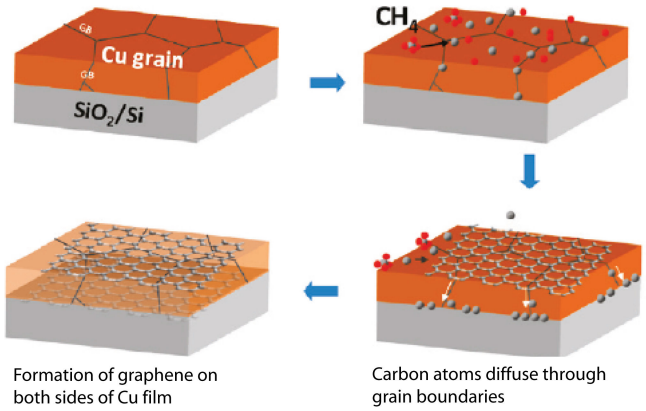


Figure 1.5: Schematic pictures of how the graphene can grow between Cu thin film and $SiO_2$ through diffusion. Picture taken from [62].

Table 1: Typical CVD parameters found in the literature, sorted by the grain morphology.

| Reference | Total P (mbar) | T (C) | $p_{CH4}$ (mbar) | $p_{H2}$ (mbar) | Duration | Size (um) | Shape |
|---|---|---|---|---|---|---|---|
| [57] | $10^{-2}$ | 1000 | Cu Pocket! | | 30-120 min | 20-250 | Dendritic Flower |
| [55] | $10^{3}$ | 1045 | 1 | 1000 | 15 min | 20-500 | Dendritic Flower |
| [52] | $10^{3}$ | 1050 | 0.05 | 60 | 10 min | 10-15 | Hexagonal |
| [58] | $10^{3}$ | 1000 | 0.05 | 20 | 30-240 min | 15 | Hexagonal |
| | | | 0.05 | 10 | >30 min | 15-20 | Flower |
| [58] | 0.5 | 1000 | 0.001 | 0.4 | ? min | 15 | Hexagonal |
| | | | 0.001 | 0.2 | ? min | 15-20 | Flower |
| [61] | > 0.05 | 1100 | 6 sccm/0.0098 | 300 sccm/0.05 | 28 min - 4h | 10-50 | Hexagon |
| This Work | 1 | 1000 | 0.05 | 25 | 5 min | 15-50 | Hexagon |
| This Work | 25 | 1000 | 0.0028 | 0.1 | 20 min | 15-50 | Dendritic |

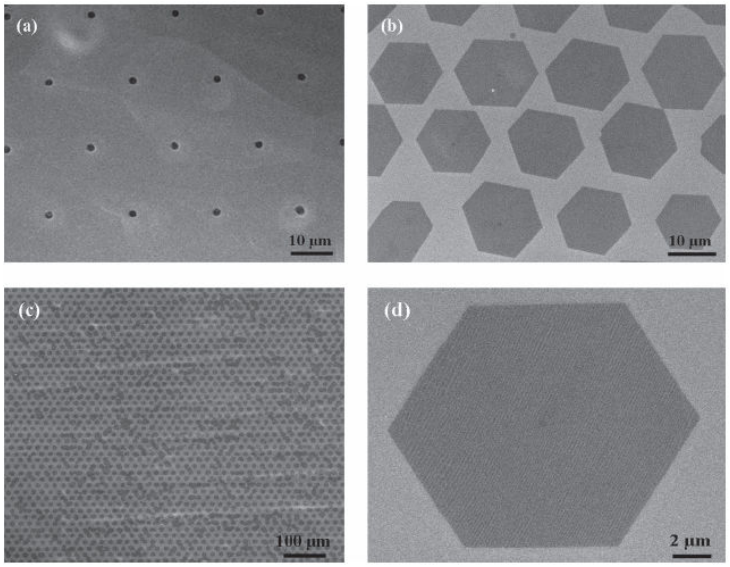


Figure 1.6: PMMA seeds pre-patterned by lithography are preferential places for graphene to nucleate, and regular 2D arrays of graphene grains are obtained after growth. Pictures taken from [63].

This diffusive nature of Carbon atoms can be used as another advantage, i.e., direct growth of graphene on insulator. For example, C. Y. Su et al have achieved a fraction of full coverage of dominantly monolayer graphene by using a thin film of Cu deposited onto insulator surface: normal CVD growth of graphene was performed, except that the thin film of Cu was finally etched away, leaving some graphene layers formed by diffused carbon atoms through the thin film [62].

### 1.2.2 *Control of graphene nucleation*

As discussed in the previous section, graphene is supposed to nucleate when a critical point is reached. Unfortunately, the nucleation cannot be well controlled so far. For example, the grain size of graphene is limited by the nucleation density, since the neighbouring grains will merge and make a grain boundary (composed of a chain of pentagon/heptagon defects ) in order to accommodate the change in crystallographic direction, unless they perfectly match each other, which does not seem to be easily achieved.

Experimental efforts have been done to better understand the nucleation of graphene during CVD growth. One of the most important experiments is the "PMMA seeds" technique [63]. PMMA arrays were pre-patterned on Cu to help initiate graphene nucleations. Interestingly, with proper size (~ 1 μm) of PMMA dots and appropriate distance (~ 20 μm) between them, graphene is confined to grow only at the place with pre-patterned PMMA dots. These PMMA dots are successfully "guiding" carbon atoms to nucleate at the seeds. This technique unambiguously proves that nucleation of graphene happens at places with a higher carbon concentration. However, when the distance between PMMA dots is increased above a critical value (tens of μm), this guiding effect breaks down.

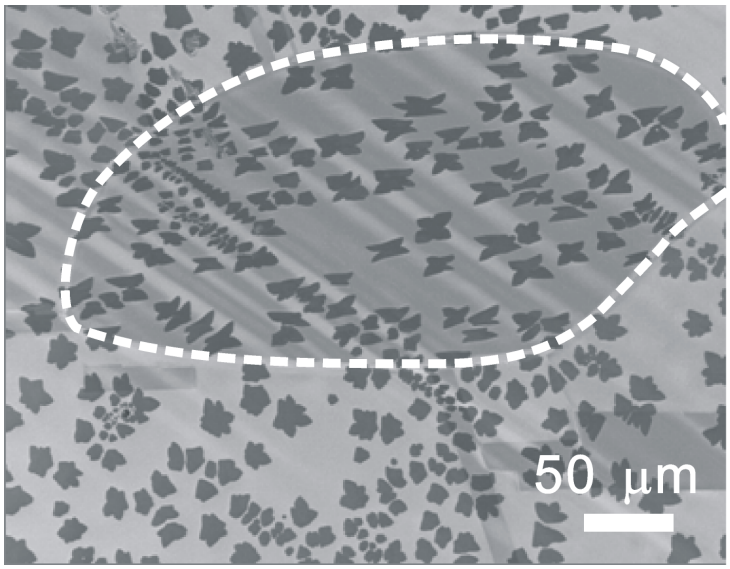


Figure 1.7: SEM Micrographs of copper foil after growth showing the dependence of graphene grain morphology with crystalline orientation of copper. Symmetry difference of graphene islands on neighbouring Cu grains with different orientations. Dashed line highlights boundaries delimiting an isolated grain, within which the graphene domains are four-lobe like, while those outside are six-lobe like.

Surface roughness is believed to have strong impact on graphene nucleation density, as it is straightforward to link the nucleation centers to the rough sites. Ways to avoid roughness include:

(1) Heat treatment, i.e. annealing, at high pressure [53];
(2) Polishing (mechanical or electro-chemical) [53, 64];
(3) Growth of single crystal Cu instead of normal polycrystalline Cu [65]. This is because Cu orientation has an impact on the graphene above it, due to different lattice constant mismatch in between carbon and Cu atoms [66]. We show an SEM picture (Figure 1.7) of graphene islands on neighbouring Cu grains obtained during the same growth batch. One can see that some of the graphene flowers are four-lobe, while in other Cu grains one finds six-lobe symmetry. This symmetry difference clearly shows the influence of Cu orientation on graphene morphology.
(4) Cu enclosed growth (as discussed in Section 2.1) is also an effective way to achieve low nucleation density [54].

While the nucleation density can be affected by Cu substrate defect density and orientation, the injection sequence of gas precursors is also believed to have an influence on the nucleation. A two-step method was described by X. S. Li et al to initiate nucleation via low carbon concentration injection, then increase the carbon partial pressure to achieve large grain size [67].

### 1.2.3 *Role of hydrogen in the CVD graphene growth process*

In most reported recipes of CVD graphene, the reacting gases injected consist not only of a carbon precursor, but also hydrogen, sometimes mixed with another inert gas, such as Ar for dilution purpose. Inert gases are used as they can reduce the partial pressure while keeping a reasonable global pressure (at least compatible with the system which is only design to withstand primary vacuum). One may wonder whether hydrogen is really necessary in graphene CVD growth? The answer is negative. Examples of graphene growth without hydrogen were reported [68, 69]. However, it does not mean that hydrogen is trivial in the process of CVD graphene growth [70, 58]. On the contrary, hydrogen has a direct or indirect involvement in the graphene growth, as discussed below.

First of all, hydrogen is needed before growth, i.e., during the annealing procedure. Hydrogen is not only able to remove the oxide at the surface of copper foil, but also able to enlarge the grain size of Cu. The as-received Cu foil from the factory has typical grain sizes of 10 μm. After annealing in hydrogen at 1000°C for half an hour or more, the grain size can increase to cm scale (they can be checked by the bare eye by tilting the sample). However, normal pressure annealing will not fully eliminate the surface terraces (up to 100 nm in lateral size) of Cu foil, as shown in Figure 1.8. To remove the surface roughness (terraces), one has to do either high pressure annealing of Cu [53], or to melt the Cu into liquid form [61]. Interestingly, graphene can grow over these copper terraces like a carpet (also on Ir terraces [71]), resulting in a continuous film even though the landscape beneath is somehow rough. A scanning tunnelling micrograph (STM) image of a graphene covered local area on the copper foil is shown in Figure 1.9.

More than just the cleaning action of an annealing gas, hydrogen can help to fine tune, for example, the morphology of graphene domains, as already listed in Table 1. Experimentally, hydrogenation of graphene can be realized by hydrogen plasma treatment, thus giving the so-called graphAne [72], a material useful for its reversible electronic properties from insulating to metallic like, as it can be easily reversed to graphene by dehydrogenation.

*Some experimentalists [73] claim that hydrogen would never be cracked by Cu catalyst. Instead, they propose it is rather oxygen impurities in the hydrogen gas who plays the role of graphene etchant. However, their arguments need to be further confirmed by other experimental results [74].*

Moreover, hydrogen plasma is reported to act as a reducing agent capable of etching back graphene. It etches graphene at the pre-defined defect sites, and produce hexagonal pits anisotropically along supposedly zigzag edges. Recent reports show similar results by hydrogen gas during CVD graphene growth at high temperature. So far, it is still disputable how exactly hydrogen is taking effect during growth. It is known that bonding energy in hydrogen is about 5 eV [75], while thermal energy at 1000°C is only about 0.1 eV. Therefore, the catalytic metal surface must play an important role in cracking the very stable hydrogen molecules. A widely accepted mechanism is that hydrogen and/or hydro-carbon is dissociated by the hot metal surface, which can be described as [70]:

$$M + H_2 \rightleftharpoons M + 2H \tag{1}$$

$$C_xH_y \rightleftharpoons xC + yH \tag{2}$$

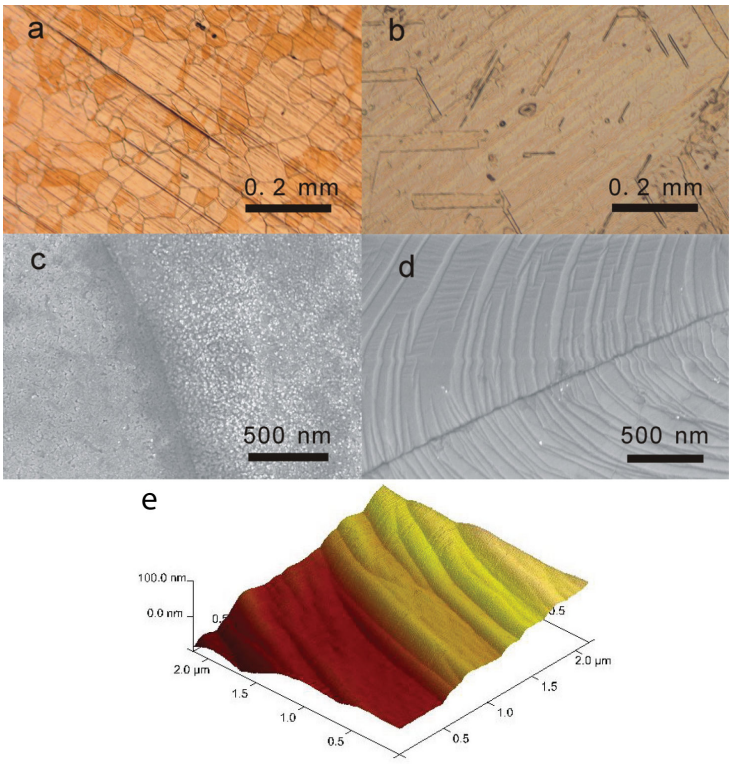


Figure 1.8: Optical micrographs of Cu grains. a) before and b) after annealing in hydrogen at 1000°C for half an hour. c) original Cu foil, d) the SEM image of the Cu terraces after hydrogen annealing, terraces can be clearly seen, leaving atomically smooth copper in between sharp and high steps. e) An AFM scan of local area in d).

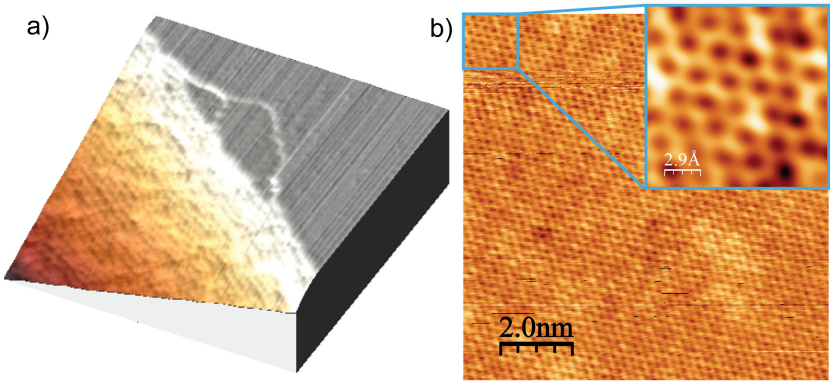


Figure 1.9: STM scan of a local area on graphene-covered Cu. Step edges can be seen in a). Atomic resolution of graphene lattice in the flat region in a) is shown in b), with a zoomed-in micrograph shown in the inset. STM measurements were carried out by Jean Yves Veuillen and Pierre Mallet (Néel Institute).

The above reaction tells that chemisorbed hydrogen can "take away" already deposited carbon, giving rise to a graphene back-etching effect [70, 58]. Due to the very stable $sp^2$ bonding in graphene lattice, it is easier to etch away carbon atoms which are not valence-saturated, such as defected graphene or graphene edges [76, 77].

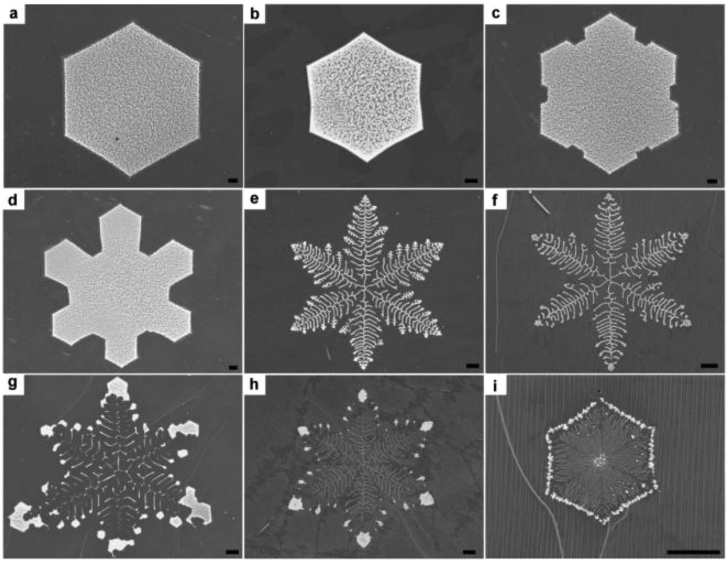


Figure 1.10: Back etching of a graphene crystal by hydrogen, which shows the fractal shapes induced by hydrogen reduction. Picture taken from [78].

In particular, as far as edges are concerned, it is known that zigzag or armchair edges of graphene have different stability energies. It is preferential to form zigzag edges when annealed in the atmosphere of $Ar/N_2$ [79], but there is no preferential orientation under tear force or TEM irradiation [80], nor by hydrogen plasma etching under certain conditions [76]. When carbon precursors are injected together with hydrogen, growth of graphene and hydrogenation/etching of dangling-bonded carbon atoms happen at the same time. The competition between these two reactions induce differences in the final graphene shape. Interestingly, a recent experiment showed that by engineering the parameters of injected gases, graphene can be etched into well controlled anti-flowers, sometimes even a fractal pit [78, 64], shown in Figure 1.10.

### 1.2.4 *Other methods of growing CVD graphene*

As previously discussed, transferable nature of graphene on Cu was thought to be one of its major merits, since Cu can be easily etched by chemicals which seem not possible for noble metals like Pt, Au, etc. This etchable nature is especially important when transparent electrodes are needed.

However, a recent experiment shows that graphene grown on Pt foil can be peeled off safely by hydrogen bubbling without hurting the Pt substrate [81]. Furthermore, graphene grown on Pt can reach mm single hexagonal crystal in lateral size, which is only possible on Cu when Cu foil is specially treated by electro-chemical polishing plus high pressure (2 bar) annealing [53].

Except for metallic substrates such as Ir [82], Au [83], Pt [81], direct growth of CVD graphene onto insulator has aroused intensive interests of experimentalists [84, 21, 19, 62, 85, 86, 87, 88]. As the final step of graphene electronics is always to transfer graphene from a metal onto an insulating wafer, it would be great if one could obtain graphene with good quality directly on an insulator. Indeed

recent progress in this area is rapid and fruitful. Representative works for direct growth of graphene on insulators is listed below:

(1) The diffusion method described in [62, 89].
(2) Plasma enhanced 1575°C growth on sapphire [90]; 950°C growth on sapphire [91],
(3) Dewetting of Cu [20],
(4) Self-assembled monolayer of butyltriethoxysilane with a Ni capping layer [92],
(5) Direct growth of graphene nanopads on exfoliated BN [21], as shown in Figure 1.11. Very recently, epitaxially grown graphene directly on h-BN was reported by Yuanbo Zhang and co-workers [93]. It is supposed that when lying on BN, graphene is least influenced by environmental doping, not only because of the inertness of BN, but also because BN has a similar lattice parameter to graphene, which provides a super-flat matrice for graphene.
(6) Non-contact Cu vapour assisted direct growth on $SiO_2$ [85].

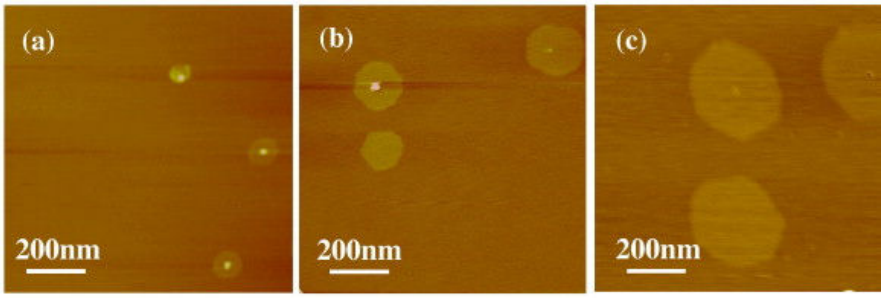


Figure 1.11: AFM image of graphene nanopads grown directly on BN. Picture taken from [21]. Note the size of flakes make the applications difficult.

Apparently, some of the above experimental observations about direct growth of graphene on insulators are in contrast to the conception of CVD as described in section 1.1. Maybe the conventional CVD is in crisis – how can carbon atoms rearrange themselves without a catalyst surface? The answer is not trivial, and further studies are needed.

## 1.3 MULTI-LAYERS SEEN IN GRAPHENE GROWN ON CU

So far, we have mainly discussed in this chapter the basics of CVD graphene growth on Cu. Even though in the past few years it has progressed a lot technically, graphene produced following this growth method is far from ideal: defect-free macroscopic monolayer single crystal graphene. It rather comprises of diverse types of disorders, namely:

(1) mosaicity due to presence of disoriented grains (thus presence of grain boundaries);
(2) wrinkles;
(3) multilayered patches.

All these three types of disorders are recognized as important and timely issues since they limit device engineering and applications. They should be controlled and eventually suppressed to further promote the use of CVD-grown graphene in applications requiring homogeneity.

Considerable efforts during the last few years have been undertaken to try to avoid the above three types of inhomogeneities, and have achieved remarkable improvements since the seminal experiments [15]. For example, the formation of wrinkles, that hamper electron transport [94], may be circumvented by modifying the transfer procedure over the desired substrate [95]. The recent exploration of the growth parameter space allows one to prepare millimeter-size single-crystal graphene [53], thus reducing the influence of grain boundaries which are known to generate electron scattering barriers that limit large scale electron mobility [52].

One of the highlights of the present thesis work is the success in completely preventing multilayer patches from formation via a facile method during CVD growth of graphene on Cu. To address our work in this section, we will first demonstrate the disadvantages of those multilayers in Section 1.3.1. Secondarily, we propose the mechanism of how these parasitic multilayers are formed during CVD process in Section 1.3.2. Finally, we will describe in detail how to suppress them in Section 1.3.3.

### 1.3.1 *The drawbacks of multilayer in CVD graphene*

Before going any further, we will show here an optical image that is commonly seen for CVD graphene transferred onto a 285 nm $SiO_2$/Si wafer (transfer of graphene onto arbitrary substrate will be discussed in Chapter 3), as shown in Figure 1.12. It can be seen that except for a background layer of graphene, there are two other features: (1) wrinkles, and (2) multilayer patches randomly scattered throughout the sample surface.

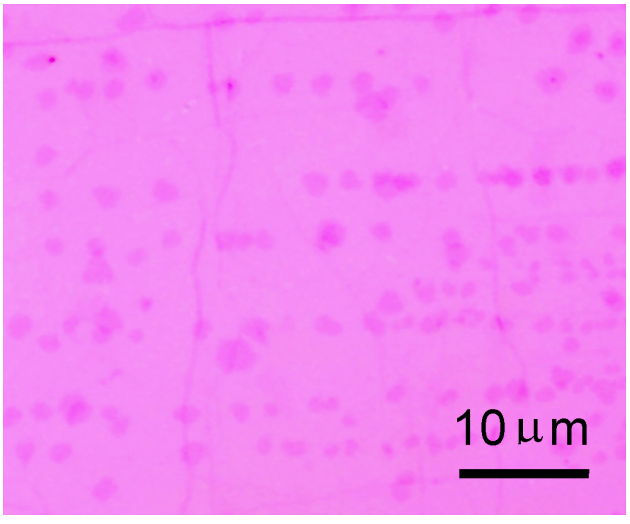


Figure 1.12: Optical micrograph of graphene transferred onto $SiO_2$ wafer. The graphene was grown by the standard CVD method, with parameters shown in Table 2 (Page 53).

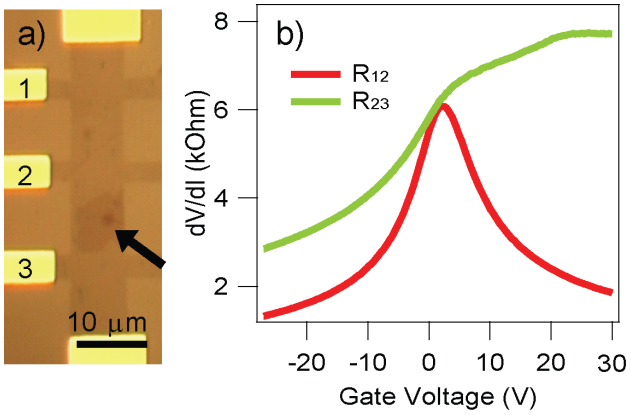


Figure 1.13: a) Optical micrograph of Hall-bar device made using standard-CVD on Cu followed by transfer, plasma etching in Hall bar shape and connection to gold electrodes with two adjacent regions (indicated by an arrow). A multi-layer patch is present between electrode 2 and 3, indicated by the arrow. b) Differential resistance of the two adjacent regions with (green) and without (red) multi-layer patch.

Due to the minimum conductivity, light absorption in graphene is quantized to about 2.3 %, which makes the number of layers easy to recognize under optical or scanning-electron microscope (see Chapter 2.1.2). Thus those multilayers are seen as a higher contrast spot, proportional to their number of layers.

Some may argue that it could be useful to have such multilayers. For example, bilayer graphene with a Bernal-stacking order (i.e., the top layer of graphene is sitting in a manner that the top atoms are right in the center of the hexagonal ring of the bottom ones) is believed to have interest in band-gap engineering. Unfortunately, experimental observation show that in CVD-grown multilayer graphene, the stacking order between layers is rather random [58]. So far only one group claims that they can grow absolutely Bernal-stacking graphene up to wafer scale, which, never been reproduced, seems very unlikely to be true [96].

Except for the optical disorder, we also find that the multilayers are leading to disorder in electronic transport properties of graphene.

*Effect of multilayer patches on electron transport*

To demonstrate the detrimental effect of multilayers on the transport properties of graphene, we have grown graphene based on the seminal CVD process (we will refer to this as standard-CVD) [15]. 10 devices such as the one depicted in Figure 1.13.a were fabricated, with two Hall bars on the same graphene grain, using electron beam lithography followed by oxygen plasma etching. One of them includes a multilayer patch, while the other device serves as a control. We compared the field effect curves in the two parts and observed a systematic reduction of the mobility in the samples with multilayered regions.

As can be seen in Figure 1.13.b, the room temperature mobility decreases from 5000 ($R_{12}$) to about 1000 $cm^2V^{-1}s^{-1}$($R_{23}$). Furthermore, this reduction of mobility is associated with the appearance of several resistance maxima in

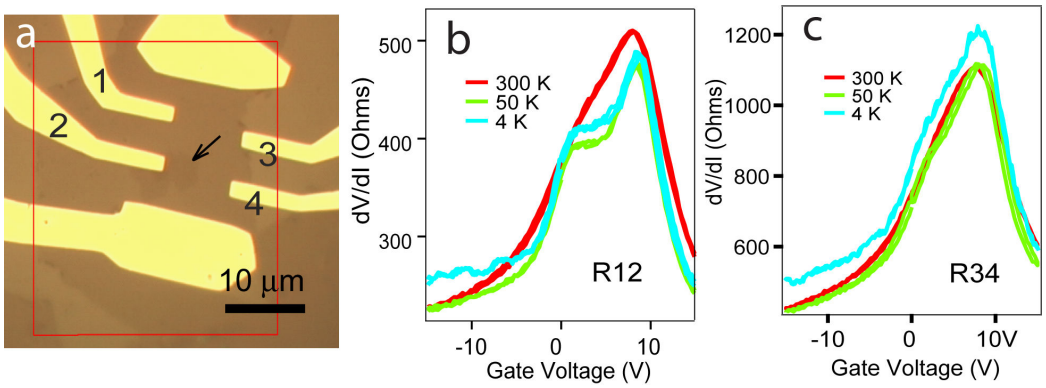


Figure 1.14: a) Optical micrographs of a graphene transistor with two pairs of voltage terminals, one of the pairs (12) is in contact with the central multi-layers region, while another (34) is relatively further from that multi-layer region. b) and c) are field effect measured from each pair of voltage terminals at different temperatures from 300 K down to 4 K.

the field effect curves, indicating that multilayer patches introduce a significant inhomogeneity in the local doping.

It is noticed that such multi-maxima behavior in field effect becomes more pronounced at lower temperature, and/or when the electrodes get closer to the multilayer patch, as shown in Figure 1.14. We understand these features are related to the presence of a p-n junction at the multilayer edge [97].

It is known that randomly stacked graphene layers do not allow coherent interlayer transport [98], but tend to remain decoupled monolayers with only poor interlayer conduction [99, 100, 101, 102]. Therefore, one expects that the multilayer region only participates marginally to the transport, and is under the protection of the top layer from environmental contamination, thus giving rise to a differently doped region. This inhomogeneity in the local doping explains the multi-Dirac-peak structure, increased resistance and decreased mobility.

### 1.3.2 *Mechanism of multi-layer formation on Cu*

For improving the CVD process, one pursues to remove these parasitic multilayers which are optically and electronically contaminating. Before doing that, we need first to understand how the multilayers are formed during CVD growth of graphene on Cu.

Experimentally, standard-CVD process consists of mainly three steps. The first can be called pre-growth stage, when temperature is ramped up and Cu foil is annealed. Second step is the growth stage, when all reacting gases (hydrogen, carbon precursor, $CH_4$ in this work, and/or Ar) are injected in one shot, with a certain time period. After that, the final post-growth stage is mainly cooling down. Our typical work diagram is shown in Figure 1.15.

As described in Section 1.2.1, with this standard CVD growth, one can get either dendritic or hexagonal graphene domains, if the growth is stopped before the graphene domains merge into a continuous layer. In this manuscript, we

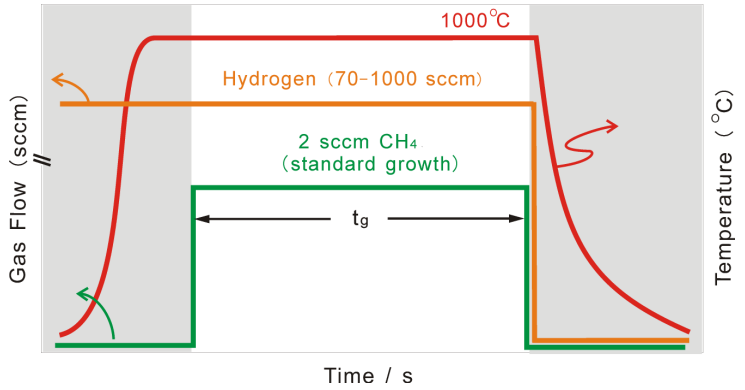


Figure 1.15: Process flow comparing the time evolutions of furnace temperature and injected gases for standard-CVD (continuous) growth.

use two growth conditions to have both regimes of graphene shape, as listed in tables 2 and 3.

Cu foil (25 µm) of 99.8 % purity (Alfa-Elsar) is used in the CVD process. A home-made CVD reactor with a 4-inch diameter quartz tube and effective heating length of about 30 cm was built during the first months of this thesis. Temperature is kept constant using a 3-zone furnace with independent PID feedback control loops. All components are automated by a home-made program, which enables real-time control of flow rate (electronic mass-flow controller) and injection time of reacting gases, as well as pressure (by adjustment of pump speed) and temperature control. Cu foils are loaded into the CVD reactor after acetone cleaning, followed by forming gas annealing at 1000°C for 2 hours. For safety reasons, hydrogen is used diluted in Ar at 10%.

| Regime | $CH_4$ (sccm) | $H_2$ (sccm) | Ar (sccm) | Total pressure (mbar) |
|---|---|---|---|---|
| Dendritic | 2 | 70 | 630 | 1 |
| Hexagonal | 2 | 1000 | 0 | 25 |

Table 2: CVD conditions to obtain dendritic or hexagonal graphene domains.

| Regime | $CH_4$ (µbar) | $H_2$ (mbar) |
|---|---|---|
| Dendritic | 2.8 | 0.1 |
| Hexagonal | 50 | 25 |

Table 3: CVD conditions transformed into partial pressure according to table 2.

Scanning electron microscopy (SEM) images of the two regimes are given in Figure 1.16. Notice that except for the shape difference in the two regimes, there are also growth time duration difference, since in hexagonal regime growth the dynamic is much faster due to higher partial pressure.

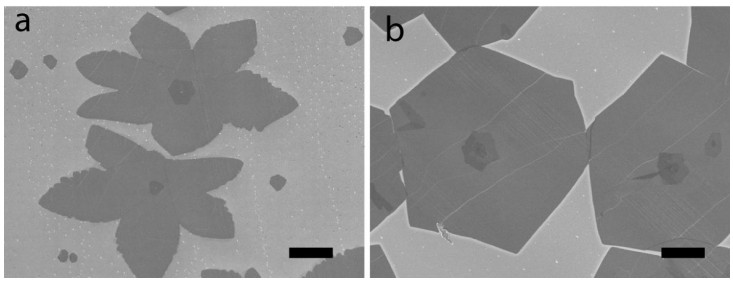


Figure 1.16: SEM micrographs showing a) dendritic and b) hexagonal graphene domains, following growth conditions in table 2, for 20 min and 5 min, respectively. Scale bars are 10 µm.

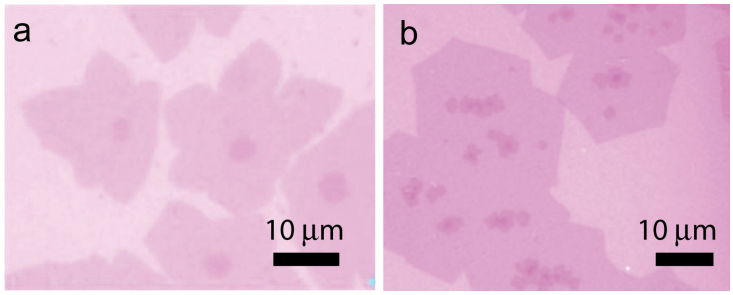


Figure 1.17: Optical micrographs of a) dendritic and b) hexagonal graphene domain transferred onto 285 nm $SiO_2$/Si.

One common point of the two SEM images is that multilayers can be easily recognized, mostly in the center of the graphene domain. The same effect can be seen after the graphene is transferred (for details about transfer method see Chapter 2) onto $SiO_2$ wafers, as shown in Figure 1.17.

Confocal micro-Raman (discussed in Chapter 3) mapping provides an efficient tool to assess for the quality of the obtained graphene. Intensity mapping of graphene specific Raman bands, shown in Figure 1.18, was performed on the hexagonal-regime using standard-CVD and subsequently transferred onto $SiO_2$/Si. The defect-activated D band is hardly detectable except at some edges for both batches. Except for the central region of flakes grown by standard-CVD, the G and 2D bands shows a single Lorentzian shape and are also uniform and narrow. Their full-width at half maximum (FWHM) are 18 and 30 $cm^{-1}$, respectively, with a typical deviation of about $\pm$ 2 and $\pm$ 4 $cm^{-1}$ over the surface of a single flake. These features are typical for high quality single-layer graphene [103]. The central part of the flakes prepared by standard-CVD exhibits non-uniform G and 2D bands, pointing out the presence of few-layer (two, three, or even more) graphene.

Due to the low carbon solubility in copper [48], CVD of graphene on Cu is a surface-confined process which is self-terminated once no more catalytic surface (bare Cu) is available, i.e., once a single layer of graphene covers the whole surface [16]. The occurrence of multilayer patches in graphene prepared by CVD on Cu seems in contradiction with this common wisdom.

A scenario reconciling this apparent contradiction has been proposed recently: carbon adatoms were argued to intercalate in between graphene and Cu via the

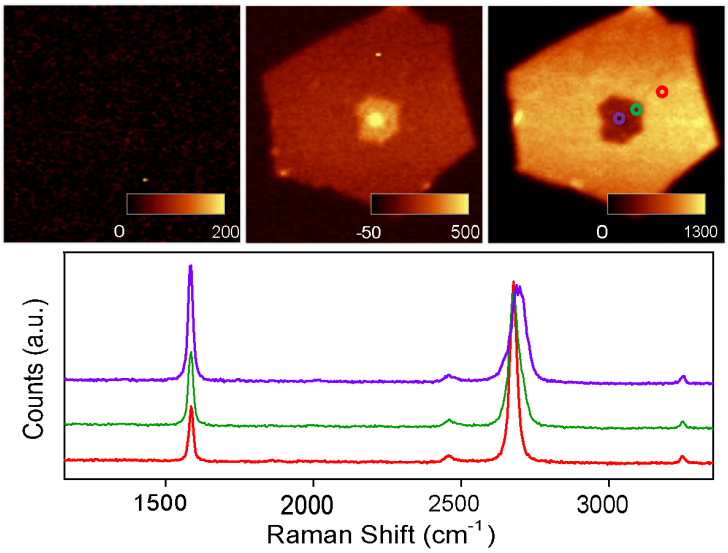


Figure 1.18: Intensity maps (scan area is 20×20 $\mu m^2$) obtained by scanning confocal micro-Raman of graphene grains obtained in the hexagonal regime. Top panel, from left to right, are D, G, and 2D bands. Bottom panel, single spectrum of dotted area.

edges of graphene and condense in the form of a graphene multi-layer patches at the center of the large flake [17].

However, this scenario can hardly account for the fact that multilayer regions of similar shape and size are not only observed at the center of large dendritic flakes, but also in between them (Figure 1.16a), which seem to be a different growth mode than those dendritic flower-like domains.

Actually, all the self-limiting growth mechanism is based on the assumption that Cu surface has a very low carbon solid solubility everywhere, which is not the case as defects are present on normal Cu foils. We therefore interpret this observation by invoking an alternative scenario, in which extended defects in Cu play a central role. Such defects (e.g. Cu grain boundaries) have been shown to be pathways for carbon atoms during CVD of graphene [62]. Another example was demonstrated by manually introducing scratches on Cu surface, which resulted in preferential nucleation sites for multilayer graphene [104]. It can be understood that high carbon solubility and large diffusion coefficient of carbon are taking place at defects such as grain boundaries, dislocations, surface roughness, etc. Prolonged exposure to methane at high temperature during standard CVD, must hence lead to a carbon saturation of the defects. A carbon supersaturation at these defects during CVD, a decrease of the carbon equilibrium concentration along these defects upon cooling down, or a combination of the two, will lead to surface segregation of carbon yielding the observed multilayer graphene patches.

We carried out an easy "scotch-tape" experiment, i.e., to rip off the as-grown continuous standard CVD graphene which is then transferred onto a $SiO_2$ wafer. The result directly proves that those multi-layers are indeed underneath the top layer, since most of them stayed while their "capping-layer" is partially ripped

off (Figure 1.19). This is consistent with the observation elsewhere [17], and also reveals that it is logical to assume the defect-driven formation of the multilayers.

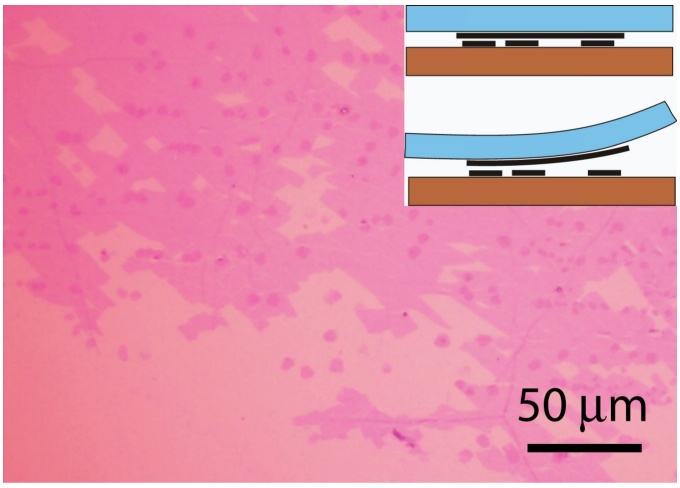


Figure 1.19: Optical micrograph showing the result of scotch-tape exfoliation of our CVD graphene after transferred on silica. The top layer has been partially ripped off on purpose, leaving those multi-layers underlying the continuous layer still on the substrate.

According to all above considerations, we can now draw a schematic picture of how the multilayer can be formed (Figure 1.20). According to this schematic, we may also draw a simple conclusion – to get rid of the multilayer formation, one has two choices:

(a) to remove all possible defects in Cu foil, which is indeed proven to be true in single crystal Cu thin films [18];

(b) to prohibit the carbon atoms from "diving" into those defect sites.

The first choice is affordable in a laboratory-scale, but too costly for industrial application, imaging for example a large scale 30-inch touch screen.

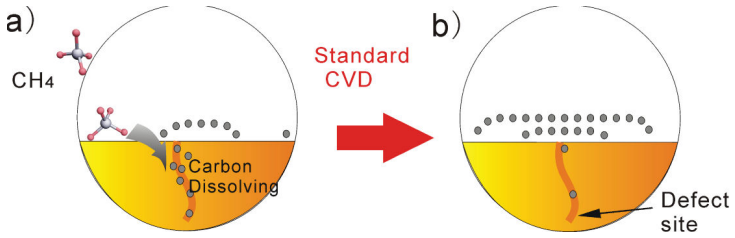


Figure 1.20: Schematics highlighting the comparison of growth mechanisms near a defect site on copper for standard CVD.

### 1.3.3 *Removing multilayer graphene on Cu by a novel Pulsed-CVD method*

As already discussed in Section 1.2.3, hydrogen is supposed to be a powerful element to etch away carbon atoms that are valence-nonsaturated [58, 70, 76, 77]. Moreover, hydrogen etching can lead to well-defined zigzag and/or armchair edges in graphene, as shown in Figure 1.21

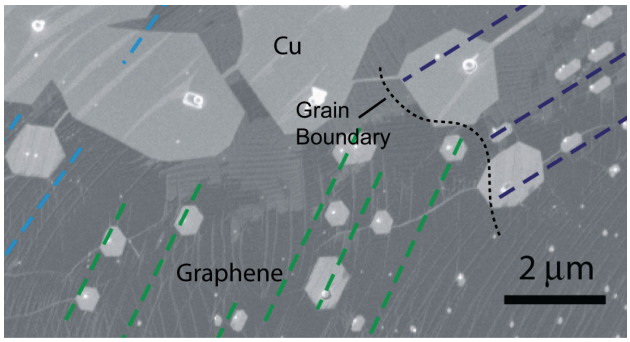


Figure 1.21: Hexagonal pits made by annealing our as-grown graphene in hydrogen gas for 40 min at 1000°C. Dashed straight lines indicate the hexagonal pits that have their edges aligned in the same direction. The three series of straight lines confirm the polycrystalline nature (mosaic like) of continuous graphene films.

At first thought, if one can control the first etch step, which makes a zigzag/armchair edge, and let carbon precursors come again, then a new line of zigzag/armchair can be added if everything is under perfect control. Thus, an epitaxial-like growth could happen, which will only expand along the frontier of one zigzag edge line, as shown in Figure 1.22.

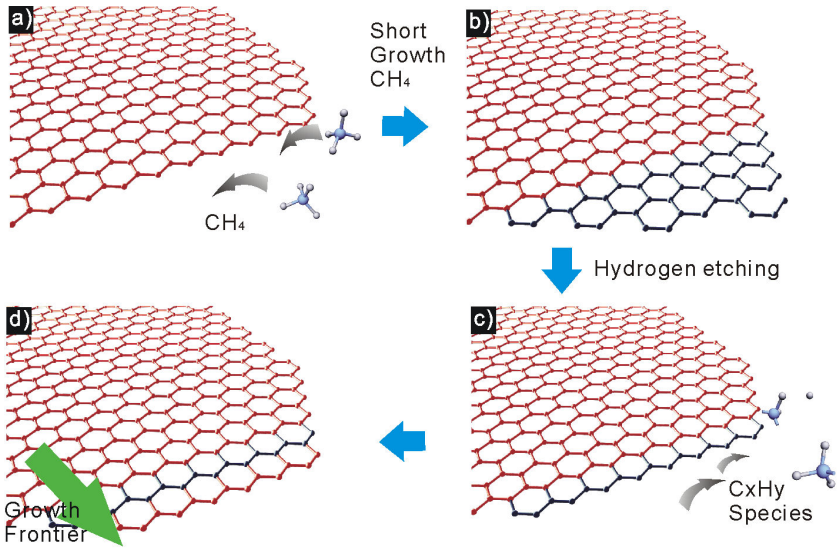


Figure 1.22: a) to d) Schematics about the conjecture of having "epitaxially" grown frontier of graphene edges via alternative "hydrogen etching" and "carbon addition" steps. Here we suppose a zigzag edge.

Inspired by the above idea, we designed a pulsed manner of injecting the carbon precursors. We call it "pulsed-CVD", as it consists in exposing the catalytic substrate to the carbon precursor (methane) in an intermittent fashion during the growth steps (Figure 1.23). More precisely, pulsed-CVD is composed of a sequence of methane injection pulses of time duration $t_1$ (typically a few seconds) separated by idle steps of duration $t_2$, during which methane injection is halted while the hydrogen flux is kept constant to the same value as that during

the growth steps. We have found optimal (in terms of multilayer removal) sets of parameters for dendritic, and hexagonal regimes to be ($t_1$=10 s, $t_2$=50 s) and ($t_1$=5 s, $t_2$=55 s), respectively. More experimental details such as the influence of $t_1$ and $t_2$ on the growth will be discussed later.

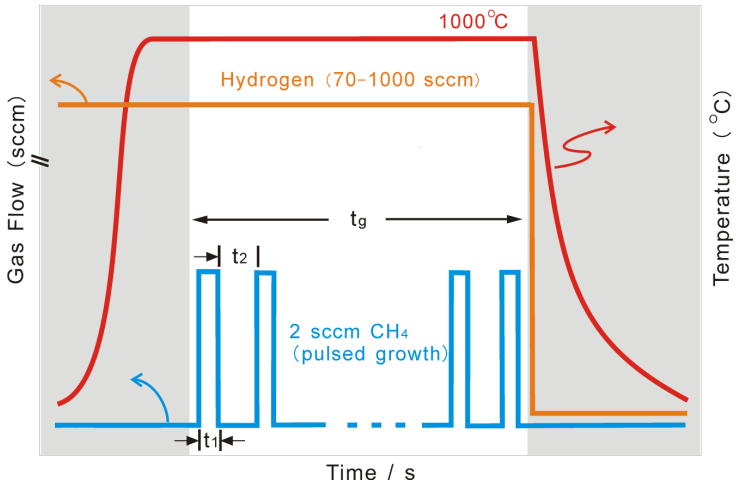


Figure 1.23: Schematic workflow of pulsed-CVD, which is characterized by carbon injection pulse time $t_1$, and idle time without carbon exposure $t_2$, and total growth time $t_g = N(t_1 + t_2)$, with N being the total pulse numbers.

Surprisingly, the result of our as-designed pulsed-CVD growth was not the one we expected at all. As shown in Figure 1.24, instead of the expected epitaxially grown graphene along a specific edge, graphene grown in both dendritic and hexagonal regime shows smoothed edges compared to the standard one. A significant modification of grain shape is observed for pulsed-CVD in the hexagonal regime, in which the hexagonal shape is partially removed, giving rise to a more rounded polygon, a shape that we attribute to be the hallmark of pulsed CVD growth. Such a shape results from the back-etching by hydrogen during idle time, as it shows a multi-faceted grain with an almost circular general shape. After being transferred onto $SiO_2$/Si wafers, one can see that the shape of the pulsed-grown graphene at both dendritic and hexagonal regimes are the same as observed by SEM.

Notice that when looking into the sample throughout the wafer surface (cm size), one could find only one contrast of graphene flakes on silicon wafer. This means that, the number of layers is homogeneous.

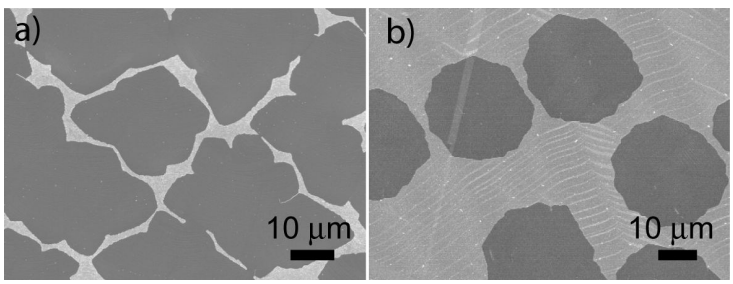


Figure 1.24: SEM micrographs of graphene domains grown by pulsed-CVD at a) dendritic and b) hexagonal regimes.

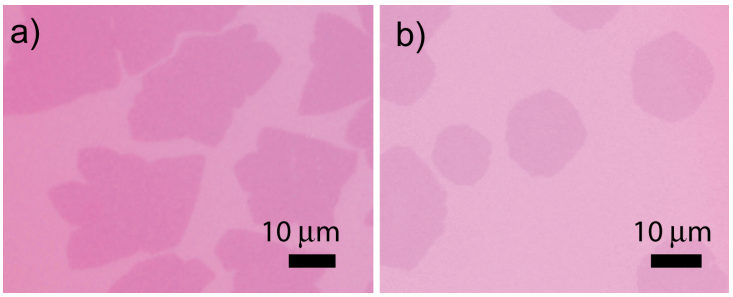


Figure 1.25: Optical micrographs of graphene domains transferred onto $SiO_2$/Si wafers, grown by pulsed-CVD at a) dendritic and b) hexagonal regimes.

To cross-check the number of layers, we carried out Raman measurements on the pulsed-grown samples. Taking the hexagonal regime sample for example, it turns out that the Raman signal of the sample shows uniform intensity as seen in the mapping of D, G and 2D bands in Figure 1.26. Single-Lorentzian profiles of G and 2D peaks unambiguously show a monolayer graphene feature. Furthermore, no noticeable D band can be found in the graphene domains, suggesting high quality graphene obtained by this pulsed-CVD method.

At this point, we have observed a totally new phenomenon rather than what we were thinking at the very beginning: an absolute single-layered graphene was obtained. To understand it, our assumption of defect-driven segregation of multi-layer during CVD still holds.

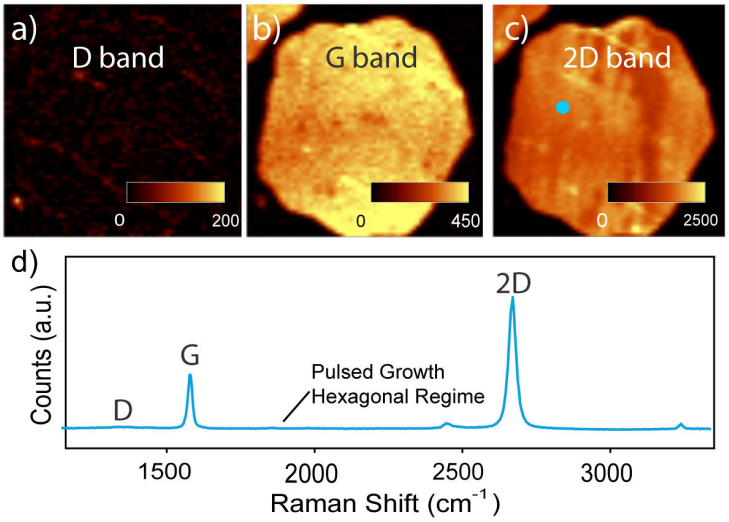


Figure 1.26: Raman maps of a) D, b) G, and c) 2D band of pulsed-CVD grown graphene grains at the hexagonal regime. d) is a single spectrum taken at the blue-dotted area. Faint D band is found along grain ripples but overall quality is good.

By means of pulsed CVD, the carbon concentration at Cu defects is reduced, most probably due to the presence of the reducing $H_2$ atmosphere, so that no segregation takes place. In that case, only surface-confined growth mode is activated. The smoother edges of graphene domains in pulsed CVD can be understood as the hydrogen not only etches carbon away at the defect sites in Cu, but also at the edges of the already-grown graphene islands. Except for the

lowest coordination sites, at corners, the cohesion of graphene, both inside the flake due to the stable carbon $sp^2$ bonding (~ 5.9 eV [75]), and at their edge, presumably due to stabilizing Cu-C bonds, makes the etching of the as-grown graphene a relatively slow process. Thus, an adequate choice of the methane pulse and idle times allows consuming the whole carbon feedstock inside the extended defects in Cu, while only marginally etching the pre-existing graphene flakes. The subsequent methane pulse will then further extend the graphene flake, and so on until full coverage by a single-layer of graphene free of any multilayer patch, as shown in the schematic picture in Figure 1.27. Notice that the pulses are not meant to be identical in their flow rate, one can also adjust them in an incrementally pulsed-growth.

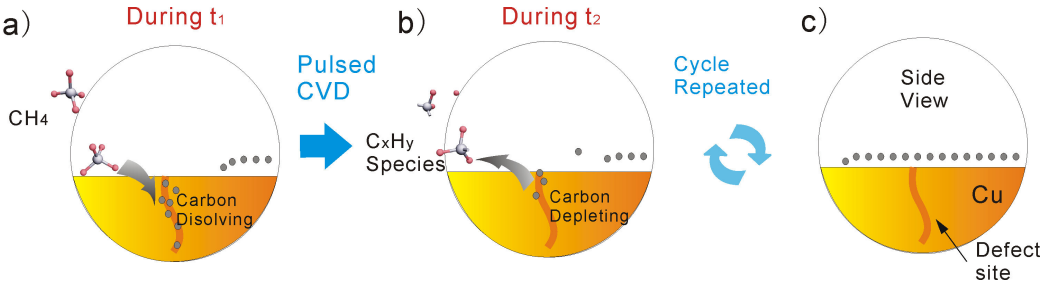


Figure 1.27: Schematics of growth mechanism near a defect site on copper during pulsed CVD. The idle time leads to discharge of the carbon content that is trapped.

The key point is that, the times $t_1$ and $t_2$ must be well controlled. Indeed we found that a good tuning of $t_1/t_2$ ratio is crucial to achieve exactly one monolayer, since too long $t_1$ will let C segregation at defects re-appear, while too long $t_2$ will lead to low coverage of graphene and prevent formation of continuous films. For example, when $t_1$ is kept at 10 s, while $t_2$ is increased to 180 s, one can see no graphene coverage is obtained, as shown in Figure 1.28.

The fact that $t_1$ needs to be kept very short is easy to understand, since one has to let the carbon atoms to have no chance to dissolve in an extended defect site. Therefore, a high enough concentration of reductive hydrogen environment should be present before any carbon precursor is injected. When the first $t_1$ is triggered, carbon in a very small amount can become surface adatoms and "swim" on the Cu surface. This amount is high enough to trigger some nucleation, but small enough to avoid massive dissolution into defects. Following $t_2$ thus evacuates all free carbon atoms, except for the as-nucleated $sp^2$ bondings, as they are much more stable energetically. If this procedure is repeated in a controlled manner, graphene islands will get extended in 2D, but without any dissolved carbon covered underneath, until a complete coverage is obtained.

The short injection time of a few seconds, but hundreds of cycles are controlled by a home-made program. However, CVD growth conditions can vary from one set-up to another, due to a different chamber size, different controller for gas injection, carbon precursor concentration, etc. Figure 1.28 lists several $t_1/t_2$ ratios, which is a simple guide-line for a starting point to search for a monolayer-parameter point according to one's own CVD set-up. A more complete diagram for our set-up may be given in the future.

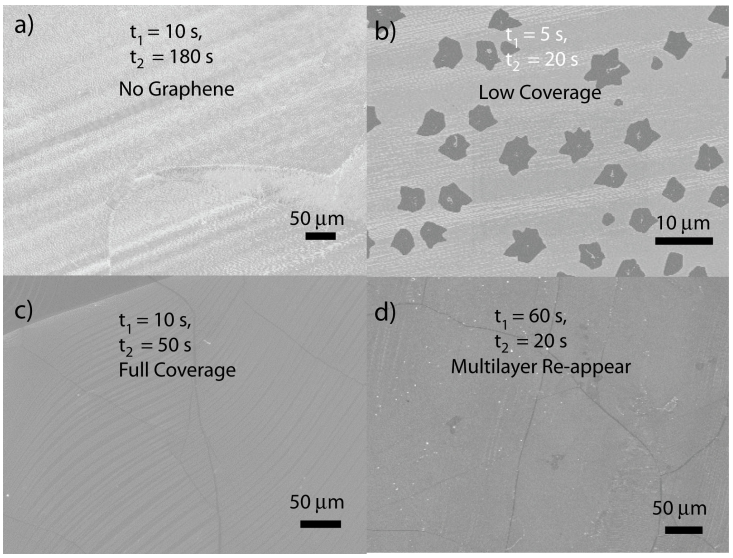


Figure 1.28: SEM micrographs showing that different $t_1$-to-$t_2$ ratios lead to different surface coverage of graphene on Cu. a) No graphene coverage can be found when idle time $t_2$ is too long. d) When $t_1$ is too long, reappearance of multilayers occurs. Growth conditions for the four cases are based on same partial pressure, temperature, and same total dose of carbon precursor, namely, flow rate multiplied by total injection time of 6000 sccm·s.

As a control experiment, graphene devices made from pulsed-CVD are also measured at room temperature on $SiO_2$/Si substrates, showing the best mobility of 6780 $cm^2V^{-1}s^{-1}$, and a mean value of about 5000 $cm^2V^{-1}s^{-1}$ (see Figure 1.29). This suggests that the pulsed-CVD technique does not degrade the graphene quality, in agreement with the previous Raman measurements.

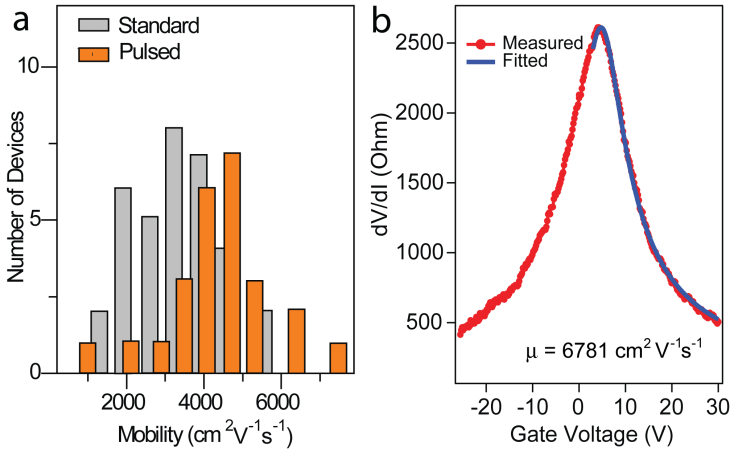


Figure 1.29: a) Statistics of electronic mobilities of graphene devices on 285 nm $SiO_2$, grown by standard and pulsed-CVD, respectively. b) The best mobility obtained in pulsed-CVD graphene, which is 6781 $cm^2V^{-1}s^{-1}$.

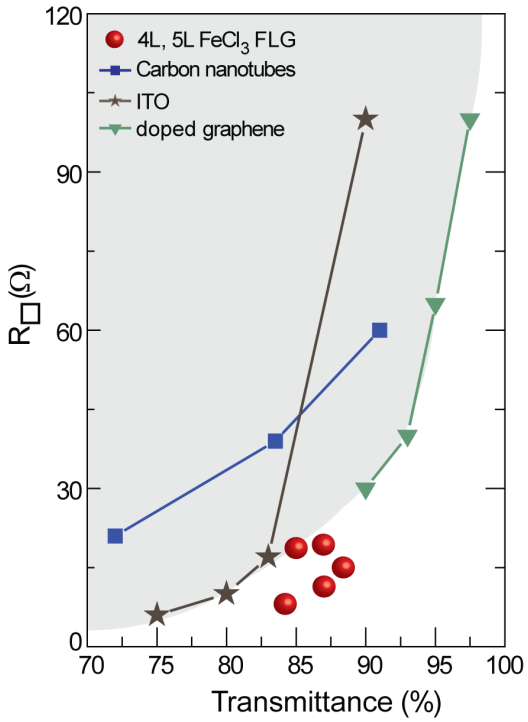


Figure 1.30: Square resistance versus transmittance at 550nm for 4-layer and 5-layer $FeCl_3$-FLG (GraphExeter), comparing with ITO, carbon-nanotube films, and other doped graphene materials. $FeCl_3$-FLG outperforms the current limit of transparent conductors, which is indicated by the grey area. Adapted from [105].

### 1.3.4 *Optical properties of graphene improved by Pulsed-grown graphene*

The inhomogeneity in the number of layers has also important consequences on the optical transparency of transferred graphene layers. Indeed, due to quantized optical absorption (see Ref. [1], N-layered regions at patches show optical density increased N times compared to the monolayered zone, at least for N<10 as formed in our patches), as shown in Figure 1.31. Our pulsed-CVD technique provides the opportunity to suppress such dark spots for applications in a low-cost and easy-accessible way.

Taking as an example the prospect of using these layers for transparent and flexible electrode applications, which appear as one of the most realistic short-term industrial use of graphene, we have fabricated a graphene stack by repeating transfers on top of each other.

The importance of stacking graphene layer by layer is to reduce the effective sheet resistance $R_\square$, while keeping a reasonable total transparency. It is therefore suitable for flexible transparent electrode applications.

The optical transparency of five monolayer-thick samples becomes comparable to that of ITO-based materials while presenting a superior electronic conductivity [4]. Recently, it has been shown that when ferric chloride molecule doped few layer graphene, the so-called GraphExeter, the optical performance reported is better than ITO, see Figure 1.30 [105]. Due to random position of patches,

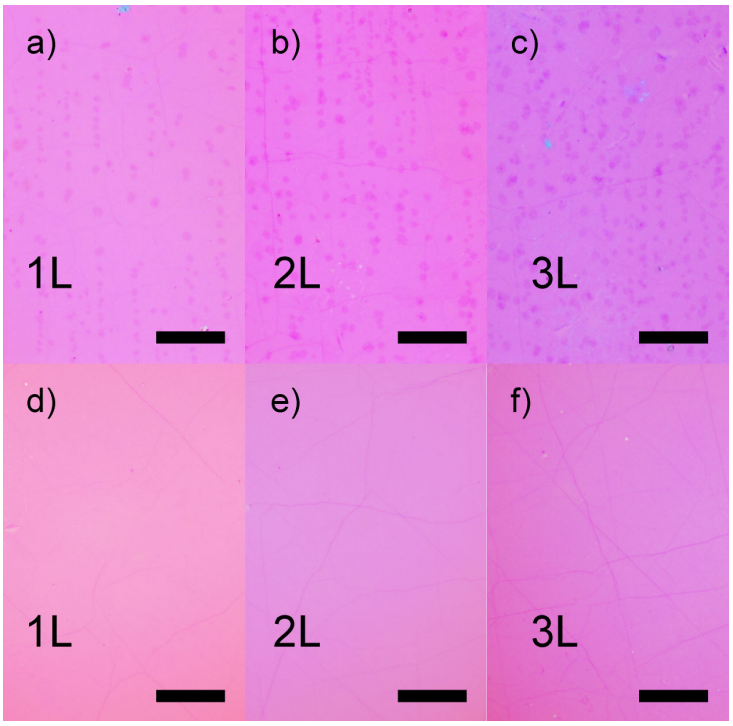


Figure 1.31: Optical micrographs of the continuous standard a)-c) and pulsed d)-f) multilayers CVD graphene transferred layer by layer (up to three layers) onto $SiO_2$/Si. Scale bars are 50 µm. The random position of multi-layer patches worsen the optical homogeneity in a)-c).

the stacking of graphene prepared by standard-CVD further amplifies the filling factor of the multi-layer inhomogeneity, resulting in high density of dark spots. This effect can be clearly seen in Figure 1.31.a-c, in which optical images of full-coverage standard-CVD graphene transferred layer-by-layer (up to three layers) onto $SiO_2$/Si are shown. On the contrary, as shown in Figure 1.31.d-f, homogeneous optical contrast is seen without any multi-layer patch dots for those grown by pulsed-CVD. Notice however some faint lines showing higher contrast, which come from wrinkles or folds without direct connection to the graphene grain boundaries [16].

## 1.4 CONCLUSION OF CHAPTER 1

We have developed a novel CVD process which allows growing fully homogeneous and continuous single-layer graphene up to the macroscale, totally free of multilayer patches that are usually ubiquitous to standard-CVD on copper foils. This method is based on the repeated pulsed injection of methane, under a constant hydrogen/argon atmosphere. Pulses allow suppressing carbon segregation above the extended defects in bulk Cu.

We have found that the parasitic multilayers in standard-CVD, which were widely overlooked thus far, have noticeable consequences on both the electronic and optical properties of graphene: they reduce the electron mobility, induce local doping, and yield large deviations of the optical transparency of graphene.

Graphene prepared by pulsed-CVD exhibits high mobility on $SiO_2$ substrate (mean value of 5000 $cm^2V^{-1}s^{-1}$) as well as exceptional optical homogeneity from microscopic to macroscopic scales. Pulsed-CVD is a versatile technique which can be readily implemented in CVD reactors employed routinely in graphene research, under a broad range of pressure conditions, and presumably also on a variety of substrates for graphene growth (e.g. Pt, Ni).

The pulsed process is rather easy to scale up and lead to unprecedented high quality monolayer. We have thus applied to a US patent on this technique. This is a scalable technique literally allowing "vacuuming multilayer graphene patches that are usually hidden under the carpet", which enables precise monolayer-by-monolayer engineering for future applications such as physical layer deposition of graphene heterostructures, and engineering of transparent electrodes.

# 2

# TRANSFER AND CHARACTERIZATION OF CVD-GRAPHENE

*In this chapter, we introduce several methods of transferring graphene from the metal surface onto arbitrary substrates. We demonstrate our prototype flexible transparent electrode made of CVD graphene. Cross-characterization techniques such as TEM, AFM, Raman are also introduced. Eventually, we discuss the perspective of a novel type of graphene hetero-structure made by the so-called physical atomic layer deposition.*

Since the first isolation of graphene in 2004 [106], the outstanding properties of graphene have been explored by extensive research works. It thus has made graphene the cutting-edge topic in condensed matter physics and in future nano-electronic applications, such as:

1) *Nanomechanical engineering.* In modern technology, microscopic mechanical machines, such as smart-phone motion sensors, are among the most important components. The emergence of one atom thick graphene layer has dramatically reduced the mass of resonators, but with the highest Young's modulus [107]. It enables super-sensitive mass detection down to around 1 zeptogram ($10^{-21}$ g), which is about two gold atoms, at low temperature [8]. Recently, batch fabrication of MHz frequency resonator arrays was realized thanks to the large size CVD graphene [108].

2) *Optical systems.* Graphene is known as a zero-gap semiconductor. It has the gate-tunable charge carrier density of 2D electron gas. It is easily coupled with optical systems and leads to new generation of optical devices. For example, graphene has been manifested in prototypical devices such as broad band optical modulator [109], optical cantilever [110], etc. The open surface of graphene is also amenable to be coupled with moleculars for optical studies [111].

3) *Biology platforms.* Being a carbon material, graphene has good biological compatibility with cells and various biomolecules. It is widely studied in gene and drug-delivery, cancer treatment [112, 113], and nanoporous membrane for study of DNA translocation [114].

4) *Anti-corrosion coating.* Graphene is stable against oxidation, and leak-proof. Therefore, a coating of graphene can protect the metal from being corroded [115]. The development in CVD-grown graphene has also enabled one to transfer, layer by layer, the thinnest ever anti-corrosion coating.

5) *Transparent conducting electrodes.* Nowadays, transparent electrodes are ubiquitous as they are key components for front panel displays. The material used is a thin film of ITO (indium tin oxide), which offers a transparency of 80% for a sheet resistance of 10 Ω. Indium mining has increased from 70 to 500 tons per year over the last 20 years to meet demand and the estimated resources are 20,000 tons, putting indium in the class of non-sustainable resources. Analysts are warning that global supplies of indium could be exhausted sooner than expected. As a result, the price of indium has rocketed in recent years: it went from

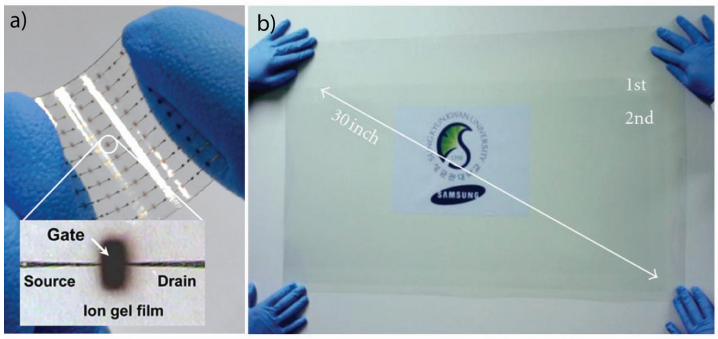


Figure 2.1: a) Flexible electrode made of graphene on polymer, reproduced from [3]. b) Demonstration of a 30-inch-size graphene continuous sheet transferred on PET film, reproduced from [4].

$ 60 per kilogram in 2003 to $ 1,000 in just three years. Worldwide production of indium metal is currently 475 tons per year from mining and a further 650 tons per year from recycling. However, a single LCD monitor screen typically contains less than 0.5 g of ITO, so recovering such a tiny amount from electronic products is expensive and energy-intensive. Finally indium salts are known to be toxic therefore there is a clear need to find a replacement.

Graphene seems to be the light in the tunnel as it may play a role in the substitution of ITO. The quantized light transmittance [1], together with the conducting nature, will probably push doped graphene to become a new generation of transparent conducting material, shown in Figure 2.1 [4, 3].

For almost all kinds of industrial and fundamental physics applications, CVD graphene is transferred onto a substrate, either a polymer, or an insulator such as $SiO_2$, sapphire, etc. Some groups have also tried to get graphene directly grown on insulators, yet their resultant graphene is still far from high crystallinity [19, 20], or far from large size [21]. Most of the applications are realized thus far by transferring graphene from a metal surface such as Cu, as described in Chapter 1.

Despite the fast-development of CVD graphene growth and transfer activities, the challenge remains in obtaining a high quality, large size graphene transfer. Moreover, a recently raised topic of hetero-structures based on graphene has triggered new interests for fundamental physics, such as ultra clean 2D electron gas [116], super-lattice induced pseudo-potential [117], and electron-electron interactions [118].

## 2.1 WET TRANSFER OF GRAPHENE POLYCRYSTALLINE MEMBRANES AND CRYSTALLINE GRAINS

### 2.1.1 *Transfer onto $SiO_2$/Si substrates*

Various transfer methods are currently developed to prepare graphene onto dielectric substrates for device fabrication. One way to reach this goal is to cover the graphene with a polymer supporting layer (PMMA, for example) to prevent graphene from collapsing, and then etch the underneath Cu foil. Besides increasing visibility and facilitating the handling, the supporting layer is also necessary as bare graphene may collapse due to surface tension. As shown in schematic Figure 2.2, and a real work flow Figure 2.3.

The graphene transfer procedure is well described in the literature [15], so we will not discuss in details here, but only describe two important issues: wafer cleaning and etchant-selection.

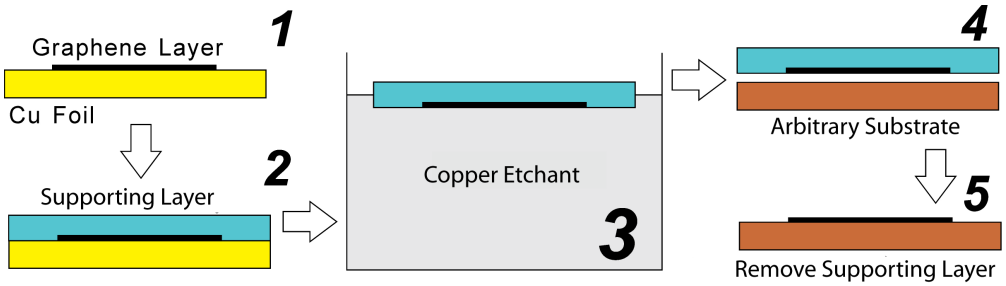


Figure 2.2: A work-flow of polymer-assisted wet transfer technique. Here we use PMMA as the supporting layer.

In this manuscript, Cu is the metal of interest as it provides at the same time a catalyst for monolayer graphene CVD growth and a sacrificial layer leading to a clean removal. We have tested several etchants to remove Cu, such as $FeCl_3$, $Na_2S_2O_8$, $(NH_4)_2S_2O_8$. All of them can efficiently remove Cu, however, not all of them are ideal for the job of graphene transfer. For example, we found that $FeCl_3$ leaves some dark colour on graphene, which may be residual Fe ions based salts, as shown in Figure 2.4. $Na_2S_2O_8$ is cleaner compared to $FeCl_3$, but long time etching of $Na_2S_2O_8$ will induce disorder in graphene, which will be discussed in Chapter 5. Among the above, $(NH_4)_2S_2O_8$ is the best choice for Cu removal. A proper concentration and etching duration can range from 0.02 g/ml and about 12 hours, to 0.1 g/ml and about 2 hours.

Since this transfer method is based on a liquid phase target substrate, its four main steps are listed below:

1) Etching and swimming. This step is to remove Cu underneath graphene. PMMA/Graphene/Cu layer is floating on the etchant for a desired duration, as shown in Figure 2.3a.

2) Fishing. This step is to scoop out from below the floating graphene/PMMA stack after Cu is totally removed, as shown in Figure 2.3b.

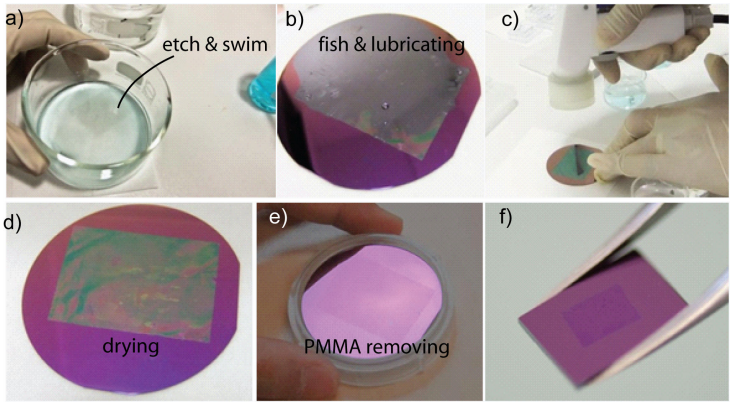


Figure 2.3: A work-flow of PMMA-assisted transfer technique. Graphene up to 20-30 $cm^2$ transferred on 2 inches wafer have been successfully produced in our group. Step a) is the etching and swim process of removing Cu from underneath of the graphene, b) depicts the step of fish and lubricating process. Graphene/PMMA stack is fished onto a target wafer. c)-d) let the stack dried in air. Eventually PMMA is removed by acetone, only graphene stays.

3) Lubricating the film. This means that when graphene is fished onto the substrate, there is a water layer between graphene and substrate, thus allowing one to adjust the position of graphene.

4) Drying and PMMA-removing. This layer of water will wick out after some time. However, there might be doping effect of the remaining salt molecules from the water solution. PMMA is eventually removed for example by acetone.

When placed onto target substrate, water is inevitably trapped below. It is therefore called "wet-transfer". Thus even when the whole stack is later dried, water residues (probably loaded with ions) can stay below graphene and will act as scattering centers for electron transport. Yet this is the most popular and industrially-compatible method to transfer graphene from Cu.

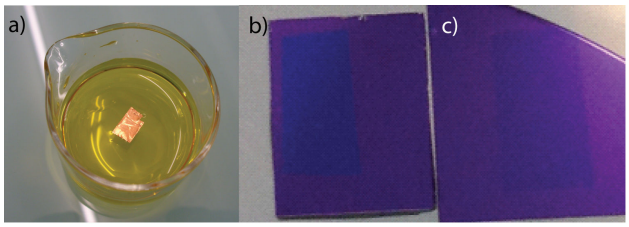


Figure 2.4: a) PMMA/Graphene/Cu floating on Cu etchant solution of 0.1 g/ml $FeCl_3$. Graphene transferred onto $SiO_2$ from b) $FeCl_3$, and c) $(NH_4)_2S_2O_8$. It can be seen in b) the colour of graphene shows a bright bluish colour compared to the one in c).

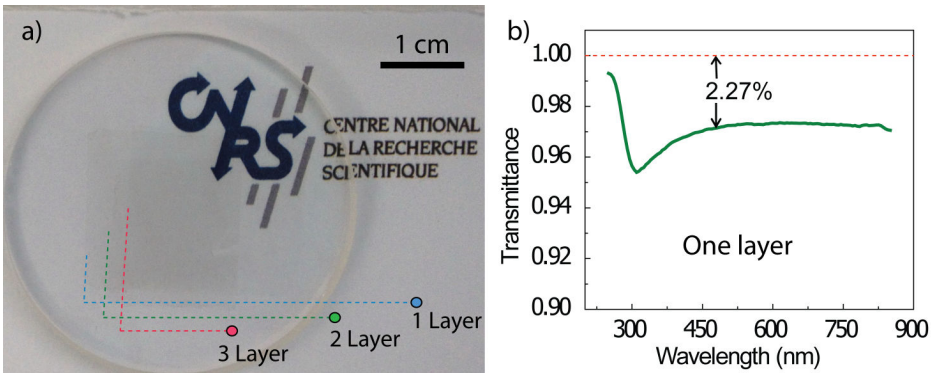


Figure 2.5: a) Three layers of CVD graphene transferred layer by layer onto a transparent glass substrate. b) Transmission spectrum of a monolayer CVD graphene in the wavelength range of 300 to 900 nm. Data measured with the help of Valéri Reita.

### 2.1.2 *Graphene transferred on transparent substrates*

The transfer method mentioned in Section 2.1 was first developed by Rodney Ruoff's group at Austin in 2009 [15], and has been modified into many other manners according to the needs. For example, a roll-to-roll lamination technique was developed based on it [4], that led to the production of continuously long and large size graphene. As the previous subsection mainly introduces the transfer of CVD graphene from Cu onto $SiO_2/Si$ for transistors. Here, we will briefly describe the transfer of CVD graphene onto polymer substrate for flexible transparent electrodes application. The basic ideas are the same as for wet-transfer of graphene onto $SiO_2/Si$, but the substrate is now a transparent layer, either flexible (PDMS, Polyethylene) or rigid (Glass soda lime, Quartz plate, etc.).

In Figure 2.5.a, we demonstrate a layer by layer transfer, up to a 3 layer stack of graphene onto a glass window. It can be seen that the layers of graphene are easily identified by the bare eye. This is due to the nature of quantized absorption of graphene monolayer [1].

*Optical transmittance of graphene monolayers*

Suppose the space is separated by graphene with each half space of reflection coefficient of $\epsilon_1$ and $\epsilon_2$. Graphene has an ac conductivity $\sigma(\omega)$, which is $e^2/4\hbar$ ([119]) at charge neutrality. In the thin film limit, Fresnel's equations can be written in the form of transmittance T as [120]:

$$T = \sqrt{\frac{\epsilon_1}{\epsilon_2}} \frac{4(\epsilon_1\epsilon_2)^2}{\left|(\sqrt{\epsilon_1\epsilon_2}+\epsilon_1)\epsilon_0 + \sqrt{\epsilon_1}\sigma(\omega)/c\right|^2}. \tag{3}$$

If both sides of graphene are in free space, i.e., $\epsilon_1 = \epsilon_2 = 1$, Equation 3 reduces to $T = (1 + 2\pi\sigma/c)^{-2}$, where c is the speed of light, $\sigma$ is the conductivity. Therefore, absorptance turns out to be $1 - T = \pi\alpha \approx 2.3\%$, where $\alpha$ is the fine structure constant defined as $e^2/\hbar c$. That is to say, by measuring T of graphene, one can extract the exact number of $\pi$ (Figure 2.6), as the other parameters are

well-defined physical constants. The measured optical transmittance with wavelength from 300 nm to 800 nm in a monolayer graphene transferred onto glass (Figure 2.5.b) shows a good agreement with the above theory. This quantized absorption has been widely examined to be true [1, 4]. Interestingly, there is a small dip in the transmission spectrum at wavelength of about 300 nm. This is discussed to be related to inter-band scattering in graphene [121].

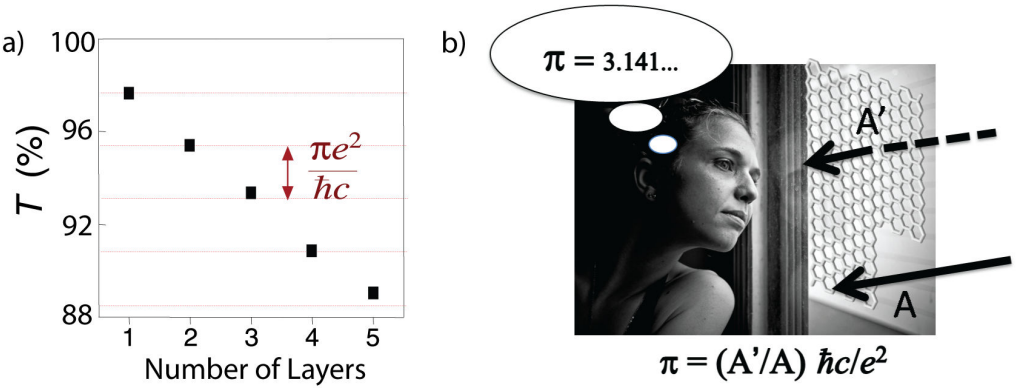


Figure 2.6: a) Quantized transmittance with number of layers of graphene. The step height between two levels is $\pi e^2/\hbar c$, adapted from [1]. b) Measuring $\pi$ by looking through a monolayer graphene window.

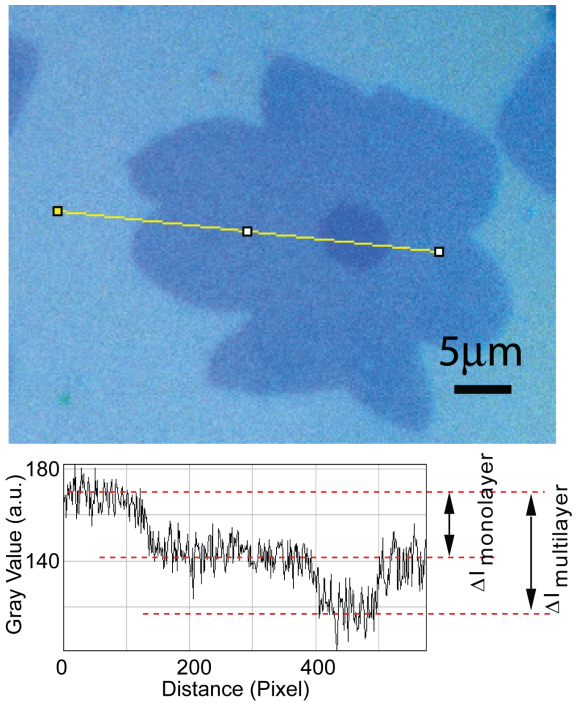


Figure 2.7: Top: number of layers of graphene are easily identified optically because of the quantized optical contrast. Bottom: cross section of the optical micrograph (shown as yellow line), indicated as grey value extracted by an image analysis software (Gimp).

The quantized 2.3 percent optical absorption is a very important physical property of graphene, as it explains the easy identifiable number of layers by means of optical and/or electronic measurements, such as transmission electron microscope (TEM), SEM. Most importantly, when graphene is placed on $SiO_2$ with an appropriate thickness (90 and 285 nm, due to interference of light [122]), one can just select the number of layers by "looking" at it, according to the color and contrast without any other technical assistance, as shown in Figure 2.7. This directly helped Geim and Novoselov during their pioneering studies to sort graphene multilayers and successfully identify and isolate a monolayer graphene, and that eventually led to their Nobel Prize in 2010.

However, if one looks into the 2.3 % absorption carefully, the minimum conductivity of $e^2/4\hbar$ is actually only valid close to the Dirac point (see Chapter 3, electronic structure of graphene) That is to say, if graphene is gate-tuned into a high doping level, the transmission can be changed. Indeed, experimental observation shows that the reflectance of graphene on $SiO_2$ wafer is gate-tunable [123]. Therefore, based on the above idea, one can design an experiment by using a transparent conductive substrate, to study the optical absorbance of graphene as a function of the charge carrier density. For example a sandwiched structure involving Indium Tin Oxide (ITO), insulating spacer and graphene can be used. It is possible to gate graphene with ITO and at the same time light transmitted through the whole structure can be tuned, giving rise to a graphene "smart window".


Figure 2.8: In-situ measurement of the electrical conductivity during mechanically folding an undoped CVD graphene layer transferred onto polyethylene film. Prospect of using graphene for flexible electrodes is great, as ITO is brittle and cannot be folded.

Among many perspective applications of graphene, the flexible transparent electrode is the closest to the real market. Touch- or flexible-screens need neither a very high crystallographic quality of graphene, nor a very high mobility. This makes their use in wide spread applications the most technically feasible. We demonstrate here graphene on a plastic membrane for flexible electrode applications, as shown in Figure 2.8. One can see that with a monolayer graphene, sheet resistance of about 3 k Ω is easy to achieve without any gating or chemical doping.

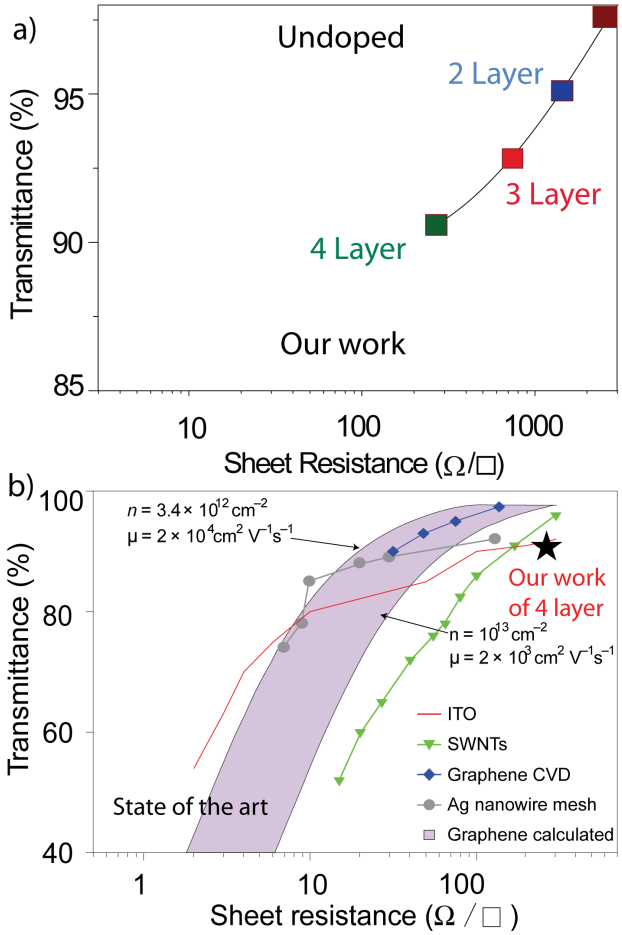


Figure 2.9: a) Sheet resistance versus number of layers of our CVD graphene transferred onto a plastic film. Solid line is to guide the eye. b) Performance of transparent conductive electrodes. The data point of our 4-layer transferred CVD graphene is highlighted by the black star.

To have the state-of-the-art properties for transparent electrodes ready for industrial applications, one should achieve as low a sheet-resistance as possible (several Ω/□ to several tens), as well as the highest possible transparency (higher than 90 %). To compensate the relatively high sheet-resistance of monolayer graphene, one can either increase the doping, or increase the number of layers. Of course the latter will sacrifice the transparency.

We transferred layer by layer graphene monolayers, and the sheet resistance is indeed significantly decreasing from 3 kΩ/□ for a monolayer, to 200 Ω/□ for 4 layers, as indicated in Figure 2.9.a. Our data point is indicated by the black star in Figure 2.9. b, and compares favourably with the state-of-the-art.

### 2.1.3 *Transfer onto TEM Grids*

Using the same wet-transfer method, we also demonstrated the transfer of CVD graphene membranes onto TEM grids. Two kinds of TEM grids were tested, the lacey-carbon one, and the $Si_4N_3$ one. It turned out that graphene is able to stick

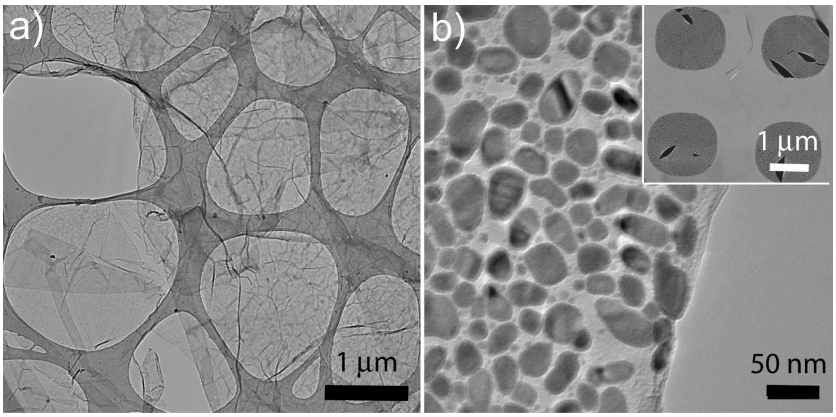


Figure 2.10: a) TEM micrographs of CVD graphene transferred onto a lacey carbon TEM grid, imaged with 80 kV acceleration voltage. b) CVD graphene transferred onto a $Si_4N_3$ TEM grid. Sn nanoparticles are deposited onto graphene by thermal evaporation. See last chapter for details. Inset of b) is an SEM micrograph of the zoomed-out $Si_4N_3$ TEM grid with CVD graphene transferred on it.

on the surface of both kinds of grids, and can be fully suspended over areas up to several $\mu m^2$ (Figure 2.10). The wet-transfer method is used, and the surface of lacey carbon TEM grids does not need specific treatment. Surface of $Si_4N_3$ TEM grids can be cleaned by acetone, and a short period of plasma or pirahna etching, which can help graphene to stick.

Since graphene is impermeable to almost all kinds of molecules [24]), it can serve as a load membrane for micro-liquids, molecular, or nanoparticles [13, 23]. An example of Sn nanoparticles sprayed onto graphene was tested on a $Si_4N_3$ TEM grid with 4 $\mu m^2$ holes, as shown in Figure 2.10b. It can be seen that graphene is robust enough to support a mass load which is much heavier than itself. Graphene is also quite homogeneous and transparent as a TEM back ground, which is already better than the lacey carbon (amorphous carbon mainly).

Interestingly, by accident, one of the $Si_4N_3$ TEM grid was broken and curled up, with Sn nanoparticles deposited on it. This enables us to image at a grazing angle and make a cross section imaging of the interface between graphene and Sn nanoparticles. As shown in Figure 2.11.c, it is observed that Sn nanoparticles are in a pie-shape, with negative wetting angles. This trick may be used for studying interface of other kinds of small objects loaded onto graphene. Details of physical attachment and electrical doping of these nanoparticles to graphene will be discussed in Chapter 6.

## 2.2 DRY TRANSFER OF GRAPHENE

Besides the wet transfer method, a dry transfer technique has also been developed [57, 124]. Here, we briefly introduce two ways of doing a dry transfer. Both are modified from wet-transfer, but with the advantage that graphene is free of water before being placed onto the target substrate.

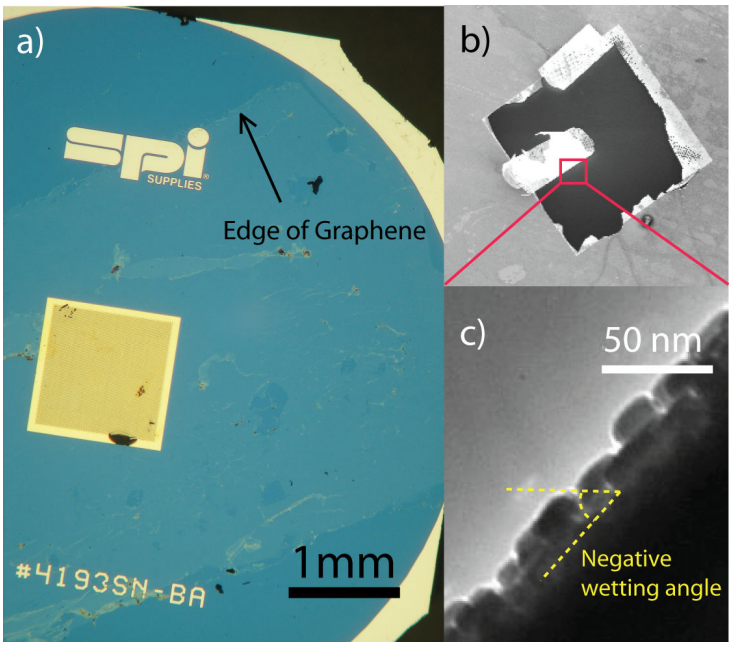


Figure 2.11: a) Optical micrograph of CVD graphene transferred onto a commercial $Si_4N_3$ TEM grid. b) SEM image of the grid, whose center is broken and curls up, with Sn nanoparticles loaded. This provides us the grazing angle view of the interface between graphene and nanoparticles. c) TEM image of the nanoparticle from the side-view.

### 2.2.1 *Transfer using thermal release tape*

The thermal release tape is a special kind of plastic tape which contains glue film that permanently looses its adhesion properly when heated above a threshold temperature. This allows for graphene that is sticking on it, to be released when heated to a certain temperature, as shown in Figure 2.12.

The reason that motivated the use of thermal release tape is because PMMA is too soft and does not hold together with further handling. For example, if one needs to flip the PMMA/graphene stack, it is almost impossible, since PMMA (hundreds of nm in thickness) will be folded and will never be recovered in its original flat state. Therefore, a layer that is stiff enough, but leaves no contaminations is desired. Thermal release tape meets these requirements for that purpose.

We tested the Thermal Release Tape REVALPHA (Nitto Denko) for graphene transfer, by the following steps:

1) Spin coat PMMA onto graphene on Cu.

2) Apply the thermal release tape on the PMMA/graphene/Cu stack, press with gentle force as homogeneous as possible.

3) Put the whole sample into $Na_2S_2O_8$, to etch away Cu.

4) The thermal release tape/PMMA/graphene stack, floating on etchant, should be flipped and thoroughly rinsed by DI water, followed by a gentle $N_2$ gas blow dry. This is critical, and thanks to the thermal release tape, we do not have to undergo the water lubricating step, thus no water will be trapped in between graphene and substrate any more.

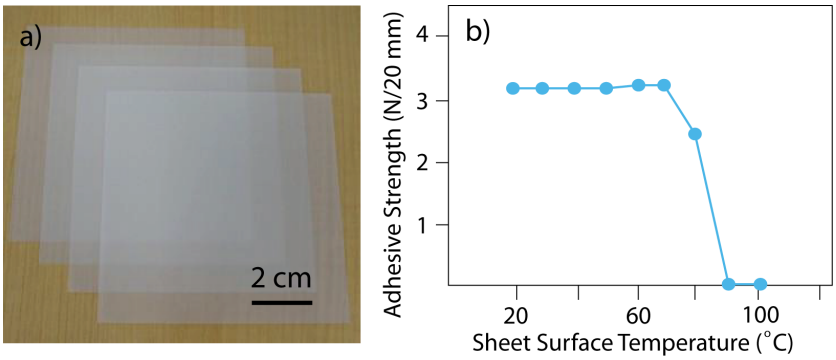


Figure 2.12: a) Photo of the Thermal Release Tape REVALPHA (from Nitto Denko Corp.). b) Its adhesive strength versus temperature curve, duplicated from the website of Nitto Denko company.

5) Place the dried graphene onto a cleaned wafer, press again with gentle force as homogeneous as possible.

6) Bake the sample on a hot-plate at 100 °C for 1 min. This thermal release tape looses its adhesiveness by the baking.

7) Removal of the PMMA can be done by acetone. Rinse the sample with Isopropanol (IPA) after the PMMA has been removed, and blow dry it, leading to a final sample as shown in Figure 2.13.

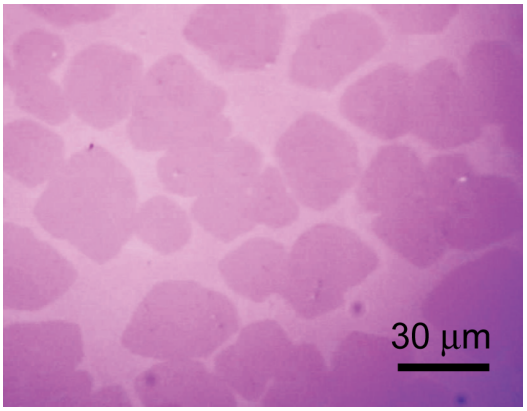


Figure 2.13: Optical micrograph of CVD graphene transfer using thermal release tape. Graphene used here is grown by pulsed-CVD method (short growth leading to non percolating grains).

In terms of optical observation and Raman, the quality of graphene transferred by dry-transfer method is almost the same as wet-transfer. However, electronic performance is reported to be much improved with respect to the wet-transferred samples: one order of magnitude larger electronic mobility is observed [57], because the interface between graphene and $SiO_2$ is now free of water. However, thermal release tape still has its limitations. For example, when dealing with large size continuous CVD graphene, the force applied onto the tape cannot be microscopically homogeneous. Therefore, some parts of graphene cannot stick well to the target wafer, leading to cracks or torn micro-parts.

### 2.2.2 *Polymer (PMMA) assisted dry-transfer method*

Recent studies of graphene/BN heterostructures are developing rapidly. However, even if BN is flat and neutral, it is not effective if you have water trapped at the interface by wet-transfer. Here we focus on the dry-transfer method developed especially in this area.

Basically, it is the same idea as using thermal release tape, with the purpose of removing residual water trapped between graphene and the substrates. PMMA with a stiff enough frame is used instead of thermal release tape. For example, Kapton tape for cryogenics can be an option, as demonstrated in Figure 2.14.a. Work flow of such transfer is shown in Figure 2.14.b.

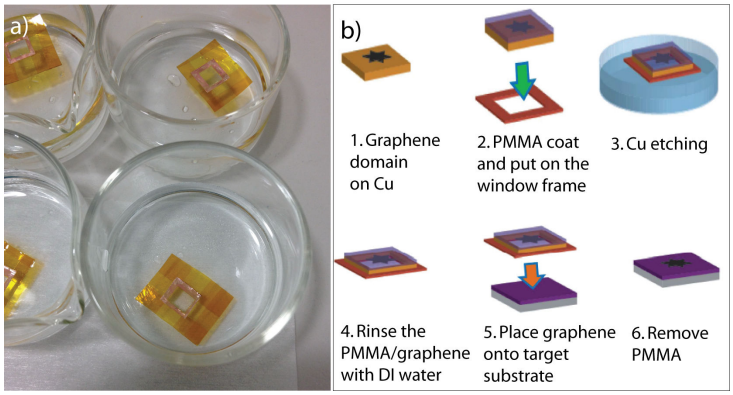


Figure 2.14: a) PMMA/Graphene is floating on the Cu etchant held by the supporting frame made by Kapton tape. b) Work flow of this kind of dry-transfer, adapted from [57].

By using this dry-transfer technique, the electronic mobility of graphene can be as high as 24500 $cm^2V^{-1}s^{-1}$ on $SiO_2$, and as high as 44900 $cm^2V^{-1}s^{-1}$ on h-BN [57], at 1.6 K temperature. Note that the wet-transferred graphene shows mobility ranging from only 500 to 10000 $cm^2V^{-1}s^{-1}$ on $SiO_2$ [51, 15, 125, 52].

One of the major advantages of dry-transfer in graphene/BN heterostructure studies is that even though the surface of BN-hosted substrate is not hydrophilic (that is the common case for wafers after exfoliation), transfer can still work. Meanwhile, this is rather difficult for wet-transfer, since de-wetting of DI water tends to shrink up the water below the PMMA/graphene stack, leading to failed transfer. Of course one can try to make the BN-loaded wafer hydrophilic by using, for example, Piranha etching, but in that case, BN is no more pristine and its interface with graphene might be less clean due to interface charge.

## 2.3 TRANSFER GRAPHENE ONTO OTHER KINDS OF SUBSTRATES

In our group, we also demonstrated successful transfer of graphene onto exotic substrates. Two examples are given below.

One is by patterning arrays of nano-pillars with distance d (kind of nano-Fakir-carpet). When distance d is less than a critical value $d_c$, a graphene membrane can be macroscopically suspended, theoretically up to an unlimited size, as shown in Figure 2.15.

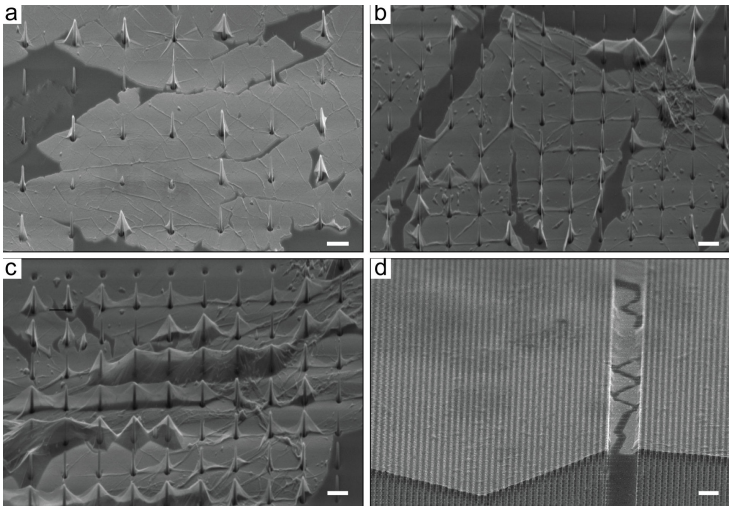


Figure 2.15: SEM micrographs of CVD graphene transferred onto Fakir carpet. When distances between the nano pillars is reduced from a) to d), full suspension of graphene is achieved. Picture credit: Dipankar Kalita (Néel Institute).

Another example is the demonstration of a nanodrum: a graphene membrane is suspended over nano holes on a silicon substrate. With this nanodrum, one can tune the pressure difference between inside and outside the drum, thus allowing stress engineering of graphene. Furthermore, via an AC gate, the nanodrum can be actuated into resonance, which allows for studies of NEMS. An AFM image is shown in Figure 2.16.

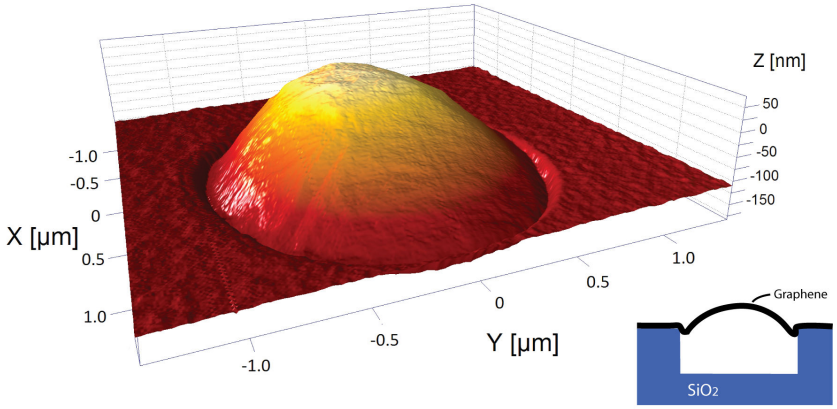


Figure 2.16: AFM image of a nanodrum made of graphene suspended over a nanohole on silicon substrate. Notice that the graphene is making a dome shape, because outside the nanodrum is vacuumed, and because of the leak-proof properties of graphene, trapping residual gas in the volume below. It becomes "inflated" like a balloon. Inset shows a schematic picture of the cross section. Image courtesy: Cornelia Schwarz (Néel Institute).

## 2.4 CROSS CHARACTERIZATION OF CVD GRAPHENE

### 2.4.1 *Transmission electron microscopy studies*

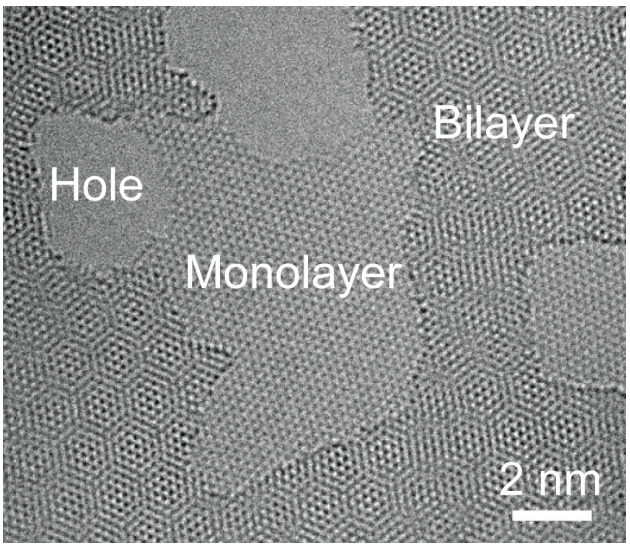


Figure 2.17: a) High-resolution TEM micrograph of monolayer graphene, and b)bilayer graphene, as clearly seen by the Moiré pattern. Graphene is grown by the standard-CVD method. The holes may come from electron beam irradiation, or from the transfer process. Image taken by Hanako Okuno (MINATEC-INAC).

A question often arises: how do you know you have a monolayer or bilayer graphene? The answer seems trivial for the experts, but not at all for people who are new in graphene field.

We have already shown in this chapter that, due to the quantized absorbance, one can distinguish from the optical and/or SEM images the number of layers. However, these 2 techniques need a calibration of the background level, namely, a as-proved monolayer, to counter another image. Otherwise, people may still question that the monolayer you claim is actually a bilayer that is perfectly overlapped! Therefore, we need cross characterizations of graphene.

One method could be provided by the transmission electron microscope (TEM). For example, when doing atomic resolution image, one can easily see the honeycomb lattice of a monolayer graphene, while the Moiré pattern will show up if it is bilayer graphene, as shown in Figure 2.17. If one does electron diffraction or Fourier transform of the spot, the twisting angle of the bilayer can be obtained. This twisting angle of bilayer has aroused great interests for both experimentalists and theoreticians, due to the properties such as van Hove singularities [126]. TEM can definitely distinguish graphene number of layers and its local crystallinity, but still has its limitation because of the localized observation, and the difficulty in sample preparation (especially for CVD graphene, lots of contaminations are present due to the use of PMMA).

### 2.4.2 *Atomic force microscopy of transferred graphene layers*

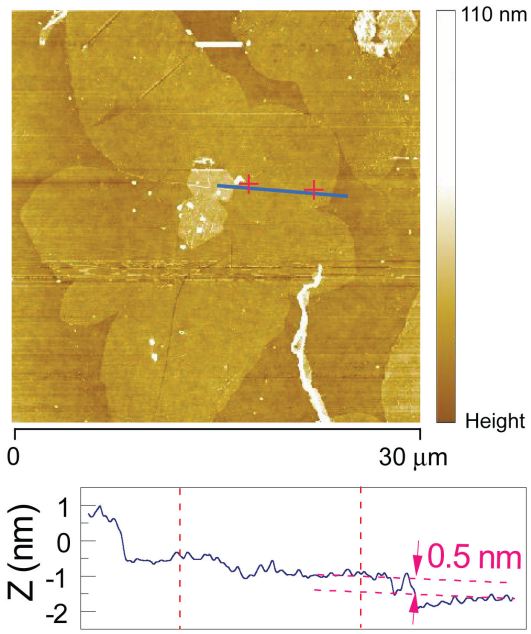


Figure 2.18: AFM image of a graphene flower, same growth condition as in Fig. 1.14a.

As well as other scanning probe microscopy techniques, AFM is another widely used technique to characterize graphene. It has several advantages. It has both contact and non-contact modes. It can scan areas up to 100 µm in lateral size. Therefore, it is a very powerful tool to map the morphology, such as surface cleanliness or number of layers, of graphene. As shown in Figure 2.18, an example of dendritic graphene was scanned by AFM and flower-like structure of the graphene domain can be seen. Moreover, those nanoparticles contamination, PMMA residues, wrinkles and/or cracks are also seen by this technique. The monolayer graphene often shows a thickness below 0.5 nm in the AFM height measurement.

More than just for morphology mapping, AFM can be used to perform lithography by locally oxidizing graphene or to clean the surface by sweeping the residues out of the surface.

### 2.4.3 *Raman spectroscopy*

In this section, we will come to another powerful tool for characterizing graphene: Raman spectroscopy. Raman scattering of phonons can be coupled to the movement, interference and scattering of electrons. Therefore, defects, edges configurations, doping or magnetic field can all influence the final Raman scattering procedure, allowing one to probe the phonon, in order to understand the electron behaviour deep behind.

When a light with frequency $\omega$ and polarization $P$ is incident onto any material, it generates elastically scattered light (Rayleigh) and inelastically scattered

light (Raman), which can be written as $P = P_{Rayleigh} + P_{Raman}$. $P_{Rayleigh}$ is the polarization vector with same frequency as the incident light, when the system returns to its initial state, and the frequency of the emitted photon remains the same as the incident one. $P_{Raman}$ is the polarization modified by the lattice vibration of the target material. Raman scattering has two inelastically scattered components with frequency $\omega - \omega_0$ (Stokes) and $\omega + \omega_0$ (anti-Stokes), as shown in Figure 2.19. Feynman diagram of the Stokes and Anti-Stokes processes are shown in Figure 2.20. In the literature, most Raman spectra are Stokes measurements plotting the intensity of the scattered light versus the difference between incident and scattered photon energy, the so called "Raman shift".

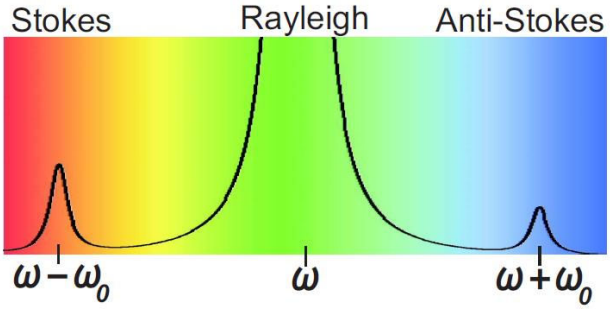


Figure 2.19: Schematics of the scattering of an incident light with frequency omega: Rayleigh scattering, and Raman scattering with two components $\omega - \omega_0$ (Stokes) and $\omega + \omega_0$ (anti-Stokes). Picture adapted from [127].

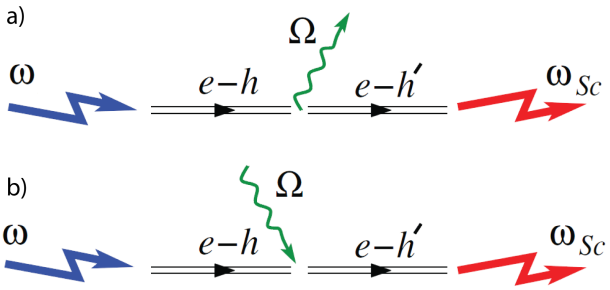


Figure 2.20: Feynman diagram of a) Stokes scattering. An incoming photon $\omega$ excites an electron-hole pair $e - h$. The pair decays into a phonon $\Omega$ and another electron-hole pair $e - h'$. The latter recombines, emitting a photon $\omega_{Sc}$. (b) Anti-Stokes. The phonon is absorbed by the $e - h$ pair. Picture adapted from [128].

Raman scattering can be treated back to the calculation of light absorption of an electron (with charge $-e$) on a generic crystal using the Shrödinger equation with a time dependent perturbation. First-order approximation describes phonons at the center of the first Brillouin zone. Second order expansion then leads to two different phonons contributed to the Raman scattering with wave vectors $q_a$ and $q_b$ and frequencies $\omega_a$ and $\omega_b$. This two-phonon Raman scattering has the selection rule $q_a \pm q_b \sim 0$. The second order Raman in the case of graphene often has high intensity, because of (one phonon, double phonon, or triple phonon) resonant Raman scattering. When there exists a defect with wave

vector d, the Raman selection rule is then $q_a \pm d \sim 0$, which corresponds to the Raman D band.

The above is about the basic conceptions of Raman scattering on any material. It becomes specific when dealing with graphene, because graphene is an atomic structure. Graphene has two atoms per unit cell, thus six normal modes (3 degrees of freedom for each atom, but actually two of the modes are doubly degenerate) at the Brillouin zone centre Γ Figure 2.21. These vibrating modes come from the phonon dispersions of single-layer graphene, which comprises three acoustic (A) and three optical (O) branches, as shown in Figure 2.22.

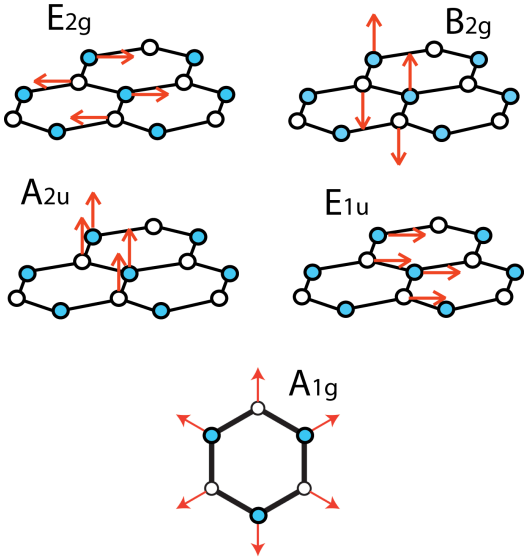


Figure 2.21: Lattice vibrating modes of graphene.

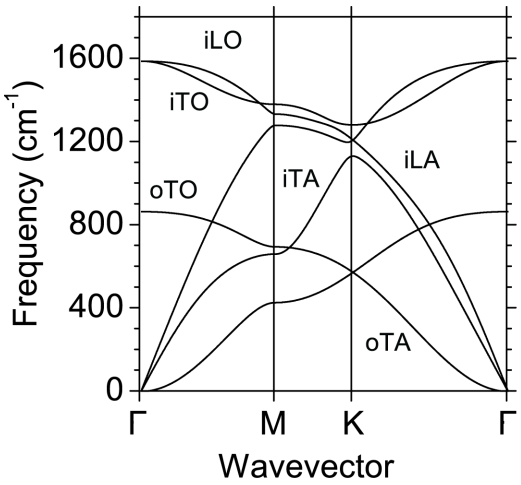


Figure 2.22: Phonon dispersion of graphene [129].

Confocal micro-Raman spectroscopy was performed with a commercial Witec Alpha 500 spectrometer set-up. A measured Raman spectrum of monolayer graphene on 285 nm $SiO_2$/Si wafer, with a 532 nm laser, is shown in Figure 2.23. One can see that there are several characteristic bands as below:

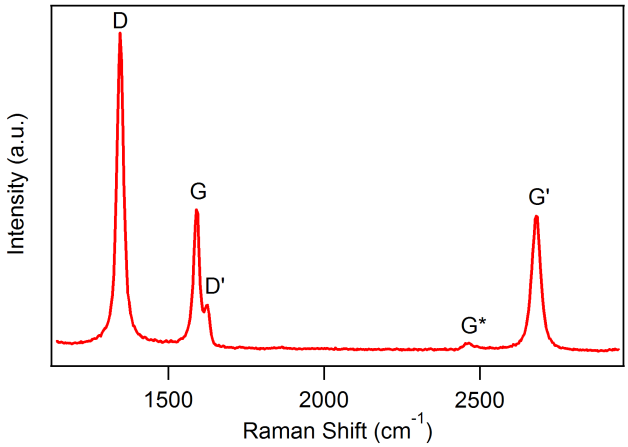


Figure 2.23: Typical Raman single spectrum of our defected monolayer CVD graphene, as the D peak at around 1300 $cm^{-1}$ has high intensity, together with a D' peak at the right shoulder of the G peak. The method of inducing defect in CVD graphene is introduced in Chapter 5.

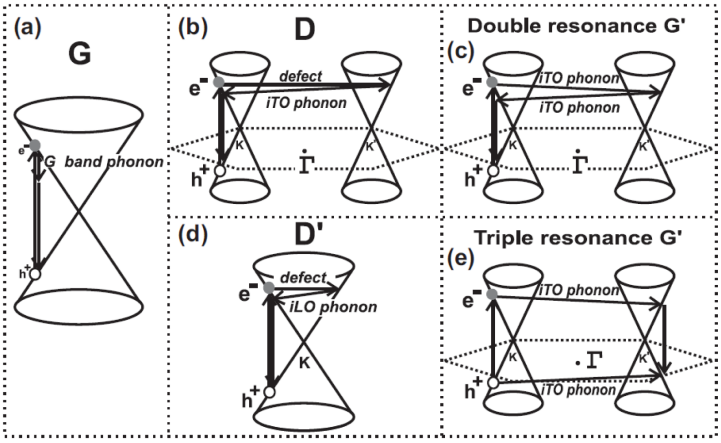


Figure 2.24: Schematics of Raman scattering processes involved in the different Raman peaks of graphene. Picture adapted from [127].

(1) The G band (~ 1582 $cm^{-1}$, for laser excitation at 2.41 eV) can be found in all $sp^2$ carbon allotropes, whose energy is insensitive to the incident laser, but can be influenced by factors that can affect the C-C bond, such as strain, doping, or temperature. Moreover, G band intensity is proportional to the number of graphene layers (up to about 10 layers). The G band is associated with the doubly degenerate (iTO and LO) phonon mode ($E_{2g}$ symmetry) at the Brillouin zone center, which is the only band coming from a normal first order Raman scattering process in graphene systems [130].

(2) The D band (~ 1350 $cm^{-1}$, for laser excitation at 2.41 eV) is due to the breathing modes of six-atom aromatic rings. It comes from iTO phonons around the Brillouin zone corner K ($A_{1g}$ symmetry), it requires a defect to activate the double resonance, which is strongly dispersive with excitation energy, due to a Kohn anomaly at K.

(3) The 2D (also called G′, ~ 2700 $cm^{-1}$, for laser excitation at 2.41 eV) band originate from a second-order process, involving two iTO phonons near the K point. As mentioned before, 2D is a second order Raman process and is less probable than a first order one, but due to the resonance effect it is present and more intense then the G band. 2D is also dispersive with excitation energy.

(4) The D′ band located near the right shoulder of G band (~ 1350 $cm^{-1}$, for laser excitation at 2.41 eV), and is due to double resonance of an intra-valley process connecting two points at the same cone (K or K′).

The 2D peak is the D-peak overtone, and the 2D′ peak is the D′ overtone. Because the 2D and 2D′ peaks originate from a process where no defects are required, they are thus always present in a monolayer graphene Raman spectrum.

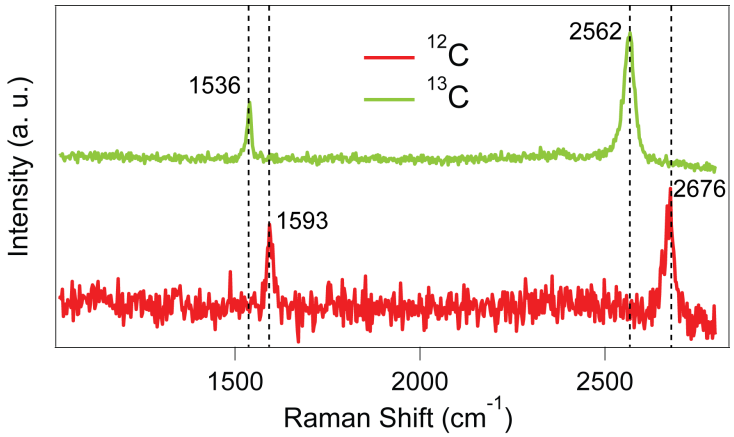


Figure 2.25: Comparison of Raman single spectra of our $^{13}C$ graphene and $^{12}C$ graphene grown on Cu, showing clear isotopic effect, as the down-shift of Raman mode is seen for $^{13}C$ graphene.

Raman can non-invasively probe graphene, to understand the electron-phonon interactions. It contains profound information by measuring a single spectrum. For example, doping [131, 132, 133, 134] and/or strain [135, 136] can affect the full-width at half-maximum, peak area, peak position of G and 2D band. Moreover, for multilayers, the 2D band gives information on the twisting angle between layers. One can de-convolute the peaks into sub-peaks and assign the number of layers [137], etc. When performing Raman mapping, one can collect spatially the information, and thus map sample quality, sample doping, etc. Moreover, Raman is a good method to probe the isotope of carbon $sp^2$ bondings, for example, $^{13}C$ graphene and $^{12}C$ graphene can be easily identified, as shown in Figure 2.25. The frequency shift of the Raman bands in the $^{13}C$ enriched material originates from the increased mass of atom mass [138]: $\omega_0 - \omega/\omega_0 = 1 - [(12 + c_0)/(12 + c)]^{1/2}$, where $\omega_0$ is the frequency of a particular Raman mode in the $^{12}C$ sample, c = 0.99 is the concentration of $^{13}C$ in the enriched sample, and $c_0$ = 0.0107 is the natural abundance of $^{13}C$. Therefore, the down-shift of the G, and the 2D bands is expected to be 56, and 95 $cm^{-1}$, respectively. Our experimental results give down-shifts of G and 2D bans of 57, and 114 $cm^{-1}$, in good agreement with the above estimation. Notice that the larger shift in our case originates from the larger wavelength of excitation laser.

## 2.5 PHYSICAL ATOMIC LAYER DEPOSITION OF GRAPHENE

As already mentioned at the beginning of this chapter, graphene hetero-structures seem to be a topic enriched with profound physics and the possibility for potential applications. For example, graphene-BN systems have been reported not only to have ultra-clean graphene [116], but also graphene with Moiré superlattices [139, 117] or electron-electron interaction systems [118]. Recently, in-plane [140] and lateral [141] graphene-BN heterostructure have been fabricated in a controlled manner, which significantly promotes the kind of heterostructures needed for future applications.

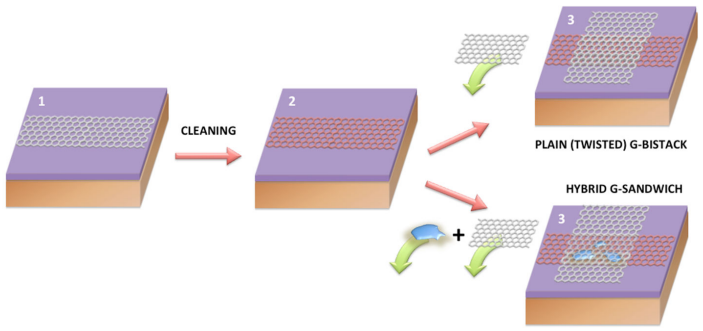


Figure 2.26: Principle of the PALD technique: step 1 is a direct transfer of a CVD graphene stripe on an oxidized silicon wafer. Step 2 is a physicochemical treatment to clean (and optionally functionalize) the bottom graphene surface. Step 3 is a wet (or dry) second transfer (with or without functionalization) of the top graphene layer leading to a fully addressable stacked bilayered heterostructure.

Here, we show that by transferring one layer onto another, i.e, Physical Atomic Layer Deposition (PALD), graphene can serve as a new platform for nanoelectronics. The aim is to obtain 2D macroscopic bilayer hetero-structures which contain two layers of graphene stacked on top of each other (and that can be scalable to any number of stacked layers). Each graphene layer, previously grown on metal by chemical vapour deposition (CVD) will be transferred on a substrate that can be polarized with an electrostatic back gate (for doping control) while remaining accessible from the top-side for subsequent in-depth sample characterization (optical and scanning probe) and post-preparation (chemical) treatments. A schematic picture is given in Figure 2.26.

Actually, the idea of making stacked graphene heterostructure has been conducted by several research groups, such as the nanoparticle-encapsulated graphene multilayers [142], cross-bar structure of bilayer graphene stack for quantum Hall measurement [143], stacked CVD graphene domains for Raman twisting angle studies [144], etc., as shown in Figure 2.27.

However, above examples either do not focus on the electronic transport of such kind of cross-bar [142, 144], or do not include external intercalates in between graphene crossing layers [143]. Moreover, the twisting angle, which determines the consequent Moiré super-lattice, is neither included in the electronic transport of graphene cross-bar. Based on the above discussions, we designed a four-probe crossed structure of bilayer graphene, as indicated in Figure 2.28.

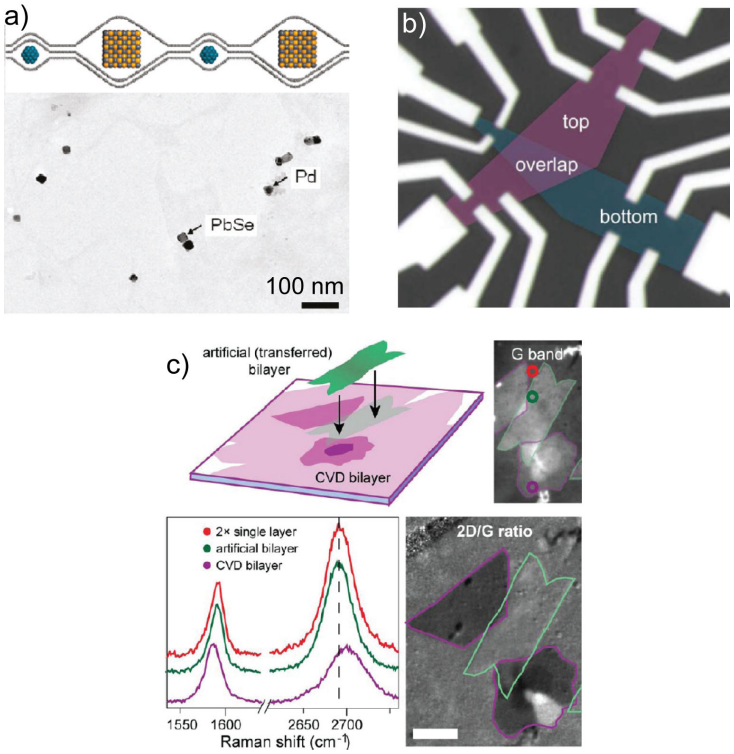


Figure 2.27: Demonstrations of graphene as encapsulating layers for nano-heterostructures. a) Nanoparticles encapsulated by transferring CVD graphene layer by layer, adapted from [142]. b) Cross-bar stack of bilayer exfoliated graphene, adapted from [143]. c) Raman studies of twisting angle between manually stacked CVD graphene domains, adapted from [144].

With this kind of structure, one can investigate various devices. For example, if the overlapping zone is filled with optical-sensitive molecules, one can measure the optical properties of those molecules by measuring the electronic transport of graphene. Furthermore, since graphene is playing the role of protecting the materials from the environment, those non-stable metals, such as Ca, K, etc., can be filled and protected from oxidization in the overlapping zone. This is one of the major advantages of this structure, as normally the study of alkali metal intercalated graphite [145] requires a high vacuum environment, which hampers the thinning down and transport measurements of graphene intercalated with alkali metals.

So far, our preliminary results show the success in fabricating such cross bars (Figure 2.28), and further works are ongoing.

## 2.6 CONCLUSION OF CHAPTER 2

As a conclusion to this chapter, we have shown the process of transferring CVD graphene onto arbitrary substrates. Transparent electrode is given as a special example as it is one of the most promising applications in the near future. We have illustrated the principle of making wet- and dry-transfer of CVD graphene

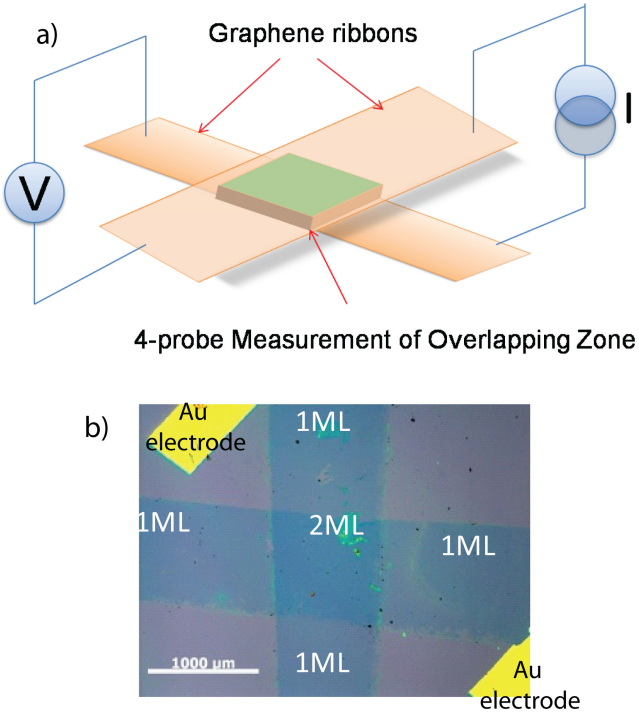


Figure 2.28: a) Schematic picture of two graphene layers stacked with an overlapping zone, where target materials can be wrapped. The crossbar structure is designed in a four-probe configuration, thus current flowing in the bottom layer can be detected in the top one. b) Real device made by transferring CVD graphene one after another. Image courtesy of Shelender Kumar (Néel Institute).

onto target substrates. In addition, we have demonstrated cross characterization techniques, such as AFM, TEM, and Raman. This chapter is the base of technical knowledge for this thesis. We also proposed a new generation of graphene heterostructure with a cross-bar geometry, which provides possibilities in exploring electronic or optical properties of the encapsulated materials.

# 3

# ELECTRONIC PROPERTIES OF GRAPHENE

*In this chapter, we briefly introduce the fundamental electronic properties of graphene. Electronic transport measurements, such as the field effect and the quantum Hall effect, are discussed in monolayer graphene. The basic concepts and formulas in this chapter will be very useful for the further studies presented in this thesis.*

Graphene consists of hexagonally organized carbon honey-comb lattice in 2D. The unit cell of a graphene layer, as shown in Figure 3.1, contains two sub-sets of identical triangle lattice related to each other with a displacement transition. The two atoms inside a unit cell are defined as A and B atoms spaced by a distance of $a = 1.42$ Å[146]. Within the graphene plane, each atom has 3 $\sigma$-bonds formed from $sp^2$ hybrid orbitals, which are tied up between the neighbouring carbon atoms. The unbound fourth electrons are called $\pi$-bonds, formed from $p_z$ orbitals extending vertically above and below the graphene plane, as shown in Figure 3.1c. The conducting nature of graphene comes from the hybridization of these $\pi$-bonds spreading across the whole graphene sheet, in a periodic potential (*i.e.* the energy bands described below).

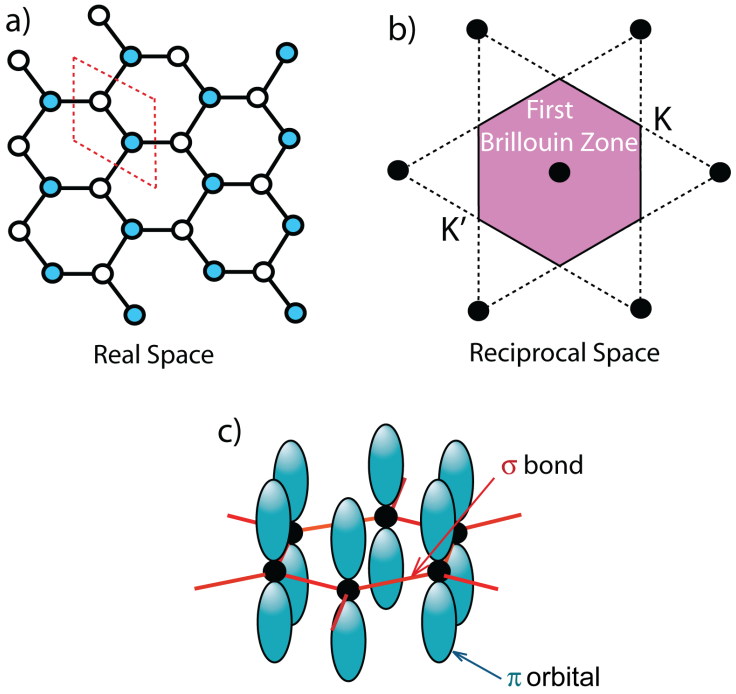


Figure 3.1: Schematics of graphene lattice in real (a) and reciprocal space (b). Its first Brillouin zone is in hexagonal shape, with two inequivalent corners called K and K', while the central point is called $\Gamma$ point. Red dotted line delimits the unit cell. c) $\sigma$ and $\pi$ bonds in graphene.

## 3.1 BAND STRUCTURE OF GRAPHENE

The band structure of a crystal is decided by its lattice configuration. Graphene's band structure has been calculated extensively, based on the tight-binding model developed since the 1940s [147]. Details about the derivation can be found in the literature [148, 149, 150, 151]. Here we directly give the result, which is the energy dispersion relation in $\mathbf{k}$ space:

$$\varepsilon_{\pm}(\mathbf{k}) = \pm t\sqrt{3 + 2\cos\left(\sqrt{3}k_x a\right) + 4\cos\left(\sqrt{3}k_x a/2\right)\cos\left(3k_y a/2\right)}, \tag{3.1}$$

where t is the hopping parameter between nearest neighbours. Experimental value of the hopping parameter is about 3 eV. The 3D plot of Eq. (1) is shown in Figure 3.2.a, which is known as the band structure of monolayer graphene. The conduction band is touching the valence band at the 6 corners of the first Brillouin zone (K and K′ points), without any band gap.

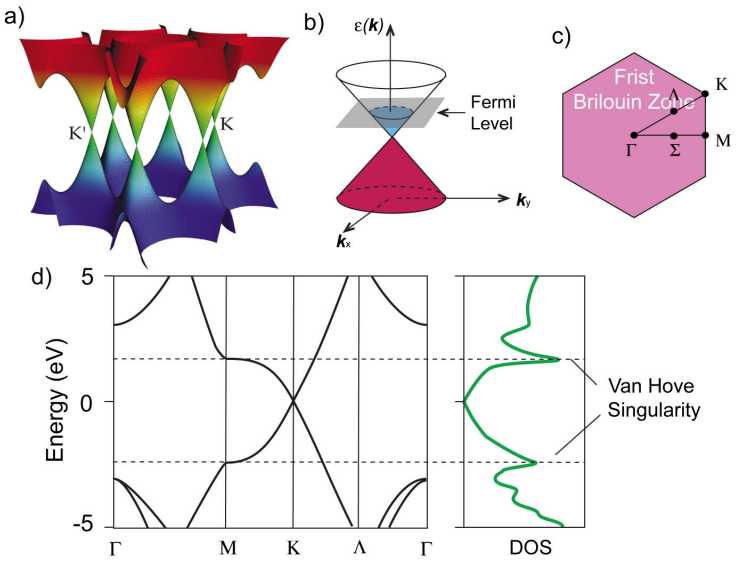


Figure 3.2: a) Band structure of graphene plotted from Equation 3.1. Picture taken from [152]. b) Zoom of the low energy region around K point. Valence band (Red cone) and conduction band (blue cone) intersect at the K point (so-called Dirac point). For neutral graphene, the Fermi level is at the Dirac point. d) The band structure plotted as a cut of the 3D picture in a), along the high-symmetry $\Gamma - M - K - \Gamma$ directions in c), with the DoS plotted on the right side. Picture reproduced from [153, 154, 155].

Low energy expansion of Eq. (1) at K(K′) yields the famous relation of energy versus the k-vector (with respect to K(K′) point):

$$\varepsilon(\mathbf{k}) = \hbar v_F \mathbf{k}, \tag{3.2}$$

as plotted in Figure 3.2.b. Unlike the conventional 2D electron gas (whose dispersion relation is parabolic, written as $\frac{\hbar^2}{2m}\mathbf{k}^2$), the dispersion of graphene at low energy is linear and has a point contact between upper and lower bands, similar to the band structure of photons. Instead of the Schrödinger equation, the

quasi-particles in this low-energy regime are formally described by the Dirac-like Hamiltonian $H = -i\hbar v_F \sigma \bigtriangledown$, where $\sigma = (\sigma_x, \sigma_y)$ are the Pauli matrices [156, 151, 157]. And $v_F$ is the Fermi velocity, defined as

$$v_F = \left| \frac{\partial \varepsilon}{\partial k} \right|_{K \text{ point}} = \sqrt{3} a t/2 \approx 10^6 \text{ m/s}. \tag{3.3}$$

Graphene is often referred to as a massless Dirac fermion. This is mainly because of (in the low energy regime) the linear band structure. However, effective mass (or cyclotron mass) of graphene is not zero [9]. In usual nanoelectronics, graphene Fermi energy is small compared to 1 eV. That makes the validity of the low energy approximation always hold. So far, graphene is one of the only few examples of condensed matter that are known to be a Dirac fermion 2D system.

## 3.2 FROM DENSITY OF STATES TO ELECTRON TRANSPORT

From the dispersion relation, it is now easy to count for the density of states (DOS). First of all, in a 2D electron gas, the total number of states $n$ is the area of a cut at certain energy, as indicated by the shadowed plane in Figure 3.2.b, divided by per unit:

$$n = \underbrace{g}_{\text{degeneracy}} \cdot \underbrace{\pi \mathbf{k}^2}_{\text{area}} \cdot \underbrace{\frac{1}{(2\pi)^2}}_{\text{per unit}}, \tag{3.4}$$

where $g = 4$, since graphene has 2 spin and 2 valley degeneracies. As a result, the Fermi vector in k-space is:

$$k_F = \sqrt{\pi n}. \tag{3.5}$$

According to Equation 3.2, the DOS (shown in Equation 3.5), *i.e.*, the number of states available at each energy level can then be written as [157]:

$$N(\varepsilon) = \frac{\partial n}{\partial \varepsilon} = \frac{2}{\pi \hbar^2 v_F^2} \varepsilon = \frac{2}{\pi \hbar v_F} |\mathbf{k}|. \tag{3.6}$$

Equivalently, DOS can be derived from the definition [158] $N(\varepsilon) = \sum_k \delta\left[\varepsilon - \varepsilon(\mathbf{k})\right] = \frac{1}{4\pi^2} \int_{-\pi}^{\pi} d\theta \int_0^{+\infty} k dk \delta[\varepsilon - \varepsilon(\mathbf{k})]$, which gives the same result as Equation 3.6. Only the electrons near the Fermi level participate in electron transport.

Interestingly, as can be seen from Equation 3.6, the energy dependence of DoS ($\epsilon$ *vs* DoS) in pristine graphene at low Fermi energy is linear, similar to the dispersion relation ($\epsilon$ *vs* k) shown in Equation 3.2. A plot of electron dispersion beside its DoS is shown in Figure 3.2d.

We first start with the diffusion equation (Fick's Law), that is, flux of a species $j_x$ in a concentration/potential gradient (here is the charge carrier concentration): $j_x = D \frac{\partial n e}{\partial x}$, where $D$ is the diffusion constant, $e$ is the elementary charge. The above formula can be written into

$$j_x = D \frac{\partial (n \cdot e)}{\partial x} = De \frac{\partial n}{\partial \varepsilon} \frac{\partial \varepsilon}{\partial x} = De \cdot N(\varepsilon) \frac{\partial \varepsilon}{\partial x}. \tag{3.7}$$

For simplicity, we only consider the transport along the x direction. By the definition of the electric field $eE = \frac{\partial \varepsilon}{\partial x}$, and that Ohm's law gives $j = \sigma E$. $\sigma$ is therefore related to D and $N(\varepsilon)$ as:

$$\sigma = D \cdot N(\varepsilon) e^2. \tag{3.8}$$

As a result, combining Equation 3.6 and Equation 3.8, conductivity of graphene is decided by its Fermi energy (tuned by doping), which is:

$$\sigma_{Graphene} = \frac{2e^2 D}{\pi \hbar v_F} |\mathbf{k}_F| = \frac{2e^2 D}{\pi \hbar v_F} \sqrt{\pi n}. \tag{3.9}$$

if we replace the D with $l$ by using [159]:

$$D = v_F^2 \tau_{sc}/2 = v_F l/2, \tag{3.10}$$

where $\tau_{sc}$ is the scattering time, and $l$ is the distance an electron wave travels until its initial momentum is destroyed, called mean free path. One gets

$$\sigma_{Graphene} = 2\frac{e^2}{h} k_F l. \tag{3.11}$$

In the right part of Equation 3.11, $e^2/h$ is known to be the quantum of conductance, and the quantity $\mathbf{k}_F l$ is an important value in mesoscopic physics, which will be discussed later. A more explicit deduction of Equation 3.11 can be found in [158], using the Landauer formula. However, Equation 3.11 is a crude approximation, since random charged impurities are not taken into account [160].

### 3.2.1 *Graphene field effect transistor*

One of the most fascinating properties of graphene is due to the linear band structure of graphene. Combined with the absence of charge screening due to atomically thin layer, the charge can be adjusted in density and sign with an applied gate voltage on a large range. This makes graphene the first atomic thin ambipolar field effect transistor. From Equation 3.5, it is clear that by changing $n$, the Fermi level of graphene is tuned toward a certain energy as shown in the shadowed cut in Figure 3.2.b, and thus the electronic conductivity. When $n$ is tuned into a minimum, minimum $\sigma$ is achieved. This very point in field effect curve is often referred to as the Dirac point $V_d$, or the charge neutrality point $V_{NP}$.

Experimentally, by transferring graphene on top of a thick dielectric layer (e.g. 285 nm $SiO_2$), by capacitive coupling $Q = CV$, the charge carrier concentration induced per unit area, per unit Volt, is:

$$n_{unit} = \frac{\epsilon \epsilon_0}{de} \sim 7.56 \times 10^{10} cm^{-2} V^{-1} (\text{for a typical 285nm capping oxide silica}). \tag{3.12}$$

where $d$ and $\epsilon$ are the thickness, and the dielectric constant of $SiO_2$, respectively.

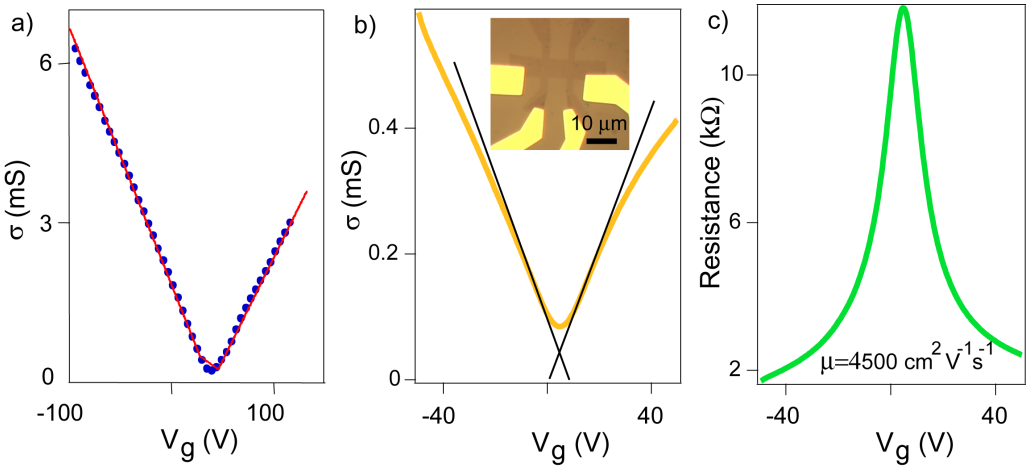


Figure 3.3: a) Field effect curve measured at 70 K, plotted in conductivity versus gate voltage, data taken from [106]. b) Sample measured at 300 K, from our CVD-grown graphene single crystal grain. A graphene flake is etched in a Hall bar shape by oxygen plasma etching, followed by Au 50nm/Ti 5nm electrodes deposition. A final device is shown in the inset of b). c) Same data as b), but plotted in resistivity versus gate voltage.

Notice that n is proportional to the gate voltage. An example of the field effect of graphene sample is given in Figure 3.3.a, showing that actually within a large gate voltage range, the conductivity is quite linear.

If one looks back to Equation 3.9, one can see that the transport of graphene is determined by its charge carrier density, as well as diffusion constant D. The latter quantity is a measure of the electron scattering inside graphene, which is also a function of $\mathbf{k}_F$. For example, to have linear $\sigma$ against $V_g$, one has to have a D proportional to $\sqrt{n}$. If we consider that the charge mobility is defined by $\sigma = ne\mu$ (we assume mobility for electrons and holes is the same due to the symmetric band structure), then for the sample in Figure 3.3.a, $\mu$ is a constant throughout $V_g$.

Actually, in many cases, the $\sigma$-$V_g$ field effect curve is not very linear, as shown in Figure 3.3.b, due to different scattering mechanisms. One can make a linear fit near to $V_d$, but it diverges from linearity at higher $V_g$. In this case, a constant $\mu$ is only approximately valid close to $V_d$. One has to use a variable $\mu$ to do fittings over a large range of $V_g$.

Another feature, as can be seen from Figure 3.3, is that none of the conductivity curves really go to zero at $V_{NP}$, which should appear according to the band structure, *i.e.*, a zero-DOS at the Dirac point. This is because the substrate that supports graphene is not free of charge. It often causes the so-called charge-puddles in graphene [161], leading to a non-zero minimum conductivity.

### 3.2.2 *Mobility extraction*

In graphene, the scattering mechanisms include [162]:

*Elastic scattering*, including:

(1) charge impurities, which are long range scattering (Long range means an interaction which is decaying slower than $r^{-d}$, where d is the dimensionality. Coulomb interaction is proportional to $r^{-2}$, therefore it is long range),
(2) Neutral defects, which are short range,
(3) charge transfer from doping or scattering, and (4) surface roughness.

*Inelastic scattering*, including:
(1) graphene phonons,
(2) substrate phonons.
According to Matthiessen's rule, the effective mobility is then written as

$$\frac{1}{\mu_{eff}} = \sum \frac{1}{\mu_i} \tag{3.13}$$

where $\mu_i$ denotes one of the scatterings described above.

It is rather complicated to fully explain the measured graphene field effect curve. Since effective mobility is depending not only on the various scattering inside graphene, but also on the electrodes contact, and the size of graphene. For example, when the distance d between electrodes is smaller than the mean free path l, the system reaches a so-called ballistic regime. In the mean time, electrons start to interference with themselves and give Fabry-Perot resonances [163]. Moreover, mobility in the ballistic regime is defined as two terms, *i.e.*, $\mu_n$, and $\mu_{bal}$. The latter is called ballistic mobility, and is defined as $\mu_{bal} = 2\pi ed/(\hbar k_F)$ [164, 165]. Assuming a graphene with good quality, for example, $n = 10^{12} cm^{-2}$ and $\mu_n = 10000 cm^2 V^{-1} s^{-1}$ when there is no confinement due to the electrodes. Once the electrode width is narrowed down to 10 nm, $\mu_{bal}$ is about a few hundreds of $cm^2 V^{-1} s^{-1}$. According to $\frac{1}{\mu_{eff}} = \frac{1}{\mu_n} + \frac{1}{\mu_{bal}}$, the effective mobility is also at the same order of magnitude, even though the graphene is of good quality.

Below is the protocol that we used to fit a field effect curve by the approximation of a constant mobility. One can extract mobility (diffusive regime) through the following:

$$G = \frac{1}{R - R_C} = \sigma \frac{Wt(=1)}{L} = ne\mu \frac{W}{L}, \tag{3.14}$$

while the charge carrier is often written as

$$ne = \sqrt{(n_0 e)^2 + [C(V_g - V_{NP})]^2}. \tag{3.15}$$

By re-formalizing Equation 3.14 and Equation 3.15, one will get

$$R = \frac{L}{We\mu\sqrt{(n_0)^2 + [7.56 \times 10^{10}(V_g - V_{NP})]^2}} + R_C, \tag{3.16}$$

where W/L is the width divided by length (aspect ratio) of device, $R_C$ is the contact/residual resistance (can be gate dependent [166]), and $n_0$ is residual carrier concentration. By measuring resistivity-$V_g$, one can then fit the mobility as well as $R_C$ and $n_0$. Notice that field effect curve of graphene devices are often asymmetric. That can be attributed to the inhomogeneity of the graphene sample, and/or the asymmetric Schottky barrier formed between electrodes and graphene for electron and hole sides [166].

### 3.2.3 *Liquid ionic gating on graphene*

Besides the conventional back/top gate, charge carrier concentration of a transistor can also be tuned by electrolyte gating.

Electrolyte gating is a method to induce ultra-high carrier concentration in low dimension systems, which provides a platform to investigate electron correlations in a regime that ordinary gating can not reach.

Normally, an electrolyte consists of a matrix (in liquid or gel form), with the mobile ions embedded. The electrolyte is in direct contact with the surface of a target material (graphene, for example). Ions inside get polarized once an electrical field is applied, giving rise to the negatively and positively charged layers, *i.e.*, the so-called electric double layer (EDL) on the surface of target material. By tuning the externally applied electrical field, EDL can be tuned into different concentration, thus playing the role of gating.

The difference between normal oxide gating and EDL is that the thickness of an oxide ranges from tens of nm to several hundreds of nm. Taking the standard 285 nm $SiO_2$ for example, as already discussed in the previous section in Equation 3.12, maximum induced n can be in the order of $10^{13}$ $cm^{-2}$, since the breakdown voltage of 285 nm $SiO_2$ is usually no more than 100 V. Sheet carrier density that swings up to $10^{15} cm^{-2}$ can be induced [167].

However, in the case of EDL, the distance between the two ionic layers is only around 1 nm, therefore the coupling capacitance per unit area $C = \epsilon_0 \epsilon / d$ is then 2 orders of magnitude stronger than the case of $SiO_2$. That is to say with only a few Volts, the same charge carrier density as that of 100 $V_g$ in oxides gate can be reached, as shown in Figure 3.4.

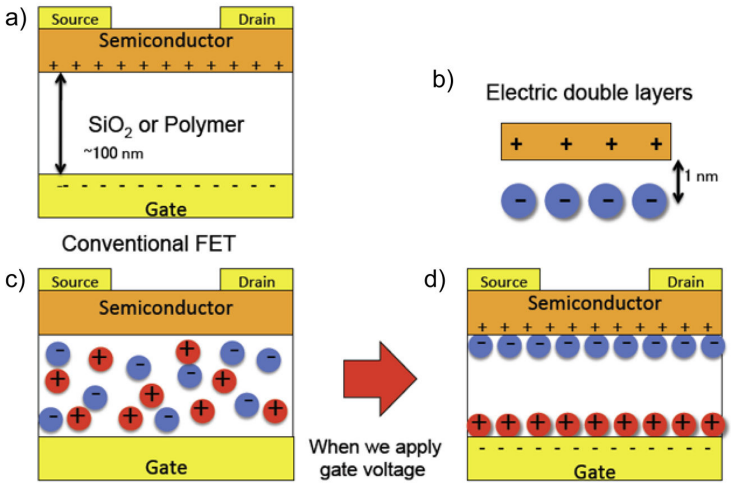


Figure 3.4: Schematic picture comparing different types of electrostatic doping using: a) conventional oxide gate and b) EDL. c) and d) show the polarized charges via conventional oxide gate, with the opposite charges separated by the thickness of oxide. Note that in b) the distance between the two ionic layers is only around 1 nm. Picture Courtesy of Shimpei Ono.

Recently, electrolyte gating has aroused intensive interests in various mesoscopic systems, for example, electrolyte gate-controlled Kondo effect in $SrTiO_3$

[167], electric field controlled superconductivity in insulators such as $SrTiO_3$ [168], $KTaO_3$ [169], $La_{2-x}Sr_xCuO_4$ [170, 171], ZrNCl [172], and $MoS_2$ [173, 174], etc.

It is also believed that when electron carrier concentration of graphene has reached a critical value, *i.e.*, doped into a nested Fermi surface and the density of states is singular, d-wave superconductivity can emerge from repulsive electron-electron interactions. The consequence may be, for example, a chiral superconductivity [175], namely, the resistance-free current flows in one direction, but not the opposite. This effect breaks time-reversal symmetry, and could be useful in constructing quantum computers. This predicted peculiar superconductivity in graphene has inspired many groups to perform EDL experiment on CVD graphene.

Actually, studies of electrolyte gating in graphene have been launched several years ago. For example, a $T^4$ temperature dependence of electron transport in graphene at carrier densities n up to $4\times10^{14}cm^{-2}$ was reported in exfoliated graphene[176, 177], and more recently, charge scattering mechanism in suspended graphene was studied by EDL [178], as well as the relations between quantum- and EDL-capacitances [179]. Kondo like behavior of graphene is also seen in graphene gated up to $3\times10^{15}$ $cm^{-2}$ charge carrier density [180]. However, superconductivity induced by this mean has not been reported so far.

### 3.2.4 *EDL on CVD graphene for low temperature transport*

CVD graphene with a dimension of about 200 μm × 400 μm was patterned into a Hall bar geometry. Pt/Au electrodes are deposited by thermal evaporation. A side pad is also evaporated for biasing the ionic liquid, which is provided by our collaborator Shimpei ONO. A carrier concentration of about $2\times10^{13}cm^{-2}$ can be induced. The device is shown in Figure 3.5.a-c.

We measured the room temperature field effect curve of the EDL graphene samples, with two of them illustrated in Figure 3.5.d-e. First of all, compared with Figure 3.3.c, whose width of the peak in the R-$V_g$ curve is about 30-40 V. With EDL gating, it is less than 1 V. This indicates a much stronger coupling via electrolyte gating. Secondarily, the Dirac point differs a lot from sample to sample. For example, there is about 1 V difference between the two figures in Figure 3.5.d-e. Moreover, the hysteresis also differs from sample to sample.

The goal of our study is to probe R-T dependence at high carrier concentration in CVD graphene, and try to look for new superconductivity inside this system. To achieve that, one has to apply a gate voltage on the side-pad, and cool down the sample while keeping the voltage. The measurement is carried out in a vacuum probe-station, and the probes may move around during cooling down, resulting in the lost of contact. Special care on this issue should be taken while measuring. Furthermore, since a chemical reaction can happen at the electrode (Au, or Pt in our experiment), 3 V is the upper limit of the gate voltage.

Unfortunately, the cooling of all our devices fails at a certain temperature. As shown in Figure 3.6.a, a R-T curve at linear response (small V-bias ), EDL gating shows quite constant relation until the sample is cooled down to about 100 K. At this point an abrupt increase of resistance takes place, with an open circuit

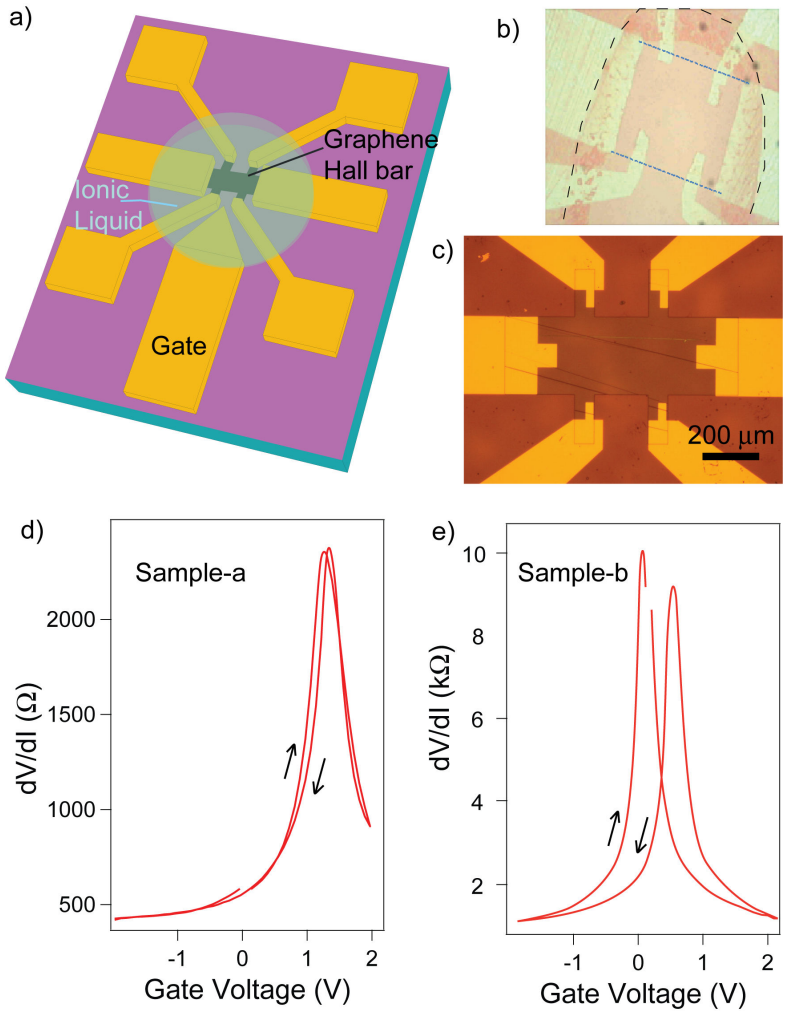


Figure 3.5: a) Schematic picture of the EDL-gated graphene device. b) Real device with the droplet of ionic liquid on it. Back dashed line indicates the contour of the ionic liquid, blue dotted lines indicate graphene. c) Device with photo-resist covering graphene during the fabricating process. d) and e) are field effect curves of two samples measured at room temperature. Arrows in field effect curves denote trace and re-trace. Collaboration with Shimpei ONO.

occurring. The circuit could not be recovered when warmed up again, and the optical image (Figure 3.6.b) of the sample after removing the EDL liquid shows there is peeling-off of the Au/Pd electrodes, as well as random holes and cracks in the graphene. This problem is systematic to us, since repeating the same experiment gives similar result: the sample becomes an open-circuit at a non-fixed low temperature. According to Figure 3.6.b, we attribute this problem to a possible shrinking of the liquid when it is frozen, as illustrated in Figure 3.6.c.

To avoid this from happening, there might be two ways:

1) replace the present liquid by another one, which has a smaller thermal expansion coefficient;

2) reduce the graphene size to a smaller area, for example, leave only a small transversal line between the electrodes.

Works on these issues are now in progress.

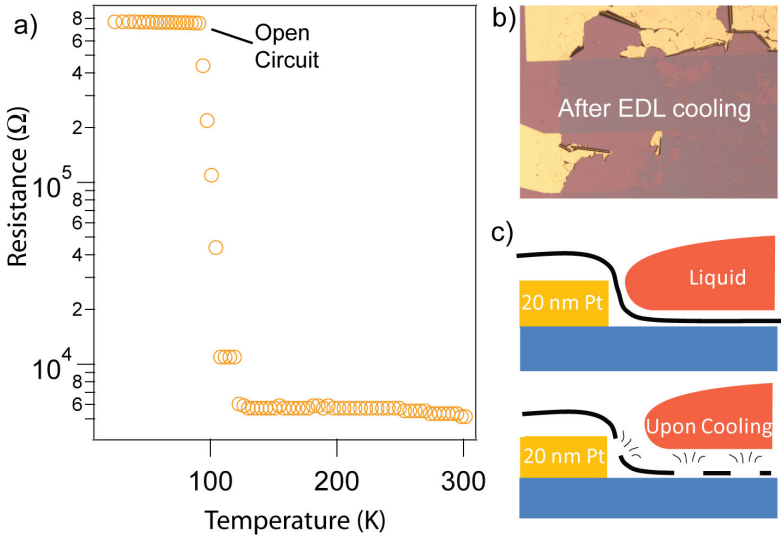


Figure 3.6: a) R-T curve of the device with EDL at zero gate voltage. Curve shows a dramatic increase in resistance at around 100 K, which is due to the open circuit. b) Optical image of the sample surface after EDL cooling, cracks and holes can be seen clearly. c) Schematic picture showing the possible situation.

## 3.3 LANDAU LEVEL AND QUANTUM HALL EFFECT IN GRAPHENE

In the history of physics, there are only few examples like the Hall effect, which has been already entitled to the Nobel prize for a total of 3 times (and probably will be more). Edwin Hall in 1879 won the first one because of his discovery of the conventional Hall effect [181]. More than a hundred years later, in 1985, the second one was given to the integer quantum Hall effect (QHE) discovered in MOSFET heterostructure by Klaus von Klitzing and co-workers. 13 years after that, the fractional quantum Hall effect (FQHE) won a Nobel prize, due to its challenge posed to the validity of symmetry breaking theory [182]. Unlike the above three kinds of Hall effect, there exist also anomalous Hall effect, which originates from spin-orbit interaction and does not require an external magnetic field. In 2013, the so-called "quantum Hall Trio", *i.e.*, quantum Hall, quantum spin Hall, and quantum anomalous Hall, were finally completed [183], as shown in Figure 3.7.

### 3.3.1 *Classical picture of Hall effect*

We first start with a classical approach of the QHE.

Suppose an electron is the only type of carrier inside a conducting slab. Under an external perpendicular magnetic field, the motion of the electron will be distorted by the Lorentz force -e$\mathbf{v} \times \mathbf{B}$, and will thus go towards the edge (at the same time holes will accumulate at the other edge) until the equilibrium of the electrical static force is balanced by Lorentz force:

$$e\mathbf{E} = e\mathbf{B} \times \mathbf{v}, \tag{3.17}$$

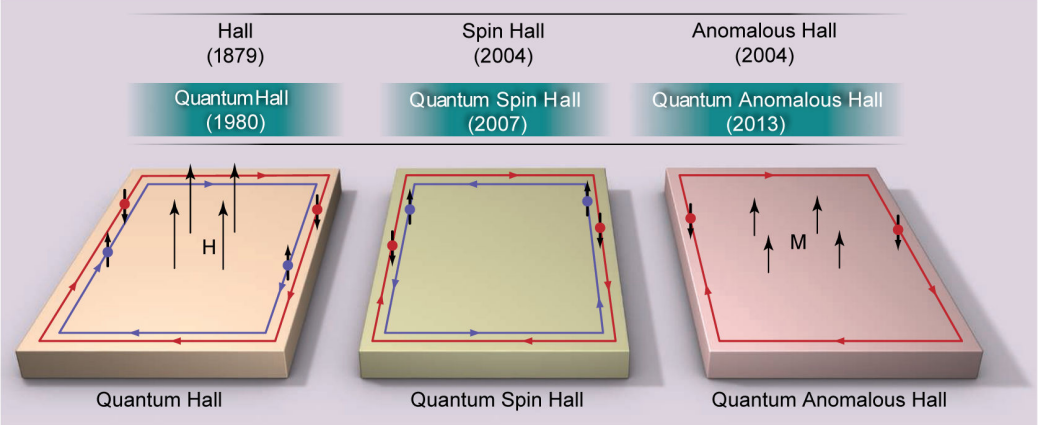


Figure 3.7: The three main types of quantum Hall effect (classical vs quantum, with dates of observation). Adapted from [183].

where $\mathbf{v}$ is the velocity of the electrons. Given that current density is defined as $\mathbf{j} = -ne\mathbf{v}$, and Ohm's law $\sigma = \frac{j}{E}$, one can re-write the conductivity $\sigma$ into:

$$\sigma = \frac{j}{E} = -\frac{nev}{Bv} = -\frac{nh}{eB} \cdot \frac{e^2}{h} = \nu \cdot \frac{e^2}{h} = -\frac{h/e}{B/n} \cdot G_0, \tag{3.18}$$

where $G_0 = e^2/h = 1/(25812.807572\ \Omega)$ is the quantum conductance ($h/e^2$ is the Von Klitzing constant $R_K$), and $\nu$ is the filling factor in QHE. Here the electrical conductivity tensor is simplified into a scaler quantity.

The physical picture of the electron motion in the classical Hall effect can be described as the electrons undergoing the cycloid motion, *i.e.*, a superposition of a circular motion and a constant drift, as shown in Figure 3.8.

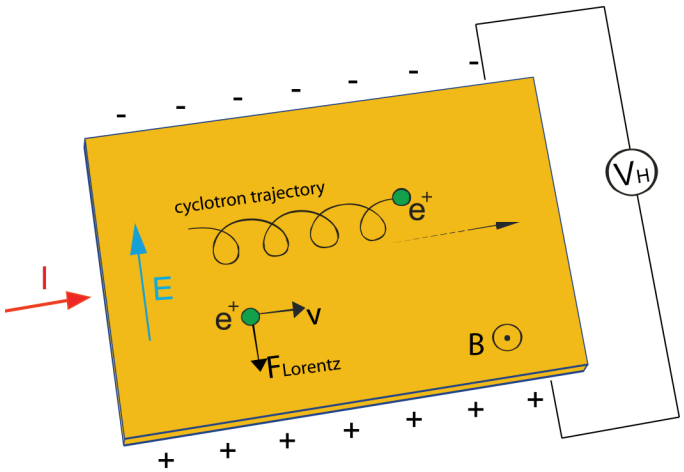


Figure 3.8: Schematic picture of classical Hall effect. Current I flows through a slab of a conductor subjected to a perpendicular magnetic field B. Electrons and holes are induced at the two edges, leading to a transverse voltage drop $V_H$.

Notice that the quantity in the right part of Equation 3.18 can be written as:

$$\frac{h}{e} = \Phi_0, \tag{3.19}$$

$$\frac{B}{n} = \Phi_e, \tag{3.20}$$

where $\Phi_0$ is defined as the quantum flux (the minimum flux quanta), and $\Phi_e$ is defined as flux per electron. Therefore, $\Phi_0/\Phi_e$ is a measure of flux quanta per electron.

### 3.3.2 *Landau levels and quantum Hall effect*

Let's consider the free 2D electron gas situation first. Quantum mechanically, the Hamiltonian of a free electron is $H = \frac{(\mathbf{P}+ie\mathbf{A}/c)^2}{2m}$, where $\mathbf{P}$ is momentum and $\mathbf{A}$ is the vector magnetic field. By solving the Schrödinger equation, one will get the eigenstates of the simple harmonic oscillator:

$$E_n = (L+1/2)\hbar\omega_c, \quad L = 0, 1, 2, \ldots, \tag{3.21}$$

with $\omega_c = \frac{eB}{m}$ the cyclotron frequency of electrons, and L is an integer number called the Landau Level (LL) index, with each Landau energy separated with $\Delta E = \hbar eB/m$, shown in Figure 3.9.a.

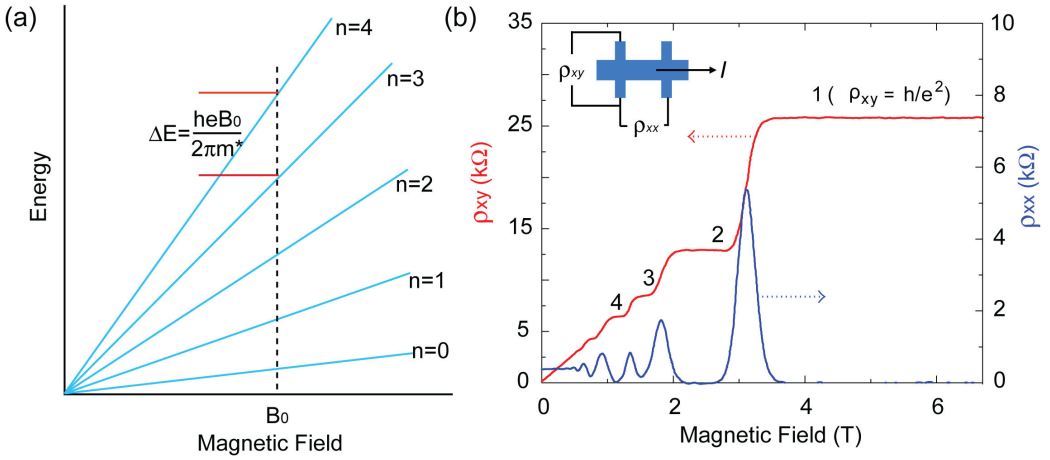


Figure 3.9: a) Schematic pictures of Landau levels of 2D free electron gas in a magnetic field for the non-relativistic case. b) Typical example of quantized transverse resistivity $\rho_{xy}$ and the corresponding longitudinal resistivity $\rho_{xx}$. Inset shows the sample configuration. Adapted from [40].

The total number of states Equation 3.4 of a free 2D electron is written as:

$$N_s = \frac{mE_F}{\pi\hbar^2}, \tag{3.22}$$

with $E_F$ the Fermi energy equals to the highest occupied LL. Combing Equation 3.22 and Equation 3.21, and substituting the carrier concentration n with $N_s$ in Equation 3.18, one gets the conductivity that is contributed by every LL:

$$\sigma = -\frac{N_s e}{B} = -\frac{L \cdot e^2}{h} \quad L = 0, 1, 2, \ldots \tag{3.23}$$

As a result, the Hall conductivity is quantized. The precisely quantized plateaus (Figure 3.9.b), despite sample preparation and defects, have been widely observed experimentally and become an important metrological standard of electron resistance with precision as high as $10^{-9}$ ($R_K$=25812.807557(18) Ω).

The above very simplified derivation does relate the kinetic-energy quantization to the resistance quantization. However, it does not take into account the fact that the quantum Hall plateau is affected neither by a particular disorder distribution nor a particular sample geometry. In fact, the topological protection of the integer QHE can be viewed as a quantization of averaged charge transfer, which is related to the so-called topological quantum number (Laughlin Theory and Chern number [184]).

### 3.3.3 *Visualization of quantum Hall effect*

One way to visualize the electron motions in the quantum Hall effect, is to imagine that the electrons are confined to iso-potential lines, as shown in Figure 3.10a [185]. Due to the existence of negatively and/or positively charged impurities in the 2D sample, there are closed isopotential lines, which form the "potential landscape" in the 2D bulk. Electrons are then localized inside these isopotential lines, and do not participate in transport (a bulk insulator). This is proven by experimental observations in a 2D electron gas quantum Hall system, as shown in Figure 3.10c.

However, the sample edge plays a role of confinement potential, which opens the isopotential lines of charge impurities, and makes a continuous line along the edge. As shown in Figure 3.10b, energy dispersion along the transverse direction shows that the LLs are bent upwards when approaching the sample edge.

Electrons with fixed chemical potential will occupy, for example, from 0 to $n^{th}$ LLs. When increasing the magnetic field, the cyclotron orbital reduces, thus evacuating electrons from the nth LL. This will lead to the loss of one quantum of conductance $e^2/h$ (since one LL contributes to one $G_0$), seen as a jump of a plateau in the Hall resistance (Figure 3.9b).

If the magnetic field is fixed, one can also tune the chemical potential of the electrons by gating, this plays the role of pumping electrons or holes into the occupied LLs, therefore influencing the quantized Hall resistance.

We now come to the longitudinal resistance ($R_{xx}$). As can be seen in Figure 3.9b, corresponding to each plateau in $R_{xy}$, $R_{xx}$ shows a zero-resistance state. To understand this, we recall the Landauer-Buttiker formula of quantum transport:

$$G = \sum \frac{e^2}{h} T_n. \tag{3.24}$$

In this equation, conductance of a mesoscopic system is described by the sum in all the conduction channels of quantum conductance multiplied by the transmission coefficient $T_n$ in each conduction channel. Comparing with the transport formula for integer QHE Equation 3.23, one can see the $T_n$ in quantum Hall regime is equal to 1, meaning a ballistic transport in each Landau channel, with

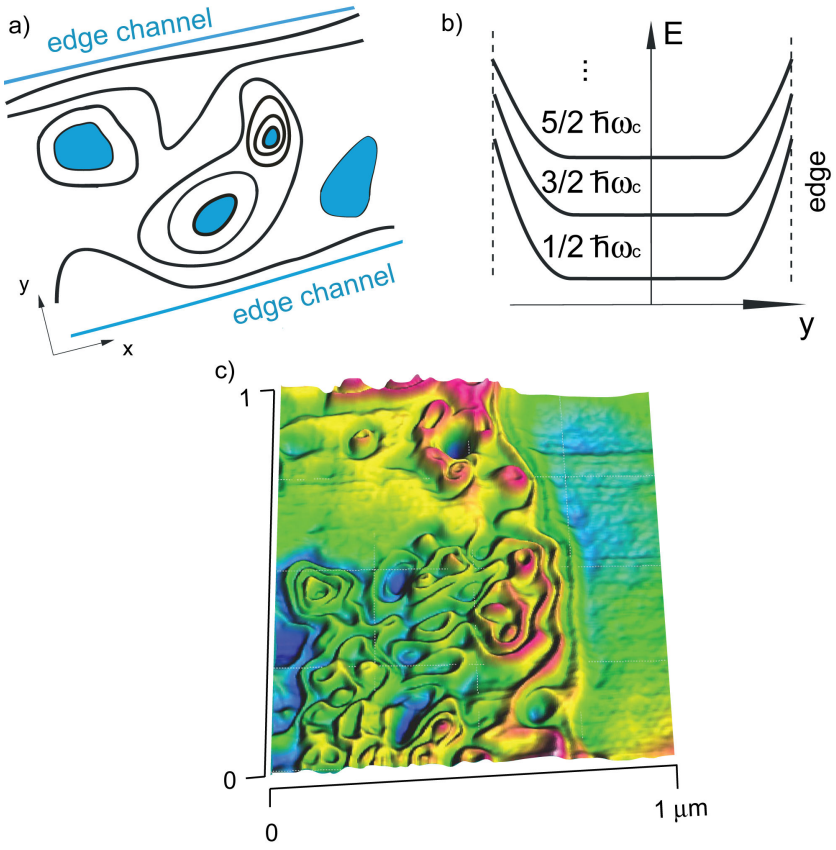


Figure 3.10: a) Schematic picture of the potential landscape in a 2D sample, reproduced from [186]. b) The energy dispersion of Landau level along transverse y-axis in a sample shown in a), in which Landau levels are bent upwards at the edges due to the confinement potential. Picture reproduced from [187, 188]. c) Scanning probe map of the local potential of a 2D electron gas sample by SPM microscopy (Scanning capacitive mode). Image courtesy: Prof. Gleb Finkelstein [189, 190].

no scattering or reflection of the electrons along the longitudinal axis. That explains the zero-resistance $R_{xx}$ in each LL.

### 3.3.4 *Quantum Hall effect of graphene*

Graphene as a 2D material, it has a QHE which was reported by Kim's and Geim's group simultaneously in 2005 [10, 9]. Unlike the non-relativistic 2D free electron described in the previous section, graphene follows the pseudo-relativistic theory. Therefore, specific quantum mechanical treatment is needed. The quantized LL for massless Dirac fermions is [191]:

$$E_L = \pm\sqrt{L}\cdot\hbar\omega_c = \sqrt{L\cdot 2\hbar eBv_F^2}, \quad L = 0, 1, 2, \ldots \tag{3.25}$$

An important difference from the non-relativistic Landau levels is the existence of an energy state with E=0 (when L=0). The schematic picture of the relativistic LL is shown in Figure 3.11. In graphene, the above mentioned zero

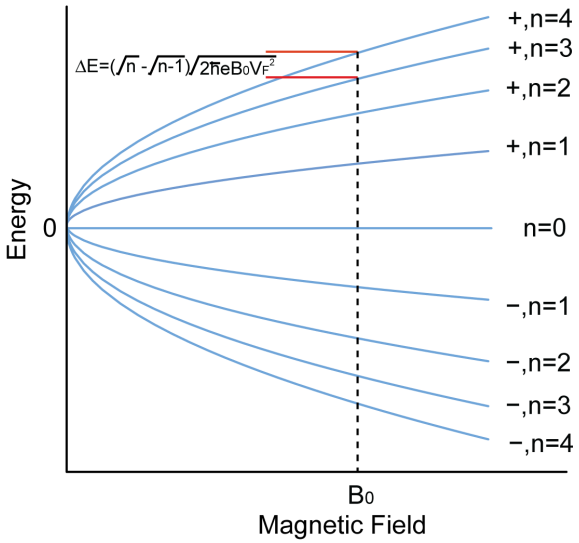


Figure 3.11: Schematic pictures of Landau levels of 2D massless Dirac fermoins.

energy state is shared by both electrons and holes, that is to say, degeneracy of this zero-energy LL are twice smaller than all the other LLs. Thus, the quantized sequence of conductance is defined as:

$$\sigma_{xy} = g_s g_v (L + \frac{1}{2}) \frac{e^2}{h}, \quad L = 0, 1, 2, \ldots \tag{3.26}$$

where $g_s = 2$ and $g_v = 2$ are the degeneracy of spin and valley. In the following, we will focus only on the QHE in monolayer graphene. More information about the QHE in bilayer graphene, and the fractional QHE in graphene can be found in [148, 192, 193, 194, 195].

### 3.3.5 *CVD monolayer graphene: towards a resistance standard*

As described in previous sections, the quantum Hall plateau is determined by two fundamental physical constants: the Planck constant h and electron charge e. It therefore provides high precision of resistance metrology, which is of great importance in industrial, scientific and technological applications.

Due to the unique band structure, graphene exhibits large LL spacing with high charge mobility, which can demonstrate QHE at a surprisingly high temperature [196], and thus makes this system much more favourable compared to the conventional semiconductor case [197, 196].

Here, we show an example of the QHE on mm-size CVD graphene. The graphene was grown using the standard-CVD on Cu, and was transferred on a 285 nm $SiO_2/Si$ wafer. Lateral size of the CVD graphene sheet is about 6 mm $\times$ 3 mm. Silver paint was put onto the edge of graphene to define a Hall bar geometry, as shown in Figure 3.12.

The measurements were done with the help of Cecile Naud in her 4 K cryostat with maximum 14 T magnetic coil. As shown in Figure 3.13, field effect at 4 K suggests a mobility of about 1000 $cm^2 s^{-1} V^{-1}$, using the fitting formula in

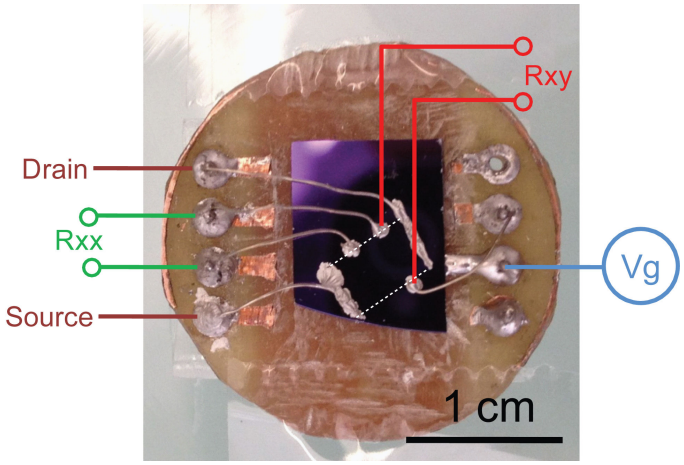


Figure 3.12: Optical photograph of a CVD graphene sample for quantum Hall measurements. 6 mm × 3 mm graphene layer (dashed lines) was transferred onto a $SiO_2$/Si chip, loaded on a 2.5 mm diameter holder. Graphene is grown by standard-CVD, with multilayer-patches. Electrodes of a Hall bar geometry were patterned by silver paint. Sample was measured at low temperature with the help of Cecile Naud.

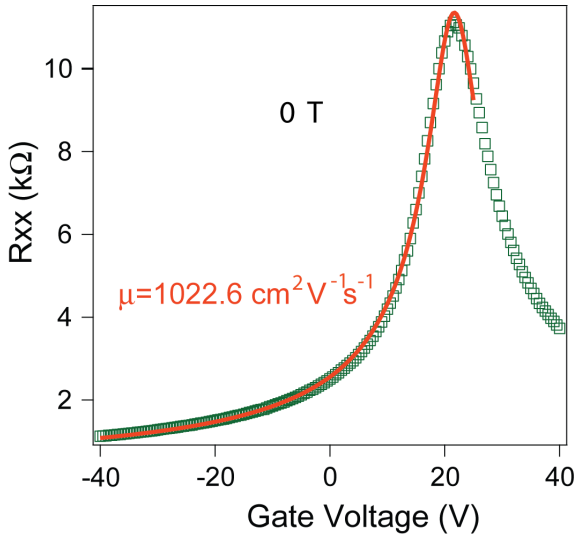


Figure 3.13: Longitudinal resistance at 4 K temperature as a function of gate voltage of the sample shown in Fig. 3.12.

Equation 3.16.

When subjected to a magnetic field perpendicular to the sample surface, the Dirac fermions inside graphene start to be quantized into LLs. It can be seen that a small split of the Dirac peak starts to develop at about 4 T in Figure 3.14b.

Usually, to observe QHE, one has to reach three conditions [40]:

1) high quality of the sample, in order to minimize scattering of electrons,

2) strong enough magnetic filed, in order to lift off the LLs, *i.e.*, to have electron cyclotron frequency $\omega_c$ be higher than the broadening of the LLs ($\omega_c \tau_{sc} \gg 1$),

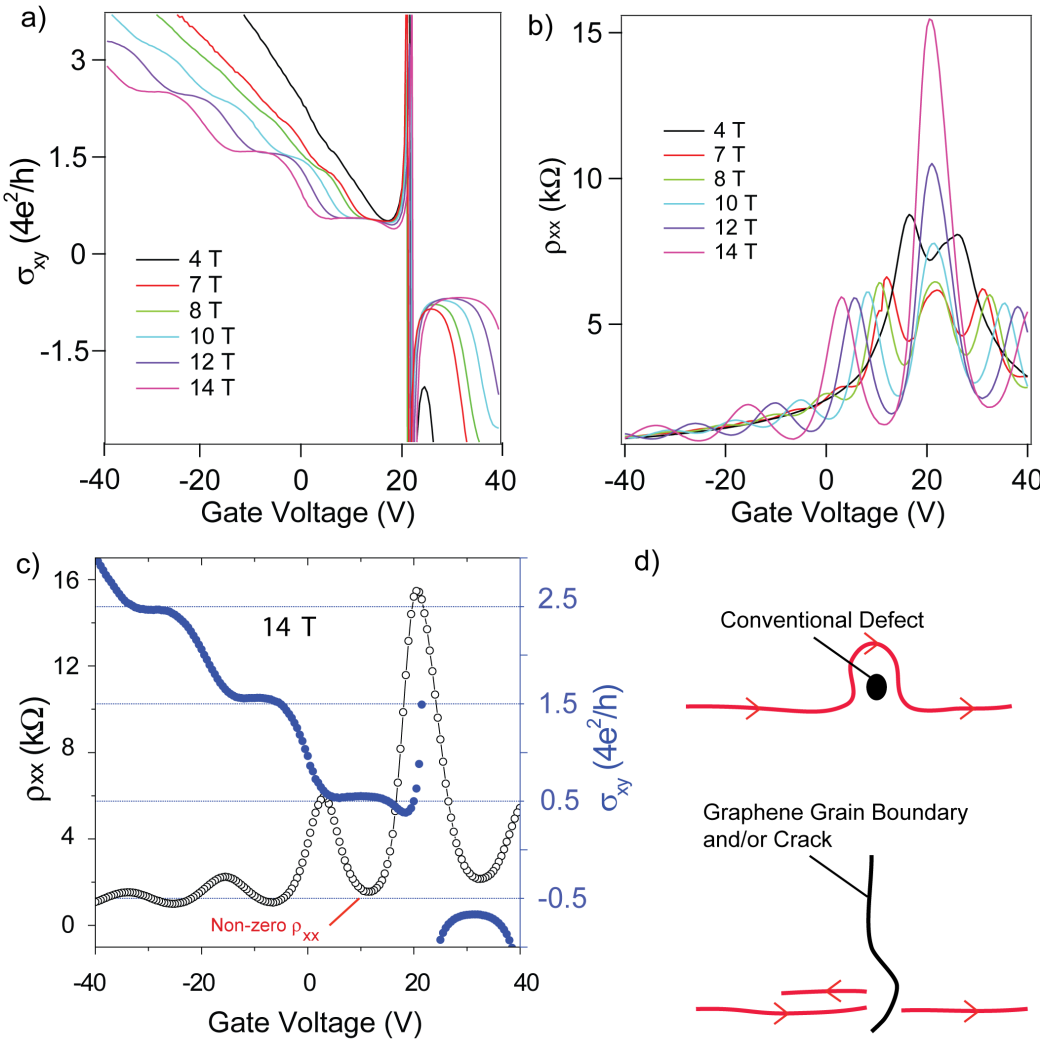


Figure 3.14: a) Transverse conductivity $\rho_{xy}$, and b) longitudinal resistivity $\rho_{xx}$ at different magnetic fields. c) $\rho_{xx}$ and $\sigma_{xy}$ in the same plot, under magnetic field of 14 T. In the Hall plateau regime, longitudinal resistivity $\rho_{xx}$ is not zero, which may be due to the scattering at graphene boundaries, indicated by schematics in c). All measurements were carried at 4 K.

3) low enough temperature to avoid broadening of LLs by thermal fluctuations ($K_B T \ll \omega_c$).

QHE was observed at room temperature in a magnetic field of 39 T for exfoliated graphene sample with a 10,000 $cm^2V^{-1}s^{-1}$ mobility [196]. In a ultra-clean suspended graphene sample, QHE was seen at only 0.5 T at 2K [194]. In our case, the Hall plateau was fully developed at magnetic field of 14 T, as shown in Figure 3.14a.

Quantization of Hall resistance at 14 T is shown in Figure 3.14c. Clear filling factors of 2, 6, 10 can be found in the blue curve, known as the half-integer QHE in monolayer graphene [10, 9]. Multilayer patches in the sample did not affect the QHE, since they are inside the 2D surface, and not affecting the edge channels. Notice that in the longitudinal resistance there is a residual resistivity of

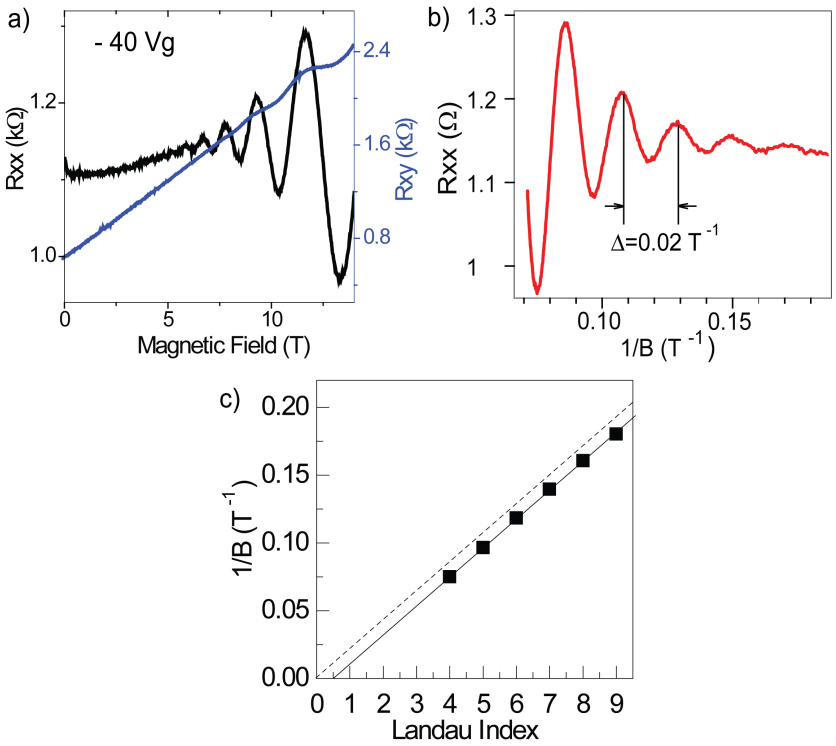


Figure 3.15: a) Transverse and longitudinal magneto-resistance at gate voltage of -40 V. b) $R_{xx}$ plotted against the inverse of magnetic field. c) 1/B plotted as a function of Landau index, extracted from b). Instead of going through the origin (dashed line), the line extrapolates to 1/2 Landau index, due to the Berry's phase in monolayer graphene [9].

about 1-2 kΩm instead of 0 (Figure 3.14c). This non-zero resistivity is also seen in other works ([198]), which may be due to the scattering of graphene grain boundaries at the edge channel. Suppose there is a conventional defect, such as a vacancy, at the edge channel, the iso-potential line will not be affected, and electrons can pass around it, while keeping the ballistic transport in the longitudinal edges. However, if the defect is a crack or a grain boundary (commonly seen in CVD graphene due to the poly-crystallinity) that plays a role of high barrier, transmission of the electron can be less than 1, even in the quantum Hall regime, thus leading to a residual $R_{xx}$, as illustrated in Figure 3.14d.

Magneto-resistance of the sample at -40 Vg was examined in Figure 3.15a. Shubunikov de-Hass Osillations (SdHOs) can be clearly seen at high magnetic filed. It is known that the SdHOs are periodic as a function of the inverse magnetic field 1/B, with the frequency $1/B_F$ called the SdHO frequency [10]. According to the 0.02 $T^{-1}$ SdHO frequency in Figure 3.15b, $B_F$ is then about 50 T. Thus one can assign the SdHO peak at 0.08 $T^{-1}$ as the $4^{th}$ Landau index. The SdHO frequency is then plotted against the Landau index in Figure 3.15c, which appears to be linear. This is in agreement with the LLs in monolayer graphene in Equation 3.26, and also agrees with reports in the literature [10, 9, 198]. Notice that the linear dependence of SdHO and Landau index in Figure 3.15c does not go through the origin of the coordinates: instead it intersects with the 1/2 Landau index, which is due to the Berry's phase in graphene [9].

### 3.3.6 $\nu = 1$ *filling factor in the QHE in our CVD monolayer graphene*

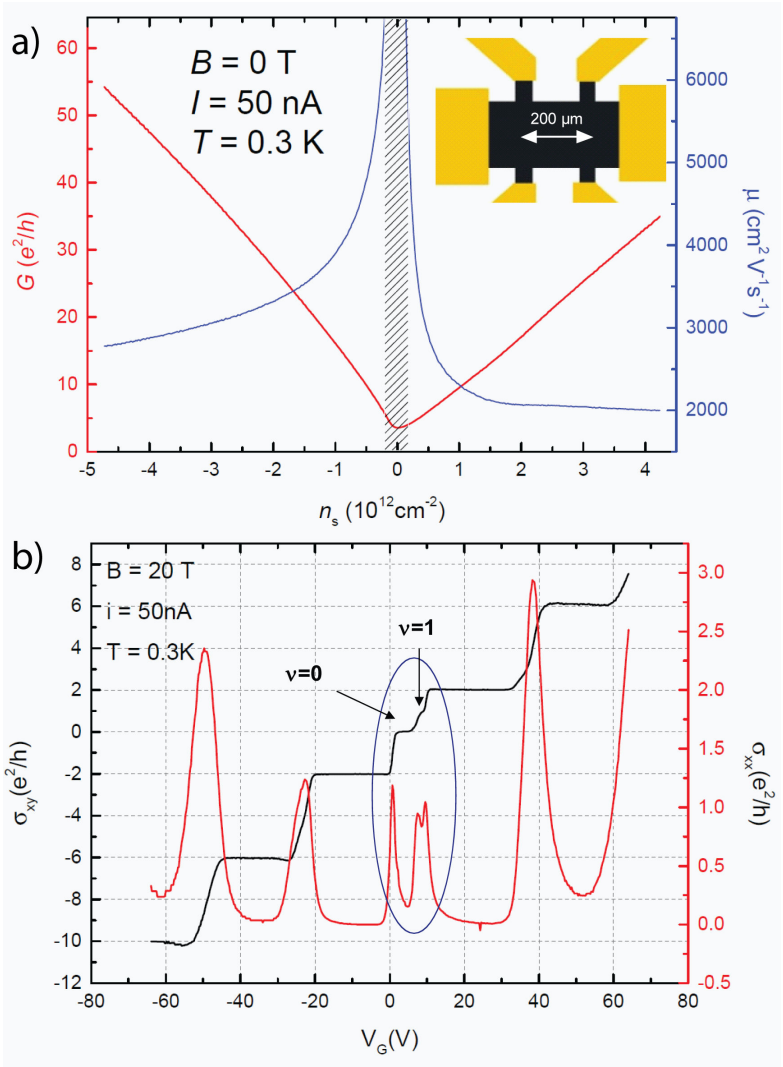


Figure 3.16: a) Field effect of the Hall bar sample, with the x-axis renormalized to the unit of carrier concentration. The extracted mobility is plotted in the same figure, showing the mean value of 2000 $cm^2V^{-1}s^{-1}$ away from the Dirac point. Inset in a) shows the schematics of the sample geometry. b) Transverse and longitudinal conductivity plotted in the same figure. Filling factor of $\nu = 0$ and $\nu = 1$ are indicated by the arrows. Image from F. Lafont and W. Poirier at LNE.

Our collaborators from LNE Paris measured one of our CVD samples. The sample they used is 200 μm in lateral size (inset of Figure 3.16a), which is much smaller compared with the one we measured in the previous subsection. The sample shows a mobility with a mean value of about 2000 $cm^2V^{-1}s^{-1}$, as shown in Figure 3.16a.

Interestingly, at 0.3 K, plateaus at filling factors $\nu = 1$ and $\nu = 0$ appear. These two plateaus are rarely reported in CVD graphene, especially on the CVD samples supported by $SiO_2$ wafer. More details for understanding this behavior are needed and this will be an important part of our future collaborations.

## 3.4 RAMAN OF MONOLAYER GRAPHENE UNDER MAGNETIC FIELD

In the previous chapter, we have briefly introduced Raman scattering (optical phonons) in monolayer graphene without the presence of a magnetic field. When high enough magnetic filed is applied perpendicular to graphene, the linear DOS transforms into discrete LLs with a degeneracy of $\frac{eB}{h}$. Therefore, the continuous interband electronic excitation spectrum transforms into discrete excitations along LLs. When its energy matches the optical phonons, the large electron density of states in the LLs dramatically enhances the electron-phonon interaction, giving rise to the magneto-phonon resonance (MPR) [199].

In this section, we will introduce first the Kohn anomaly induced by electron-phonon interaction, then the inter LLs excitation under magnetic field. So far, the existing literatures are mostly focusing on magneto-phonons in graphene/-graphite that are fixed in the Fermi energy while sweeping magnetic field. Alternatively, here, we will show that by tuning the Fermi level in monolayer graphene with a back gate, one can probe the effects on MPR under fixed magnetic fields.

### 3.4.1 *Kohn Anomaly*

Kohn anomaly is an anomaly in the dispersion relation of a phonon branch in a metal. It is seen as a discontinuity in the derivative of phonon dispersion, produced by the abrupt change in the screening of lattice vibrations by conduction electrons [200, 201]. It is demonstrated by calculations and experimentally verified that graphene phonon dispersions have two Kohn anomalies at the $\Gamma$-$E_{2g}$ and K-$A_1'$ modes [200].

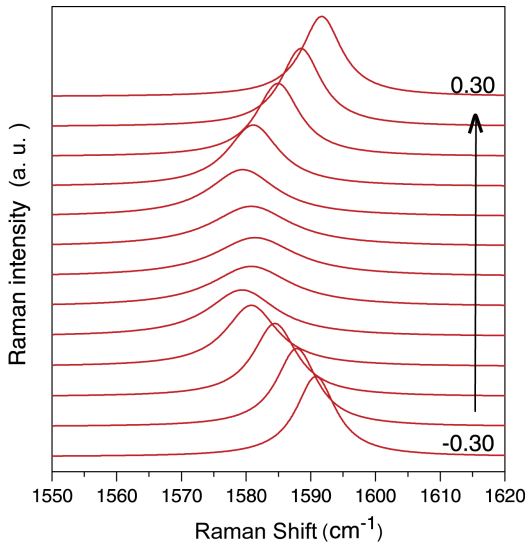


Figure 3.17: Calculated Raman spectra in the high-frequency region including the G-mode for different Fermi energy shifts $E_F$ from -0.3 to 0.3 eV, adapted from [201].

When electric field is applied onto graphene, the Fermi level is tuned away from the neutral point. The carriers therefore interact with long-wavelength

optical phonons in a tuned manner, which can be probed by Raman scattering experiments. G band is found to be markedly sensitive to coupling with Dirac fermion excitations at small wave vectors (long wavelengths close to the Γ point in reciprocal space), while the 2D band has reduced impact, but offers insights on the coupling to particle-hole pairs at large wave vectors [202].

According to the time dependent perturbation theory, at the approximation of linear dispersion near the Dirac point, change of G band phonon energy is described by [203]:

$$\hbar\omega_G - \hbar\omega_G^0 = \chi\left\{|E_F| + \frac{\hbar\omega_G}{4}\ln\left|\frac{2|E_F| - \hbar\omega_G}{2|E_F| + \hbar\omega_G}\right|\right\}, \tag{3.27}$$

where $\omega_G^0$ is $\omega_G$ at the Dirac point, $\chi = 9A_{uc}\lambda^2/4\pi\hbar\omega_G M v_F^2$, with M the carbon atom mass, $A_{uc}$ the area of the graphene unit cell, and $\lambda$ the electron-phonon coupling strength. At high Fermi energy, the linear term dominates over the logarithm term. When $|E_F| < \omega_G/2$, the $E_{2g}$ phonons can decay into electron-hole pairs, thus the phonon lifetime decreases. Experimentally, when the Fermi level is approaching zero, the Raman G peak is down shifted with the peak intensity decreased, together with a broadening of the peak width, as shown in Figure 3.17.

### 3.4.2 *Inter Landau Level Excitations*

Now we come to the discussion of inelastic Raman scattering on inter-LL excitations (the so-called magneto-plasmons).

In magnetophonon measurements, circularly-polarized Raman is often used, because it allows to control the angular momentum transfer. Crossed-circular polarization configurations are often noted as $\sigma^{\pm}/\sigma^{\mp}$, i.e., incident and outgoing photons have opposite circular polarization. While co-circular polarization configurations are noted as $\sigma^{\pm}/\sigma^{\pm}$, i.e., incident and outgoing photons have the same polarization.

*Notice that Raman $E_{2g}$ (G band) phonons carry angular momentum of $\pm 1$. It is therefore seen only in $\sigma^{\pm}/\sigma^{\mp}$ configuration [204].*

Raman scattering selection rules for inter-LL electronic excitations have been well established. Graphene LLs are illustrated in Figure 3.18. Three types of excitations according to the change in the absolute value of the LL index $\Delta|n| = |n_f| - |n_i|$ are illustrated, where the subscript f and i are the index of the final and initial LL index, with the corresponding transition labelled as $n_i \to n_f$. $\Delta|n| = \pm 2$ and $\Delta|n| = \pm 1$ excitations are expected to be active in the crossed-circular polarization configuration $\sigma^{\pm}/\sigma^{\mp}$, and $\Delta|n| = \pm 0$ excitations are expected to be active in the co-circular polarization configuration $\sigma^{\pm}/\sigma^{\pm}$ [205].

### 3.4.3 *Magnetic phonon resonance of Raman G band in graphene*

When the energy spacing between LLs (electronic excitations) is tuned to match the energy of optical phonons, the inter-LLs electron excitations interact strongly with optical phonons, which is called magneto-phonon resonance (MPR) phenomenon. At the resonant magnetic fields for which the energy of inter LL excitations match that of optical phonons, electronic excitations hybridize with

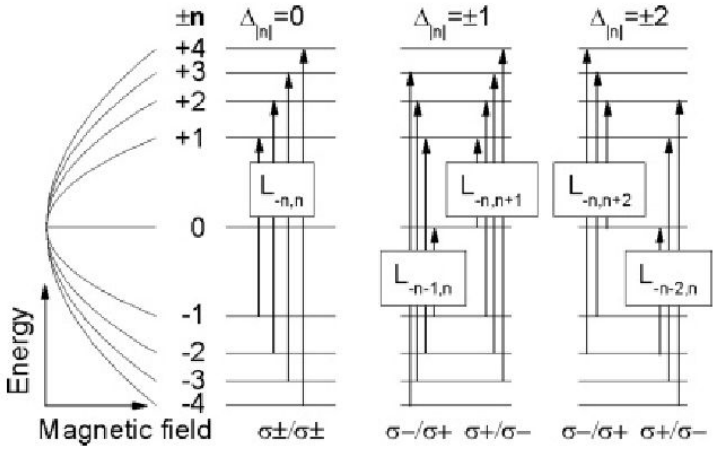


Figure 3.18: Schematic graphene LL spectrum with three types of electronic excitations. Selection rules for the inelastic light-scattering processes are indicated. Picture adapted from [204].

optical phonons. Experimentally, this electronic-optical phonon hybridization is seen as an avoided crossing behavior between these modes as seen through Raman scattering experiments, as shown in Figure 3.19.

Early works predicted that only the inter-LL excitation with $L_i \rightarrow L_f$ = -n-1→n, and -n→n+1 can be hybridized with Raman G band ($E_{2g}$ phonons) [203, 199]. However, recent report shows that -n→n series was also possible for having MPR on the surface layer of graphite [206].

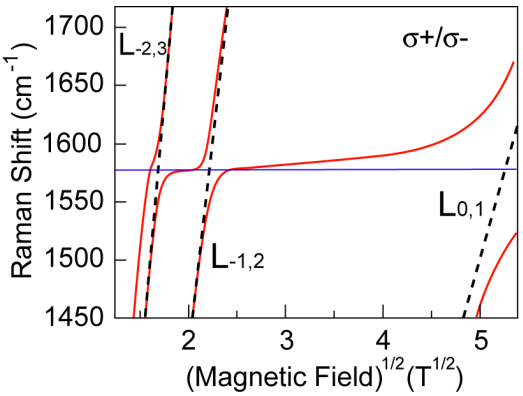


Figure 3.19: Schematics of avoided cross in the G band Raman shift at resonances with the inter-LL excitations. Dashed lines are inter-LL excitation energy, while solid red lines are the hybridized $E_{2g}$ Raman mode. Picture adapted from [204].

For electronic excitations with energy of $\Delta_{i,f}$, the energy of electron-phonon coupled modes can be described, in the case of a neutral graphene system, by [206]:

$$\epsilon^2 - \epsilon_0^2 - 4\epsilon_0 \sum_{k=0}^{\infty} \frac{\lambda}{2} E_1^2 \left( \frac{f(\nu) T_k}{\epsilon^2 - T_k^2} + \frac{1}{T_k} + \frac{f'(\nu) I_k}{\epsilon^2 - I_k^2} \right) = 0,$$

where $E_1 = v_F\sqrt{2e\hbar B}$, $T_k = (\sqrt{k}+\sqrt{k+1})E_1$ stands for inter-LL excitations, $I_k = (\sqrt{k+1}-\sqrt{k})E_1$ stands for intra-LL excitations, $\epsilon_0$ is the G band energy of the neutral system at zero magnetic field, $\lambda$ is the electron-phonon coupling constant, $f(\nu)$ and $f'(\nu)$ take values between 0 and 1, describing the occupancy of the Landau levels. According to Equation 3.27, at high $E_F$, the second term on the right part reduces to zero, the G band energy has a linear dependence with $E_F$. Therefore, one can experimentally extract the slope and thus $\lambda$.

*MPR of graphene with fixed Fermi energy while sweeping the magnetic field*

For neutral graphene, the Fermi level is always pinned in $L_0$ Landau level, it thus allows all inter-LL excitations, and MPR takes place at each time when the energies match: $\Delta_{-n(-n-1),n+1(n)} = \epsilon_0$. However, when the Fermi energy of graphene is tuned away from neutrality, some of the electronic excitations are forbidden due to the Pauli blocking effect. P. Kossacki et al [204] have shown that MPR in graphene can be classified into three distinct regimes (Figure 3.20), according to the Fermi energy at zero magnetic field $E_{F0}$:

1). $2|E_{F0}| < \epsilon_0$. In this regime, all $L_{-n-1(n)} \rightarrow L_{n(n+1)}$ transitions are active and can be hybridized with G band phonon.
2). $\sqrt{2}\epsilon_0 < 2|E_{F0}| < \sqrt{6}\epsilon_0$. Only $L_{-1} \rightarrow L_0$ transition is active, and reasonably hybridize with the G band phonon. All other excitations are Pauli blocked, because no electrons are available in the LLs that can have excitations with energy matches $\epsilon_0$.
3). $2|E_{F0}| > \sqrt{6}\epsilon_0$. In this regime, electron/hole concentration is high enough, all resonant hybridizations of the $E_{2g}$ phonon with $L_{-n-1(n)} \rightarrow L_{n(n+1)}$ excitations are quenched.

*MPR of graphene with fixed magnetic field while tuning the Fermi energy*

As described above, by tuning Fermi energy in graphene, filling factors of carriers in each LL is tuned, thus leading to different amplitudes of the anti-crossing in the MPR [199]. This is actually our aim of study in the next subsections: to study the filling factor dependence of MPR in CVD graphene by gating. Here we focus on the excitations of $L_{-1(0)} \rightarrow L_{0(1)}$ (B ~ 25T), since the Raman G mode splitting is most pronounced at this magnetic field [199].

It is known that in monolayer graphene, fully filled Landau level (L) corresponds to filling factor $\nu = 4(1/2 + L)$. The general trend of G band splitting at the MPR of $L_{-1(0)} \rightarrow L_{0(1)}$ transition can be summarized as follows:
1). At $\nu$= 0, corresponding exactly to a half-filled n = 0 LL, the coupling strengths of $\sigma^+/\sigma^-$ and $\sigma^-/\sigma^+$ polarizations are equal.
2). 0 <$\nu$< 2 corresponds to more than half-filled n = 0 LL, the $L_{-1} \rightarrow L_0$ transition becomes partially blocked, while the $L_0 \rightarrow L_{+1}$ transition is enhanced, giving rise to different splitting in the fine structure of $\sigma^+/\sigma^-$ and $\sigma^-/\sigma^+$ polarizations.

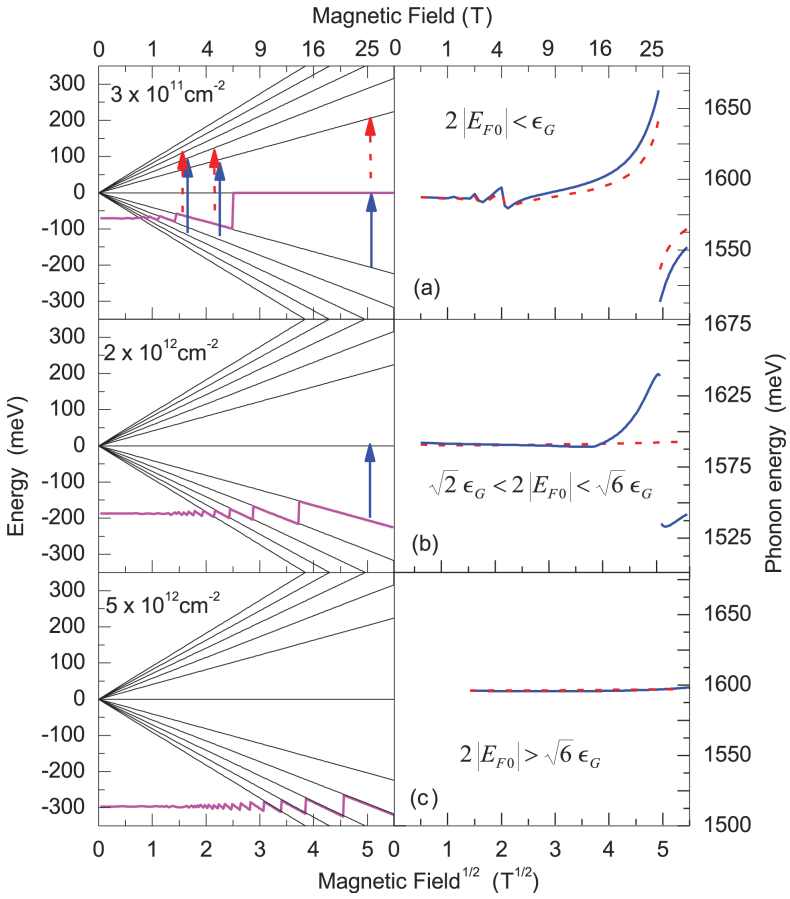


Figure 3.20: Three regimes of the Fermi energy (only hole doping is shown, but it should be the same for electron doping) and its impact on the magneto-phonon effect. Left panels represent fan charts of the Landau levels with marked excitations being in resonance with the $E_{2g}$ phonon. Solid and dashed arrows represent excitations in $\sigma^-/\sigma^+$, and $\sigma^+/\sigma^-$ polarizations, respectively. The purple line shows the Fermi level. Right panels show the evolution of the phonon energy versus the magnetic field. Picture adapted from [204].

3). For 2 <ν< 6, n = 0 LL is fully occupied, no MPR takes place for the $\sigma^-/\sigma^+$ phonon, whereas n = +1 LL is partially occupied, resulting in an MPR-induced fine structure in the $\sigma^+/\sigma^-$ phonon lineshape (with maximum splitting at ν= 2).

Experimentally, it is predicted that the G mode splitting in the vicinity of MPR at $L_{-1(0)} \rightarrow L_{0(1)}$ transition behaves as illustrated in Figure 3.21. In the figure, λ is the electron-phonon coupling constant, and $\gamma = 3\sqrt{3}a^2eB/2\pi$ with $a = 1.4$ Åthe distance between neighbouring carbon atoms.

### 3.4.4 *Gating CVD graphene at the vicinity of MPR*

As we mentioned, so far, the existing works on the MPR of graphene are mainly focused on samples that are fixed in the Fermi energy while sweeping the magnetic field. Here, we show that by tuning the Fermi level in monolayer graphene with a back gate, one can probe the effects of MPR on G band Raman spectrum

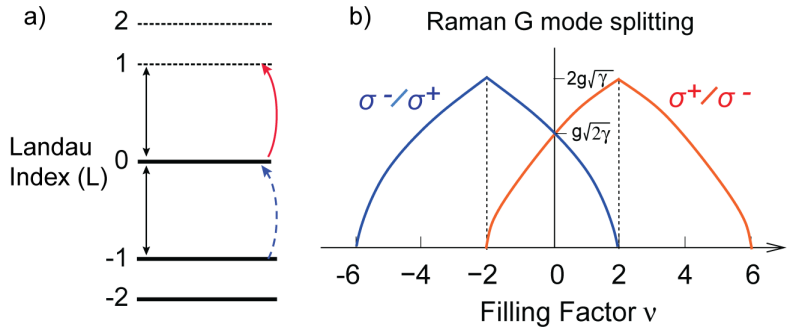


Figure 3.21: a) Schematics of the Landau index. b) Raman G mode splitting at the vicinity of MPR at the transition of $L_{-1(0)} \rightarrow L_{0(1)}$, under a fixed magnetic field of B ~ 25 – 30T). Picture adapted from [199].

of graphene under fixed magnetic fields.

Non-percolated CVD graphene domains are grown by the standard-CVD method at the hexagonal regime, same as shown in Figure 1.15b. After being transferred onto doped silicon oxide wafer, those randomly scattered graphene grains are finally contacted with arrays of long metallic leads (50 nm Au/5 nm Ti), with each lead serving as an individual ground when performing Raman measurements, as illustrated in Figure 3.22a.

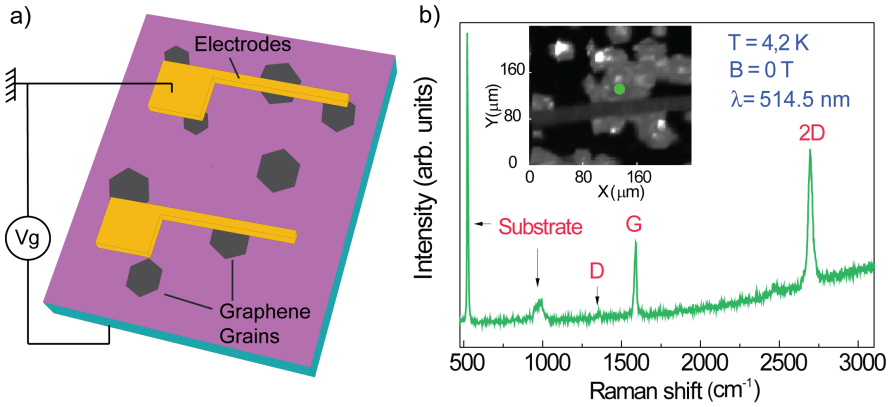


Figure 3.22: a) Schematic picture of the graphene domains contacted with separated electrodes for gated Raman measurements. b) A typical Raman single spectrum of the sample under test. The low D band indicates good quality of the CVD graphene sample. Inset in b) shows a Raman G-band map of the sample. Spectrum in b) is taken at the position of the green dot in the inset.

Magneto-Raman scattering measurements were carried out in collaboration with Clément Faugeras and Przemyslaw Leszczynski at the LNCMI-CNRS, Grenoble. The gated graphene sample was mounted on x-y-z piezo stages in a $^4$He vacuum cryostat, kept at 4.2 K. Raman measurements were performed using an excitation laser beam with λ = 514.5 nm at the power of 4 mW and a laser spot of about 1 μm diameter. For more experimental details, one can refer to [206].

*Zero magnetic field Raman measurements*

A typical single spectrum of the graphene sample in this study is shown in Figure 3.22b. Good quality of the CVD graphene can be seen from the very low Raman D band intensity. We first mapped the sample surface to locate the electrode which was grounded (numbered with lithography), and then focused our laser beam on a fixed point of one of the monolayer graphene grains to do the magneto-Raman measurements.

As shown in Figure 3.23a, the Raman G band spectra are plotted as a function of gate voltages. Similar behavior as in Figure 3.17 can be seen: minimum Raman shift of G band is observed close to the Dirac point (about -10 V). We know that according to Equation 3.2, 3.6 and 3.13, gate voltage can be renormalized into Fermi energy. Therefore, one can plot the single-Lorentzian-fitted peak position and FWHM of Raman G band as a function of Fermi energy, shown in Figure 3.23b.

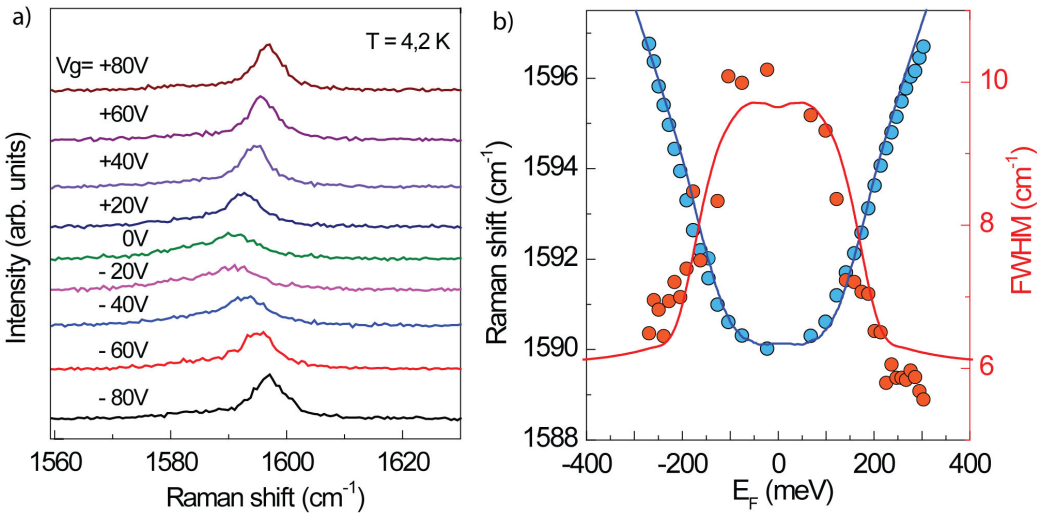


Figure 3.23: a) Gate dependence of Raman G band spectra at zero magnetic field. b) The peak position and FWHM fitted with single Lorentzian from the measured G band spectra, plotted as a function of Fermi energy. Solid lines are fitted by Equation 3.27, with a Gaussian convolution of the Lorentzian shape [207].

Taking the hole side of Figure 3.23b, the linear part at high $E_F$ can be fitted as $\hbar\omega_G = 1585.78 + 0.043 \times E_F\ (cm^{-1})$. According to Equation 3.27, this slope of 0.043 gives an electron-phonon coupling constant of about 0.6 eV/ Å.

*G band splitting at the $L_{0(-1)} \rightarrow L_{1(0)}$ transition MPR*

We now come to the part of filling factor dependence of Raman G mode at several different magnetic field: 14 T, 22 T, 26 T, and 28 T. Gate voltages can be transformed from carrier concentrations $n$, which is determined by the gate voltage according to Equation 3.13. It is known that for each LL in graphene, electron degeneracy is $eB/h \sim B \times 2.418 \times 10^{10} cm^{-2} \cdot LL^{-1}$. Therefore, filling

factors can be transformed from n, obeying the relation $\nu = (7.56 \times V_g)/(2.418 \times B)$.

The key points of our observation are listed below:

(1) At B=22 T, we observe an additional feature at higher energy,

(2) At B=26 T (very close to the resonance at 25 T) we observe both high and low energy additional components,

(3) At 28 T, we observe only the low energy additional feature.

These above features are actually well described by the theory [203]. As shown in Figure 3.24b, the Raman mode shift for neutral graphene is given. Arrows below and above the resonance at 25 T indicates the high energy or low energy shifts. When tuning the Fermi energy of the graphene at each fixed magnetic field, G mode splitting happens as described in Figure 3.21. Color maps of Raman G band as a function of filling factor at 22, 26, and 28T are plotted in the left panel of Figure 3.25.

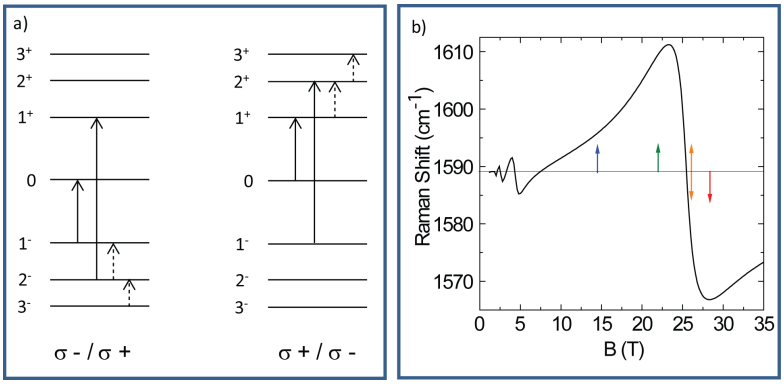


Figure 3.24: a) Schematics of the electron excitations: solid arrows are inter-Landau level excitations, and dashed arrows are intra-Landau level excitations (Cyclotron excitations). b) Raman G-band shift for neutral graphene.

G-peak positions fitted from the color map shows that the splitting is symmetric with respect to polarization (Figure 3.26), being maximum at ν=-2 in one polarization and at ν=+ 2 in the other polarization. Our global experimental results fit reasonably well with Ando's theory [203] (Figure 3.25) in the resonant regimes (between ν = -6 and ν = 2 in one polarization and between ν = -2 and ν = +6 in the other polarization). Outside of the resonance (for high or lower filling factors), we see some deviations, probably due to cyclotron resonance or to confined plasmons (see Figure 3.26). To better understand these large deviations, further studies are needed.

## 3.5 CONCLUSION OF CHAPTER 3

As a conclusion, we have briefly introduced the band structure of mono-layer graphene, and related the electron transport properties of gaphene to the fundamental electronic structures. Examples of graphene transistors on conven-

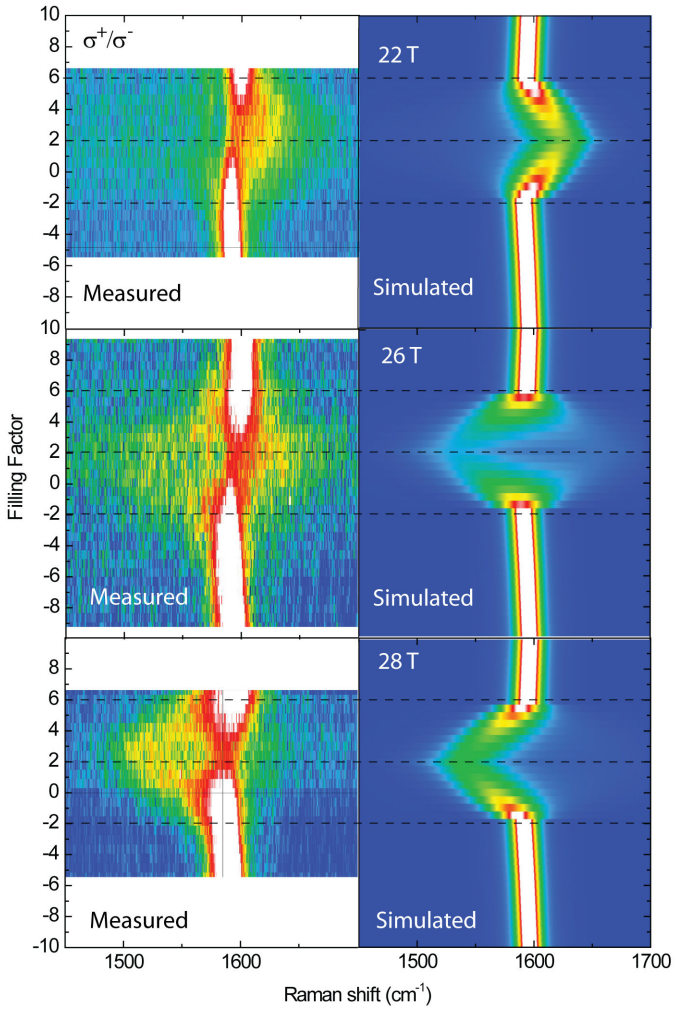


Figure 3.25: Color Map of G band Raman shift as a function of filling factor at ± 22, 26, and 28 T with $\sigma^+/\sigma^-$ polarizations. The left panels are measured data, while the right panels are simulated from [203].

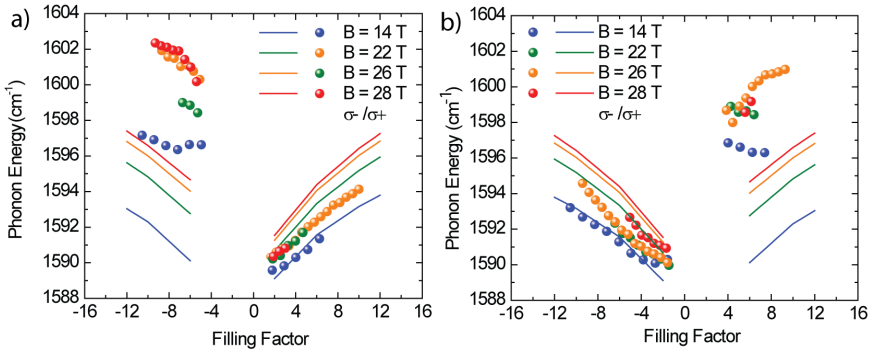


Figure 3.26: Raman G-peak position fitted from the left panel of Figure 3.25 for a) $\sigma^-/\sigma^+$, and b) $\sigma^+/\sigma^-$ polarizations. Solid lines are calculated curves according to [203].

tional $SiO_2$, or by EDL method were introduced. So far, the EDL on large scale CVD graphene needs further optimization in terms of experimental conditions

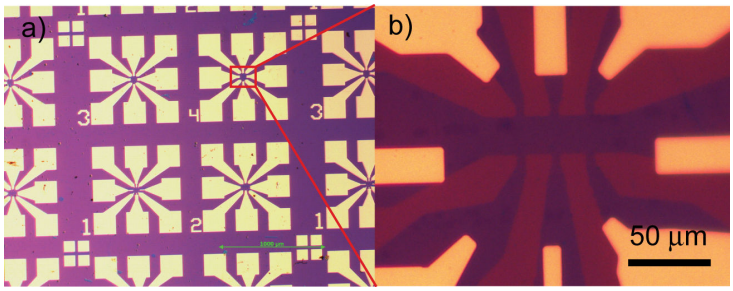


Figure 3.27: a) Arrays of CVD graphene Hall bar with Au electrodes, fabricated by optical lithography. b) Zoom-in optical micrograph of the boxed area in a), showing a graphene Hall bar with three pairs of transverse electrodes and one pair of source and drain electrodes.

to avoid problems such as frozen liquid caused cracks in graphene. Finally, we discussed about the Landau level and quantum hall effect in graphene, with the demonstration of centi-meter sacle graphene sample. We show that with the high mobility CVD-grown graphene, batch fabrication of Hall bars is possible, as shown in Figure 3.27. CVD graphene provides great opportunity for quantum resistance standard applications.

We have briefly reviewed the electronic excitations between LLs and the Magneto-phonon resonances of monolayer graphene. We are able to tune the Fermi energy in the CVD monolayer graphene transferred on silicon oxide with a back gate. We studied the change of electron-phonon coupling in non-resonant regime of 14 T, 22 T, and also the resonant regime at 26, 28 T. A splitting behavior of G band as a function of filling factor is observed at $\sigma^+/\sigma^-$ and $\sigma^-/\sigma^+$ polarizations. We also found that the asymmetry observed in G-mode splitting is having much higher amplitude than described by theory. This is not yet fully understood. We speculate that it may be an effect of confined plasmons.

# 4

# CLEANING GRAPHENE

*The aim of this chapter is to summarize the most popular methods of cleaning graphene. In many studies, the surface of graphene is open to the environment. It is easily contaminated and thus its electronic properties will be degraded. It is therefore important to have graphene as clean as possible, especially for the studies that require high electronic mobility and low doping. Among the methods reported in the literature, we found that the acetic acid cleaning process seems to be an efficient way of cleaning graphene.*

Graphene consists of basically two surfaces and no bulk. In real life applications, its top (and/or bottom) surface is in most cases exposed to the environment. Therefore it is very sensitive to environmental doping, yet it is easily contaminated during sample fabrication process. For example, the typical problem of PMMA residues adhering on the surface, encountered in graphene transistors, degrades a lot of the charge mobility and has aroused recent interests to remove it [208, 209, 210, 211, 25]. Another issue of the cleanliness of graphene is not about graphene itself, but about the substrate on which graphene is resting. It is known that $SiO_2$ is rough, corrugated, and sometimes charged. Therefore, graphene on $SiO_2$ often experiences many scattering centers for electron transport. To solve this problem of substrate scattering, several methods have been developed: a novel way of cleaning the $SiO_2$ wafer [212], the suspension of graphene over two electrodes, or transferring graphene onto other suitable materials, such as hexagonal Boron Nitride (h-BN) [116, 213, 214].

In this chapter, we will briefly introduce several popular methods we applied to our devices for cleaning graphene, in order to improve the electronic performances of graphene devices [215, 216, 214].

## 4.1 THERMAL ANNEALING

Thermal annealing is a rather traditional method, as it is easily accessible in most labs. It is argued that by thermal annealing. PMMA or other lithography resists can be efficiently removed and thus improve the mobility of graphene [217, 218].

Among the thermal annealing recipes, the annealing gases are mainly hydrogen and/or Ar [116, 213], while some use only high vacuum [218]. We have performed a test of such kind of thermal annealing. The conditions we used are 140 °C, 10 sccm Hydrogen and 100 sccm Ar gas under 1 mbar pressure for 12 hours. Indeed the Dirac point of the sample was brought closer to 0 V, and the mobility has increased from several hundreds to 3800 $cm^2V^{-1}s^{-1}$, as shown in Figure 4.1. When the annealing temperature is increased to, for example 400°C, defects start to show up in graphene. And hexagonal pits (confirmed to be zigzag edge by STM) start to form at even higher temperature [79], as shown in Figure 4.2. These hexagonal pits are very similar to those reported after hydrogen plasma treatment [77].

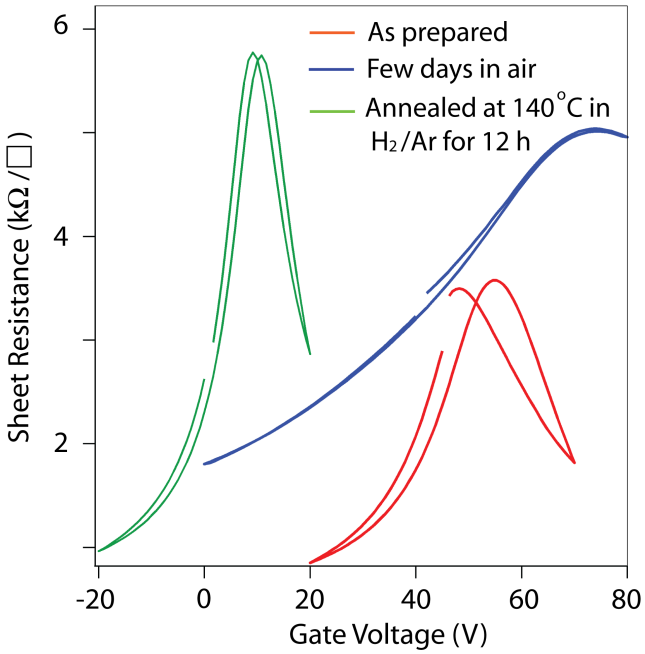


Figure 4.1: Evolution of the field effect for the CVD graphene same sample transferred on $SiO_2$ wafer, with different annealing steps. Degradation of field effect happens after stored in air for 3 days. Annealing in 10 sccm $H_2$/ 100 sccm Ar gas under 1 mbar pressure for 12 hours however brings the Dirac point closer to neutral.

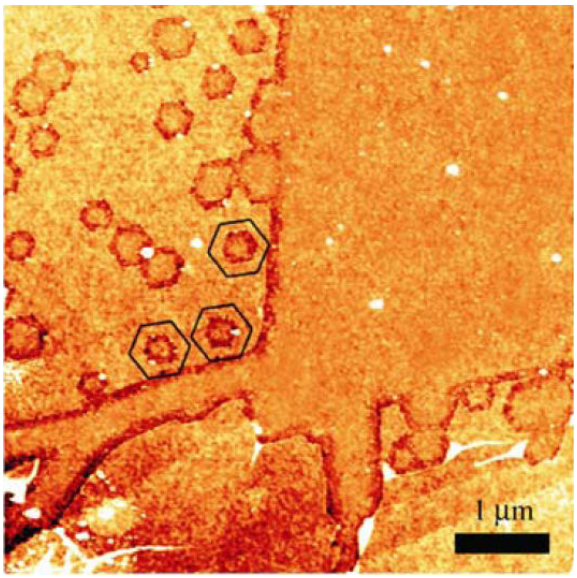


Figure 4.2: Hexagonal pits with zig-zag edges show up after thermal annealing in $O_2/N_2$ mixture at 500 °C for 40 min, followed by a consecutive Ar annealing at 700 °C. Picture adapted from [79]. Notice that there might be a reaction of graphene with silicon.

The problem is that thermal annealing depends a lot on the cleanness of the oven, and also on the purities of the gases used. Results from thermal annealing are not so reproducible. Sometimes graphene becomes more doped after anneal-

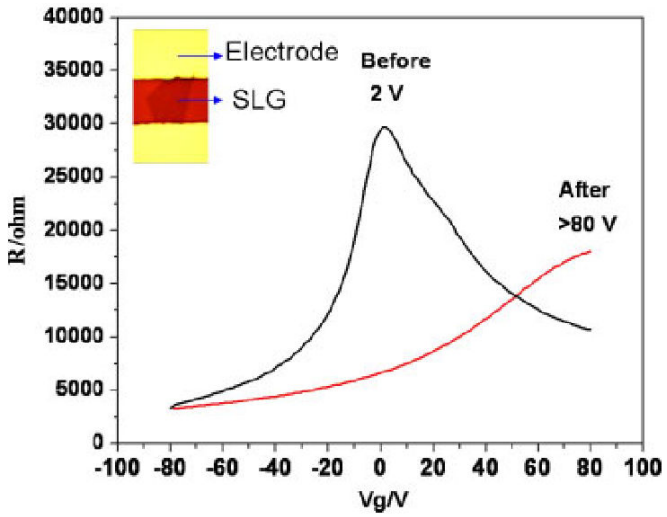


Figure 4.3: A bad example of thermal annealing of CVD graphene, whose field effect performance degraded after annealing. Picture adapted from [219].

ing [219], as shown in Figure 4.3. Therefore, a dedicated annealing chamber is highly needed for graphene cleaning.

## 4.2 CURRENT ANNEALING

The second way of cleaning graphene was first developed by J. Moser et al [211], and ever since is has been widely adopted in the field of cleaning suspended graphene. It has been shown that the electronic temperature can be as high as 2000 K when graphene is biased with high current densities in the saturation regime [220].

During the current annealing, a current or voltage is applied to the sample and at the same time, the real-time power or resistance of the sample are monitored in order to estimate Joule heating and avoid possible runway of the annealing (similar to the electro-migration process for preparing a nanogap). One should increase by small steps so that heating of the sample can be stopped as soon as there is a sudden drop of sample resistance. Once there is a resistance drop, one should ramp current/voltage back to zero, and check the mobility of the sample. If it is not improved enough, current annealing should be executed once more. Notice that it may need to sweep current/voltage towards both positive and negative signs, as shown inFigure 4.4.

Even though current annealing is widely used, it still has its limitations. For example, when the sample is patterned into a Hall bar geometry, due to the geometry nature, current can not pass through the whole sample surface homogeneously, leaving some dead-space with dirt that never gets off. Also, when the sample is not suspended, the efficiency of current annealing is significantly decreased. Figure 4.5 gives an example of a graphene Hall bar that is manually decorated with some low melting-point metal nanoparticles (Sn) with the same diameters. One can monitor the heat flow by looking at the change of those nanoparticles. Indeed, as can be seen, the places where contacts are made seem

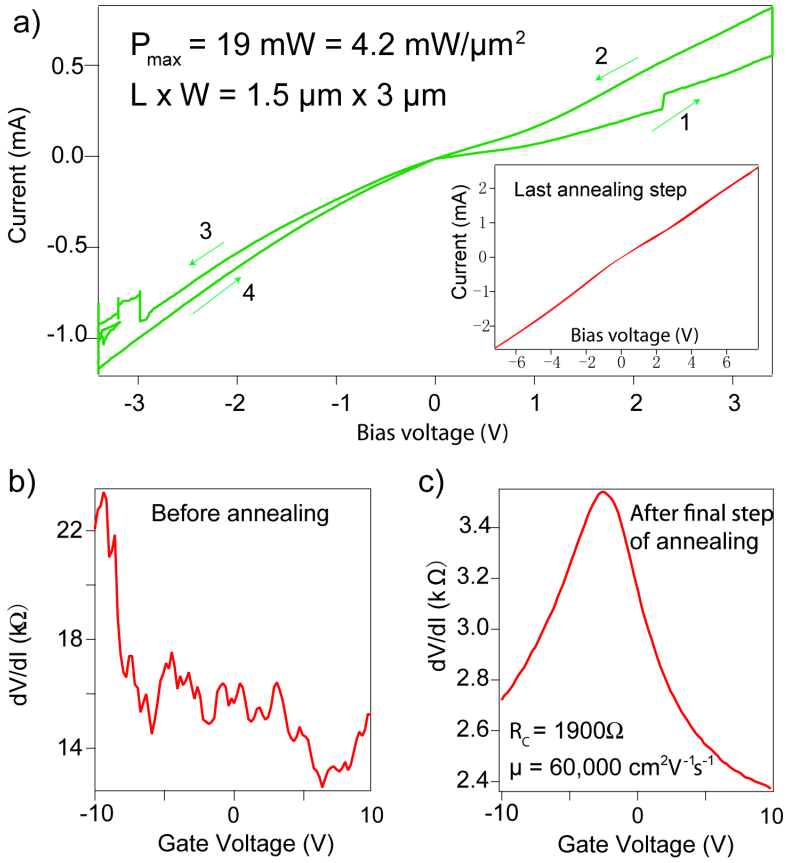


Figure 4.4: Joule heating steps and their effect on mobility at 4 K. a) Typical I(V) curve recorded during the annealing process. The vertical lines correspond to places where the voltage ramping was paused to let the system get clean. Inset: last annealing step. The maximum dissipated power was 19 mW. b) Field effect curve before annealing, and c) after the last annealing step. Figure adapted from Adrien Allain's PhD thesis, page 204.

"hotter" than other places on the sample surface. This is simply because of the Ohm's law that states that when the resistance is higher (the case for contact resistance), it dissipates more current, and thus makes the nanoparticles melt and change in size. However, when the contacts are good, the most dissipative zone is in the centre of the sample surface [221].

## 4.3 HEXAGONAL BORON NITRIDE SUBSTRATE

h-BN is a semiconductor with 5.97 eV band gap and a very similar lattice geometry to graphene, with only 1.7 % lattice mismatch. It is free of dangling bonds and free of charge traps, thus it is much more suitable as a substrate for graphene nanoelectronics [116, 213, 214].

To have an idea about the improvement, we compared two field effect curves on $SiO_2$ and on BN side by side in Figure 4.6. It can be seen that the Dirac peak is much sharper for the graphene devices made on h-BN. As already introduced in Chapter 2, dry-transfer method is usually applied in graphene/BN heterostructures. Studies show that graphene will be even better protected by

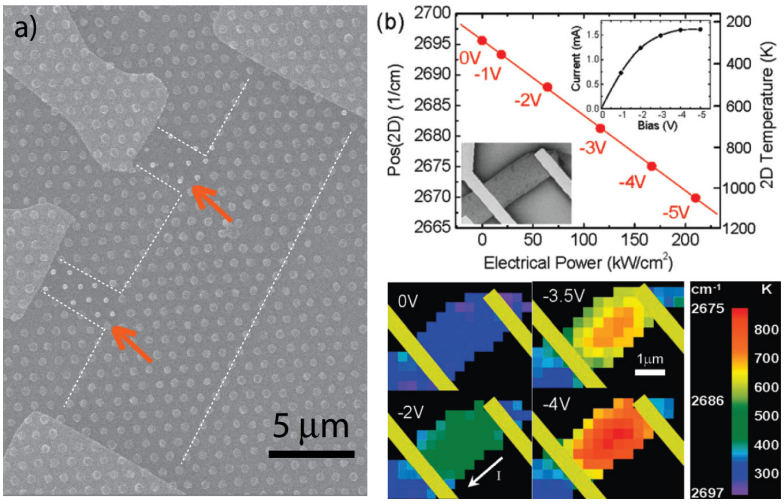


Figure 4.5: a) CVD graphene Hall bar, the Sn nanoparticles decorating graphene are made by electron beam lithography. It is seen that most heated parts are close to the electrodes, which are dominated by contact resistance. Arrows indicate the partially evaporated Sn nanoparticles. The sample here is fabricated for use in the last chapter in this thesis. b) Raman 2D band position as a function of the biased current in two-probe graphene device. Electron temperature is extracted from the position of Raman 2D peak position. Picture adapted from [221].

BN from environmental doping if one can make a BN-Graphene-BN sandwich structures. Notice that even placed on BN, at each step of device fabrication, thermal annealing is still needed.

However, given the fact that BN crystals used in nano-electronic studies are mostly obtained by mechanically exfoliating a bulk BN, the size of devices is therefore very much limited. Efforts are now devoted to the growth of CVD BN and even graphene directly on BN by CVD methods [222, 21].

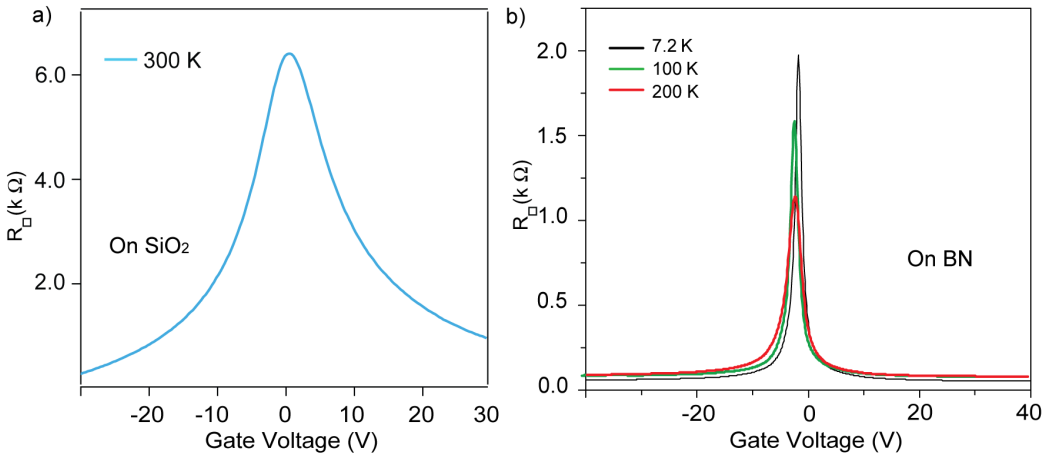


Figure 4.6: a) and b) Field effect curves of graphene device on $SiO_2$ and on BN, respectively. Data on BN are adapted from [116].

## 4.4 HYDROGEN PLASMA ETCHING

If hydrogen plasma is irradiated onto graphene with a considerably strong power, graphene will be hydrogenated, leading to the so-called graphAne [72]. However, if one exposes graphene to a mild hydrogen plasma, it will only etch along the edges that are energetically favourable for hydrogen to etch, giving rise to hexagonal pits, and nano-ribbons [77].

Indeed, recent work shows that a controlled hydrogen plasma reaction at 300°C can etch graphene or its nano-ribbons selectively at the edges over the basal plane [76]. They also show that Raman mapping reveals no D band in the planes of single-layer or few-layer graphene after the plasma reaction, confirming that the controlled hydrogen plasma does not introduce defects in the basal plane. It is reasonable that the PMMA contaminations are less stable than the $sp^2$ bonding inside graphene plane, and they could be removed by mild hydrogen plasma etching. A recent work showed the possibility of this method, but their results are still far from ideal [223].

## 4.5 AFM SWEEPING CLEANING

Mechanical sweeping with an AFM tip with contact mode is also proven to be able to remove most of the resist on top of graphene. Field effect curve taken after the AFM contact mode sweeping is indeed much improved than before [208, 209]. However, this mechanical technique is limited to the lateral size of the order of 100 μm.

## 4.6 ACETIC ACID TREATMENT

Non-invasive cleaning of graphene is a challenging but a mandatory task for transport studies of ultra-clean graphene, such as fractional quantum Hall effect, ballistic graphene junction, etc. Among the methods mentioned in the previous sections, thermal annealing and hydrogen plasma cleaning are compatible with large scale CVD graphene. Moreover, we know that STM is a powerful technique to probe local tunnelling spectrum of a conducting sample, and to achieve atomic resolution of sample topography. However, when the PMMA residues are present, STM tips have difficulties in finding a tunnelling current, and most of the cases they crash.

Here, we introduce another chemical route of removing the residual resist on graphene, which is also compatible with large size graphene treatment. We first tried to remove PMMA by solvents, as PMMA is usually dissolved in Ethyl Lactate or Anisole. However, it seems that the remaining parts of PMMA on graphene is extremely difficult to dissolve in the two above solvents. For example, after being dipped in Ethyl Lactate for 48 hours, there are still bluish PMMA contaminations on the graphene surface.

Recently, a research group found that by using acetic acid instead of conventional acetone, the graphene surface can be cleaned resulting in much less PMMA residues [25]. Following their method, we tested one of our CVD graphene

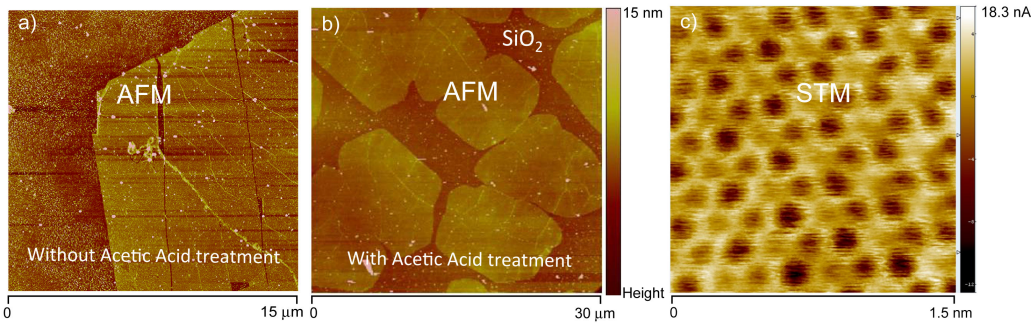


Figure 4.7: AFM tapping mode scan of surfaces of CVD graphene transferred with PMMA assisted method on $SiO_2$. a) PMMA is removed by acetone, and b) PMMA is removed by pure acetic acid for 48 hours. c) a zoomed-in look of the graphene surface cleaned by acetic acid. Image a) is measured by Dipankar Kalita in our group, and image c) is measured by Toai Lequang and Claude Chapellier, from CEA-INAC, Grenoble.

transferred onto $SiO_2$/Si wafer. The sample is dipped into pure Acetic acid for 48 hours, and rinsed with acetone, IPA, respectively, follow by $N_2$ blow dry.

As shown in Figure 4.7a, before acetic acid treatment, there is a lot of granular like contamination, which can actually be removed by AFM contact mode. That means these contaminations are soft matter, and very likely to be PMMA residues. After putting into pure acetic acid for 48 hours, the sample surface becomes rather clean, as shown in Figure 4.7b. A roughness measurement of the cleaned graphene shows that Rq is about 0.39 nm. Knowing that the Rq for bare $SiO_2$ wafer is about 0.23 nm, it indicates good flatness of graphene surface. After the acetic acid treatment, the graphene surface is compatible with STM measurements, as shown in Figure 4.7c.

## 4.7 CONCLUSION OF CHAPTER 4

Cleaning is a crucial technical problem in graphene studies, as graphene is often exposed to the environment and easily gets doped. For studies such as STM, the sample is very easily contaminated, which makes the STM tip crash. Moreover, the electronic properties of graphene will be degraded without a proper cleaning process.

To have as clean CVD graphene as possible is very challenging, since the nature of the transfer and sample fabrication usually make graphene inevitably comes in touch with lithography resists - that are extremely hard to be atomically removed. We found that among many methods reported in the literature, acetic acid cleaning seems to be the most efficient way of cleaning graphene.

We have summarized most of the popular methods of cleaning graphene, including:

(1) Mechanical way by AFM.

(2) Boron nitride sandwiching.

(3) Physical way by current annealing, or thermal annealing.

(4) Hydrogen plasma etching
(5) Acetic acid treatment.

These last two methods are compatible with large scale CVD graphene cleaning, and may be the future direction of cleaning CVD graphene.

# 5

# CHEMICAL CONTROL OF DISORDER IN GRAPHENE

*This chapter makes the crossover from "clean" graphene to "dirty" graphene in a controlled manner. We have discovered a new chemical way of inducing disorder in graphene by simply dipping graphene into the $Na_2S_2O_8$ solution. This enables us to have one more knob of tuning graphene properties, which opens the possibility of a variety of physics.*

Graphene consists of two sub-lattices that lead to quasi-particles described by a Dirac equation. When graphene is free of disorder, its band structure at low energy is the well-known Dirac-cone structure, with a Fermi velocity of 1/300 the speed of light [11]. However, the above standard picture of graphene electronic structure is based on a single-particle model in ideal graphene, *i.e.*, electrons are free of interactions.

Thanks to the pseudo-spin, ideal graphene should be immune to back scattering. In real applications, graphene is however never ideal, and its properties are affected by intrinsic and extrinsic disorders. Surface ripples (bending of $\pi$ orbital) and topological defects (structural defects of the honeycomb lattice like pentagons, heptagons) are the major types of intrinsic disorder. Extrinsic disorder then includes: adatoms, environmental charges, and extended defects such as cracks and edges.

Defects such as vacancies in graphene locally modify the on-site potential, and they act as scattering centres, which may cause a reduction of the Fermi velocity. Nevertheless, when a defect is present in graphene, enormous new physical phenomena are predicted theoretically and observed experimentally. For example, 1) magnetism is predicted to emerge due to the interplay of pseudo-relativistic electrons [224, 225, 226, 227], and 2) band gap opening is seen in graphene nanomesh [228, 229, 230]. On the other hand, lattice distortions of graphene can also modify the Dirac equation that describes its low-energy band structure, giving rise to the so-called gauge field disorder [11].

As discussed above, electronic properties of graphene depend largely on disorder. It is therefore of great interest to control the microscopic disorder in graphene, thus controlling the electronic properties. In this chapter, we focus on the transport properties of disordered graphene. We briefly introduce electron localization mechanisms, and ways of inducing disorder in graphene. A new chemical method of controlling disorder in CVD graphene is discussed in detail with indepth and detailed characterizations.

## 5.1 SCATTERING MECHANISMS IN GRAPHENE: WEAK AND STRONG LOCALIZATION

When electron waves propagate in imperfect crystalline materials, they are scattered by the defects, which causes the so-called localization of electrons [231].

To characterize the strength of localization, a decay length $\xi$ is defined since the localized electron wave can be described as:

$$|\psi(\mathbf{r})| \sim exp(|\mathbf{r} - \mathbf{r}_0| / \xi). \tag{5.1}$$

When $\xi$ is short, *i.e.* disorder is strong, the conductance G exhibits an exponential temperature dependence because electron transport occurs via thermally activated hopping between the localized states. The general thermal activation law in 2D systems can be expressed as below:

$$\sigma \propto exp[-(T_0/T)^{\alpha}], \qquad \alpha = \begin{cases} 1 & Arrhenius-like\ hopping\ [232] \\ 1/3 & Mott's\ variable\ range\ hopping\ [233] \\ 1/2 & Efros-Shklovskii\ correction\ [234] \end{cases}. \tag{5.2}$$

On the other hand, in the weak disordered limit, $\xi$ can be quite long, exceeding either the electron mean free path $l_e$, or the sample size $L_S$. In the weak disorder case, the conductance decreases logarithmically with decreasing temperature.

### 5.1.1 *Abrahams's Localization Scaling Theory*

Let us first introduce the conception of dimensionless conductance $g_L$. In a system with size L, $g_L$ is defined as:

$$g = \frac{E_T}{\delta}, \tag{5.3}$$

where $E_T = \frac{\hbar D}{L^2}$ is the Touless energy, while $\delta = \frac{1}{N(\epsilon)L^d}$ is the mean level spacing, with $N(\epsilon)$ the density of state, D diffusion coefficient, and d the dimension. According to the definition of conductance $G = \sigma \cdot L^{d-2}$, together with Equation 3.9, g can be rewritten as:

$$g = \frac{\hbar D N(\epsilon) L^d}{L^2} = \frac{\hbar G}{e^2} = \frac{G}{G_0}, \tag{5.4}$$

where $G_0 = \frac{e^2}{\hbar}$ is the quantum of conductance. In the absence of spin-orbit interaction, Abrahams et al proposed a single-parameter scaling equation [235]

$$\beta(g) = \frac{\partial ln[g(L)]}{\partial ln(L)}. \tag{5.5}$$

The above equation approaches to $d-2$ for large g. That is to say, in the 2D case, $\beta$ is always negative. Integrating both sides, the resultant g is then 0 for large L. This is the famous argument that all states in 2D are localized.

### 5.1.2 *Influence of the electron-electron interactions*

The localization theory described in the previous subsection deals only with non-interacting electrons. Its validity was soon questioned by other works using real-space re-normalization-group transformations [236].

B.L. Altshuler and co-workers studied a fermion system subjected to random external potential interacting with a weak short-range potential. Within the metallic regime, *i.e.*, $k_F l \gg 1$, a disordered two-dimensional conductor has a logarithmically temperature dependent correction [237, 238]:

$$\delta\sigma_{ee} = -\frac{e^2}{2\pi^2\hbar} \cdot g_{2D} \cdot \ln(\frac{\hbar}{k_B T \tau}), \tag{5.6}$$

where $g_{2D}$ is a pre-factor, $\tau$ is the electron scattering time, which satisfies the relation with mean free path $l = \tau \cdot v_F$.

### 5.1.3 *Weak localization effect*

Assuming the system is sufficiently clean, then the Fermi wavelength is much shorter than the mean free path $k_F l \gg 1$. Within a total distance $L_\phi$ the electron waves can still preserve their phase coherence, then interferences can take place if electrons are propagating along closed trajectories. This quantum effect is called weak localization. It becomes more obvious at low temperatures, leading to corrections to the classical expressions for the conductivity.

Weak localization is usually due to the positive interference between two paths along closed loops, traversed in opposite directions, shown in Figure 5.1 [239]. As a result, the probability that the electron goes back to the origin is enhanced (localized), giving rise to a decrease of conductivity. Therefore, in most metals, the weak localization effect gets destroyed by applying a small magnetic field, leading to a negative magneto-resistance.

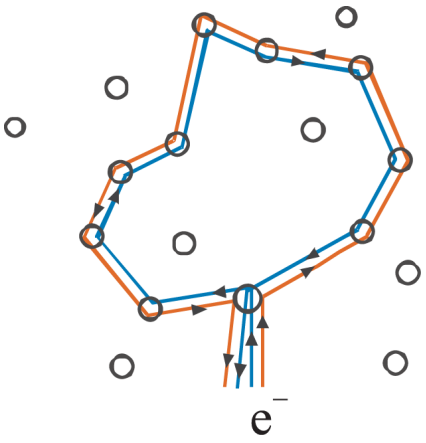


Figure 5.1: The trajectories of an electron scattered by impurities that give rise to a quantum correction to the conductance. Adapted from [239].

However, graphene has an additional Berry's phase of $\pi$ [10]. As a consequence, the motion of electrons along two closed paths interfere destructively in

graphene, leading to a suppression of backscattering. Hence, a positive magneto-resistance, *i.e.*, weak anti-localization is expected. However, the Berry's phase comes from the chirality of valleys [11, 240]. Therefore, in order to observe anti-localization, an electron should not be subjected to strong inter-valley scattering, which requires clean graphene.

The magneto-resistance at high charge carrier concentration has been well developed in graphene [241]. The correction to the Drude conductivity reads as:

$$\delta\sigma = \frac{e^2}{\pi h}\left[F\left(\frac{\tau_B^{-1}}{\tau_\phi^{-1}}\right) - F\left(\frac{\tau_B^{-1}}{\tau_\phi^{-1}+2\tau_{inter}^{-1}}\right) - 2F\left(\frac{\tau_B^{-1}}{\tau_\phi^{-1}+\tau_{inter}^{-1}+\tau_{intra}^{-1}}\right)\right]. \quad (5.7)$$

Here $F(z) = \ln(z) + \Phi(0.5 + z^{-1})$, with $\Phi$ the di-gamma function. $\tau_B^{-1} = 4eDB/\hbar$, and $\tau_\phi = L_\phi^2/D$ the phase coherence time.

Experimentally, when weak localization dominates the correction to graphene conductivity, one can fit the measured magneto-resistance at different gate voltages with Equation 5.7. Using the fitted time scales $\tau_x$, one can extract the parameters such as phase coherence length, etc.

### 5.1.4 *Inter- and intra-valley scatterings in graphene*

Graphene's band structure has two valleys, and electrons propagating in the energy band can be scattered either within one valley (intra-valley), or between valleys (inter-valley) [242].

Intra-valley scattering is characterized by the time $\tau_{intra}$, which originates from charge impurities, and ripples [239]. Inter-valley scattering (characterized by $\tau_{inter}$) is caused by short-range defects (such as the edges of the sample) that are able to scatter electrons between the two valleys. While small $\tau_{intra}$ suppresses interference within a valley, small enough $\tau_{inter}$ restores it by mixing the two valleys, which have opposite chirality.

Different scattering mechanism leads to different time scale. For example, when weak point disorder is the major source of inter-valley scattering, $\tau_{inter}$ is defined by $\tau_{inter} = \sigma_{sr} \cdot h/(2e^2 \cdot v_F\sqrt{\pi n})$. If charge-impurity is the intra-valley scattering source, $\tau_{intra} = h/(2e \cdot v_F\sqrt{\pi}) \cdot \mu \cdot \sqrt{n}$ [26]. Here $\sigma_{sr}$ denotes short-range conductivity, and $\mu$ is the electronic mobility.

## 5.2 WAYS OF INDUCING DISORDER IN GRAPHENE

Recently, a few works have been devoted to functionalizing graphene by disorder. For example, defect scattering centres were introduced in graphene using Ne and He ion irradiation [243]. Oxidizing graphene is also an effective approach to make graphene disordered [244, 245]. Interestingly, graphene oxides can be easily reduced back to $sp^2$ graphene by thermal annealing or chemical reactions. Very similar behaviours are found in hydrogenated graphene with partially $sp^3$ bonds via hydrogen plasma irradiation [72]. Ozone treatment was recently used to induce defects, in order to make the transition of weak-localization to strong-localization in graphene [26].

In this section, rather than plasma treatment, graphene grown by the CVD method shows an increased disorder by being dipped in the Cu etchant for longer time. This method of inducing disorder gives first a hint to the CVD graphene device fabrication process: since the solution we used to induce disorder is also the Cu etchant, graphene quality may be degraded during transfer process, as Cu removal is a routine process. That is to say, many of reported poor quality graphene is possibly due to this reason.

CVD graphene was grown under the standard-CVD condition in Chapter 1, and was then transferred onto $SiO_2/Si$ wafer for further measurement. The samples were then dipped in a 0.1 g/ml $Na_2S_2O_8$ solution for a controlled duration. We found that the disorder in graphene increases with increasing etching time, as we will discuss in details in the following subsections.

### 5.2.1 *Field effect in disordered graphene*

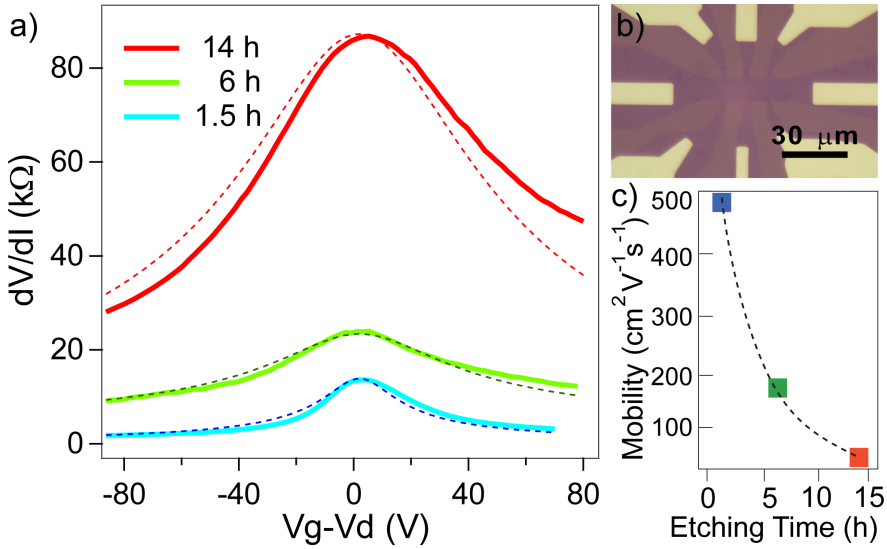


Figure 5.2: a) Gate dependence of resistance of the sample dipped in 0.1 g/ml $Na_2S_2O_8$ for 1.5 h, 6 h, and 14 h, respectively. Dashed lines in a) are fitted curves using Equation 3. 17. b) shows the optical micrograph of the device under test. c) Charge mobility extracted from fitted curves in a), plotted as a function of etching time. Clear decreasing trend can be seen, and the dashed line in c) is a guide to the eye.

Graphene devices with four-probe electrode configuration are fabricated (see Figure 5.2b) for transport studies. The sample was dipped in the $Na_2S_2O_8$ solution, and was taken out at different durations for field effect curves measurement at room temperature. As shown in Figure 5.2a, there is an increase of total resistance with increasing etching time. Notice that the Dirac point of the three curves are normalized to 0 V, since residual doping is not under control, and the measure of residual doping is meaningless.

By fitting the curves with Equation 3.17, we found that room temperature mobility of the sample decreased from about 500 to 30 $cm^2V^{-1}s^{-1}$, for etching

times from 1.5 h to 14 h. The degradation of mobility can be simply explained by increased scattering by defect sites.

### 5.2.2 *Raman characterization of defected graphene*

As described in Chapter 3, Raman peak position at around 1300 $cm^{-1}$ stands for defect-activated phonons, whose intensity is a measure of the level of disorder. Intensity maps of D band are measured for the same set of samples as shown in Figure 5.2.

As it can be seen, when graphene is let in etchant for only 1.5 hours, no strong D peak can be found except for the edges. This is due to the oxygen plasma etching procedure when patterning graphene into a Hall bar geometry. Oxygen plasma creates random defects along the edges and leaves a strong Raman D signal. When the etching time is increased to 6 hours, graphene shows a higher Raman D peak. The D band becomes strong and homogeneous in the sample etched for 14 hours, where the D band intensities at the edges and inside the 2D bulk were hardly distinguishable before, as shown in Figure 5.3c. The Raman map was performed with a resolution of 300 nm. Homogeneous D-band maps indicate homogeneous microscopic defects in the graphene. This provides a controllable way to induce disorder in CVD graphene in applications such as quantum switches [13].

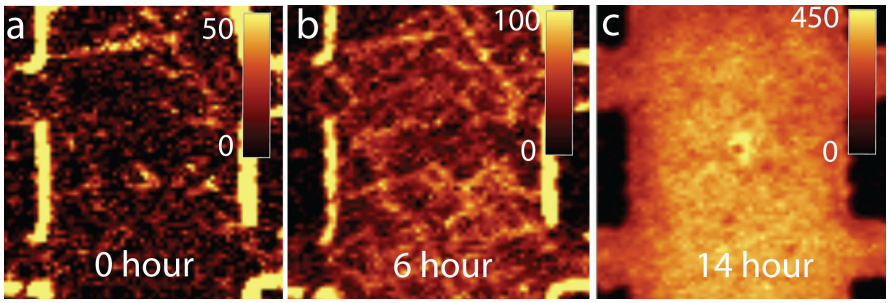


Figure 5.3: Raman D-band intensity map of the same sample etched in 0.1 g/ml $Na_2S_2O_8$ for a) 0 hours, b) 6 hours, and c) 14 hours. Image size 15 × 15 $\mu m^2$. Data obtained with the help of Dipankar Kalita (Néel Institute).

Another set of samples are examined by both Raman and resistance measurements. Single Raman spectra were taken for samples etched for different durations. As shown in Figure 5.4a, D band intensity increases as a function of etching time, consistent with the maps in Figure 5.3. At each point of etching time, sample sheet resistance was also measured, as shown in Figure 5.4b. An almost linear increase of room temperature sheet resistance with etching time was seen. Unlike the field effect shown in Figure 5.2a, sheet resistance in Figure 5.4b was measured with no gate-polarization, meaning a natural doping in the sample. However, the general trend is clear with the error bar included in the plot. Figure 5.4c exhibits the corresponding D-peak area for different etching times. In agreement with the sheet resistance, D-peak area is also increasing, from 0 to 200 counts, for etching times of 1.5 to 19 hours, respectively.

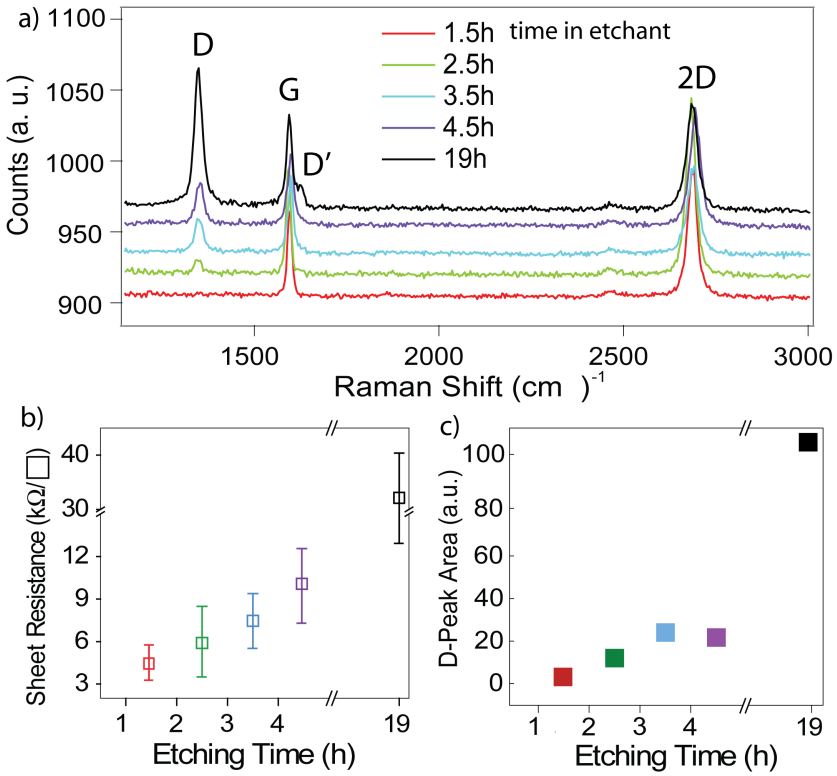


Figure 5.4: a) Raman spectra of graphene treated in 0.1 g/ml $Na_2S_2O_8$ for different time durations, and b) their corresponding sheet resistance, showing an almost linear increase of room temperature sheet resistivity with etching time in $Na_2S_2O_8$ solvent. c) The D peak area extracted from a), plotted as function of etching time. Measured by Jinxing Liu (Néel Institute).

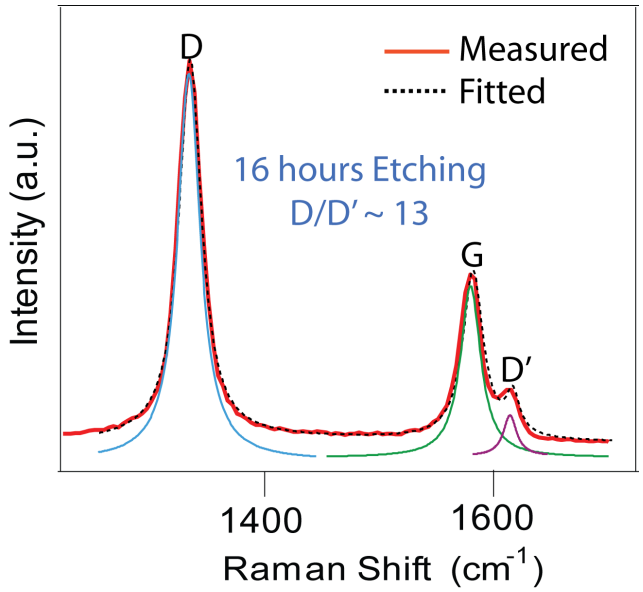


Figure 5.5: Deconvolution of Raman single spectrum for the sample etched in 0.1 g/ml $Na_2S_2O_8$ for 16 hours. D-to-D′ intensity ratio is fitted to be around 13.

When etched for a long enough time (16 hours for example), a D′ peak starts to show at the right shoulder of G peak. It is reported that by evaluating the

peak intensity of D/D′ ratio, one can extract the information of the defect type, which is $sp^3$ when D/D′ is higher than 6, vacancies if D/D′ is around 3 [28]. In our case, we performed the same analysis in the sample etched for 16 hours. It turned out that D/D′ ratio is about 13, indicating $sp^3$ type defects, as shown in Figure 5.5.

### 5.2.3 *TEM observation of defected graphene*

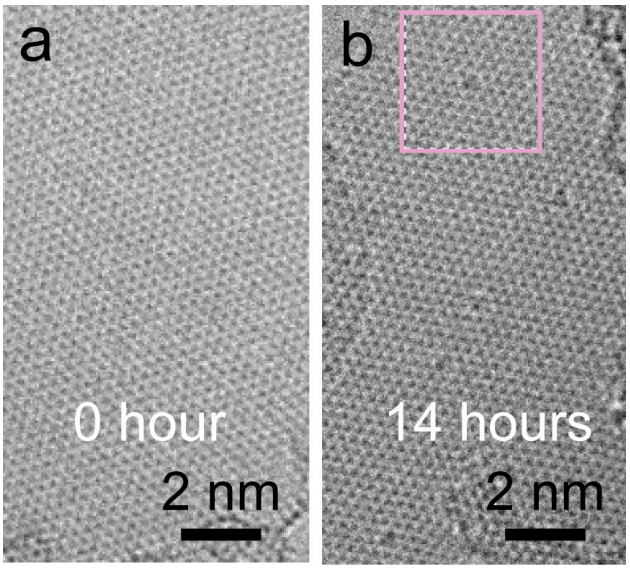


Figure 5.6: a) TEM image of a non-defected graphene on lacey carbon grid. The graphene was grown by pulsed-CVD, cleaned by normal acetone and annealed at 120 °C in vacuum for 2 hours. b) TEM image of the CVD graphene after dipped in 0.1 g/ml $Na_2S_2O_8$ for 14 hours. Boxed area highlights the defect site. TEM images taken by Hanako Okuno from CEA-INAC, Grenoble.

To check the defects microscopically, we performed the TEM observation of graphene sheets treated by $Na_2S_2O_8$ for different etching times. As shown in Figure 5.6a, graphene without treatment shows good crystallinity, while the one after 14 hours etching in $Na_2S_2O_8$, in Figure 5.6b, exhibits defect sites throughout the sample. However, here we do not have high enough resolution to image the type of defects.

### 5.2.4 *XPS measurements of the defected graphene*

X-ray photoelectron spectroscopy (XPS) is another common tool for surface characterization. The working principle can be described as follows. When monochromatic X-ray photon is incident onto the sample surface, electrons get knocked out due to a photoelectric effect:

$$E_{binding} = E_{X-ray\ photon} - (E_{kinetic} + \phi), \tag{5.8}$$

where $E_{binding}$ is the binding energy of the electron emitted, $E_{X-ray\ photon}$ is the energy of the X-ray photons being used, $E_{kinetic}$ is the kinetic energy of the electron measured by the instrument and $\phi$ is the work function of the spectrometer (not the material). Measuring the kinetic energy and number of electrons that escape from the top 1 to 10 nm of sample surface then gives the information of chemical composition and amounts of certain elements. For most applications, it is a non-invasive technique that measures the surface chemistry of materials.

We performed XPS measurements on the sample etched by 0.1 g/ml $Na_2S_2O_8$ for 2 hours and 14 hours, respectively. The peak intensity at binding energy of about 285 eV, corresponding to $sp^2$ bonding, is normalized to unity. A clear increase of peak intensity at binding energy of 287.2 eV can be seen, indicating the C-O bonds have a higher ratio in the defected sample, as shown in Figure 5.7a.

According to the Raman spectra, together with the XPS measurement, we found that our CVD graphene etched by $Na_2S_2O_8$ behaves similarly to graphene oxide (GO). Indeed, very high D peak intensity in Raman, and strong CO bond in XPS are found in GO [246]. Also, the field effect is found to have huge resistance with low mobility [244, 245]. D-to-D' Raman peak intensity ratio indicates the $sp^3$ type C-C bonds, as described in Section 5.2.2. With all the above evidence, we presume that, after 14 hours of etching in 0.1 g/ml $Na_2S_2O_8$, we have graphene oxide. This seems to be rather possible since $Na_2S_2O_8$ is a strong oxidizer.

## 5.3 ELECTRONIC TRANSPORT PROPERTIES OF DEFECTED GRAPHENE

### 5.3.1 *Temperature dependence of the field effect*

Temperature dependence of resistivity contains information such as electron-phonon and electron-electron interactions, as described earlier in this chapter. Here, we measured samples etched in 0.1 g/ml $Na_2S_2O_8$ for 1.5, 4, and 14 hours, respectively. Field effect curves are taken at temperatures from 300 down to 10 K in a cryostat probe station, as shown in Figure 5.8. For the sample with 1.5 h etching time, the field effect is kept almost unchanged from room temperature to 10 K. However, for the ones with more disorder, *i.e.*, 4 h and 14 h samples, sheet resistance increases from several kΩ to several tens of kΩ, in general. The sample also becomes more resistive by lowering the temperature, especially near the Dirac point. Notice that the Dirac point shifts a bit while cooling down for all the three samples, probably due to the environmental doping inside the cryostat.

For the sample etched for 4 hours, we recorded the temperature dependence at two fixed gate voltages, namely, V-$V_d$= 0 and -70 V. Data are plotted as a function of $T^{-1/3}$, as shown in Figure 5.9. It is interesting that for the gate voltage close to the Dirac point, the dependence is quite linear, in agreement with the Mott's variable range hopping correction of resistance Equation 5.2. However, at gate voltage far away from the Dirac point, the dependence is no longer of the Equation 5.2, which may be a mix of electron-electron interaction and hopping transport due to localization.

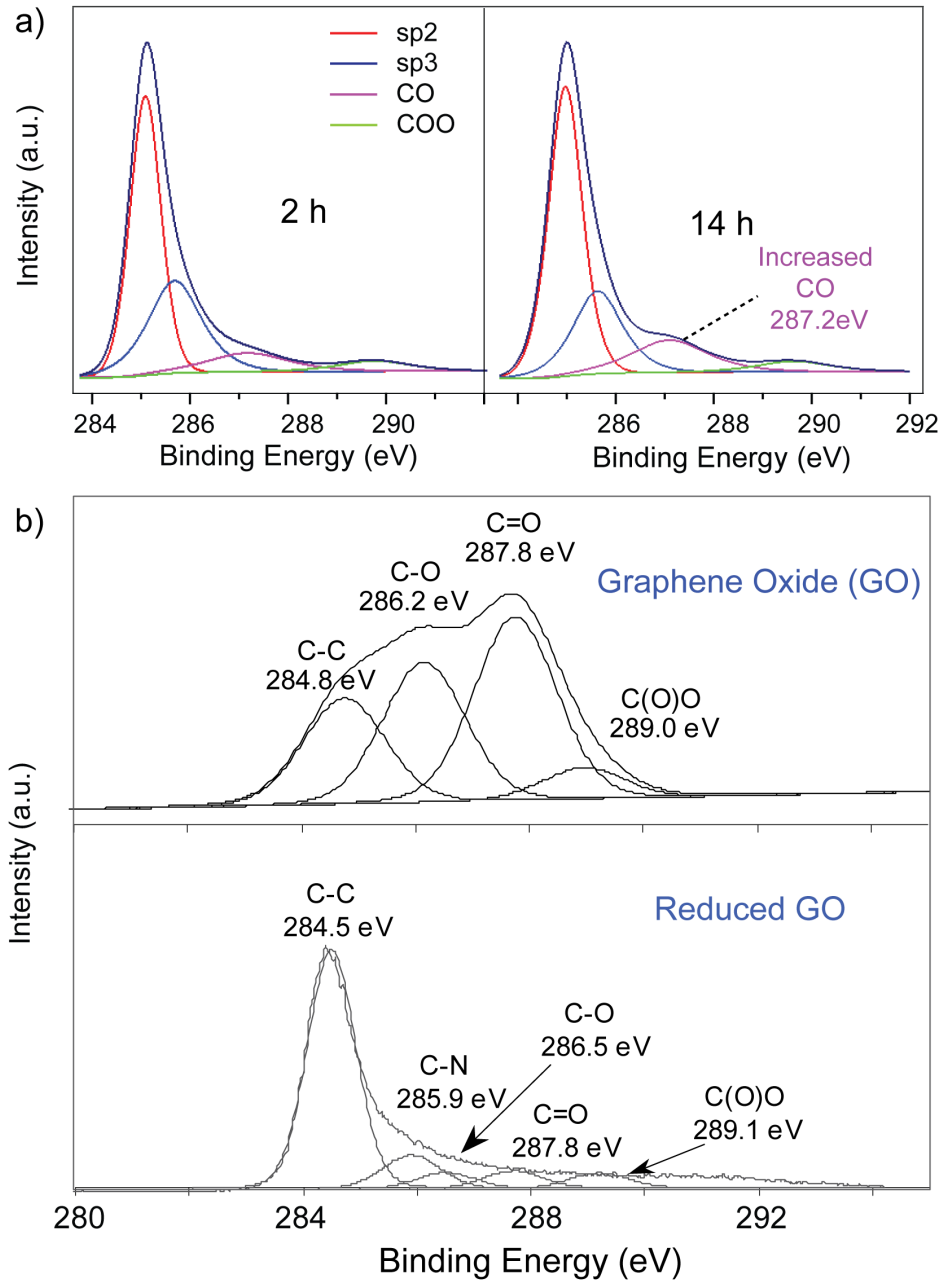


Figure 5.7: a) XPS spectra of sample etched in 0.1 g/ml $Na_2S_2O_8$ for 2 and 14 hours. b) XPS of graphene oxide and reduced-graphene oxide, taken from [246].

We performed even lower temperature (from 200 mK to 10 K) characterization of a macroscopic sample with dimension of 9 mm × 5 mm, dipped in 0.1 g/ml $Na_2S_2O_8$ for 14 hours. A macroscopic sample was chosen in this case, in order to avoid universal conductance fluctuations, which are commonly seen in mesoscopic systems at low temperature. As can be seen in Figure 5.10a, near the Dirac point, sample sheet resistance increases by 3 orders of magnitude when cooled from 10 K down to 200mK, going to an insulating state.

Magnetic response of the macroscopic sample was also measured. The magnetoresistance was recorded at a single temperature T = 200 mK. Figure 5.10a

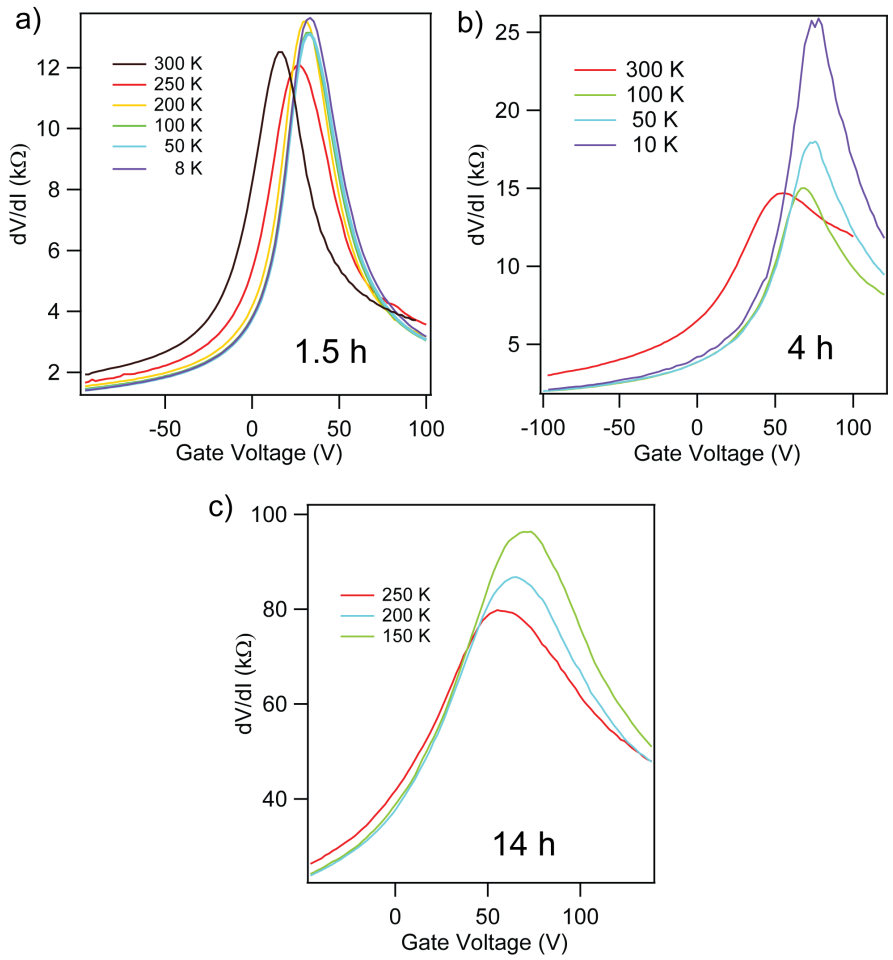


Figure 5.8: Temperature dependence of field effect curves for samples etched in 0.1 g/ml $Na_2S_2O_8$ for 1.5, 4, and 14 hours, respectively. The sample in c) was broken after the 150 K cooling.

shows the magnetoresistance taken at the Dirac point, where the sample is already in the MΩ range, and Figure 5.10b shows it in the region far from the Dirac point, where the sample is still weakly localized.

The curve in Figure 5.1b was simply impossible to fit to the weak localization theory of McCann [241]. However, by changing the aspect ratio of the sample from L/W = 1.8 to L/W = 10.5, the fitting worked quite well and gave reasonable values. The value of the phase coherence time $\tau_\phi$ is in good agreement with the values found in [248]. The inter-valley $\tau_{inter}$ and intervalley $\tau_{intra}$ scattering times are found to be both smaller than $10^{-14}$ s. This corresponds to mean free paths smaller than 10 nm. The small mean free path seems to be consistent with the TEM observations in Figure 5.6b.

## 5.4 CONCLUSION OF CHAPTER 5

To summarise, we have studied the effect of etchant on graphene quality. We speculate that the defects are of $sp^3$ type, with a increasing density when graphene is let in the etchant for longer times. The evolution of Raman spectra, field ef-

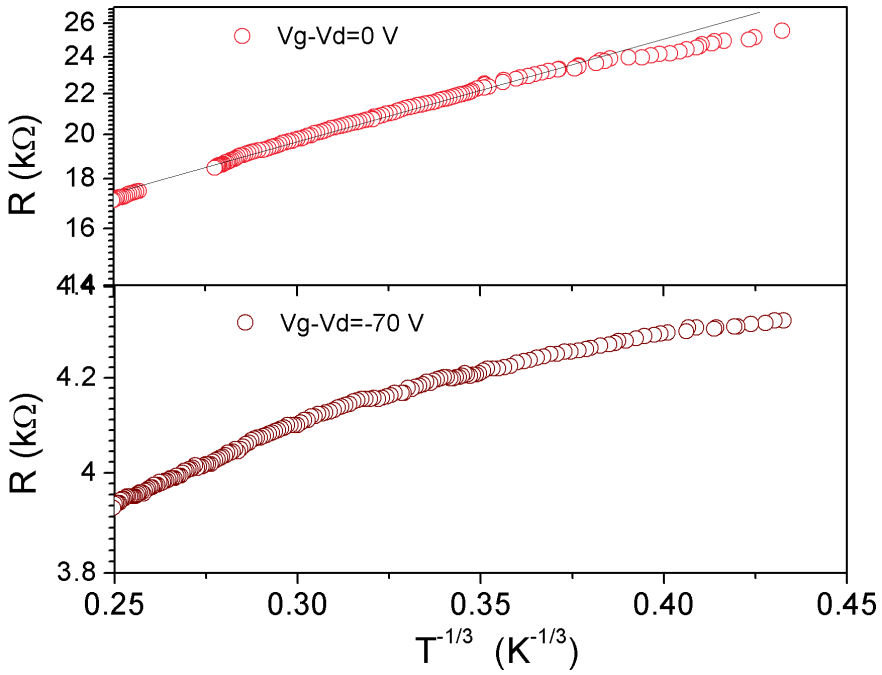


Figure 5.9: Temperature dependence of resistance for the sample etched by 0.1 g/ml $Na_2S_2O_8$ for 4 hours. 0 V (top), and -70 V (bottom) away from the Dirac point. The dashed straight line is a guide to the eye.

fect, temperature dependence of resistance, and XPS, are studied as a function of etching time.

In the transfer process of CVD graphene on Cu surface, graphene has to be inevitably exposed to the etchant for removing the metal. Therefore, the final device obtained often suffers from damages both physically and chemically. The chemical damage to graphene is often overlooked in the literature.

We conclude that in order to get high quality graphene, not only the growth, but also the transferring process is crucial. Graphene is more defected with longer etching time. Nevertheless, this opens another door to design graphene with controllable disorder. Based on this, gate-tunable defected 2DEG, metal-insulator transition, or superconducting-insulator transition can be realized when coupled with superconductors [13].

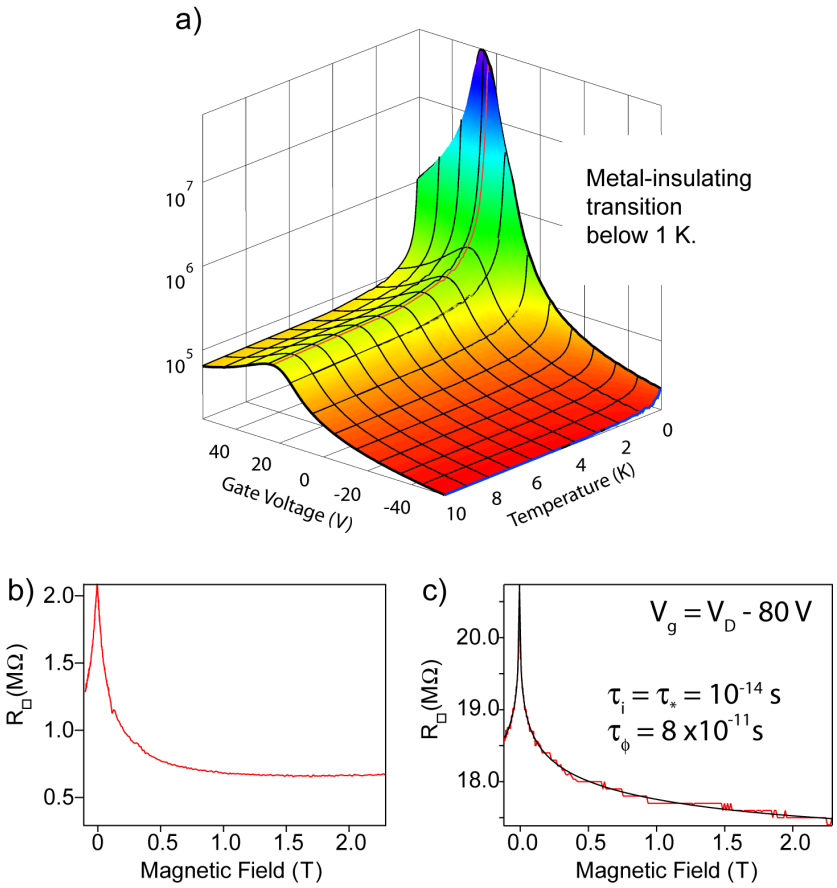


Figure 5.10: a) Low temperature 3D map of the sheet resistance as a function of gate voltage and temperature. Magnetoresistance of the sample at T = 200 mK: b) at the Dirac point in the strongly localized regime, and c) far from the Dirac point in the weakly localized regime. The black line is a fit to equation Equation 5.7. Data taken from Adrien Allain's thesis [247], Page 78.

# 6

# QUANTUM PHASE TRANSITION IN PROXIMITY ARRAY COUPLED GRAPHENE

*In this chapter, we will explore the most fundamental part of the thesis. The techniques developed in the previous chapters including graphene synthesis, transfer, cleaning, etching and functionalizing will be applied to generate hybrid devices composed of metal decorated graphene. The low temperature properties of these devices will be explored here.*

Our studies start from some recent theoretical advances [35, 34], which predict when an array is built with a network of hybrid superconductor/normal-metal/superconductor (SNS) junctions, a quantum phase transition from superconducting to metallic state can take place above a critical junction normal state resistance $R_N$. The ensuing quantum state terminating superconductivity is a new metallic state ruled by quantum fluctuations.

To experimentally observe the above mentioned effect, one has to engineer Josephson junctions made from a material with a tunable $R_N$ on a rather wide range. Graphene is an ideal platform to study the transition between ground states, because of its two-dimensional electronic transport and its gate-tunable resistance. Moreover, graphene has two surfaces that are open to the environment, thus enabling direct coupling with exterior materials.

## 6.1 INTRODUCTION TO MESOSCOPIC JOSEPHSON JUNCTIONS ARRAYS

A tunnel junction in general is composed by two conductors separated by a thin insulating layer. When the two conductors are made superconducting, the resulting device may let superconducting current flow though the insulating barrier, a very peculiar non linear effect known as the Josephson junction (JJ), as was first studied by B. D. Josephson [249]. When a series of JJs are connected spatially into networks, the resulting device is referred to as Josephson junction arrays (JJA). Their superconducting properties depend on a series of parameters such as the intensity of the coupling, the topology of the network, the applied magnetic field and the electrostatic properties of the "metallic islands" isolated from each other by the set of JJs. Such arrays have been extensively studied for the last 30 years and are prototypical systems to study 2D quantum phase transitions [250, 251, 252].

Josephson junctions, originally made of metal/insulating/metal junctions, have recently moved towards other materials, where the insulating layer is replaced by materials like normal metals, semiconductors, molecules, carbon nanotubes etc [253, 254]. In such "hybrid" systems, the Josephson effect is somewhat different as the materials sandwiched in between the two superconductors behave very differently from the insulator. For example, in a normal metal, superconducting correlations can extend to large distances (of the order of μm) due to the

proximity effect. There are also peculiarities due to the quantum confinement inside this sandwiched system.

## 6.2 METAL DECORATED GRAPHENE: A MODEL SYSTEM TO STUDY PROXIMITY-INDUCED SUPERCONDUCTIVITY IN TWO-DIMENSION

In our group, three PhD theses have been previously published on metal decorated graphene to study the onset of superconductivity by percolation of superconducting islands by the proximity effect. Brian Kessler and Caglar Girit [255] have shown in 2009 that graphene decorated by tin nanoparticles exhibits a 2D superconducting state (governed by the so-called Berezinskii-Kosterlitz-Thouless transition), in which the superconducting temperature is controlled by the electric field applied to the graphene layer. Later, in 2012 Adrien Allain [247] (using samples prepared by the techniques developed in chapter 5) discovered that inducing defects within the graphene layer allows control of the quantum phase transition from superconducting to a strongly insulating state. All these experiments were done by decorating graphene with a dense and random array of tin nanoparticules (Figure 6.1), a situation far away from the theoretical studies that triggered initial studies (Figure 6.2). The idea in this chapter is to pursue these initial studies by looking to other limits and better controlled samples, as a system proposed by theory [34, 35].

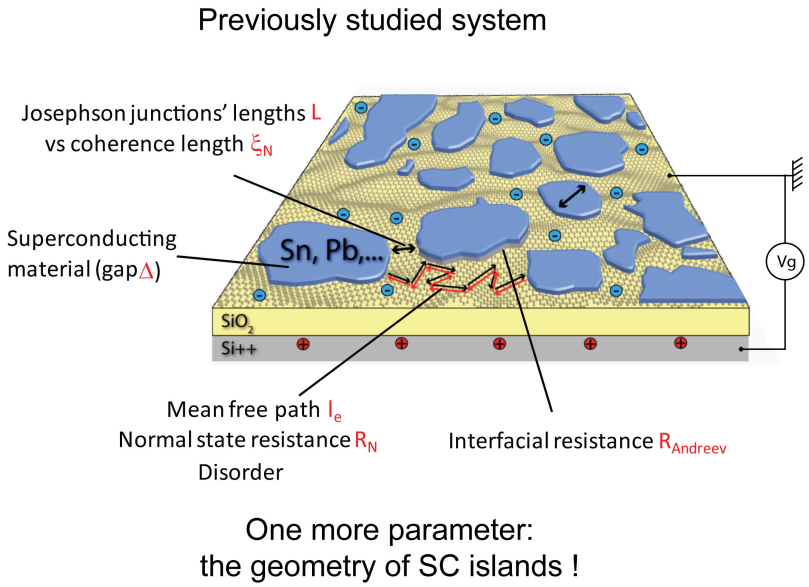


Figure 6.1: Schematic picture showing the previously studied hybrid system in our group: graphene decorated by random array of superconducting nano-islands. Possible tuning parameters are the island materials, the graphene disorder. Picture credit to A. Allain.

Due to the specific electronic properties of graphene, it is endowed with profound physics when coupled with superconductivity. It has a gate-tunable $k_F$, according to Equation 3.10 and 3.11, mean free path $l_e = \sigma h/2e^2 k_F$, *i.e.*, the diffusion constant $D = v_F l_e/2$ is tunable. Therefore, the coherence length of prox-

imity effect $\xi_N = \sqrt{\hbar D/k_B T}$ is tunable. As a result, as shown in the system depicted in Figure 6.1, one can vary the parameters such as the materials of the islands (which determines the superconducting gap), and the disorder in graphene (which determines $l_e$). However, there is another important parameter one can modulate: the geometry of the islands. How would the system behave if the islands are designed as a regular array as shown in Figure 6.2?

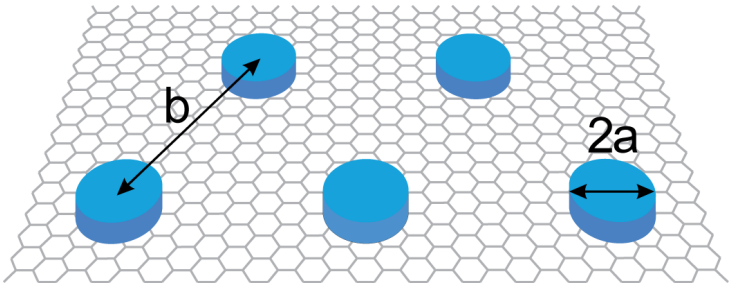


Figure 6.2: Schematic picture showing graphene film decorated by regular array of superconducting nano-islands. Picture adapted from [14].

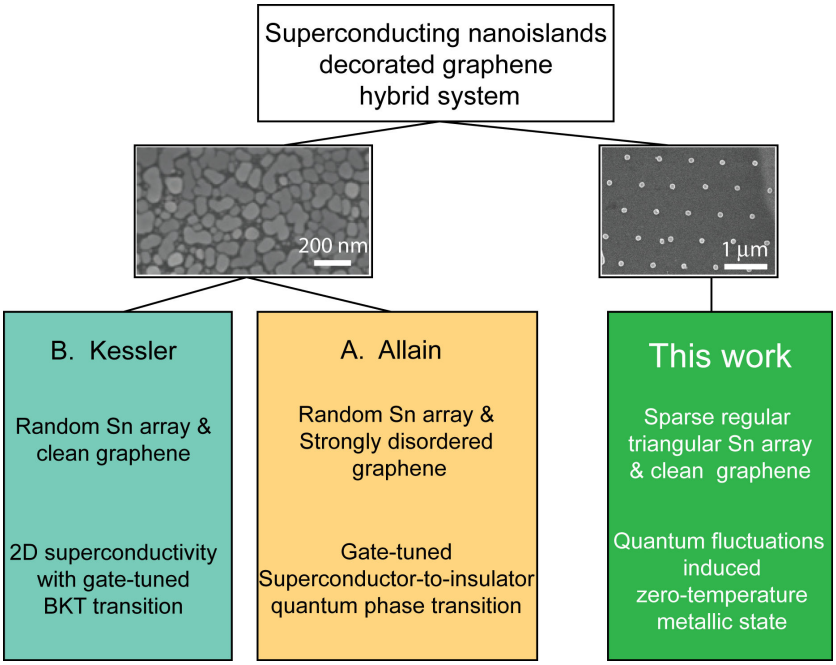


Figure 6.3: A diagram showing the main differences between thesis conducted in our group previously (B. Kessler [255], and A. Allain [247]) and the work in this thesis.

In this chapter, we show that decorating graphene with a sparse and regular array of superconducting nano-islands, as illustrated in Figure 6.2, enables one to continuously gate-tune the resulting superconducting Josephson junction array into a zero-temperature metallic state, in which superconductivity is suppressed by quantum fluctuations of the superconducting phase of the islands. A diagram summarizing the differences between the systems previously studied and this work is shown in Figure 6.3

We know that zero temperature metallic states are reported in systems such as amorphous superconducting thin films. In our proximity-array/graphene hybrid system, at some critical $R_N$, the superconducting states will collapse into a metallic state. What is the essential difference between those metallic states found in thin superconducting films and the proximity arrays coupled to graphene discussed in this manuscript? This question is our major contribution of this manuscript work, and will be explained in detail in the coming parts of this chapter.

As a general structure, we will arrange our work in the following two parts by several key questions, and answer them accordingly.

1. *With respect to the conventional one dimensional SNS junction, what are the new features when the system is built up with a periodic array? Namely, how does the so-called collective proximity effect play a role? What is the theoretical density needed to still get superconductivity?*

2. *What is the origin of quantum phase fluctuation? How does it affect the quantum phase transition from superconducting state to metallic state?*

3. *Since a magnetic field is supposed to decrease Josephson coupling between islands, how does the superconducting state evolve as a function of magnetic field?*

We will divide this chapter into two parts. Part one is the theoretical introduction about the proximity array coupled 2D diffusive metal (Graphene), which deals with conceptional introductions. Part two will focus on the experimental observations in our tin-decorated CVD graphene transistor.

Chapter 6, Part I

# THEORETICAL PREPARATIONS

## 6.3 SUPERCONDUCTOR-(METAL)-INSULATOR TRANSITIONS IN TWO-DIMENSIONS

When space is reduced to two dimensions, all kinds of electronic interactions behave differently. For example, *non-correlated* electrons in a perfect 2D crystal are propagating in a Bloch-wave fashion. At zero temperature, they can still move throughout the crystal. However, once there is a tiny disorder, the electron waves become exponentially decaying, and are thus spatially localized, leading to a 2D insulating state [235].

Nevertheless, 2D electrons are sometimes correlated between each other and their behavior is changed completely. One example is the attractive correlation described by the BCS superconducting mechanism. Namely, electrons, normally repelling each other via Coulomb interaction, become paired at low temperature, giving rise to a non dissipative zero resistance state. The so-called Cooper pairs are actually condensed in a single ground state, sharing the same wave function described by $\Psi = |\Delta| e^{i\varphi}$ [256]. Its breakdown can be either the diminish of amplitude $|\Delta|$ in a mean field fashion, or the lost of coherence due to fluctuations of phase $\varphi$. At very low temperatures, amplitude can be seen as constant, thus making it a phase-only problem.

One thing that needs to be clarified is that the formation of Cooper pairs does not necessarily mean a zero-resistance state. Only a global phase coherence can induce superconductivity. Moreover, quantum uncertainty principle tells that the number of Cooper pairs $n$ and their phase $\varphi$ are conjugate variables, *i.e.*, they follow the Heisenberg relation: $\Delta n \cdot \Delta\varphi > 1$. Only one of the two variables can be well defined at a given time, the other being affected by quantum fluctuations. It can then be pictured that when the system is superconducting, the phase must be well defined, thus strong fluctuations of $n$ is allowed. On the other hand, once the Cooper pairs are unable to move freely, due to, for example, an isolating barrier, a strong quantum fluctuation of phases takes over, leading to the breakdown of superconductivity and thus an insulating state.

The transform from superconducting to insulating state is caused solely by the quantum uncertainty principle, and can take place at zero temperature, termed a quantum phase transition (QPT). On the contrary, classical phase transitions are normally driven by thermal agitation. A scaling theory was proposed in QPT [257]. Briefly speaking, near any critical point, the correlation length $\xi$ diverges. As a non-temperature parameter $g$ in the Hamiltonian is brought close to its critical value $g_c$, $\xi$ can be scaled with a power $\nu$:

$$\xi \sim |g - g_c|^{\nu}. \tag{6.1}$$

Here $g$ is a general parameter, which can be, for example, thickness of a thin film (effective disorder) [257, 258], magnetic field [259, 260], charging energy and Josephson coupling $E_C/E_J$ [261], etc.

In the past decades, superconductivity has been one of the most popular systems for studying QPT, especially in 2D.

*Why 2D superconductivity is interesting?*

*Notice that, in 2D Josephson junction arrays, BKT transition can lead to 2e charge insulating phase, or vortex superconducting phase, according to the ratio of $E_J/E_C$ [262]. BKT transition is not a phenomenon only observed in the superconducting state, but also in the single electron state, which shows a dipole insulating state below the transition temperature [262].*

2D superconducting systems are of special interest, because of the unique physics that does not exist in 3D or 1D, making them ideal platform for studying quantum fluctuations, dissipation, Coulomb interaction, and various phase transitions. Also, in 2D, the screening of electrons is absent, thus allowing for electrostatic control of superconductivity.

For example, when charges (or vortices) are interacting logarithmically in distance, the Berezinski-Kosterliz-Thouless (BKT) transition of $T_c$ exists in only 2D, due to vortex-antivortex pairing [263]. Moreover, as described in chapter 5, Abrahams's re-normalization group theory argument suggests that a 2D electron gas tends to be an insulator when disorder is present [29]. It is therefore a fundamental issue to investigate the 2D superconductivity, especially when disorder and/or quasi-particle dissipation is present.

### 6.3.1 *Pioneering works on superconducting thin films*

Even though a 2D superconducting state is highly susceptible to quantum phase fluctuations, it is thought to exist at the atomic scale. It has been recently proven to exist in thin layers down to one or two atomic layer [264, 265], or down to a few molecules [266].

Early studies on superconductor-to-insulator transition are mainly conducted in amorphous thin films with thickness at the order of few Å, which in many cases are not strictly an atomic monolayer.

The interests of studying the disordered 2D superconducting thin films can be traced back to the 1980's. By varying the thickness of amorphous or granular superconducting thin films, a superconductor-to-insulator (SI) phase transition that can be extrapolated to zero-temperature. Since thermal fluctuations are suppressed, the transition is then seen as a quantum phase transition (QPT). Strikingly, the SC and IN phases are often separated by a universal resistance close to $R_Q = 4e^2/h$, which is the quantum resistance of charge $2e$. Such separation can be a temperature-independent R-T line, seen, for example, in homogeneous ultrathin Bi films, as shown in Figure 6.4a [267, 269].

Even if the SI QPT are not separated by a temperature-independent R-T line, the normal state resistance can still sometimes be normalized to $R_Q$ in the plot of $R_{T\to 0}$ against $R_N$, shown in Figure 6.4 b-c.

At the same time, SI QPT in thin films were also often found without a critical resistance of $R_Q$ [31]. The observations in SI QPT then aroused extensive arguments with respect to the $4e^2/h$ critical resistance. For example, a theory based on the quantum transport of a quasi-stable Cooper pair fluid was proposed to explain the case in homogeneous thin films [270].

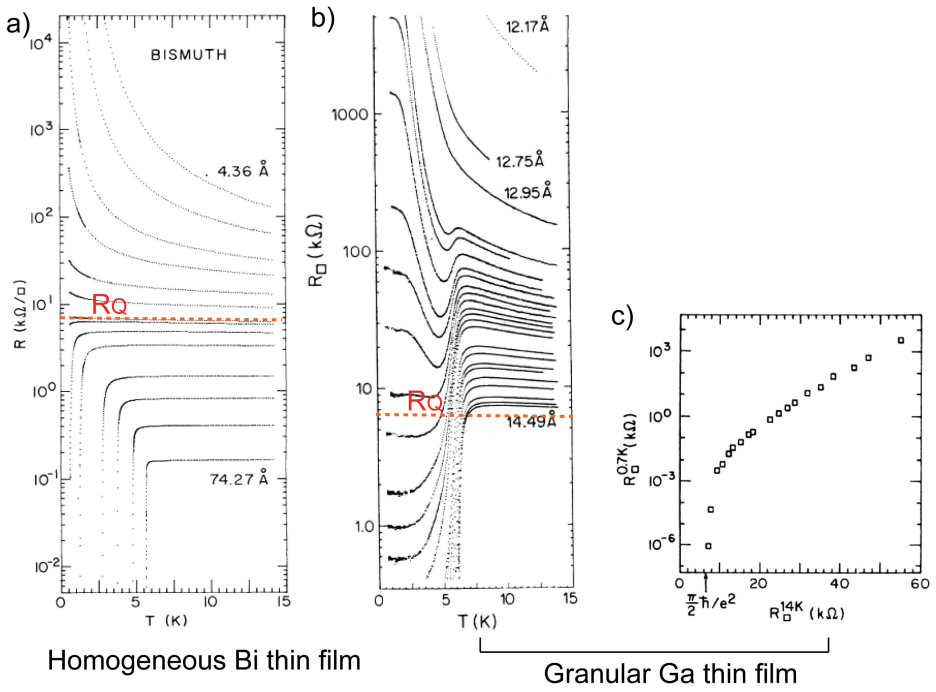


Figure 6.4: a) SI transition in Bi homogeneous film, with a critical resistance separating superconducting and insulating states at $R=R_Q$, adapted from [267]. b) SI transition with no temperature independent R-T curve, as the dashed red line in a), but renormalized to $R_Q$ in the plot of $R_{T=0.7K}$ vs $R_{T=14K}$ in c), adapted from [268].

### 6.3.2 *The Josephson junction arrays*

A Josephson junction array is composed of a 2D arrangement of interconnected JJ. It is a model system for 2D superconductivity. BKT transition as well as SI QPT are found in it. In general, in micro-fabricated Josephson junction arrays, SI transitions very similar to Figure 6.4b were observed [271, 261].

Naturally, the amorphous or granular thin films are thought to be a type of superconducting islands separated by insulators [268, 272, 252]. Such kind of quenched thin superconducting films can be modelled as random network of metallic clusters coupled by Josephson tunnelling junctions (SIS junctions), and the SI transition comes from the competition between charging energy $E_C = e^2/2C$ and Josephson coupling $E_J$ [251, 252, 250].

*A review on the relative theoretical models on QPT in Josephson junction arrays can be found in Ref [273], by Fazio et al.*

Extensive works on the subject of SI QPT were performed by modelling the resistively shunted Josephson junction (SNS junctions) arrays [274, 272]. The normal metal serves as a medium for correlated electrons (Andreev current) and a dissipative channel (shunt resistor). Superconducting phase in 2D Josephson junction array is predicted [275] to exist as long as shunting resistance $R_S$ is lower than $R_Q = 4e^2/h$, regardless how weak the Josephson coupling is. An opponent theory was soon reported [276] with no universal critical conductivity, which is claimed to be a new universality class of the SI transition, by adding a local Ohmic dissipation for the phase of the superconducting order parameter

[277].

Experimental results did agree with Fisher [275] that zero-resistance state of the array develops with a critical normal state resistance $R_C$ below $R_Q = 4e^2/h = 6.5k\Omega$, but it develops sometimes when $R_C$ is almost $2R_Q$ [278, 279].

### 6.3.3 *Mattew Fisher's dirty boson theory*

Fisher and co-workers proposed a "dirty boson" model based on strong superconducting correlations. This is also referred to as the bosonic scenario, in which Cooper pairs persist in both the superconducting and insulating phase, via a duality in Cooper pairs and vortices. On the superconducting side, Cooper pairs are free while vortices (the representation of superconducting phase) are pinned, while on the insulating side, vortices are mobile, but Cooper pairs are localized [269, 280, 281]. The Hamiltonian of this model contains no dissipation terms, as no quasi-particle excitations are allowed.

Fisher's theory is in favour of a universal critical resistance of $R_Q = 4e^2/h$ for the SI phase transition, provided that both Cooper pairs and vortices are interacting logarithmically.

### 6.3.4 *Finkelstein's fermionic theory*

Also popular is the fermionic scenario developed by Finkelstein et al [282, 283]. In fact, this is an elaborated version of the BCS theory, neglecting quantum phase fluctuations. It lies on the fact that the Cooper pairs disappear at a critical film resistivity, thus differing from the bosonic approach [284, 285], and often quoted as the fermionic scenario.

The qualitative idea behind this theory is that disorder enhanced Coulomb repulsion breaks the Cooper attraction and thus the $T_c$, *i.e.*, the superconductor becomes a normal metal. Notice that it *differs from* a quantum phase transition at zero temperature.

Specifically, the superconductive transition temperature vanishes when a critical dimensionless conductance ($g = \hbar/e^2R_\square$) reaches $g_c = 1/4\pi^2 \ln^2(1/T_{C0}\tau_{sc})$ [282], where $\tau_{sc}$ is the elastic scattering time. And $T_{C0}$ is the BCS transition temperature for the bulk.

### 6.3.5 *Is there an universal critical resistance in SI QPT?*

As we have mentioned in the previous subsections, SI QPT are extensively studied both experimentally and theoretically over the past decades. However, as an universal conclusion could not be drawn, it remained an unsolved problem till now. In the three main types of samples, *i.e.*, homogeneous/granular thin films

and 2D Josephson junction arrays, SI QPT are observed, but the issue of $R_Q$ is not at all conclusive (Table. 1).

| - | Homogeneous film | Granular film | 2D Josephson junction arrays |
|---|---|---|---|
| $R_Q$=6.5 kΩ | [267] | [268] | [278] |
| No $R_Q$ | [286, 260] | [31, 287, 288, 289] | [261, 279] |

Table 4: In the three main type of samples, *i.e.*, homogeneous/granular thin films, and 2D Josephson junction arrays, SI QPT are all observed, but the critical resistance of $R_Q$ is not universal and still under debate.

## 6.4 THE INTERVENING METALLIC STATE

The problem which interests us in this chapter is the focus on the intervening metallic state that could appear in between S & I, as indicated by the red dashed line in Figure 6.4a, which can be extrapolated to zero temperature. A zero-temperature metallic behavior means the levelling off of the tail of the R-T curve, *i.e.*, a finite resistance at zero temperature.

It is known that, in a typical 2D metal, the metallic state is unstable with respect to localization in the presence of weak disorder [235]. Then the intervening zero-temperature metallic ground state is of fundamental interest to physics by the following question:

*Is it always present in the SI QPT? If yes, what is the mechanism behind it, making it in direct contrast to the conventional 2D electron localization scenario?*

Indeed, if one looks back to Figure 6.4 again, one can see that the levelling off behavior of R-T curves at zero temperature is seen in both samples. But is it necessary that this intervening metallic state is only a by-product of SI QPT? Are there superconducting-to-metal (SC-M) quantum phase transitions? The answer is yes, as will be discussed in the next section.

## 6.5 QUANTUM (BOSE) METAL THEORIES

For a long period, people believe that only two ground states can exist for bosons at zero temperature: either superconductor with long-range phase coherence, or insulator with disordered quantum phases. However, as depicted in the previous section, the often experimentally observed intervening metallic state [268, 292, 261] started to trigger new discussions, in which a 2D quantum metal at zero temperature ground state is described.

For example, Denis and Philip [293, 294] suggested that the argument of the insulating phase of bosons, based on the quantum fluctuations, was not strong enough. Instead, the quartic interaction between the bosons in the quantum dis-

*There is the family of oxide-interface (MOSFET, p-GaAs/AlGaAs, etc.), which exhibit metal-insulator quantum phase transition in 2D [290, 291]. However, it is out of the scope of this thesis, since no superconductivity is included there.*

ordered regime (*i.e.* the insulating side in SI QPT) leads to a so-called Bose metal.

Their work is established on a Josephson junction array with quasi-particle collisions coming from the quartic term in the Landau-Ginzburg action, which, somehow strikingly, gives an universal finite conductivity $\sigma = (2/\pi)4e^2/h \sim 10$ k$\Omega$. However, no dissipation was included in their model, since this is based on the Bosonic scenario. Another phenomenological discussion on SI QPT was performed by A. Kapitulnik and co-workers with consideration of the effects of dissipation [295], which gives a phase diagram with the tuning parameter of disorder $\alpha$, shown in Figure 6.5. A similar phase diagram can be found in the review paper on SI QPT by Gantmakher and Dolgopolov [258].

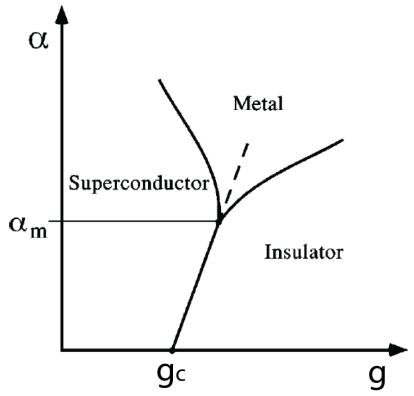


Figure 6.5: Phenomenological phase diagram of SI QPT at zero temperature. Y-axis is the disorder, while the x-axis denotes the tuning parameter in the system's Hamiltonian. $g_c$ marks the SI QPT critical point, and $\alpha_m$ marks the critical dissipation above which a metallic phase is obtained. Adapted from [295].

Alternatively, by applying a model of Josephson junction array without disorder, D. Das et al developed a theory in favor of the existence of a Bose metal. They pointed out that both phase and charge of bosons are disordered as a result of quantum frustration, which leads to a metallic state [296, 297].

## 6.6 SUMMARY ON THE HISTORICAL PROBLEMS

Up to now, we have briefly reviewed the historical problems on the issue of superconductor-to-insulator quantum phase transition in 2D. As we can see, so far, the model systems are basically thin films and Josephson junction arrays. They have somehow similar properties, since they have similar Hamiltonian. In the mean time they both suffer from different technical difficulties. For example, the tuning parameters for thin films are mostly the thickness (or the level of disorder). Therefore, in order to obtain a complete set of data, one has to make a series of samples. The reproducibility and homogeneity of the amorphous thin films are always questionable. For the case of Josephson junction arrays, the same problem can occur: even though it is cleaner than thin films, the shunt resistor can not be tuned in-situ.

In the Hamiltonian of Josephson junctions arrays, several ingredients are often taken into account: 1) quantum fluctuations, 2) dissipation, 3) quasi-particle collisions, etc. Different models therefore give different predictions. The essential divergence focuses on:

1) is there a critical resistance in the QPT? If yes, is it $4e^2/h$ or not?
2) is there a 2D metallic phase in the zero-temperature? If yes, what is its origin?

To investigate the above two questions, new more elaborated theories are needed.

## 6.7 THEORIES ON THE PROXIMITY-COUPLED ARRAY

Let us now consider a model, in which superconductors are distributed in an array-like manner onto a 2D diffusive metal, as shown in Figure 6.2. The 2D metal below the superconducting (SC) islands can be 2DEG such as oxide-interface, or, fashionably, graphene.

The advantage in this model is that it contains all the ingredients, that exist in thin films and conventional micro-fabricated JJA, for QPT studies. It includes Josephson coupling $E_J$ between islands, and dissipation channels that exist in the 2D metal. Yet it differs from conventional systems, since it can be highly well defined in geometry, thus encouraging analytic modelling. It is similar but not equal to the micro-fabricated JJA. Here, instead of tunnelling junctions, the SC islands interact with each other through the proximity effect in the long junction limit.

Most importantly, when the 2D metal is made of 2DEG, its carrier density can be tuned electrically, thus enabling in-situ tuning of parameters that can trigger QPT at zero temperature. This makes the present system much more powerful in QPT studies compared to the traditional quasi-2D thin films/JJA that require a set of samples with different thicknesses/shunt-resistors. Based on this proximity-coupled array model, recent theoretical advances have predicted a quantum superconductor-to-metal transition [34, 35]. This will be discussed in detail in the following subsections.

### 6.7.1 *Proximity effect in S/N interfaces*

When a normal metal (N) is brought into contact with a superconductor (S), in most cases, there is an interface that exists between S and N, which serves as a potential barrier. The transparency of the interface plays an important role. For example, if the barrier is an insulator (SIN junction), then the wave function on each side barely overlap [256]. On the S side, the DoS exhibits a gap of $2\Delta$, within which there exists no state for a single electron but only Cooper pairs. As a result, no transport can happen below the energy of $\Delta$ in SIN junction.

However, when the interfacial transparent is high enough in SN junctions, the influence of the wave functions on each side becomes significant. Sometimes the N is rendered into S, or vice-versa, giving rise to the so-called proximity effect.

As in the subgap energy scale, only pairs are allowed to enter the S. In the case of SN contact (with no barrier), the electron transport DOES happen. A typical process involves the incoming electron being reflected as a hole, back along the same trajectory. This phenomena is called an Andreev reflection (AR). In the manner of AR transport, the phase of a superconducting contact can be kept throughout the normal metal until reaching the other superconducting contact, making coherence of the two. For more information about AR, see (A. Allain, Thesis).

It is very important to bare in mind that the overall effect of charge transfer $2e$ from N to S, via AR, is totally different from the conventional SIS junction, in which the transport is due to Cooper pair tunnelling (same process as single-particle tunnelling), called the Josephson effect.

### 6.7.2 *Theoretical approaches of the eigenstates in NS junction*

Because of the SN boundary, the original BCS formula fails to include the broken Cooper pairs in the normal part. To describe the superconducting behaviour in SN junction, several theories have been developed.

#### *Bogoliiubov-de Gennes Equation*

Bogoliiubov-de Gennes (BdG) equations [298] are normally used to describe a superconductor system close to the boundaries or to the inhomogneities. The essential concept in BdG equations is to treat the superconductor as a coherent mixture of electrons and holes. The eigenfunctions are given by an electron-like part, $\psi e(\mathbf{r})$, and a hole-like part, $\psi h(\mathbf{r})$, expressed as

$$\begin{pmatrix} H_0 & \Delta(\mathbf{r}) \\ \Delta(\mathbf{r})^* & -H_0 \end{pmatrix} \begin{pmatrix} \psi_e(\mathbf{r}) \\ \psi_h(\mathbf{r}) \end{pmatrix} = E \begin{pmatrix} \psi_e(\mathbf{r}) \\ \psi_h(\mathbf{r}) \end{pmatrix}, \tag{6.2}$$

where $H_0$ is the Hamiltonian of a single particle, and $\Delta$ is the gap of the superconductor.

#### *Blonder-Tinkham-Klapwijk Model*

Based on BdG equations, Blonder, Tinkham, and Klapwijk developed their (BTK) model [299] for solving the transport at N/S interface with arbitrary interface barrier potentials.

By solving the BdG equations (see, for example, [300]), one gets the conductance of the SN interface as a function of voltage-bias:

$$\sigma_{SN} = 1 + A - B, \tag{6.3}$$

where the terms A and B are written as:

$$A = \begin{cases} \frac{\Delta^2}{E^2+(\Delta^2-E^2(1+2Z^2)^2)}; & E < \Delta \\ \frac{f_e^2 f_h^2}{f_e^2+(f_e^2-f_h^2)Z^2}; & E > \Delta \end{cases} \qquad B = \begin{cases} \frac{4Z^2(1+Z^2)(\Delta^2-E^2)}{E^2+(\Delta^2-E^2(1+2Z^2)^2)}; & E < \Delta \\ \frac{(f_e^2-f_h^2)Z^2(1+Z^2)}{f_e^2+(f_e^2-f_h^2)Z^2}; & E > \Delta \end{cases}, \tag{6.4}$$

where E the bias energy, Z the height of the barrier in between S and N parts, $f_e$ and $f_h$ the distribution weight of electrons and holes in the superconducting side, and $f_e^2 \equiv 1/2\left(1+\frac{\sqrt{E^2-\Delta^2}}{E}\right) \equiv 1-f_h^2$.

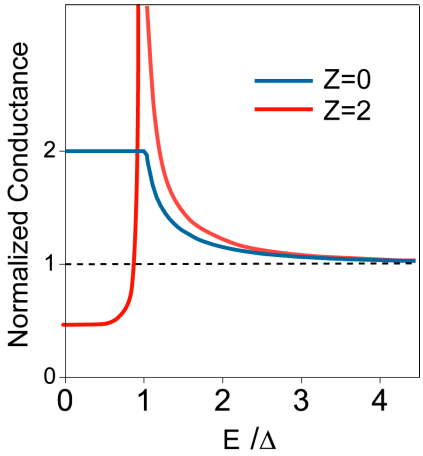


Figure 6.6: Normalized conductance as a function of the voltage applied across the interface calculated using Equation 6.3, at zero temperature, for a) Z=0, and b) Z=2.

An example of the BTK model solution is shown in Figure 6.6. It can be seen that when there is no barrier (Z=0), the normalized conductance in the subgap range is actually doubled compared to the above-gap single-particle conductance. When $Z \to \infty$, the structure reduces to a SIS junction.

Notice that BTK is very handy and popular in many systems, it however breaks down when transport is dominated by impurity scattering [301]. To include the impurity scatterings, more sophisticated mathematical treatments are needed. Modern ways to describe this problem is the use of quasi-classical Green functions. For example, using Green's functions, Gor'kov showed that the phenomenological Ginzburg-Landau theory can be microscopically derived from the BCS theory for temperatures close to the transition temperature.

*Usadel equation in the dirty limit*

When we say dirty limit, it means that the coherence length $\xi$ is larger than the mean free path $l_e$ in a material. A particle undergoes a lot of scattering before losing its phase coherence and this results in the loss of the initial momentum direction. Based on this dirty limit assumption, a set of isotropic impurity-averaged Green's functions were introduced by Usadel [302], which are the so-called Retarded, Advanced, and Keldysh Green functions: $\hat{g}_S^R$, $\hat{g}_S^A$, and $\hat{g}_S^K$.

Nazarov [303] then introduced the parametrization of two position- and energy-dependent complex functions $\theta(x, E)$, and $\varphi(x, E)$, and reformulate the $\hat{g}_S^R$, and $\hat{g}_S^A$ into:

$$\hat{g}_S^R = \begin{pmatrix} \cos\theta & \sin\theta e^{i\varphi} \\ \sin\theta e^{-i\varphi} & -\cos\theta \end{pmatrix}, \tag{6.5}$$

and

$$\hat{g}_S^A = \begin{pmatrix} -\cos\theta^* & \sin\theta^* e^{i\varphi^*} \\ \sin\theta^* e^{-i\varphi^*} & \cos\theta^* \end{pmatrix}. \tag{6.6}$$

While the Keldysh function is given by:

$$\hat{g}_S^K = \hat{g}_S^R\hat{h} - \hat{h}\hat{g}_S^A, \tag{6.7}$$

with the distribution matrix $\hat{h}$ defined as :

$$\hat{h} = \begin{pmatrix} 1-2f_e & 0 \\ 0 & 2f_h - 1 \end{pmatrix}, \tag{6.8}$$

where $f_e$ and $f_h$ are the distribution functions for electrons and holes, respectively.

For a SN interface, $\theta$ is determined by solving the Usadel-equation [304]:

$$\frac{\hbar D}{2} \bigtriangledown^2 \theta + \left( iE - \frac{\hbar}{\tau_{sf}} \cos\theta \right) \sin\theta + \Delta(x)\cos\theta = 0, \tag{6.9}$$

where $\tau_{sf}$ is the spin-flip time.

The Usadel-equation is very powerful in solving the problem of SN interface with a large variety of scattering, as it does not require to solve the Schrodinger equation, and is even more popular if projected to the Nambu$\bigotimes$spin space, with $\bigotimes$ the tensor product.

More details on other formalisms of the Usadel equation, such as the Nambu$\bigotimes$spin space representation, can be found in [305, 306].

## 6.8 ANTICIPATED BEHAVIORS IN S-N JUNCTION

### 6.8.1 *Energy scales*

It is well known that Andreev pairs can diffuse into a normal metal with length scale much larger than the superconducting coherence length in the superconductor side. What is then the maximum distance a Andreev pair can propogate into a normal diffusive metal?

Here, we first compare several energy scales, in order to understand better the physical picture. Usually, in the diffusive limit, the energy $\epsilon$ and its quantum scale $L_\epsilon$ are related by:

$$L_\epsilon = \sqrt{D\tau_\epsilon}, \tag{6.10}$$

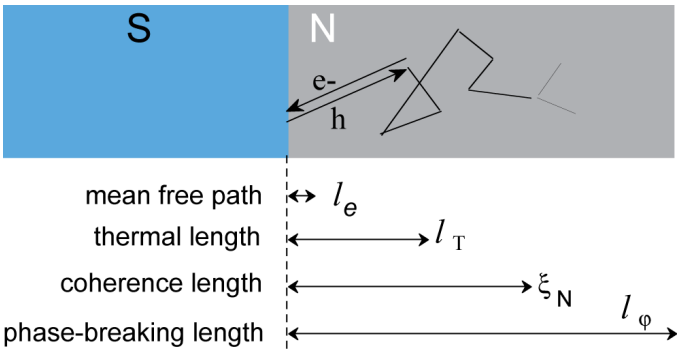


Figure 6.7: Relevant length scales with their schematic respective amplitudes in a metallic thin film. The energy-dependent coherence length $\xi_N$ is the length over which the two components of the Andreev pair acquire a phase difference of order $\pi$. Picture adapted from [307].

where $\tau_\epsilon$ is a time scale described by $\tau_\epsilon \sim \hbar/\epsilon$. D is the diffusion coefficient defined in Equation 3.11.

For example, if the 2D system has size L, an energy corresponding to its size is called the Thouless energy, written as $E_{Th} = \hbar D/L^2$. As already introduced in Section 5.1.1, the Thouless energy is an important quantity since it directly relates the mean level spacing and dimensionless conductance in a mesoscopic system.

Coherence length in the diffusive normal metal (we will note $\xi_N$ and $\xi_0$ as the coherence length in the normal, and superconducting parts respectively in the rest of this thesis) are usually treated as [36, 304]

*Coherence length in the clean limit in a proximity normal metal is given by $\hbar v_F/2\pi T$ [308]. While the bulk BCS coherence length $\xi_0$ is defined as $2\hbar v_F/\pi\Delta$, with $v_F$ the Fermi velocity of Cooper pairs, and $\Delta$ the BCS gap [256].*

$$\xi_N = \sqrt{\frac{\hbar D}{k_B T}}, \tag{6.11}$$

since the whole electron distribution is at thermal equilibrium [307].

However, other than the thermal energy which depends on temperature, and $E_{Th}$ which depends on the normal metal itself, there are other energy scales that need to be taken into account. For example, the electron itself looses coherence on a scale of $l_\phi$, which is called the phase-coherence length, same as in Equation 5.7. A schematic picture comparing the different scales is shown in Figure 6.7.

*Notice that $l_\phi$ diverges to infinity at zero temperature, as theoretically predicted [309].*

Other arguments can be found ([306]):

$$\xi_N = \min\left\{\sqrt{\hbar D/k_B T}, \sqrt{\hbar D/\Delta}, \sqrt{D\tau_{sf}}, \sqrt{D\tau_{ee}}\right\}, \tag{6.12}$$

where $\Delta$ is the pair correlation energy. $\tau_{sf}$ and $\tau_{ee}$ are the spin-flip scattering times due to magnetic impurities, and the electron-electron inelastic scattering time, respectively. In this case, at the zero-temperature limit, $\xi_N$ is dominated by other energies rather than the thermal one.

### 6.8.2 *Minigap due to proximity effect*

Since Cooper pairs manage to "leak" from S to N, it would be rather interesting to see how the local density of states in the N part looks like once they have been affected by the superconducting proximity effect.

Early experiments in a nanowire show that a suppression of DoS was found on the mesoscopic scale [310], which can be well explained by the Usadel equation in the framework of non-equilibrium superconductivity [302, 311]. Namely, a gapless-superconductor-like DoS was found in their system.

In the mean time, the DoS in the normal part in an SN junction was theoretically studied by W. Belzig et al, using the Usadel equation [312]. The model says that when a thin film (size $L \sim \xi_N$) is in good contact with a bulk superconductor, a mini-gap develops at the order of the Thouless energy $E_{Th}$, and is position-independent. Similar results were reported elsewhere [313].

In another calculation, the contact barrier strength is included in a model which couples 2DEG and superconducting islands, and the mini-gap induced in the 2DEG is reduced to a large degree with increasing interfacial barrier [314]. However in that work no spatial dependence of the mini-gap was mentioned.

## 6.9 PROXIMITY-COUPLED ARRAYS ON GRAPHENE

As depicted at the beginning of this chapter, our work is motivated by the following model: imaging a graphene layer that is decorated with regular arrays of superconductor islands of a certain radius $a$ separated by distance $b$, as shown in Figure 6.2.

In this model, theory has been fully developed for studying the behaviours of superconductivity [14]. For the convenience of modelling, several assumptions are superimposed. First of all, assume the model is at the limit of $b \gg a$. This implies that the mean free path $l_e$ in graphene should be less than $b$. Moreover, the model requires:

1. Fermi energy of graphene $E_F \gg \Delta$, with $\Delta$ being the superconducting gap of the islands.
2. Diffusion coefficient of graphene should be at the order of 100 $cm^2/s$.
3. Dimensionless conductance of graphene $g = (\hbar/e^2 R_\square) \geqslant 3$ with a high Thouless energy $E_{Th} \sim \hbar D/b^2$, namely a small enough $b$ (at the mesocopic scale).

The reason why we use graphene is that graphene is strictly a 2D material and its DOS will not have a reverse-proximity effect into the SC islands. SC islands can be in direct contact with graphene, and by selecting the correct SC material, the interface can be very transparent [12]. Traditional 2DEG is of much less use in this sense, since they are always embedded/sandwiched by insulators.

Most importantly, the reason we chose graphene is that its charge carrier can be gate tuned, which can be controlled with a desired amount of disorder, as described in Chapter 5. All the above physical properties, together with a number

of well-established theoretical models, make the present system of great interest. In the following, we will describe the predicted phenomena, such as BKT transitions, and quantum superconductor-to-metal (SC-M) transition.

### 6.9.1 *BKT transition in SC arrays on graphene*

For the single SC island on graphene, the Matsubara-space Usadel equation for the spectral angle $\theta_\omega$ and corresponding boundary conditions reads as [315]

$$D \bigtriangledown^2 \theta_\omega - 2|\omega| \sin\theta_\omega = 0, \tag{6.13}$$

$$\left[ g \frac{\partial \theta_\omega}{\partial r} + \frac{G_{int}}{2\pi a} \cos\theta_\omega \right] \Big|_{r=a} = 0. \tag{6.14}$$

Here $G_{int}$ is the SC-island-graphene interface conductance - which is the only parameter that we can not control experimentally so far. Linearization of the above two equations can be realized when $b \gg a$. The Josephson coupling, $E_J$, of the two-island problem with a high interface transparency can be analytically solved by:

$$E_J(b,T) = 4\pi g T \sum_{n=0}^{\infty} \frac{\pi^2}{\ln^2(\hbar D/2a^2\omega_n)} P\left(\sqrt{\omega_n/2E_{Th}}\right), \tag{6.15}$$

here the function $P(z) = z\int_0^\infty K_0(z\cosh t)K_1(z\cosh t)dt$, where $K_n(x)$ is the MacDonald Bessel function. And $\omega_n = \pi T(2n+1)$ is the Matsubara energy.

It is known that when extended to a 2D array, such islands with coupling $E_J$ undergo BKT transition at

$$T_{BKT} = \gamma E_J(b, T_{BKT}), \tag{6.16}$$

where $\gamma$ is a geometrical constant. In the case of a triangle array, $\gamma \sim 1.47$ [316].

Combing Equation 6.15 and Equation 6.16, one gets

$$6\pi g \sum_{n=0}^{\infty} \frac{\pi^2}{\ln^2(\hbar D/2a^2\pi T_{BKT}(2n+1))} P\left(\sqrt{\pi T_{BKT}(2n+1)/2E_{Th}}\right) = 1, \tag{6.17}$$

In the above formula, parameters such as D and $E_{Th}$ can be experimentally extracted, leaving only one parameter $T_{BKT}$, which can be easily computed.

Moreover, by neglecting quantum phase fluctuations, the pair-wise Josephson coupling at zero-temperature can be accessed by calculating the critical current $j_c$ [14]

$$j_c(0) = \frac{\pi^3}{2} \frac{egD}{b^3 \ln^2(b/a)}, \tag{6.18}$$

According to the definition of the Josephson coupling energy [317]

$$E_J = (\hbar/2e) I_1, \tag{6.19}$$

where $I_1$ is the supper current of a pair-wise islands. One gets the pair-wise Josephson coupling energy at zero temperature:

$$E_{J,T=0} = \frac{\pi^3}{4}\frac{g\hbar D}{b^2 \ln^2(b/a)}. \tag{6.20}$$

### 6.9.2 *Minigap inside graphene decorated with regular SC array*

The authors in [14] also calculated the minigap inside graphene at low temperatures when global phase coherence was reached. We will not show detailed mathematics, but briefly, by using the periodic boundary conditions in the array (assume it is triangle, ideal interface), one can get the zero-temperature spectral gap in graphene:

$$E_g \approx \frac{4\hbar D/b^2}{1.52\ln(b/2a) - 1.2} \approx \frac{2.6E_{Th}}{\ln(b/4a)}. \tag{6.21}$$

This minigap is rather large, since if one lets $b/a = 10$, it leads to $\sim 2.88E_{Th}$, much larger than the one expected in Section 6.8.2. This large minigap comes from the collective proximity effect. However, to observe it experimentally, one has to perform low temperature STM measurements.

### 6.9.3 *Weak charge quantization and quantum phase fluctuations*

In the previous section, the model based on Usadel equation does not take into account any quantum phase fluctuations, which will to some extent fail to explain the SC-M quantum phase transitions. Here, we will introduce another consideration which contains the quantum fluctuation in the model.

Since we are studying the proximity array at a very low temperature, the phase-only Hamiltonian of inter-island coupling for such an array is given by:

$$H = -\frac{1}{2}\sum_{ij} E_J^{ij}\cos(\phi_i - \phi_j). \tag{6.22}$$

At T=0, the Josephson coupling through a 2D metal is a long range interaction, as $E_J^{ij}(\mathbf{r_{ij}}) \propto 1/|\mathbf{r_{ij}}|^2$ [318]. Such a long range interaction makes it possible to theoretically treat it by the mean field approximation (MFA).

That is to say, all the interactions from other islands will be "felt" by one certain island as:

$$J\langle\cos\phi\rangle\int\cos\phi(t)dt, \tag{6.23}$$

which is determined by the condition [34]:

$$1 \leqslant \frac{1}{2\hbar}J\cdot C(T) = \frac{1}{2\hbar}J\int_0^{1/T} c_0(t)dt; \tag{6.24}$$

$$J = \sum_j E_J^{ij}, \tag{6.25}$$

and $c_0$ is the imaginary-time autocorrelation function describing the phase fluctuations of a single SC island, written as:

$$c_0(t) = \langle \cos(\phi(0) - \phi(t)) \rangle = 2 \langle \cos\phi(0) \cos\phi(t) \rangle . \tag{6.26}$$

The physical meaning of $C(0)$ is an effective charging energy $E_C^*$ which is related by:

$$E_C^* = \frac{\hbar}{C(0)}. \tag{6.27}$$

In our model system, we have the following features:

1. Existence of a non-zero effective charging energy at zero temperature, which plays a role of weak Coulomb blockade, or the so-called weak charge quantization [319].
2. Existence of Andreev conduction, which means only a charge of 2e can be transferred in/out of the SC islands at low temperature.
3. Existence of quantum phase fluctuations due to the quantized 2e charge transfer, which results in an exponentially renormalized effective charging energy[319].

Similar to the conventional picture of quantum phase transition driven by $E_J/E_C$ [250], our equation Equation 6.24 has the competition between J and $E_C^*$, while the effective charging energy is determined by the normal resistance of the 2D metal and the geometry of the SC array. That means, at a critical $b_c$, or $g_c$, the condition $J \sim E_C^*$ will be fulfilled. Therefore, the system will be driven from SC into the normal metal state, where the driving force is the quantum phase fluctuations. An imaginary-time dissipation description can be used to represent the phase fluctuations, which is similar to the process of a single-electron tunnelling in normal tunnelling junctions [320].

Technically, the key problem of this model is to find the zero-temperature condition of Equation 6.24, $J(0)$ and $C(0)$.

At the limit of a large interface transparency between the SC island and the 2D metal, $J(0)$ can be obtained by solving the Usadel equation at the limit of $\ln(b/a) \ll 1$ [34]:

$$J(0) = \frac{\pi^4}{2} \frac{g\hbar D}{b^2 \ln(b/a)}, \tag{6.28}$$

where $g = \hbar/(e^2 g_\square)$ and D is the dimensionless conductance and diffusion coefficient of the 2D metal.

To obtain $C(0)$, specific re-normalization group treatments [35] are needed. The resulting $C(0)$ is given by:

$$C(0) \sim \frac{\rho \cdot a^2}{D} e^{2\pi\sqrt{g}s}, \tag{6.29}$$

where $\rho$ is a pre-factor close to 1, and $s$ is a parameter related to the RG equation of $G_A$ (calculated in [35]). One gets the critical dimensionless conductance $g_c$ according to the condition in Equation 6.24

$$g_c \sim \left(\frac{1}{\pi}\ln\frac{b}{a'}\right)^2, \tag{6.30}$$

where a' is a reduced diameter of the island with a pre-factor, see appendix.

The above equation is an important result, since it predicts that critical sheet resistance $R_{\square c} = \hbar/e^2 g_c$ can be much less than $R_Q$, when $\ln(b/a) \leqslant 3$. This is contrary to the argument that superconductivity always persists in a JJA as long as $R_N < R_Q$ [321, 275]. We will use this to estimate the critical resistance in graphene in the second part of this chapter.

Compared to the conventional models of resistively shunted Josephson junction arrays, the above theoretical treatment has a unique and crucial feature:

*The dissipative channel in the above model is periodic in the phase difference that only 2e quanta of charge transfer is allowed, which is the case of Andreev conductance [34]. The conventional models of resistively-shunted Josephson junctions do not have this feature.*

### 6.9.4 *Quantum phase fluctuations in mesoscopic system under magnetic field*

It is well known that in the framework of the mean-field BCS theory, the critical field is temperature dependent [322]:

$$H_{c2}(0) - H_{c2}(T) \propto (T/T_{c0})^2. \tag{6.31}$$

It says that $H_{c2}$ saturates at zero temperature, with a finite value.

In this section, we emphasize that in our system - proximity array coupled graphene - except for the predicted SC-M quantum phase transition driven by quantum phase fluctuations at zero magnetic field, there is also predicted quantum phase fluctuation on the upper critical magnetic field $H_{c2}$, which gives rise to the unconventional zero temperature $H_{c2}$ compared to the BCS theory.

Theoretical considerations on the disordered 2D SC films [38] predict that quantum fluctuations of the phase of the order parameter plays a role in the value of $H_{c2}$, which can lead to an infinite $H_{c2}$ at zero temperature.

The main ideas thus far can be summarized as the following: due to the random phase of the Green's function which describes the order parameter, the Josephson coupling between SC clusters exist even under a magnetic field on the order of the glass field $H_{Glass} = \Phi_0/L^2$, where L is the size between two SC clusters. It is called glass because full frustration is achieved at the scale of $\sqrt{\Phi_0/H_{Glass}}$, and the system shows a glassy superconducting behavior, such as

a long relaxation time of resistance [323].

In the glassy SC region, the Josephon coupling is enhanced due to quantum phase fluctuations, and can be written as [38]:

$$E_J^{Glass} = [\langle (E_J - \langle E_J \rangle)^2 \rangle]^{1/2} \sim (E_{TH}/2) e^{-L/L_T}, \tag{6.32}$$

where $L_T = \sqrt{\hbar D/k_B T}$ is the thermal length. At zero temperature $e^{-L/L_T} \to 1$. The $E_J^{Glass}$ therefore can reach the order of Thouless energy - a rather high value.

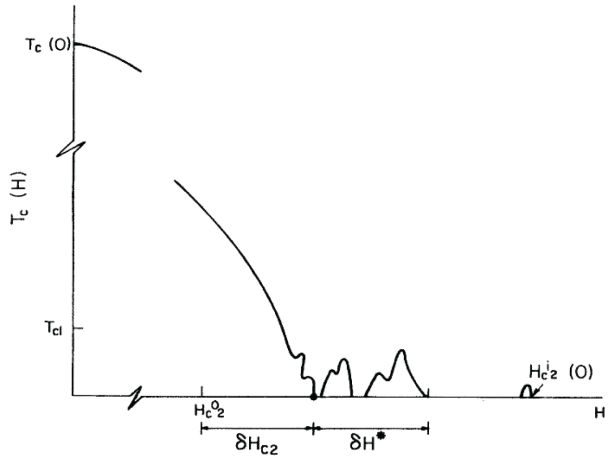


Figure 6.8: At zero temperature, quantum phase fluctuations cause reentrant of SC region at zero-temperature in the presence of a weak magnetic field, meaning that the conventional concept of upper critical magnetic field $H_{c2}^0$ does not apply. Picture adapted from [38].

The result predicted in [38] shows that there will exist regions (with probability close to 1) above $H_{c2}^0$ at zero temperature, like reentrant behavior, where the interval $\delta H^*$ can be written as:

$$\delta H^* = H_{c2}^0 g^{-2}, \tag{6.33}$$

where $g$ is the dimensionless conductance of the film. This reentrant behavior is pictured in Figure 6.8.

Estimation of $H_{c2}$ was measured for the proximity coupled array. When a weak magnetic field is present, the Josephson coupling term $J(0)$ can be written as [35]:

$$J(0,H) = J(0)\frac{\ln(l_H/b)}{\ln(l_H/a)}, \tag{6.34}$$

with the magnetic length scale $l_H = \sqrt{\pi\hbar c/eH} = \sqrt{\Phi_0/H}$. Solving the same Equation 6.24, with $J(0)$ replaced by $J(0,H)$, one gets:

$$\ln\frac{\Phi_0}{H_{c2}b^2} \approx \frac{2\ln(b/a)}{(b_c(g)/b)^2 - 1}, \tag{6.35}$$

with $b_c(g) \sim a \cdot e^{\pi\sqrt{g}}$.

The corresponding $H_{c2}$ is then approximately:

$$H_{c2} \sim (\Phi_0/b^2)e^{\sqrt{g}} \gg H_{Glass}. \tag{6.36}$$

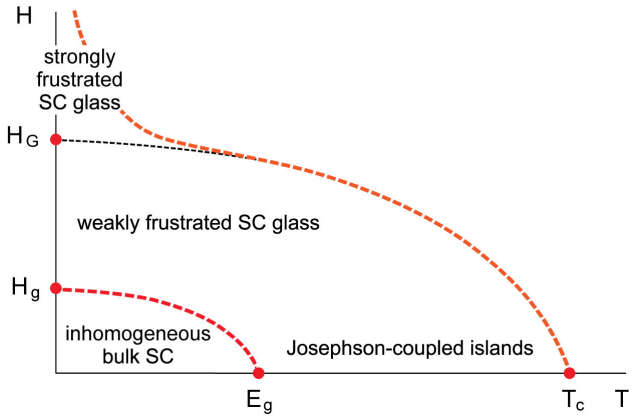


Figure 6.9: Schematic phase diagram of the graphene sheet with SC islands, adapted from [14].

The overall behaviour of the $H_{c2}$ for the proximity coupled SC array is then expected to follow the same behavior as the one depicted in Figure 6.9. Notice there is a lower bound in the picture, which is due to the existence of lower energy caused by the minigap, giving rise to a $H_g \approx \frac{0.4\Phi_0}{b^2 \ln(b/4a)}$. Below this $H_g$, the system is supposed to behave like a inhomogeneous 2D bulk superconductor [14].

With these two expected outcomes (i.e., upturn of $H_{c2}$ or reentrant SC above $H_{c2}$) we will see in the next part what is the experimental behavior of $H_{c2}$ in our SC array coupled with graphene.

Chapter 6, Part II

# EXPERIMENTAL OBSERVATIONS

## 6.10 GRAPHENE PROXIMITY DEVICES

Shortly after the isolation of graphene, a Josephson junction made of graphene and Al electrodes was demonstrated [324, 325]. In the past few years, quantum transport [326], current-phase relationship [327, 328, 329, 330], Andreev bound states [331], a prototype SQUID device [332], transport in the QHE regime [333, 334], and BKT transition [12], were all studied in graphene Josephson junctions.

*Graphene is also predicted to be intrinsically superconducting [335, 336, 175]. However, definitive experimental proof is still lacking, so far [337, 338].*

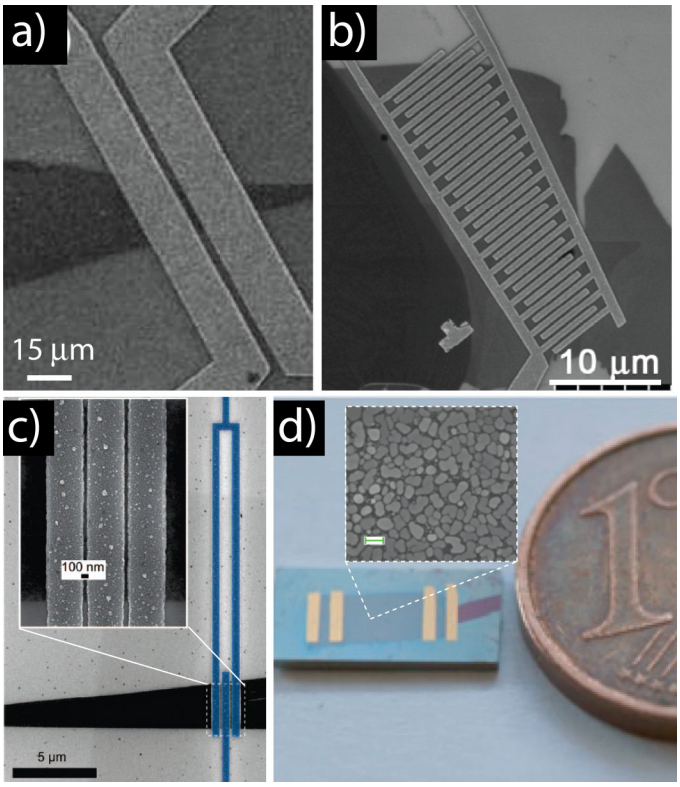


Figure 6.10: Graphene proximity devices using a) [330] and b) [327] Pb-Pd electrodes, c) Al electrodes [332], and d) tin nanoparticles decoration with normal Au electrodes [13], with scale bar in the inset of 100 nm.

Several graphene based superconducting proximity devices are illustrated in Figure 6.10. It is seen that most of them are mesoscopic in size and graphene serves as a normal metal junction, sandwiched by two superconducting leads (S-N-S). However, there is another idea, which involves the use of normal electrodes and graphene. This realization of superconductivity is to deposit on top of graphene a thin layer of electrically non-percolating superconducting nanoparticles. An illustration of the above two approaches to realize superconductivity in graphene is shown in Figure 6.11.

Due to the open surface of graphene, which can be well coupled with external metals, graphene is able to have a microscopically random network of SC nanoparticles. Each of those SC nanoparticles becomes superconducting below the $T_C$ of the bulk SC material. They can make global phase coherence between islands, and turn the whole graphene sheet into a strictly 2D superconductor [12]. Previous reports demonstrated that the global SC of such a device follows the BKT transition, which is gate dependent [12, 13].

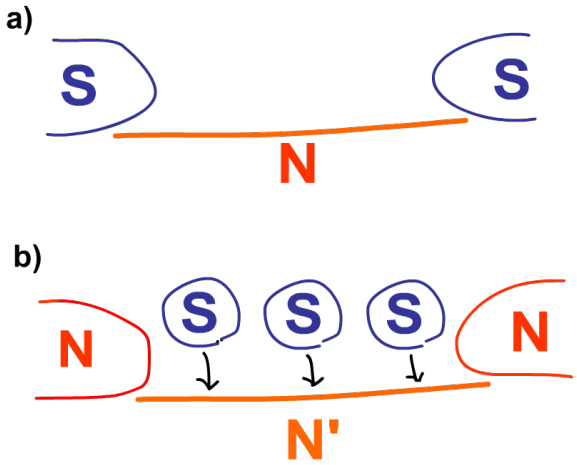


Figure 6.11: Schematics of the two approaches to realize superconductivity in graphene devices: a) S-N-S and b) N-N′-N with superconducting islands decoration.

### 6.10.1 *Graphene: macroscale 2D superconductor and more*

Following the same method as [12], we managed to extend the 2D SC in graphene into the macro-scale via using CVD graphene. This is the first time a macro-scaled (Figure 6.10d) 2D superconductor was made.

Moreover, we purposely made the CVD graphene heavily defected using the method introduced in Chapter 5, which turns the graphene into a very resistive state, but still remains gate tunability in the field effect. As a result, defected graphene decorated with random network of Sn nano-islands has a change of 7 orders of magnitude in resistance when gate tuned in the range of about 40 V at 40 mK. This quantum phase transition behavior demonstrates a new type of quantum switch from insulating to superconducting state, as shown in Figure 6.12.

## 6.11 PROXIMITY ARRAY ON CVD GRAPHENE

Unlike the device in the previous section, here we take a different approach: instead of utilizing a tight disordered array, we designed a sparse regular array on graphene. As described in Part I in this chapter, a sparse array is rich in physics, and a number of theoretical models are available [34, 35, 14], which is convenient for further comparison.

Recently, proximity arrays made of Au thin film covered with Nb nano-islands were studied, in order to search for the zero-temperature metallic state [36]. However, in their work, major drawbacks are incurred and include: (1) lack of gate-tunability, (2) existence of an inverse proximity effect, and (3) lack of a truly 2D metal substrate.

Several geometries were tested for our study, as shown in Figure 6.13. We found that if the thickness of the sample, d, is less than 30 nm (Figure 6.13b), sub-islands due to dewetting will show up inside each designed unit nanodisk

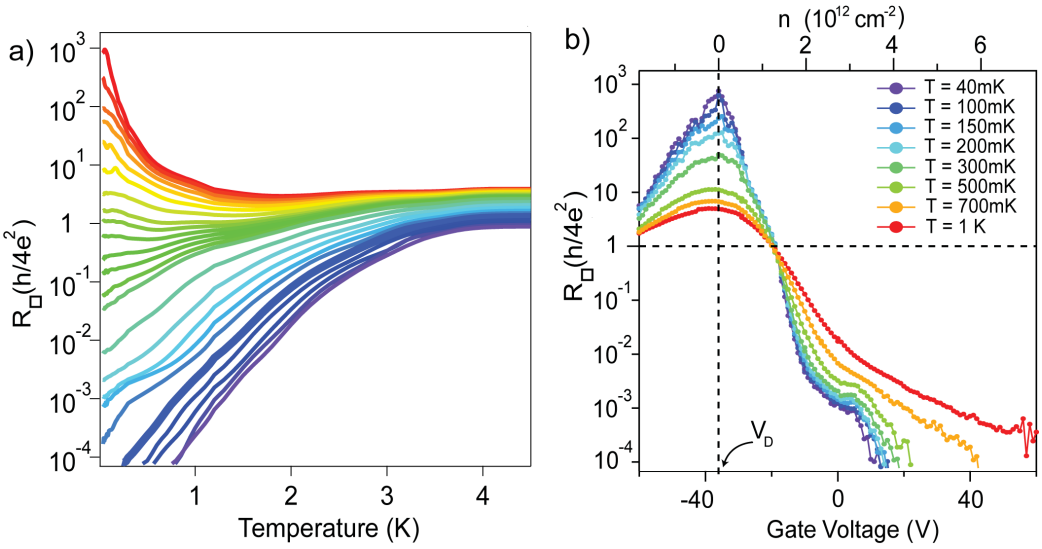


Figure 6.12: Macroscale graphene with controlled defect shows superconductor-to-insulator quantum phase transition when decorated with Sn nanoparticles. a) Temperature dependence of resistance at several gate voltages, and b) field effect curves at several temperatures. Adapted from [13]. CVD graphene was etched in 0.1 g/ml $Na_2S_2O_8$ for about 20 hours.

similar to those seen in [12, 13]. Meanwhile, samples with a nanodisk diameter of $2a < 100$nm (Figure 6.13c-d) are not superconducting at 60 mK (possibly because of the oxidation or a poor interface).

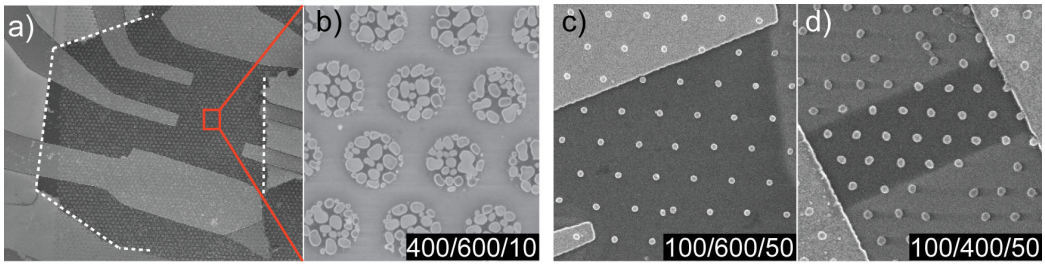


Figure 6.13: a) Hexagonal CVD graphene single domain (outlined by dashed lines) contacted with Au 50 nm/Ti 5 nm electrodes, decorated with Sn nanoparticles by standard electron beam lithography. b) Zoom-in of the boxed area in a). From b) to d), the Sn nanodisk geometries 2a/b/d are 400/600/10, 100/600/10, and 100/400/10 nm, respectively. Subislands are seen in b), while c) and d) are not superconducting.

In the coming part, we will report mainly on the measured data of the sample with 2a/b/d=400/1000/50 nm.

As shown in the inset of Figure 6.14a, the sample was fabricated by patterning a single grain of CVD graphene (transferred onto 285 nm oxidized silicon) into a Hall bar with an aspect ratio of 1 in the central part. This allows one to obtain the square resistance by a four-probe measurement. Normal leads (50nm Au/5nm Ti) were then patterned in a second step, followed by a final 50 nm thick Sn array deposition with standard electron-beam lithography Figure 6.14b-

c. These Sn nanodisks have a diameter of 400 nm, separated by 1 μm between their centres.

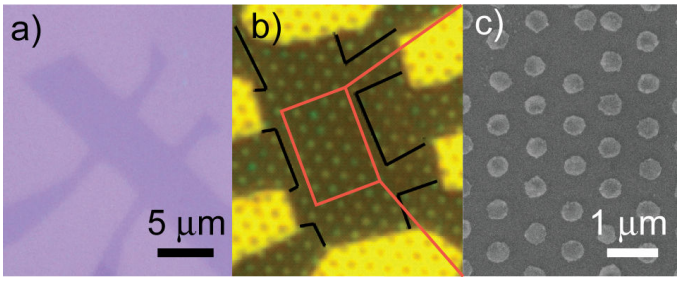


Figure 6.14: Graphene Hall bar devices with triangle array of tin nanodisk decorated on top. a) As-patterned Hall bar of CVD graphene on 285 nm oxidized silicon, b) optical micrograph of the final device, and c) SEM micrograph of boxed area in b).

The sample was tested in a vacuum $^3$He-$^4$He dilution fridge system implemented with lock-in measurements. A picture of the setup is shown in Figure 6.15.

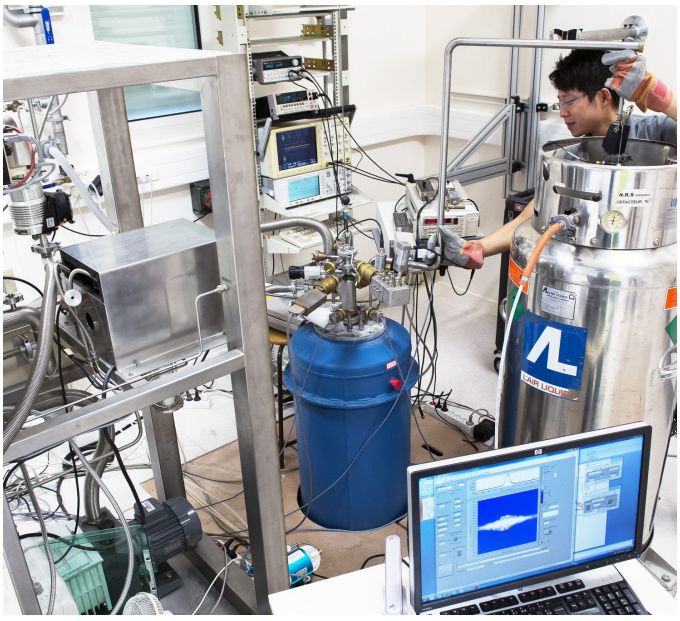

Figure 6.15: The dilution fridge setup. A Chinese spy is hidden behind the helium bottle.

### 6.11.1 *Overview of electronic transport properties of the sample*

We now have an overall description of the sample electronic transport properties while cooling down. As can be seen in Figure 6.16a, the sample shows a field effect curve with resistance from 4 kΩ at $V_g$=30 V, to about 19 kΩ at $V_g$=-14 V. Upon cooling down to 4 K, the field effect curve does not change dramatically. A fit using Equation 3.17 shows that the sample has a mobility of about 678 $cm^2V^{-1}s^{-1}$ at 4 K. We will use the 4 K field effect curve as a normal state $R_N$

for all gate voltages. At even lower temperatures, we see that the sample turns into an SC state at gate voltages higher than about -3 V.

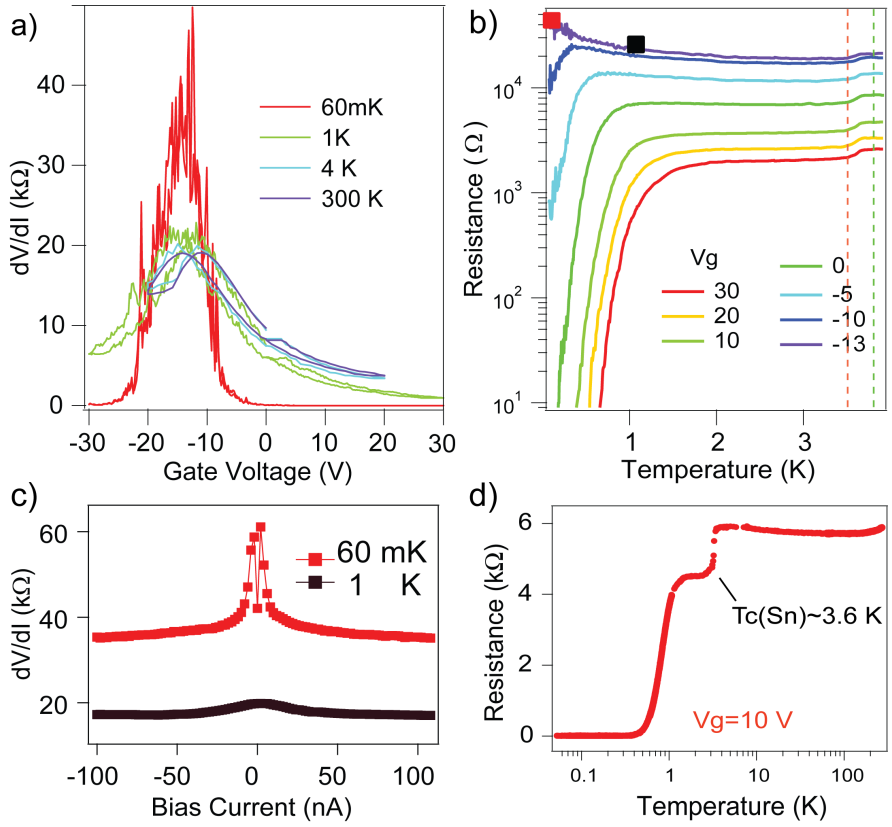


Figure 6.16: a) Field effect curves of the sample at 300 K, 4 K, 1 K and 60 mK. b) Temperature dependence of the sample resistance at several gate voltages. c) Differential resistance as a function of bias current at the specific T and $V_g$ points marked in b). d) A full R-T curve from 300 K down to 60 mK, at $V_g$=10 V.

Notice that there is some hysteresis in the field effect curve in Figure 6.16a. However, after some days, the hysteresis becomes negligible. We attribute this hysteresis to some unstable doping from the environment while cooling, which stabilizes with increasing time. With the exception of the initial data shown in Figure 6.16a, there is nearly no further occurrence of a hysteresis.

Figure 6.16b was measured by taking field effect curves while heating up the sample with a PID heat-controller and a 10 mK step from 60 mK to 1 K, 20 mK step from 1 to 2K, and 50 mK step from 2 to 4 K range. The curves are cuts along the temperature axis at several gate voltages. It can be seen that at around 3.6 K a gate-independent resistance drop was found (as indicated by the two vertical dashed lines), which is very close to the $T_C$=3.7 K of bulk Sn.

Full superconductivity (zero resistance state) only develops at a certain range of gate voltage below 1 K. As shown in Figure 6.16b, the curve at $V_g$=30 V goes down to zero at about 0.7 K. This downward trend connected with a zero resistance through a cusp (Figure 6.16d) is typical of a BKT transition. This has been proven in the system under study [12, 13].

Transport curves of the sample close to the Dirac point, shown in Figure 6.16c, were taken at 1 K and 60 mK, respectively. There is a Coulomb-peak at zero bias, while a dip appears at 60 mK. This gives a hint that even if Sn islands are superconducting at the Diract point (since a drop of R at 3.6 K is seen), superconductivity coherence does not exist at 1 K, and only some SC fluctuations were found at 60 mK, which accounts for the central dip in the current-bias curve.

*Our question is: what is the actual state of the red square point in Figure 6.16b? Is it metallic, or insulating? And how is this state driven from a full superconducting state at $V_g$=30? It will be answered in the coming sections.*

### 6.11.2 *Interface of Sn islands and graphene*

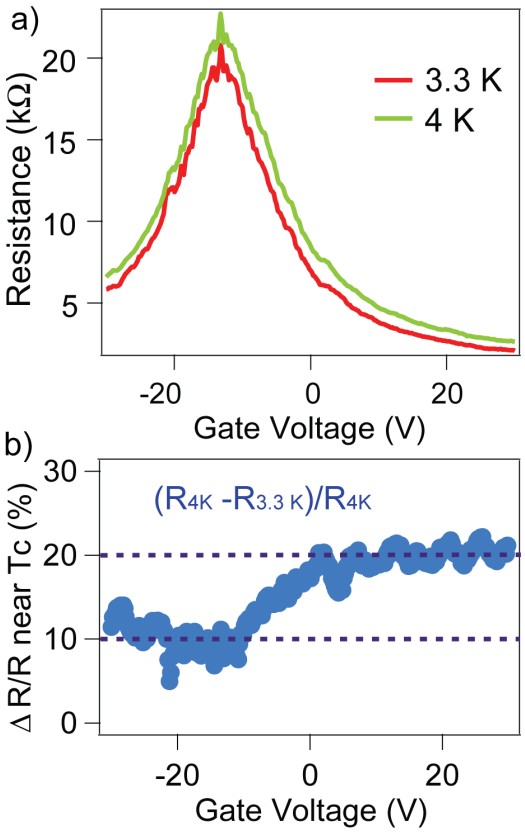


Figure 6.17: a) Field effect curves along the two dashed lines in Figure 6.16b. b) The percentage of resistance change by subtracting the two field effect curves.

To further validate our result with theoretical models, we have to access the transparency of the interface between Sn islands and the graphene, since it directly affects the modelling described in Part I. Because the interface is buried below Sn, direct measurements of (S-N) Andreev transparency is rather difficult. We therefore qualitatively estimate by the total resistance change before and after the SC transition near 3.6 K.

As shown in Figure 6.17a, field effect curves at 4 K and 3.3 K are plotted. Their difference is shown in Figure 6.17b.

Since the geometry of our triangle Sn arrays are of the dimensions of $a = 200nm$, $b = 1\mu m$, then the total surface coverage is $\sim 15\%$. This value is in reasonable agreement with the $\Delta R$ plotted in Figure 6.17b. It is interesting to see that there is a difference in $\Delta R = (R_{4K} - R_{3.3K})/R_{4K}$ at the hole side and electron side, while the transparency is about twice higher in the electron side. We understand this by the fact that Sn is an electron donor, and once graphene is tuned into the hole side, the pinning of the Fermi level starts to be significant and the resulting p-n junction that is formed does so in order to reduce the interface transparency. Similar result was obtained by Kessler [255].

### 6.11.3 *The crossing of R-$V_g$ curves between 1 and 3 K*

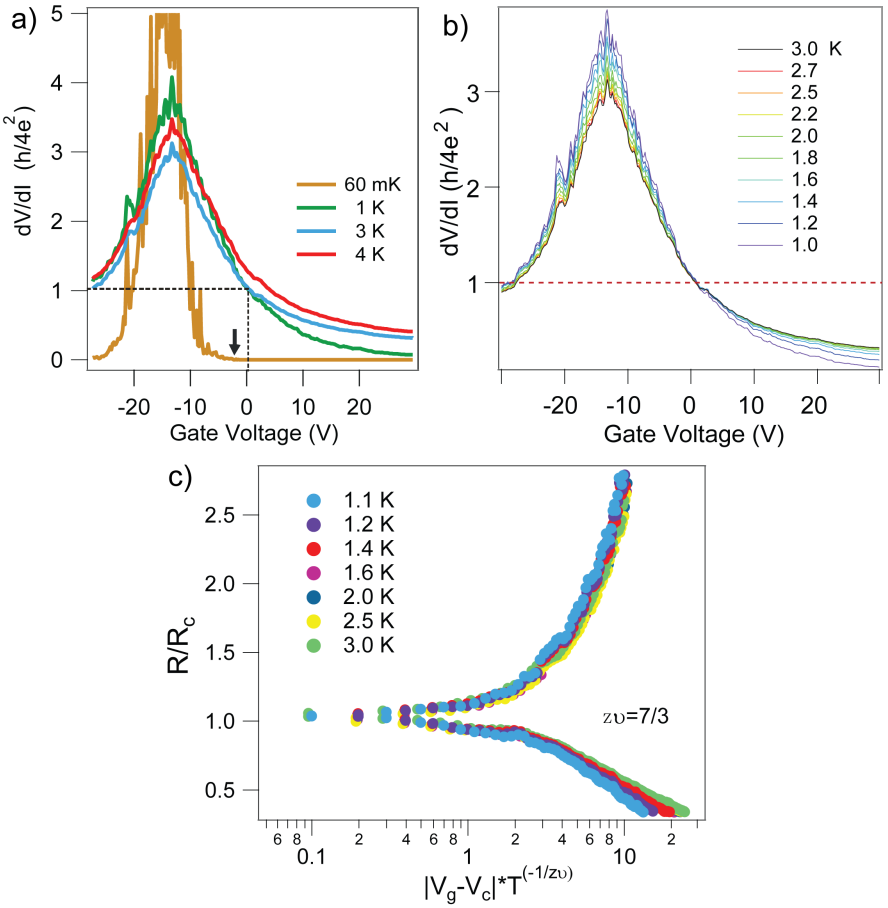


Figure 6.18: a) Gate voltage dependence of the resistance for different temperatures. b) Detail of the field effect curves between 1 and 3 K. c) Attempt to plot the curves in b) according to the scaling theory described by Equation 6.1.

We now come back to the cooling of the sample. As shown in Figure 6.18a, at gate voltages from 0 to 30 V, the resistance decreases when the temperature is lowered from 3 K to 1 K. An opposite trend is seen for gate voltages close to the Dirac point (namely, -30 V to 0 V), where the resistance is increasing, making a crossing-point at about 0V (green and blue, outlined by dashed lines, Figure 6.18a). Interestingly, this crossing-point corresponds to about 6.4 kΩ, close to

the quantum resistance for charge-2e $R_Q = h/4e^2 = 6.5k\Omega$ (Figure 6.18b). Similar behaviour was found in densely packed random arrays of Sn nanoparticles on disordered graphene, whose superconducting state resembles those encountered in some superconducting films [13, 30, 260].

We tried to treat our data at 1 to 3 K range with the scaling theory described by Equation 6.1, using the gate voltage as a critical parameter. It turns out that the critical component $z\nu$ can be $7/3$, $1/2$, or $1/3$ (Figure 6.18c), which makes little sense because no clear information can be extracted. However, multi critical components of quantum phase transition at different temperature ranges were indeed reported [339].

Further cooling extends the proximity effect through the graphene, which eventually leads to percolation of superconductivity, shown in Figure 6.18a, the brown curve at 60 mK.

## 6.12 BTK TRANSITION: EXPERIMENTAL AND THEORETICAL

We now check the superconductivity transition temperature in our proximity array. To visualize it, we plot the temperature dependence of field effect curves in a color-scaled map within the temperature range of 60 mK to 4 K, shown in Figure 6.20, where $T_{BKT}$ is drawn by the yellow contour. One can see that higher positive gate-voltages lead to higher Tc, whereas Tc vanishes in the region close to the Dirac point, ranging from -30 to -3 V.

In order to calculate the theoretically predicted $T_{BKT}$ in our array by using Equation 6.17, we first extract the parameters of diffusion constant D, and mean free path $l$, according to Equations 3.10-3.12. Here, a 4 K field effect curve is used as the normal state, assuming that the scattering is from impurities and thus the diffusion coefficient does not change at lower temperature.

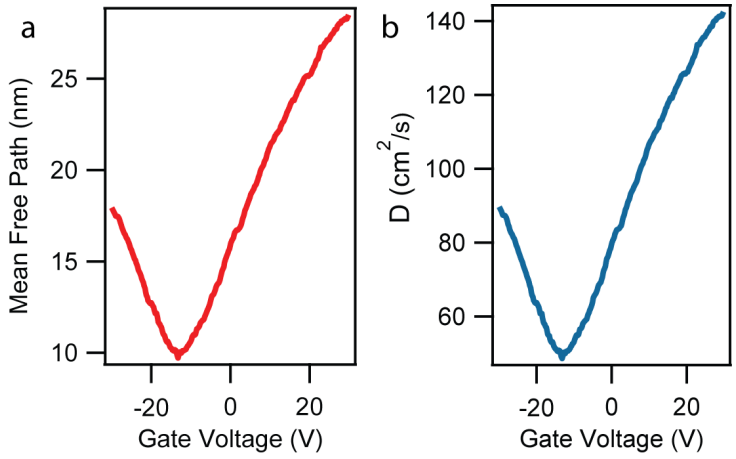


Figure 6.19: Mean free path $l$ extracted in the normal state field effect curve at 4 K temperature, by using the formula $l_e = \sigma h/2e^2 k_F$, here $k_F = \sqrt{\epsilon\epsilon_0 V_g \pi/ed}$ is the Fermi wavelength in graphene, with $\epsilon$ ~3.8 the dielectric constant, and d=285 nm the thickness of $SiO_2$ wafer. b) Diffusion coefficient D (calculated from $D = v_F l/2$, with $l$ the mean free path, and $v_F$ the Fermi velocity, $10^6$ m/s in graphene) between Sn islands in the graphene sheet.

Our extracted data shows that D is in the range of 50-140 $cm^2/s$, and g is around 2, which satisfy the conditions needed for the model [14], as discussed in Section 6.4. Moreover, we can estimate our $\xi_0$. If we consider our Sn nanodisk as dirty as the Pb nanoparticles studied in [340], then the mean free path $l_{Sn}$ in Sn should be around 2-3 times the height (50 nm) of the islands. $\xi_0^{Sn}$ is known to be about 300 nm [12]. The effective coherence length inside Sn islands should be around $\sqrt{l_{Sn} \times \xi_0^{Sn}} \sim 200nm$.

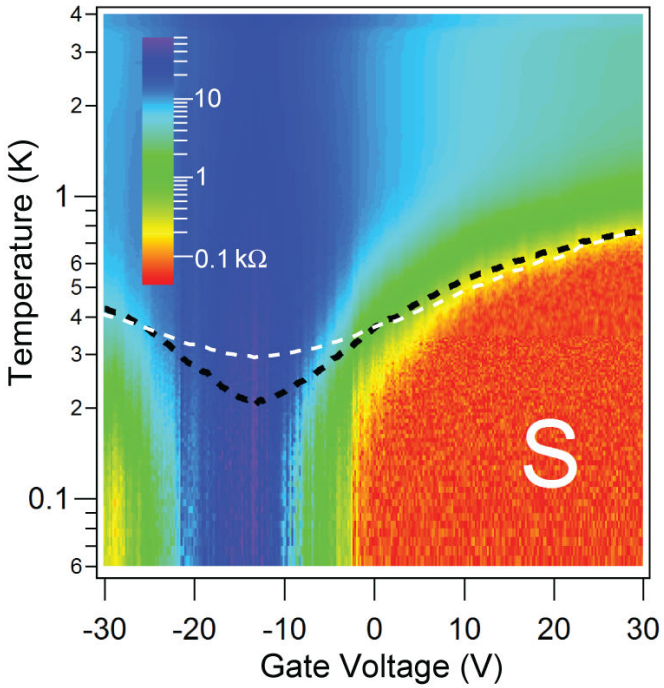


Figure 6.20: Color-scaled map of resistance versus temperature and gate voltage. Black dashed line is calculated from the theoretical prediction in Equation 6.17. White dashed line is fitted from Equation 6.37, with fitting parameter $\epsilon_{nu}$=25.

The above conditions allow us to use the model described in Section 6.4. By summing up the n of the Matsubara energy to several orders (higher orders of n do not affect the sum significantly since the function P decays rapidly with increasing n), one gets the black-dashed line as the unique solution of Equation 6.17 from experimentally extracted g and D in Figure 6.19. The calculated $T_{BKT}$ shows gate dependence which reaches a minimum around charge neutrality point where graphene conductance and diffusion coefficient are minimal. For high gate voltage, that is, Vg > 10 V, this theoretical value of $T_{BKT}$ is in excellent agreement with the sample critical temperature without any fitting parameter, thereby validating the theoretical description. The discrepancy at gate voltages lower than 10 V will be further discussed in the next sections.

For comparison, we also adopted the formula Kessler et al used to fit their data [12], which was developed on a JJA model [341], written as

$$\frac{T_{c0}}{T_{BKT}}\left[\frac{\Delta(T_{BKT})}{\Delta(0))}\tanh\left(\frac{\Delta(T_{BKT})}{2k_B T_{BKT})}\right)\right] = \frac{\epsilon_\nu R_N}{R_0}. \tag{6.37}$$

Here, $R_0 = 2.18\hbar/e^2 \sim 8.96k\Omega$, and $\epsilon_v$ is an effective dielectric constant that describes the material dependent screening of the attractive vortex-antivortex interaction. Qualitatively good fit to the measured data with an $\epsilon_v \sim 25$ is used. However, this fitting parameter $\epsilon_v$ is 10 times higher than the one reported in [12], which is unlikely to be physical.

## 6.13 ZERO TEMPERATURE BEHAVIOURS

*Critical current $I_c$ is the maximum suppercurrent a superconductor carries. However, due to the inertia of electrons or the self-heating effect [342], a hysteresis, or the so-called trapping-retrapping current, smaller than $I_c$, is often seen in Josephson junctions, noted as switching current $I_{SW}$.*

60 mK is the base temperature we can reach in our fridge, and we will use it as a quasi-zero-temperature for further analysis.

We now show the dV/dI-$I_{bias}$ curves as a function of gate voltage at 60 mK. A color map for full gate voltage range is demonstrated in Figure 6.21a. The letter "S" denotes the region where supercurrent exist, with maximum switching current reached at about 135 nA at $V_g$=30 V.

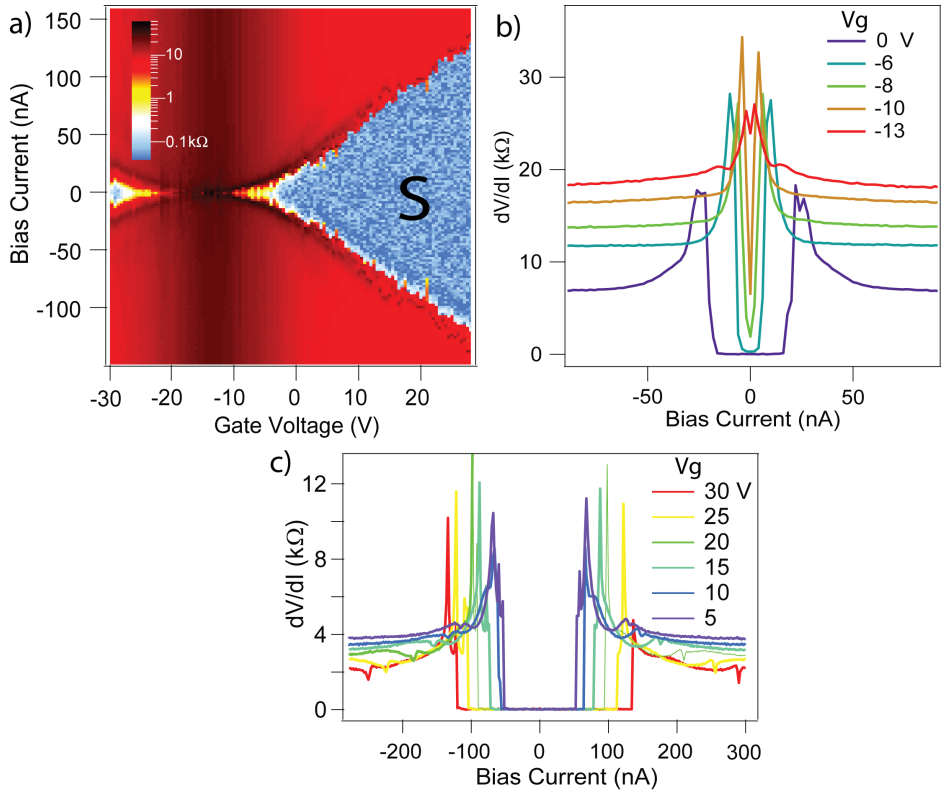


Figure 6.21: a) Gate-dependance of current-biased dV/dI curves at 60 mK. b) and c) are individual current-bias dV/dI curves at gate voltages from -13 V to 0 V, and 5 V to 30 V, at 60 mK temperature.

Not surprisingly, the maximum switching current $I_{SW}$ (notice there is a small difference of $I_{SW}$ for positive and negative $I_{bias}$ due to hysteresis) at 60 mK decreases with decreasing gate voltages from 30 V to the Dirac point of ~ -13 V. Notice that starting from about $V_g$=-4 V, the zero differential resistance disappears, in agreement with the feature observed in Figure 6.20. However, the quasi-gap feature (the gap feature in transport does not equal to the spectral gap in DoS, which has to be measured by STM) in the dVdI-$I_{bias}$ curve persists, even

close to the Dirac point, as shown in Figure 6.21b.

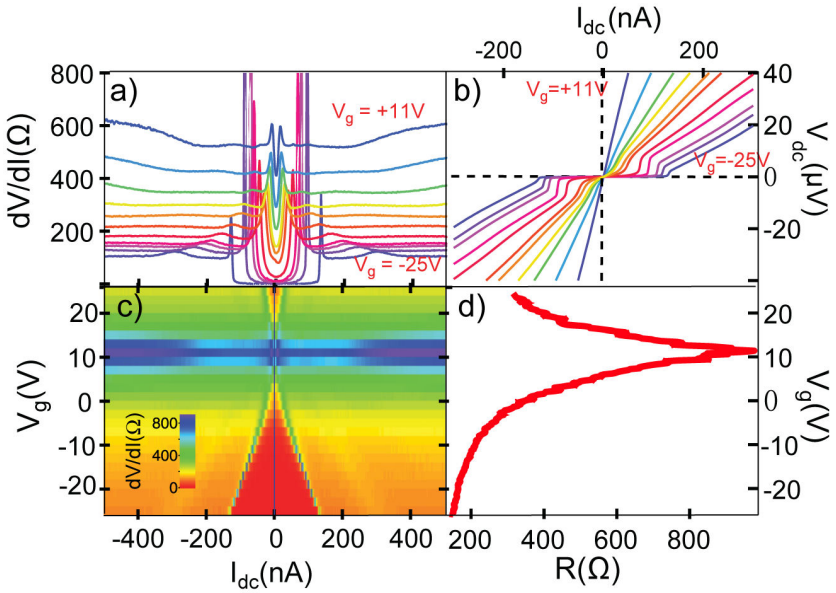


Figure 6.22: Similar paraconductivity behavior was seen in graphene Josephson junction with ReW electrodes at 55 mK. a) dV/dI-$I_{bias}$. b) I-V curve for different gate voltages. c) Color plot emphasizing the suppression of the supercurrent around the charge neutrality point. d) Normal state field effect curve achieved with a small magnetic field. Image adapted from [333].

This quasi-gap (with non-zero differential resistance) effect can be interpreted as a zero-temperature version of the Aslamazov-Larkin paraconductivity [343]. Such an effect is not seen in uniformly disordered superconducting films near the upper critical field, where T=0 paraconductivity is overcome by the opposite effect due to suppression of the density of states [344]. Recent experiment in graphene Josephson junction gives similar behavior, as shown in [333]. We conjecture that in our inhomogeneous system the contribution of the density of states correction is less singular near a quantum critical point than the Aslamazov-Larkin paraconductivity [345], which therefore leads to a strong positive contribution to conductivity even in the zero-temperature limit.

We also measured the temperature dependence of $I_{SW}$ at $V_g$=30 V. Supercurrent was found to disappear at a temperature of about 0.75 K, in good agreement with the previous data Figure 6.20. Individual $I_{bias}$-dV/dI curves at 0.4, 0.6 and 0.75 K are illustrated in Figure 6.23b. A cut along zero bias current is shown in Figure 6.23c, showing the BKT transition.

Interestingly, the $I_{SW}$ has a quite linear dependence of temperature for high temperatures, which is not so often seen. It has been shown that in the long diffusive junction limit (length of junction $b \gg \xi_0$), which is roughly our case, since $\xi_0^{Sn} \sim 300nm$, the product of critical current $I_c$ and normal resistance $R_N$ follows the dependence [346]:

*For comparison, in a ballistic tunnel junction, the* $I_c R_N = \pi\Delta/e$ *[317].*

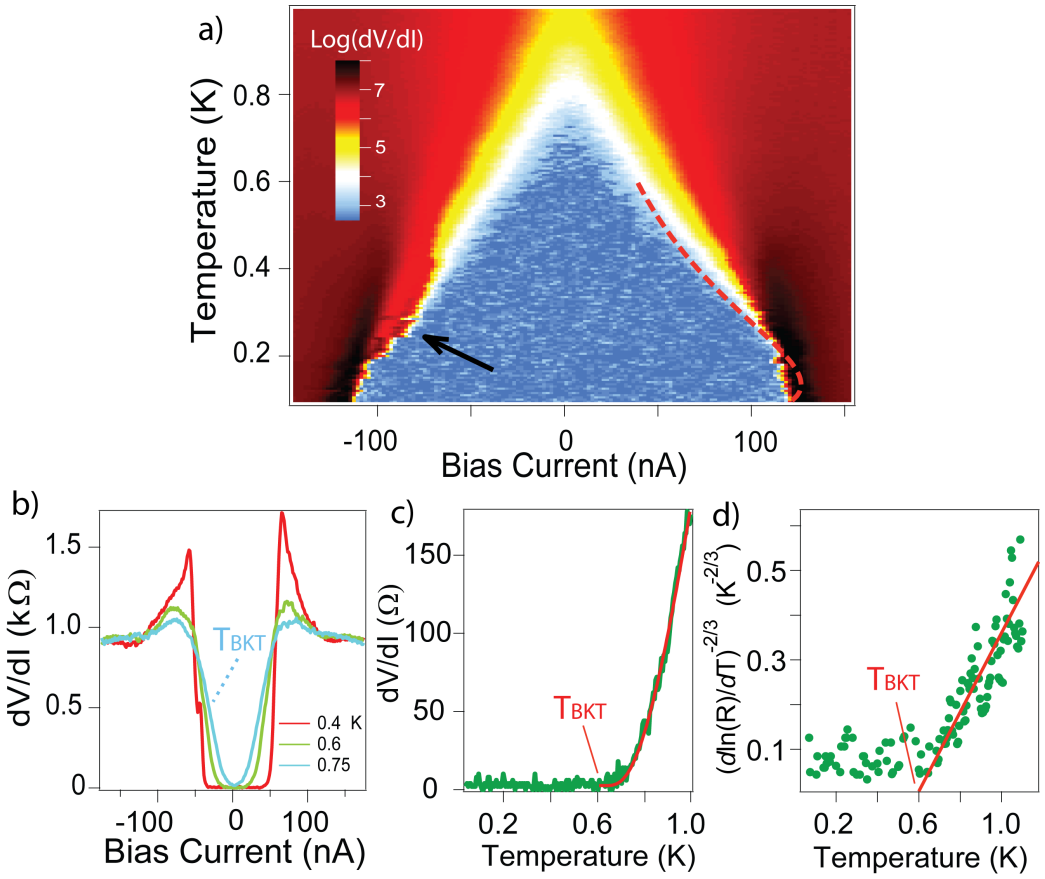


Figure 6.23: a) Temperature dependence of $I_{bias}$-dV/dI curve at $V_g$=30 V. Supercurrent disappears at a temperature of about 0.75 K, in agreement with the previous images. The fit in a) is using formula Equation 6.39, with $R_N = 2k\Omega$ and $T_0 = 0.145K$. b) Individual $I_{bias}$-dV/dI curves at 0.4, 0.6 and 0.75 K. c) Line cut along zero bias current in a), with the red solid line fitted by Equation 6.39. d) Rescaling of the sheet resistance versus temperature to extract $T_{BKT}$.

$$I_c R_N \propto \begin{cases} \pi E_{Th}/e, & k_B T \ll E_{Th} \ll \Delta \\ T^q \exp -\sqrt{T/T_0}, & E_{Th} \ll k_B T \ll T_C \end{cases}, \tag{6.38}$$

where q and $T_0$ are originally derived to be 3/2 and $E_{Th}/2\pi$. Here, we have $R_N \sim 2.6k\Omega$, and $E_{Th} = \hbar D/b^2 \sim 1 \times 10^{-34} m^2 kg/s \times 145 cm^2/s / 10^{-12} m^2$ of about $150 \times 10^{-26} m^2 kg/s^2$, divided by the Boltzmann constant $k_B = 1.38 \times 10^{-23}$ J/K. The Thouless energy is about 0.1 K.

The best fit using $I_c \propto \alpha T^q \exp -\sqrt{T/T_0}$ to the measured data on the positive bias current side is found to be $T_0 = E_{Th}/2\pi = 0.0159K$, with a pre-factor $\alpha$ of $4.4 \times 10^{-5}$.

Here, our system is actually a row of 6 Josephson junctions perpendicular to the current flow. Therefore, it is reasonable to have the above fitted value of $2\pi \cdot T_0$ to be very close to the experimentally extracted $E_{Th}$. We understand this by the fact that at a finite temperature, the array system can be treated as a sum

of every unit pairs, whose Josephson couplings are identical. A row of 6 islands enhances the total critical current, however, the $I_c R_N$ product is still proportional to the right side of Equation 6.38. The collective behavior only plays a role on the minigap inside graphene when $T \to 0$. That is why we can use a pair-like $E_J$ to calculate and fit the BKT transition of the whole array.

Notice that at the negative bias current side, there are some irregular $I_{SW}$, as indicated by arrow in Figure 6.23a, which may be due to some thermal instabilities.

We have been talking about BKT transition from the very beginning of this chapter. Now, we are going to examine the data shown in Figure 6.23c, which is a cut along the temperature axis at zero bias current. It is known that for a BKT transition, the resistance (which is proportional to the vortex population) grows as:

$$R(T) \propto A \exp\left(\frac{b}{\sqrt{T - T_{BKT}}}\right), \tag{6.39}$$

where $A$, $b$ and $T_{BKT}$ are fitting parameters. A fitting of the measured data is shown as the dashed line in Figure 6.23c, with $A = 9033.4$, $b = 2.472$, and $T_{BKT} = 0.6K$. According to Equation 6.39, the plot of $[d(\ln(R)/dT]^{-2/3}$ versus T should give a straight line with $T_{BKT}$ given by the intercept with x-axis. Indeed, such plot leads to consistent $T_{BKT}$, as shown in Figure 6.23d.

Another hallmark of the BKT transition is a nonlinear I-V characteristics: $V \propto I^{\alpha(T)}$, with $\alpha(T_{BKT}) = 3$ and growing with lowering temperature. At the transition, the exponent $\alpha$ drops from 3 to 1, and the system transforms into a dissipative state. This is because the finite energy barrier correponding to the vortex-antivortex binding energy needs to be overcome before the sample become dissipative via the vortex motion. The bias current overcomes that barrier when the opposite Magnus force exerted on the vortices and anti-vortices breaks them apart.

We plot the IV curves in Figure 6.23a in another manner, as shown in Figure 6.24a. $\alpha$ is fitted with $V \propto I^{\alpha(T)}$, at the low voltage part for different temperatures, as shown in Figure 6.24b. Indeed an exponent of 3 is found close to the foot of the BKT transition at about 0.73 K. However, no clear jump from 3 to 1 is seen. The jump of $\alpha$ in a BKT transition is rarely observed in real samples [347, 348]. Moreover, if one looks into Figure 6.24b, a change in $\alpha$ from 3 to 2 or 4 does not dramatically affect the $T_{BKT}$, we therefore will not dwell too much on this issue of critical exponent in IV dependence.

We now look back to the switching current shown in Figure 6.21a. Assuming that in our system the maximum switching current is very close to the theoretical critical current, then we can compare the measured ones with theory.

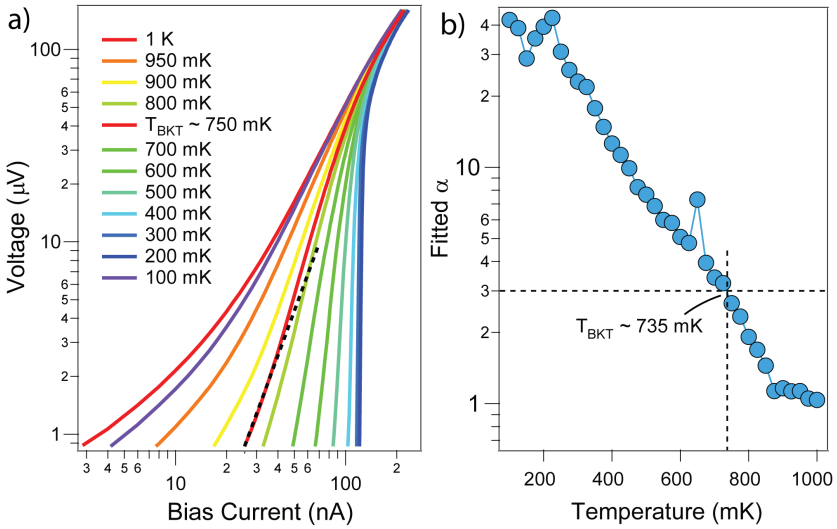


Figure 6.24: a) IV curves at $V_g = 30V$, for different temperatures. Dashed line is the curve of $V \propto I^3$, best fitted to the $T = 0.75$ K one. b) Exponent $\alpha$ is fitted at the low voltage part in a), with a $T_{BKT} \sim 0.735$ K.

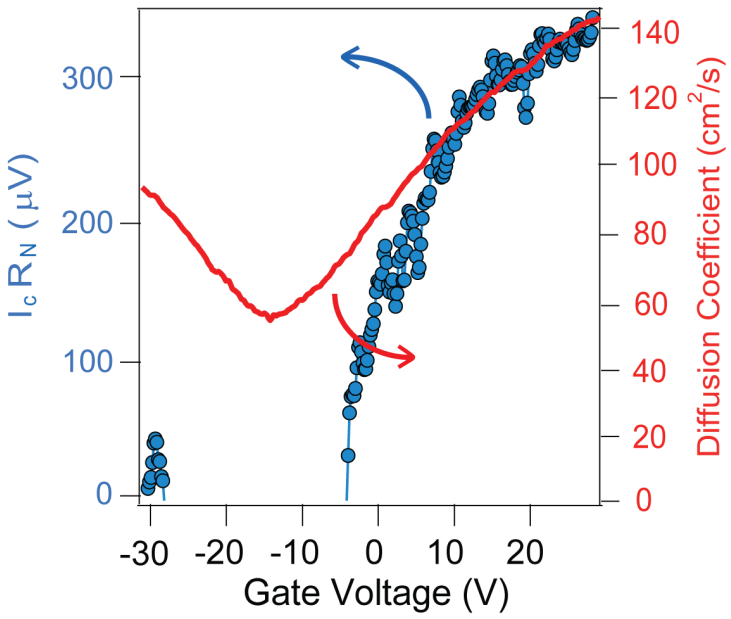


Figure 6.25: Product of $I_c R_N$ extracted from Figure 6.21 and diffusion coefficient in Figure 6.19b, as a function of gate voltage in the same graph.

As discussed in [14], when at zero temperature, Josephson coupling for each pair of islands is given as:

$$E_{J,T=0} = \frac{\pi^3}{4} \frac{g\hbar D}{b^2 \ln(b/a)}, \tag{6.40}$$

Josephson coupling energy is also defined as [317]:

$$E_J = (\hbar/2e) I_1, \tag{6.41}$$

where $I_1$ is the maximum supercurrent between neighboring islands. Our array contains 6 islands in the direction perpendicular to the direction of current flow and its total critical current $I_c$ can be estimated (neglecting small contribution to $I_c$ from non-nearest pairs of islands) as:

$$I_c \approx 6I_1 = \frac{3\pi^3 geD}{b^2 \ln^2(b/a)}. \tag{6.42}$$

According to the above relations, at $T \ll T_c$, the product of $I_c R_N$ should only depend on D for a given geometry (N denotes normal state, $R_N = R_\square$ since the sample is a square). The use of graphene as a 2D diffusive metal enables one to gate-tune the diffusion coefficient while keeping the geometrical aspects of the array constant. By extracting at the base temperature 60 mK, the experimental $I_c$ from Figure 6.21, and measuring $R_N$ at 4 K, we plot $I_c R_N$ and D as a function of gate voltage in the same graph, as shown in Figure 6.25.

Indeed this shows a very similar gate-dependence for $V_g > 10$ V, with the $eI_c R_N/\hbar D$ ratio of about $3.7 \cdot 10^9 cm^{-2}$, which is close to the theoretical value $3\pi^3/b^2 \ln^2(b/a) = 3.6 \cdot 10^9 cm^{-2}$, that depends only on the geometrical aspects (Figure 6.26). We therefore find full agreement at high gate voltages between the experimental observations and theoretical predictions for such proximity coupled arrays.

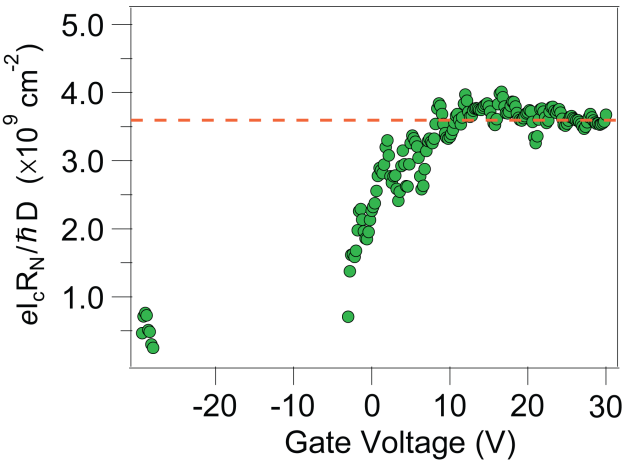


Figure 6.26: Experimental (green circles) and theoretical value (dashed line) of the $eI_c R_N/\hbar D$ ratio. Dashed line is the theoretically predicted value of $3.6 \cdot 10^9 cm^{-2}$.

However, the good agreement of $I_c$ breaks down between experiment and theory at gate voltages lower than about 8 V. Similar breakdown of the model is seen for the BKT transition. The question is:

*What makes this break down of superconductivity? And why does the model proximity array on a diffusive 2D metal fail to explain the measured data? We will give an answer in the coming sections.*

## 6.14 BEHAVIOR OF THE ARRAY UNDER PERPENDICULAR MAGNETIC FIELD

Before we go to the final section about quantum breakdown of superconductivity, we add characterization of the sample under a perpendicular magnetic field.

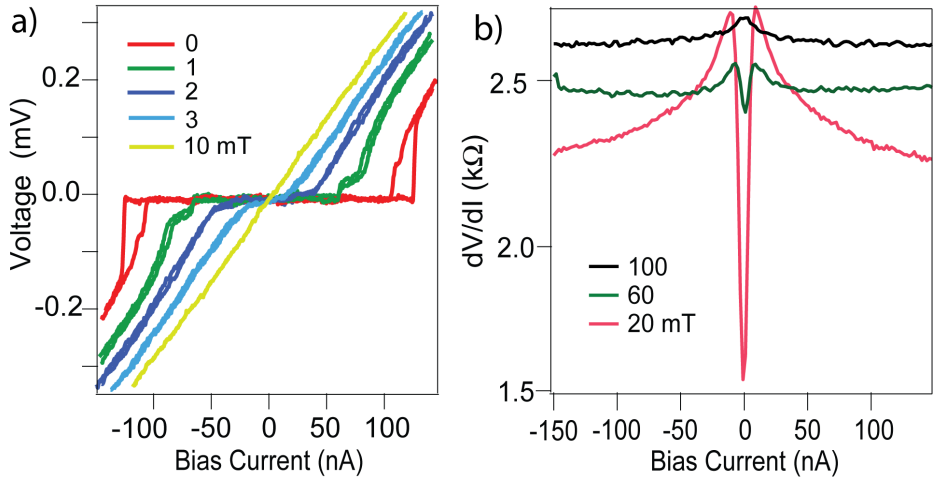


Figure 6.27: a) I-V curves at several magnetic fields, and b) dV/dI-$I_{bias}$ curves at several magnetic fields. Data maesured at $V_g$=30 V, 60 mK.

First of all, we start with a small field, and begin with examining the sample at 60 mK and at $V_g$=30 V. As can be seen in Figure 6.27a, the I-V characteristic at zero field shows a typical under-damped Josephson junction behavior, with a hysteresis in the I-V curves. When a magnetic field is applied perpendicularly, the I-V curves become more damped, and supercurrent is completely suppressed at the order of about 3 mT.

When continuing to increase the magnetic field, the zero bias dip persists, as a sign of superconductivity fluctuations, up to about 80 mT. The central $I_{bias}$ dip becomes a Coulomb peak at 100 mT, as shown in Figure 6.27b.

We further carry out higher field magnetoresistance measurements up to 2 T. Due to the heating of the magnetic coil, we have to measure the 2 T data at 100 mK. As shown in Figure 6.28a, the magnetoresistance at $V_g$=-10, 0, and 30 V are taken. A central dip in the superconducting region can be clearly seen at $V_g$=0 and 30 V. While a zoomed-in Figure 6.28b shows that even at $V_g$=-10 V, the central dip persists. Notice that in Figure 6.28c we get a fitted de-phasing length of about 200 nm. However, by tweaking the fitting parameters, one can get very different results range from 100 nm to several micrometers.

The general shape of the magnetoresistance curve looks like a superposition of weak localization of diffusive graphene and a superconductor. We performed the weak localization fit (Equation 5.7) for the curve at $V_g$=-10 V, assuming a resistive state without SC, as it turns out the phase coherence length $L_\phi$ is about 200 nm, which is of the order of $\xi_0$ estimated in the previous section.

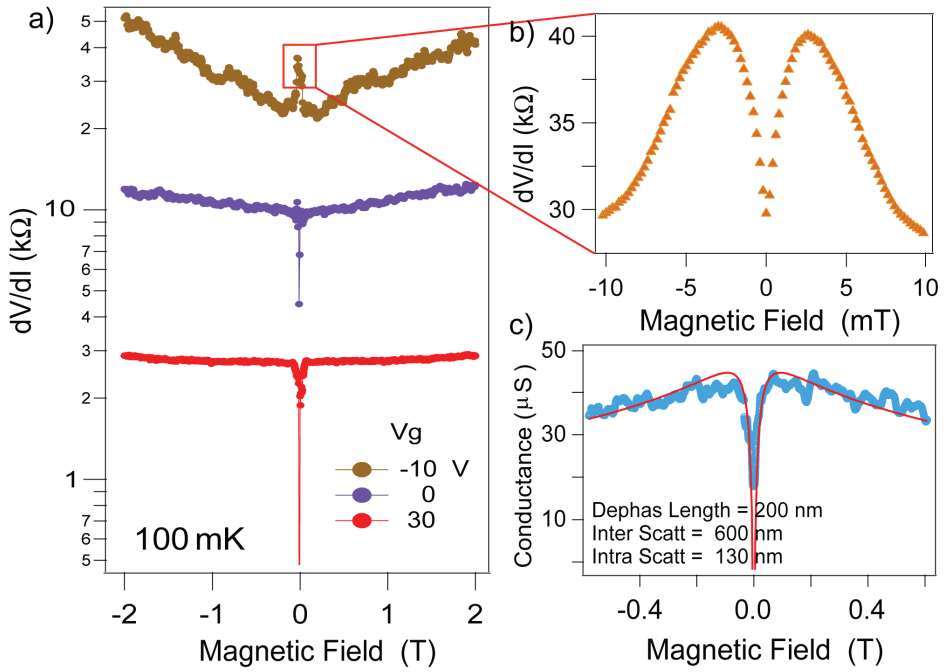


Figure 6.28: a) Magnetoresistance at $V_g$=-10, 0, and 30 V. and b) Zoom-in of the red box area in a). c) Fit of the magnetoresistance curve at $V_g$=-10 V, using Equation 5.7.

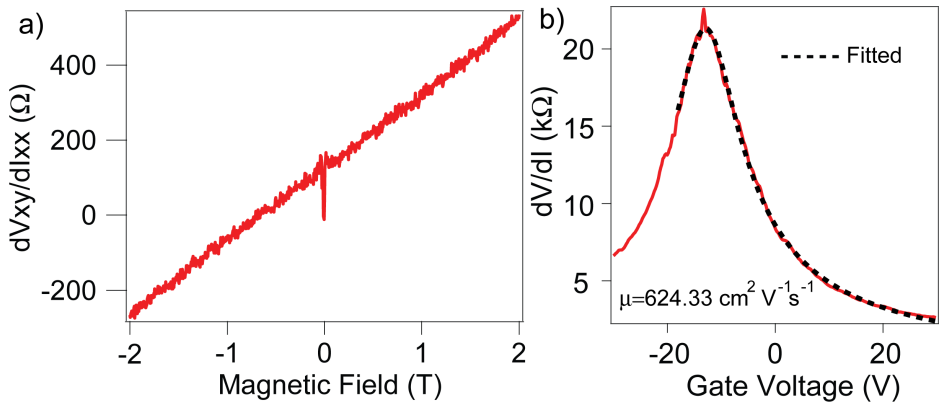


Figure 6.29: a) Hall resistance as a function of magnetic field. b) Electronic mobility fitted from 4 K field effect curve, using Equation 3.17, $\mu = 624 cm^2 V^{-1} s^{-1}$.

Electron carrier density is also extracted at gate voltage of 30 V via Hall measurement. As shown in Figure 6.29a. Carrier density $n$ is defined as

$$-\frac{1}{ne} = \frac{V_{xy}}{I_{xx}B}, \tag{6.43}$$

where $V_{xy}$ is the Hall voltage, *i.e.*, transverse voltage drop of the sample, and $I_{xx}$ is the longitudinal current that is biased on the sample. $n$ is extracted from Figure 6.29a to be about $3.19\times10^{12} cm^{-2}$. According to the definition $\sigma = ne\mu$, the electronic mobility is then estimated to be about 675 $cm^2 V^{-1} s^{-1}$.

Mobility extracted by fitting the 4 K field effect curve using Equation 3.17 is 624 $cm^2V^{-1}s^{-1}$. We found the two methods consistent since there might be a small mix of longitudinal and transverse voltage.

## 6.15 QUANTUM BREAKDOWN OF SUPERCONDUCTIVITY & QUANTUM METALLIC STATE

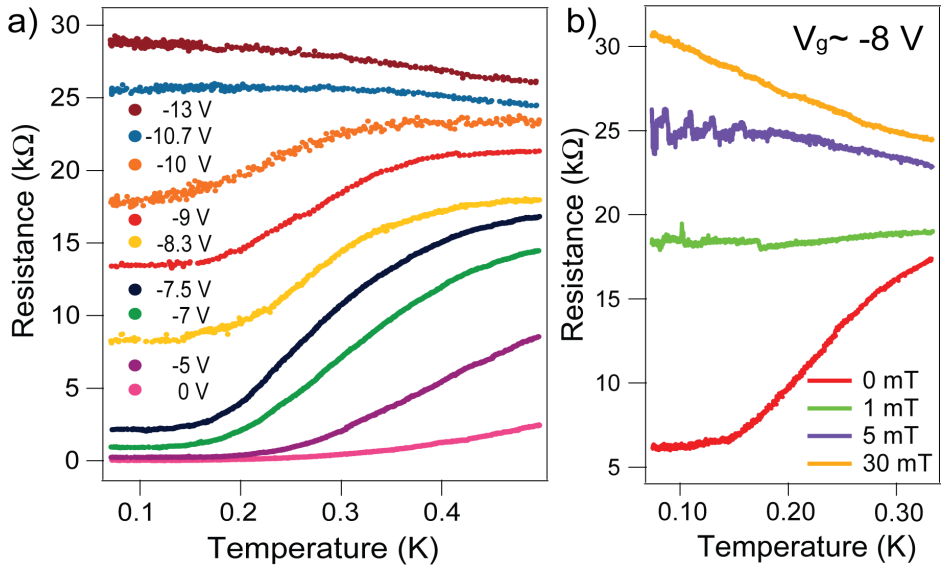


Figure 6.30: a) Temperature dependence of resistance at different gate voltages in a temperature range of 70 mK - 500 mK. b) Temperature dependence of resistance at gate voltage of about -8 V, with perpendicular magnetic field of 0, 1, 5 ,30 mT. Temperature range in b) is 70 mK -350 mK.

As discussed in the previous sections, superconductivity breaks down in the system at zero-temperature at gate voltages from -30 to -3 V. In the following we investigate the nature of this state terminating superconductivity.

We systematically measured the T-dependence of the resistance for gate-voltage close to the critical $V_g$ = -3V. As shown in Figure 6.30a, the R-T curves in the non-superconducting regime at $V_g$ < -3V show a resistance drop around 0.4 K reminiscent of the superconducting transition of those at $V_g$ > -3V, which indicates that superconducting fluctuations develop in the graphene.

However, instead of falling to a zero-resistance superconducting state, the R-T curves saturate at finite and gate-dependent values that can reach the resistance quantum $h/e^2$. Importantly we can exclude the possibility of electron heating as the origin of this metallic tail at low temperature, since in a weak magnetic field no such saturation was measured (Figure 6.30b). This saturation therefore conspicuously extrapolates to a zero-temperature 2D metallic state - as predicted by theories described in Section 6.7.3.

At this point, we can review our experimental observations:

1. *At a finite temperature*, the BKT transition shows agreement with theory from $V_g$ = 10 V to 30 V. While the theoretical prediction breaks down at $V_g <\sim 10V$.

2. *At zero temperature*, critical current shows agreement with theory from $V_g$ = 8 V to 30 V. While the theoretical prediction breaks down at $V_g <\sim 8V$.

3. *At zero temperature*, A metallic state develops at $V_g <\sim -3V$.

All these three effects are due to the gate-tuning of the graphene carrier density (corresponding to different sheet resistance).

Notice that in effects (1) and (2), the theory we applied is an Usadel equation without quantum phase fluctuations, while effect (3) is an important behavior predicted by the model focusing on zero-temperature quantum phase transition.

Therefore, we have good reason to believe that the collapse of superconductivity at zero temperature in (3) is due to quantum phase fluctuations described in Section 6.7.3. This is also the reason why, in effects (1) and (2), the data fails to be fitted by a theory without quantum phase fluctuations.

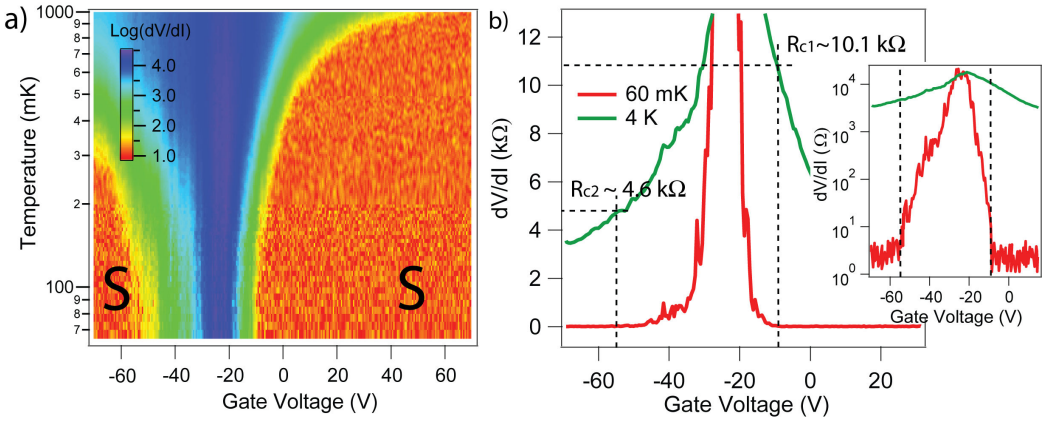


Figure 6.31: a) Color-scaled map of resistance versus temperature and gate voltage. b) $R_{\square c}$ defined by measuring the 4 K resistance (green curve) at the critical gate voltages $V_{gc}$, which are the points where SC breaks in the 60 mK field effect (red curve). Inset in b) is a log-scale of the plot.

Now, let us use the main prediction in Section 6.9.3, which is a critical resistance between two SC islands $R_N^{ij} = (R_{\square c}/\pi)\ln(b/a)$. We have measured the sample in a gate range from -70 to 70 V. However, this measurement was done after the fridge was warmed up to room temperature, and there is a shift of the Dirac point. We define the $R_{\square c}$ by measuring the 4 K resistance at the critical gate voltages $V_{gc}$: *i.e.*, the $V_g$ at which SC breaks down at 60 mK. The result is shown in Figure 6.31.

It can be seen that, on the electron side, where the interface of Sn and graphene is supposed to be rather transparent, $R_{\square c-e} \sim 10.1$ kΩ, while on the hole side (less transparent interface), $R_{\square c-h} \sim 4.6$kΩ. The two $R_{\square c}$ values correspond to the critical resistance between two neighbouring Sn islands $R_{N-e}^{ij} \sim 5$kΩ,

*The $R_N^{ij}$ is lower in the hole side than in the electron side, simply because part of the total resistance in between two SC islands is shared by the interface resistance. Here we assume that interface is not fully opaque in the hole side.*

and $R^{ij}_{N-h} \sim 2.3k\Omega$ respectively. Both are lower than $R_Q = 6.5k\Omega$. This result supports the theory in [35]. The prediction that SC always persists as long as $R_N < R_Q$ [321, 275] is actually invalid.

## 6.16 REENTRANT SUPERCONDUCTIVITY UNDER WEAK MAGNETIC FIELD

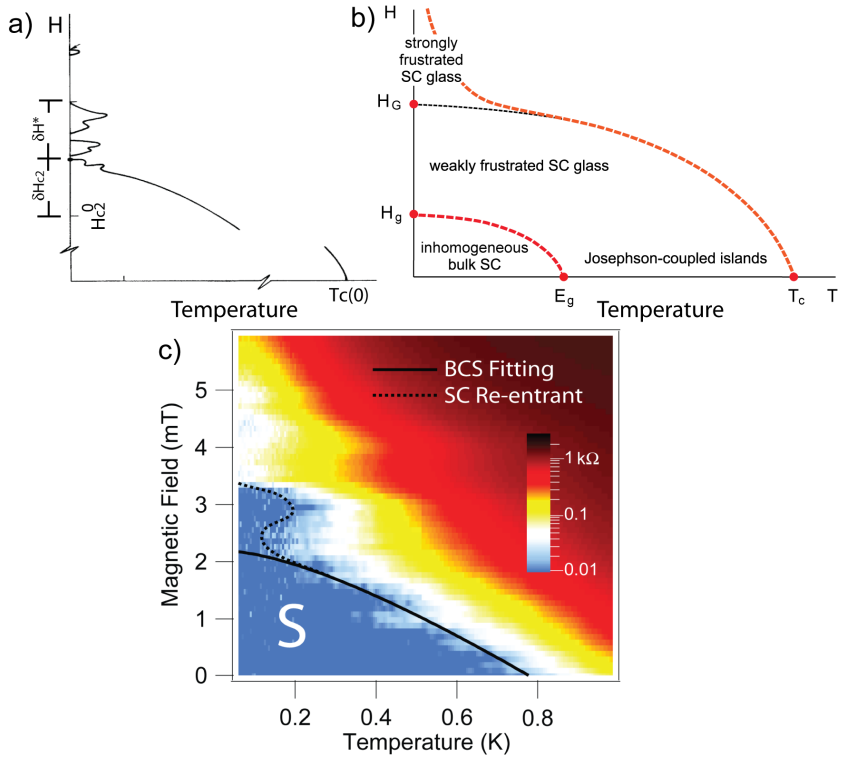


Figure 6.32: When a mesocopic system is subjected to a magnetic field, a) reentrant of SC above $H_{c2}$ adapted from [38], and b) "tail"-like up-turn of $H_{c2}$ adapted from [14], are expected due to quantum phase fluctuations. c) Plot of zero-bias magneto-resistance versus temperature of the sample at Vg=30 V. The solid line is a fit of $H_{c2}$-T dependence of dirty BCS superconductor. Dashed line is a guide for the eyes for highlighting the reentrant of superconductivity above $H_{c2}$.

As we discussed in section 6.7.4, our system - proximity array coupled graphene - is a model system to see the quantum phase fluctuation effect on the critical field $H_{c2}$. We hope to see either the reentrant of SC above $H_{c2}$ (Figure 6.32a), or a "tail"-like up-turn of $H_{c2}$ (Figure 6.32b) at zero temperature.

When our array is subjected to a magnetic field, two different effects appear.

- First, Josephson couplings become frustrated up to the degree determined by the value of $f = HS_0/\Phi_0$ where $S_0 = \sqrt{3}b^2/2$ is the area of the array elementary cell.
- Second, the magnitude of each individual Josephson coupling $E_J^{(ij)}$ between two islands $i, j$ becomes suppressed at the length-scale $L_{ij} > L_H = \sqrt{\Phi_0/H}$ (the glass field length).

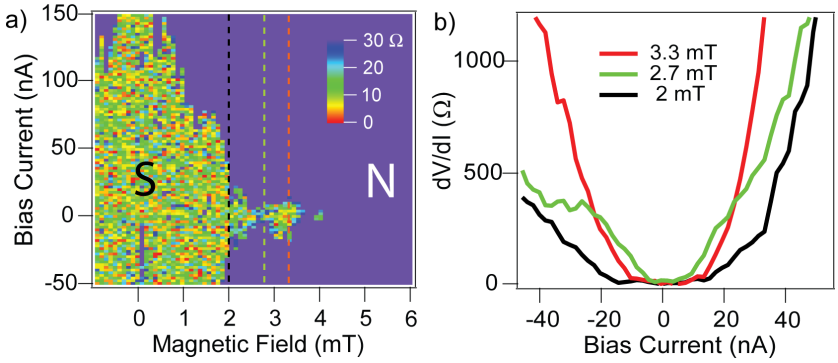


Figure 6.33: a) Magnetic field dependence of current-biased differential resistance at $V_g$ =30 V, 60 mK. b) Individual dV/dI curves at 2, 2.7, and 3.3 mT. Critical current is first suppressed at around 2.7 mT (green curve in Figure 6.33b), then is enhanced at around 3.3 mT. In the "reentrant" region (H ~ 3 mT), critical current is much weaker in comparison with the main superconductive region (0 mT < H < 2.2 mT).

Whereas the second effect always leads to enhancement of quantum phase fluctuations, the first one may lead to non-monotonic behaviour upon increasing H, see e.g. [33]. Thus we may expect either reentrant transitions between the superconducting and normal states [38], or low-temperature up-turn of the critical field [349, 14].

We performed, at 60 mK, the zero-bias magneto-resistance versus temperature of the sample at $V_g$=30 V, as shown in Figure 6.32c. The zero-resistance state is demonstrated in blue colour, indicated by "S". The qualitative feature is seen: low-temperature "superconductivity reentrance" into the region of relatively high field does exist, as highlighted by the dashed line.

A BCS fit of $H_{c2}$ is plotted in Figure 6.32c by the black solid line. One can see that the high-temperature part is well fitted, while a discrepancy is seen at the low temperature part. Moreover, the fitted $H_{c2}$ is about 2.2 mT, close to the full-frustration value $H_0 = \Phi_0/S_0 = 2.4$ mT. High-field reentrant superconductive region seen around H= 3 mT at temperatures below 200 mK qualitatively agrees with predictions of [38].

Moreover, the critical current in this reentrant region is strongly suppressed in comparison with the main superconductive region at the same temperature (Figure 6.33a), which is consistent with a low-temperature *superconducting glass* state [350, 351, 349] due to frustration of Josephson couplings, which originates from quantum phase fluctuations.

*Notice that, the quantum fluctuations that induce reentrant superconductivity at $H_{c2}$ has nothing to do with the quantum fluctuations that causes the collapse of SC at zero field. The latter comes from the Andreev conduction induced weak charge quantization, while the former comes from the random phase fluctuation (under a magnetic field) of Josephson coupling between SC clusters.*

### Q & A of Chapter 6

After having shown all the above measurements, we would like to answer all the questions we asked in the begining of this chapter.

1. *With respect to the conventional one dimensional SNS junction, what are the new features when the system is built up with an periodic array? Namely, how does the so-called collective proximity effect play a role? What is the theoretical density needed to still obtain superconductivity?*

The collective proximity effect mainly works on the spectral minigap, which will be seen by STM measurements, and is the object of our future studies. The density needed to still get SC, so far, we can say, is above 10 percent. However, we believe that even at less than 1 percent surface coverage, the system should still be superconducting. Of course, the interface plays an important role.

2. *What is the origin of the quantum phase fluctuation? How does it affect the quantum phase transition from a superconducting state to a metallic state?*

The origin of quantum phase fluctuation is the nature of the Andreev 2e charge transfer in/out of each SC island. This feature is never considered in the conventional JJA models.

The 2D metal conductance determines Andreev conductance, and the Andreev conduction (2e charge transfer) induces SC-phase fluctuations. These fluctuations play a role of an effective charging energy. Therefore, at a critical effective charging energy (which is of the order of Josephson coupling energy) at zero temperature, a SC-M quantum phase transition takes place.

3. *Since a magnetic field is supposed to decrease Josephson coupling between islands, how does the superconducting state evolve as a function of magnetic field?*

Normally a magnetic field suppresses Josephson coupling. However, due to the existence of quantum phase fluctuations, random signs of Josephson coupling is possible. The result is the appearance of SC clusters, that exist even above the $H_{Glass}$ when the fluctuation is strong enough, a global SC can be seen as a reentrant of SC, or reentrant of $H_{c2}$, at zero temperature.

4. *Is there a critical resistance in the S(M)I quantum phase transition? If yes, is it* $4e^2/h$ *or not?*

Yes, but it is not necessarily $R_Q$. See details in Section 6.15.

5. *Does there exist a 2D metallic phase at zero-temperature? If yes, what is its origin?*

Yes! And the answer is given in 2.

## 6.17 CONCLUSION OF CHAPTER 6

To conclude, we have reviewed at the beginning of the chapter the historical problem about the intervening metallic state in the superconductor-to-insulator quantum phase transition.

Then, a recent model on proximity coupled diffusive 2D metal was introduced. Using the Usadel equation without quantum phase fluctuations, the theory [14] predicts:

a) a BKT transition at finite temperature;

b) an $I_c R_N$ product proportional to the diffusion constant D of the system at zero temperature.

When quantum phase fluctuations are taken into account, the theory [35] says that, in the diffusive limit, the phase coherence of Andreev pairs will fluctuate strongly because of the weak 2e charge quantization. The quantum phase fluctuations have an effect similar to the conventional charging energy in the JJA models, which is tuned by the 2D metal conductance. The theory then predicts that:

c) at a critical normal state conductance of the 2D metal (which can be lower than $R_Q = 4e^2/h = 6.5k\Omega$), the superconductivity collapses between SC islands, leading to a metallic state.

To experimentally achieve the conditions needed for the above theories, we have fabricated triangular arrays of Sn nanodisks (diameter-to-distance ratio of 400 nm/1 μm) on diffusive graphene (mean free path at the order of ~ 25 nm, D ~ 100 $cm^2/s$). The graphene has a gate-tunable carrier concentration, thus making it an amenable system to see the effect of SC-M quantum phase just by electrostatic gating.

Our experimental observation shows quantitative agreements with the theoretical predictions (a) and (b) at the high gate voltage side ($V_g > 10V$). Nevertheless, a breakdown between theory and measured data is seen in the gate range of -30 V $< V_g <$10 V.

We see a collapse of superconductivity in the gate range of -30 V $< V_g <$ -3 V, where a metallic state establishes, and conspicuously extrapolates to zero temperature.

All the above experimental observations strongly support the quantum phase fluctuations induced is an SC-M quantum phase transition.

Moreover, when checking the $R_N^{ij}$ between islands, we found that at electron and hole side, $R_N^{ij}$ is 5 and 2.3 kΩ respectively. This result steadily validates the theoretical predictions based on the model of proximity array coupled 2D metal.

Finally, we have shown that, when subjected to a small perpendicular magnetic field, our system shows, for the first time, experimental observation of a reentrant behavior of $H_{c2}$ at a magnetic field above the $H_{Glass}$. This added value suggests that the present system under study is very rich in mesoscopic physics,

and a prototype for several kinds of quantum phase fluctuations theories.

## 6.18 APPENDIX: DERIVATION OF EQUATION 6.30

Zero temperature superconductivity breaks at the critical condition [34]:

$$1 = \frac{1}{2\hbar} J(T) \cdot C(T). \tag{6.44}$$

$J(0)$ can be obtained by solving the Usadel equation at the limit of $\ln(b/a) \ll 1$ [34]

$$J(0) = \frac{\pi^4}{2} \frac{g\hbar D}{b^2 \ln(b/a)}, \tag{6.45}$$

$C(0)$ is given by:

$$C(0) = \frac{\rho \cdot a^2}{D} e^{2\pi\sqrt{g}s}, \tag{6.46}$$

where $\rho$ is a unknown factor, and $s$ is a parameter related to the RG equation of $G_A$. By substituting Equation 6.45 and Equation 6.46 into Equation 6.44, one gets:

$$\frac{1}{2\hbar} \cdot \frac{\pi^4}{2} \frac{g\hbar D}{b^2 \ln(b/a)} \cdot \frac{\rho \cdot a^2}{D} e^{2\pi\sqrt{g}s} = 1, \tag{6.47}$$

which reduces to:

$$\frac{\pi^4}{4} \frac{g\rho}{\ln(b/a)} \cdot \frac{a^2}{b^2} \cdot e^{2\pi\sqrt{g}s} = 1, \tag{6.48}$$

which goes to:

$$\frac{\pi^2}{2} \left[\frac{g\rho}{\ln(b/a)}\right]^{1/2} \cdot e^{\pi\sqrt{g}s} = \frac{b}{a}. \tag{6.49}$$

If one introduces a self-consistent relation:

$$e^{\pi\sqrt{g}s} \sim \frac{b}{a}, \tag{6.50}$$

and replace the above relation into Equation 6.49, it turns out to be:

$$\frac{b^2}{a^2} \sim \frac{\pi^2}{2} \left[\frac{\sqrt{g}\rho}{\pi s}\right]^{1/2} \cdot e^{\pi\sqrt{g}s}. \tag{6.51}$$

This equation can be reformed into:

$$g_c \sim \left(\frac{1}{\pi} \ln \frac{b}{a'}\right)^2, \tag{6.52}$$

with

$$a' = \frac{a \cdot \pi^3 \rho^{1/2} \cdot g^{1/4}}{2s^{1/2}}. \tag{6.53}$$

Notice the relation $g_c \sim \left(\frac{1}{\pi} \ln \frac{b}{a'}\right)^2$ is only valid when $a \sim a'$, *i.e.*, $\rho^{1/2} \cdot g^{1/4} \sim 1$, since $s$ is calculated to be close to 1[35].

# 7

# GENERAL CONCLUSION AND PERSPECTIVES

In this thesis, we have demonstrated a full chain of graphene activities starting from building up a CVD machine, developing our own pulsed-CVD method to achieve fully monolayer graphene, transferring CVD graphene onto arbitrary substrates, functionalization of CVD graphene, fabricating micro-devices, and finally the work finishes by the low temperature measurements of a new quantum metallic state, on CVD graphene decorated with a regular array of superconducting nanoislands.

In chapter 1, we described the material preparation, which is the basis of this thesis work. We have reviewed the CVD growth technique developed in the area of graphene research in recent years. We have developed a novel pulsed-CVD method, which is able to suppress completely the multi-layer patches during growth. This method shortens the check-list of remaining defects in graphene research, and leads to superior optical and electrical properties of CVD graphene.

We have then shown in chapter 2 that with the CVD-grown graphene, we are able to transfer it onto different kinds of substrates. The state-of-the-art flexible transparent electrodes were demonstrated. This chapter provides the most important technical basis for the rest of this thesis, since further sample fabrication and characterization is based on this chapter.

In chapter 3, we turned to the electronic measurements of graphene. The fundamental electronic properties are briefly introduced, such as the band structure, relationship between the theoretical DOS and measured field effect, etc. Both conventional oxide back-gate and the recently popular ionic gating on graphene are briefly introduced. We also spend some time describing the quantum Hall measurements of monolayer graphene, which is an important aspect of the electronic properties of graphene. The basic conceptions and formulas in this chapter are very useful for the further studies presented in chapter 5 and chapter 6.

Chapter 4 summarizes the most popular methods to clean graphene. Cleaning is a crucial technical problem in graphene studies, as graphene is a 2D electron gas usually open to the environment. It is easily contaminated and thus its electronic properties will be degraded. To have graphene as clean as possible is very challenging. We found that among many methods reported in the literature, acetic acid cleaning seems to be the most efficient way of cleaning graphene.

Chapter 5 actually makes the crossover from "clean" graphene to "dirty" graphene, in a controlled manner. We have discovered a new chemical way of inducing disorder in graphene by simply dipping graphene into $Na_2S_2O_8$. This enables us to have one more knob of tuning graphene properties, and opens the possibil-

ity of a variety of physics. With the disordered CVD graphene, we managed to achieve macroscopic graphene quantum device decorated with random network of Sn nanoparticles, showing superconductor-to-insulator transition.

In the last chapter of this thesis, we focus on the most important part of this thesis work: electrical properties in our CVD grown graphene decorated with a regular triangle array of Sn nanodisks. By comparing our experimental measurements to theoretical works, we have understood a new quantum metallic behaviour, which is induced by quantum phase fluctuations.

Here, the importance of our observation stems from the direct coupling between artificial superconducting array (with well-defined geometry by electron beam lithography) to a truly 2D diffusive metal whose resistance can be in-situ gate-tuned. In this new hybrid system, we realized a macroscopic superconducting state at high gate voltages, whose characteristic parameters such as BKT transition temperature, and critical supercurrent are in quantitative agreement with a recently developed theory based on the Usadel equation with no quantum phase fluctuations. Furthermore, the collapse of superconductivity at gate voltages closer to the Dirac point are qualitatively in agreement with the theory of a quantum-fluctuation-driven 2D superconductor-to-metal quantum phase transition.

Our experimental results demonstrate the existence of a metallic ground state terminating the 2D superconducting state, whose origin is for the first time experimentally proven to be quantum phase fluctuations, with the critical resistance not necessarily being $R_Q$(this gives a negative answer to the long-standing question: whether there is an universal critical resistance in QPT).

Moreover, we have shown that, when subjected to a small perpendicular magnetic field, our system exhibits a re-entrant superconductivity above the BCS-type $H_{c2}$. This suggests that the present system is a prototypical system for several kinds of quantum phase fluctuation theories.

As a final remark, by exploring the parameters along the full chain of graphene studies in this thesis, we are able to control from the raw material quality, to the sample fabrication and functionalization, the low temperature measurements. CVD grown graphene is shown to be very promising in both future industrial applications, and mesoscopic physics.

**Perspectives**

*Toward even better CVD graphene.*

As we have shown in chapter 1, three main defects, *i.e.*, grain boundaries, wrinkles, and multi-layer patches, are usually present in CVD grown graphene.

We have found the solution for preventing the third kind of defect from happening during growth, but there is still room to improve the quality of CVD graphene. The problem of grain boundaries has to be solved by reducing nucle-

ation density on the metal substrate. While the wrinkles are rather difficult to be fully removed. Ultra clean, single crystal graphene remains a challenging task.

However, real application of CVD may not be far. We believe that with high electrical and optical homogeneity, the pulsed-CVD graphene is going to help boost the future market for applications, in areas such as touch screen and flexible electrodes.

*Making graphene intrinsically superconducting.*

As we mentioned in chapter 6, graphene itself is expected to be superconducting via alkali metal doping - which is absolutely reasonable since graphite doped with alkali metal was found to be superconducting long time ago - yet no direct transport has been conducted in doped graphene or few-layer graphene.

It is highly interesting and promising that graphene will show stronger or more exotic superconductivity by either electrostatic doping or elemental doping. This is one perspective we would like to emphasize, because intrinsic superconducting graphene will provide us a new platform of correlated 2D electron gas, which is exposed to the environment, and probably retains the gate tunability.

*Proximity coupled arrays: more experiments.*

As described in the theory, less than one percent surface coverage by superconducting islands will be enough to induce global superconductivity in graphene. However, our arrays showed no superconductivity with diameters less than 100 nm, as discussed in Section 6.10.1. There might be some interface oxidation which causes poor Andreev conduction. We can vary the distance between islands to approach another limit with less than one percent surface coverage of Sn.

On the other hand, we also wonder how the system will behave if the graphene becomes ballistic, or strongly disordered. In the latter case, we expect a superconductor-metal-insulator phase transition, with clear three phases. And for the ballistic graphene case (for example graphene on h-BN, or suspended), the theory based on diffusive Usadel equations ceases to be valid. Therefore, completely new physics is expected.

*Probing the interface between graphene and superconducting islands.*

Due to technical difficulties, we can now only estimate the interface conductance between graphene and Sn nanoparticles via the resistance drop at around 3.6 K.

However, experimental observations are in principle feasible. As one can design such a system: suspend the graphene on a TEM grid, and then deposit Sn nanoparticles on one side of graphene. Then one can flip the sample and perform STM measurements on the other side. That is exactly the purpose of our Figure 2.10. This is going to be our future work to better understand our proximity coupled arrays.

# REFERENCE


[1] R. R. Nair, P. Blake, A. N. Grigorenko, K. S. Novoselov, T. J. Booth, T. Stauber, N. M. R. Peres, and A. K. Geim1, "Fine structure constant defines visual transparency of graphene," *Science*, vol. 320, p. 1308, 2008.

[2] K. S. Kim, Y. Zhao, H. Jang, S. Y. Lee, J. M. Kim, K. S. Kim, J. H. Ahn, P. Kim, J. Y. Choi, and B. H. Hong, "Large-scale pattern growth of graphene films for stretchable transparent electrodes," *Nature*, vol. 457, p. 706, 2009.

[3] B. J. Kim, H. Jang, S.-K. Lee, a.-H. A. Byung Hee Hong, and J. H. Cho, "High-performance flexible graphene field effect transistors with ion gel gate dielectrics," *NanoLett.*, vol. 10, p. 3464, 2010.

[4] S. Bae, H. K. Kim, Y. B. Lee, X. F. Xu, J. S. Park, Y. Zheng, J. Balakrishnan, T. Lei, H. R. Kim, Y. I. Song, Y. J. Kim, K. S. Kim, B. Ãzyilmaz, J. H. Ahn, B. H. Hong, and S. Iijima, "Roll-to-roll production of 30-inch graphene films for transparent electrodes," *Nature Nanotechnology*, vol. 5, pp. 574–578, 2010.

[5] Y. M. Lin, C. Dimitrakopoulos, K. A. Jenkins, D. B. Farmer, H. Y. Chiu, A. Grill, and P. Avouris, "100-ghz transistors from wafer-scale epitaxial graphene," *Science*, vol. 327, p. 662, 2010.

[6] B. Sensale-Rodriguez, R. Yan, M. M. Kelly, T. Fang, K. Tahy, W. S. Hwang, D. Jena, L. Liu, and H. G. Xing, "Broadband graphene terahertz modulators enabled by intraband transitions," *Nature Communication*, vol. 3, p. 780, 2011.

[7] L. G. D. Arco, Y. Zhang, C. W. Schlenker, K. Ryu, M. E. Thompson, and C. Zhou, "Continuous, highly flexible, and transparent graphene films by chemical vapor deposition for organic photovoltaics," *ACS Nano*, vol. 4, p. 2865, 2010.

[8] C. Chen, S. Rosenblatt, K. I. Bolotin, W. Kalb, P. Kim, I. Kymissis, H. L. Stormer, T. F. Heinz, and J. Hone, "Performance of monolayer graphene nanomechanical resonators with electrical readout," *Nature Nano.*, vol. 4, p. 861, 2009.

[9] K. S. Novoselov, A. K. Geim, S. V. Morozov, D. Jiang, M. I. Katsnelson, I. V. Grigorieva, S. V. Dubonos, and A. A. Firsov, "Two-dimensional gas of massless dirac fermions in graphene," *Nature*, vol. 438, p. 197, 2005.

[10] Y. Zhang, Y. Tan, H. L. Stormer, and P. Kim, "Experimental observation of the quantum hall effect and berry phase in graphene," *Nature*, vol. 438, p. 201, 2005.

[11] A. H. Castro Neto, N. M. R. F. Guinea, K. S. Peres, Novoselov, and A. K. Geim., "The electronic properties of graphene," *Reviews of Modern Physics*, vol. 81, p. 109, 2009.

[12] B. M. Kessler, "Tunable superconducting phase transition in metal-decorated graphene sheets," *Phys. Rev. Lett.*, vol. 104, p. 047001, 2010.

[13] A. Allain, "Electrical control of the superconducting-to-insulating transition in graphene metal hybrids," *Nat. Mat.*, vol. 11, p. 590, 2012.

[14] M. V. Feigel'man, M. A. Skvortsov, and K. S. Tikhonov, "Proximity-induced superconductivity in graphene," *JETP Lett.*, vol. 88, p. 862, 2008.

[15] X. S. Li, W. W. Cai, J. An, S. Kim, J. Nah, D. Yang, R. Piner, A. Velamakanni, I. Jung, E. Tutuc, S. K. Banerjee, L. Colombo, and R. S. Ruoff, "Large-area synthesis of high-quality and uniform graphene films on copper foils," *Science*, vol. 324, p. 1312, 2009.

[16] X. Li, W. W. Cai, L. Colombo, and R. S. Ruoff, "Evolution of graphene growth on ni and cu by carbon isotope labeling," *Nano Letter*, vol. 9, pp. 4268–4272, 2009.

[17] S. Nie, W. Wu, S. R. Xing, Q. K. Yu, S. S. Pei, and K. F. McCarty, "Growth from below: bilayer graphene on copper by chemical vapor deposition," *New J. Phys.*, vol. 14, p. 093028, 2012.

[18] B. S. Hu, H. Ago, Y. Ito, K. Kawahara, M. Tsuji, E. Magome, K. Sumitani, N. Mizuta, K. Ikeda, and S. Mizuno, "Epitaxial growth of large-area single-layer graphene over cu(1 1 1)/sapphire by atmospheric pressure cvd," *Carbon*, vol. 50, p. 57, 2012.

[19] J. Sun, M. T. C. Niclas Lindvall1, T. Wang, T. J. Booth, P. Boggild, K. B. K. Teo, J. Liu, and A. Yurgens, "Controllable chemical vapor deposition of large area uniform nanocrystalline graphene directly on silicon dioxide," *J. Appl. Phys.*, vol. 111, p. 044103, 2012.

[20] A. Ismach, C. Druzgalski, S. Penwell, A. Schwartzberg, M. Zheng, A. Javey, J. Bokor, and Y. Zhang, "Direct chemical vapor deposition of graphene on dielectric surfaces," *NanoLett*, vol. 10, p. 1542, 2010.

[21] M. Son, H. Lim, M. Hong, and H. C. Choi, "Direct growth of graphene pad on exfoliated hexagonal boron nitride surface," *NanoScale*, vol. 3, p. 3089, 2011.

[22] F. Bonaccorso, Z. Sun, T. Hasan, and A. C. Ferrari, "Graphene photonics and optoelectronics," *Nature Photonics*, vol. 4, p. 611, 2010.

[23] A. Cerf, T. Alava, R. A. Barton, and H. G. Craighead, "Transfer-printing of single dna molecule arrays on graphene for high-resolution electron imaging and analysis," *Nano Lett.*, vol. 11, p. 4232, 2011.

[24] R. R. Nair, H. A. Wu, P. N. Jayaram, I. V. Grigorieva, and A. K. Geim, "Unimpeded permeation of water through helium-leakâtight graphene-based membranes," *Science*, vol. 335, p. 442, 2012.

[25] M. Her, R. Beams, and L. Novotny, "Graphene transfer with reduced residue," *arXiv:1301.4106*, 2013.

[26] J. Moser, H. Tao, S. Roche, F. Alzina, C. M. S. Torres, and A. Bachtold, "Magnetotransport in disordered graphene exposed to ozone: From weak to strong localization," *Phys. Rev. B*, vol. 81, p. 205445, 2010.

[27] J.-H. Chen, L. Li, W. G. Cullen, E. D. Williams, and M. S. Fuhrer, "Tunable kondo effect in graphene with defects," *Nature Physics*, vol. 7, p. 535, 2011.

[28] A. Eckmann, A. Felten, A. Mishchenko, L. Britnell, R. Krupke, K. S. Novoselov, and C. Casiraghi, "Probing the nature of defects in graphene by raman spectroscopy," *Nano Lett.*, vol. 12, p. 3925, 2012.

[29] E. Abrahams, P. W. Anderson, D. C. Licciardello, and T. V. Ramakrishnan, "Scaling theory of localization: Absence of quantum diffusion in two dimensions," *Phys. Rev. Lett.*, vol. 42, p. 673, 1979.

[30] A. M. Goldman and N. Marković, "Superconductor-insulator transitions in the two-dimensional limit," *Physics Today*, vol. 51, p. 39, 1998.

[31] C. Christiansen, L. M. Hernandez, and A. M. Goldman, "Evidence of collective charge behavior in the insulating state of ultrathin films of superconducting metals," *Phys. Rev. Lett.*, vol. 88, p. 037004, 2002.

[32] N. Mason and A. Kapitulnik, "Dissipation effects on the superconductor-insulator transition in 2d superconductors," *Phys. Rev. Lett.*, vol. 82, p. 5341, 1999.

[33] H. S. J. van der Zant, W. J. Elion, L. J. Geerlings, and J. E. Mooij, "Quantum phase transitions in two dimensions: Experiments in josephson-junction arrays," *Phys. Rev. B*, vol. 54, p. 10081, 1996.

[34] M. V. Feigel'man and A. I. Larkin, "Quantum superconductorâmetal transition in a 2d proximity-coupled array," *Chem. Phys.*, vol. 235, p. 107, 1998.

[35] M. V. Feigel'man, A. I. Larkin, and M. A. Skvortsov, "Quantum phase transitions in disordered two-dimensional superconductors," *PRL*, vol. 86, p. 1869, 2001.

[36] S. Eley, "Approaching zero-temperature metallic states in mesoscopic superconductor-normal-superconductor arrays," *Nature Physics*, vol. 8, p. 59, 2011.

[37] S. Eley, S. Gopalakrishnan, P. M. Goldbart, and N. Mason, "Fate of global superconductivity in arrays of long sns junctions," *arXiv:1206.5999*, 2012.

[38] B. Spivak and F. Zhou, "Mesoscopic effects in disordered superconductors near $h_{c2}$," *Phys. Rev. Lett.*, vol. 74, p. 2800, 1995.

[39] K. S. Novoselov, V. I. Falko, L. Colombo, P. R. Gellert, M. G. Schwab, and K. Kim, "A roadmap for graphene," *Nature*, vol. 490, p. 192, 2012.

[40] D. R. Cooper, B. D'Anjou, N. Ghattamaneni, B. Harack, M. Hilke, A. Horth, N. Majlis, M. Massicotte, L. Vandsburger, E. Whiteway, and V. Yu, "Experimental review of graphene," *arXiv:1110.6557*, 2011.

[41] E. V. Rut'kov and N. R. Gall, "Physics and applications of graphene experimetnts," *Book Chapter*, vol. 11, 2011.

[42] K. S. Novoselov, D. Jiang, F. Schedin, T. J. Booth, V. V. Khotkevich, S. V. Morozov, and A. K. Geim, "Two-dimensional atomic crystals," *PNAS*, vol. 102, p. 10451, 2005.

[43] J. N. Coleman, "Liquid exfoliation of defect-free graphene," *Acc. Chem. Res.*, vol. 46, p. 14, 2013.

[44] H. Chen, W. Zhu, and Z. Zhang, "Contrasting behavior of carbon nucleation in the initial stages of graphene epitaxial growth on stepped metal surfaces," *Phys. Rev. Lett.*, vol. 104, p. 186101, 2010.

[45] X. Zhang, Q. H. Yuan, H. Shu, and F. Ding, "Mechanisms of graphene chemical vapor deposition (cvd) growth," *http://myweb.polyu.edu.hk/ tcfding/pdf/book-chapter-9-4.pdf*.

[46] S. J. Altenburg, J. Kroger, T. O. Wehling, B. Sachs, A. I. Lichtenstein, and R. Berndt, "Local gating of an ir(111) surface resonance by graphene islands," *Phys. Rev. Lett.*, vol. 108, p. 206805, 2012.

[47] T. Olsen, J. Yan, J. J. Mortensen, and K. S. Thygesen, "Dispersive and covalent interactions between graphene and metal surfaces from the random phase approximation," *Phys. Rev. Lett.*, vol. 107, p. 156401, 2011.

[48] R. B. McLellan *Scripta Met*, vol. 3, p. 389, 1969.

[49] R. Alfonso, X. Jia, J. Ho, D. Nezich, H. Son, V. Bulovic, M. S. Dresselhaus, and J. Kong, "Large area, few-layer graphene films on arbitrary substrates by chemical vapor deposition," *Nano Letter*, vol. 9, p. 30, 2009.

[50] T. Kobayashi, M. Bando, N. Kimura, K. Shimizu, K. Kadono, N. Umezu, K. Miyahara, S. Hayazaki, S. Nagai, Y. Mizuguchi, Y. Murakami, and D. Hobara, "Production of a 100-m-long high-quality graphene transparent conductive film by roll-to-roll chemical vapor deposition and transfer process," *Appl. Phys. Lett.*, vol. 102, p. 023112, 2013.

[51] P. Y. Huang, C. S. Ruiz-Vargas, A. M. van der Zande, W. S. Whitney, M. P. Levendorf, J. W. Kevek, S. Garg, J. S. Alden, C. J. Hustedt, Y. Zhu, J. Park, P. L. McEuen, and D. A. Muller *Nature*, vol. 469, p. 389, 2011.

[52] Q. K. Yu, L. A. Jauregui, W. Wu, R. Colby, J. Tian, Z. H. Su, H. L. Cao, Z. Z. Liu, D. Pandey, D. G. Wei, T. F. Chung, P. Peng, N. P. Guisinger, E. A. Stach, J. M. Bao, S. S. Pei, and Y. P. Chen *Nature Materials*, vol. 10, pp. 443–449, 2011.

[53] Z. Yan, J. Lin, Z. Peng, Z. Sun, Y. Zhu, L. Li, C. Xiang, E. L. Samuel, C. Kittrell, and J. M. Tour, "Toward the synthesis of wafer-scale single-crystal graphene on copper foils," *ACSnano*, vol. 6, p. 9110, 2012.

[54] X. Li, C. W. Magnuson, A. Venugopal, R. M. Tromp, J. M. Hannon, E. M. Vogel, L. Colombo, and R. S. Ruoff, "Large area graphene single crystals grown by low pressure chemical vapor deposition of methane on copper," *J. Am. Chem. Soc.*, vol. 133, p. 2816, 2011.

[55] H. Wang, G. Wang, P. Bao, S. Yang, W. Zhu, X. Xie, and W. J. Zhang, "Controllable synthesis of submillimeter single crystal monolayer graphene domains on copper foils by suppressing nucleation," *J. Am. Chem. Soc.*, vol. 134, p. 18476, 2012.

[56] Y. Zhang, L. Zhang, P. Kim, M. Ge, Z. Li, and C. Zhou, "Vapor trapping growth of single-crystalline graphene flowers: Synthesis, morphology, and electronic properties," *Nano Letter*, vol. 12, p. 2810, 2012.

[57] N. Petrone, C. R. Dean, I. Meric, A. M. van der Zande, P. Y. Huang, L. Wang, D. Muller, K. L. Shepard, and J. Hone, "Chemical vapor deposition-derived graphene with electrical performance of exfoliated graphene," *Nano Letter*, vol. 12, 2012.

[58] I. Vlassiouk, M. Regmi, P. Fulvio, S. Dai, P. Datskos, G. Eres, and S. Smirnov, "Role of hydrogen in chemical vapor deposition growth of large single-crystal graphene," *ACS Nano*, vol. 5, p. 6069, 2011.

[59] T. A. W. Jr and L. M. Sander, "Diffusion-limited aggregation, a kinetic critical phenomenon," *Phys. Rev. Lett.*, vol. 47, p. 1400, 1981.

[60] J. M. Wofford, S. Nie, K. F. McCarty, N. C. Bartelt, and O. D. Dubon, "Graphene islands on cu foils: The interplay between shape, orientation, and defects," *Nano Lett*, vol. 10, p. 4890, 2010.

[61] D. Geng, B. Wu, Y. Guo, L. Huang, Y. Xue, J. Chen, G. Yu, L. Jiang, W. Hu, and Y. Liu, "Uniform hexagonal graphene flakes and films grown on liquid copper surface," *Proc. Natl. Acad. Sci. USA*, vol. 109, p. 7992, 2012.

[62] C. Y. Su, A. Y. Lu, C. Y. Wu, Y. T. Li, K. K. Liu, W. Zhang, S. Y. Lin, Z. Y. Juang, Y. L. Zhong, F. R. Chen, and L. J. Li, "Direct formation of wafer scale graphene thin layers on insulating substrates by chemical vapor deposition," *NanoLett*, vol. 11, p. 3612, 2011.

[63] W. Wu, L. A. Jauregui, Z. Su, Z. Liu, J. Bao, Y. P. Chen, and Q. Yu, "Growth of single crystal graphene arrays by locally controlling nucleation on polycrystalline cu using chemical vapor deposition," *Adv. Mater.*, vol. 23, p. 4898, 2011.

[64] I. Vlassiouk, P. Fulvio, H. Meyer, N. Lavrik, S. Dai, P. Datskos, and S. Smirnov, "Large scale atmospheric pressure chemical vapor deposition of graphene," *Carbon*, vol. 54, p. 58, 2013.

[65] H. Brune *Surf. Sci. Rep.*, vol. 31, p. 121, 1998.

[66] A. T. Murdock, A. Koos, T. B. Britton, L. Houben, T. Batten, T. Zhang, A. J. Wilkinson, R. E. Dunin-Borkowski, C. E. Lekka, and N. Grobert, "Controlling the orientation, edge geometry, and thickness of chemical vapor deposition graphene," *ACS Nano*, vol. 7, p. 1351, 2013.

[67] X. Li, C. W. Magnuson, A. Venugopal, J. An, J. W. Suk, B. Y. Han, M. M. Borysiak, W. W. Cai, A. Velamakanni, Y. W. Zhu, L. F. Fu, E. M. Vogel, E. Voelkl, L. Colombo, and R. S. Ruoff, "Graphene films with large domain size by a two-step chemical vapor deposition process," *Nano Lett*, vol. 10, pp. 4328–4334, 2010.

[68] Y. S. Kim, J. H. Lee, S. K. Jerng, E. Kim, S. Seo, J. Jung, and S. H. Chun, "H2-free synthesis of monolayer graphene with controllable grain size by plasma enhanced chemical vapor deposition," *arXiv:1203.0816*, 2012.

[69] L. Gao, W. Ren, J. Zhao, L. P. Ma, Z. Chen, and H. M. Cheng, "Efficient growth of high-quality graphene films on cu foils by ambient pressure chemical vapor deposition," *Appl. Phys. Lett.*, vol. 97, p. 183109, 2010.

[70] M. Losurdo, M. M. Giangregorio, P. Capezzutoa, and G. Bruno *Physical Chemistry Chemical Physics*, vol. 13, p. 20836, 2011.

[71] J. Coraux, A. T. N'Diaye, C. Busse, and T. Michely, "Structural coherency of graphene on ir(111)," *Nano Lett.*, vol. 8, p. 565, 2008.

[72] D. C. Elias, R. R. Nair, T. M. G. Mohiuddin, S. V. Morozov, P. Blake, M. P. Halsall, A. C. Ferrari, D. W. Boukhvalov, M. I. Katsnelson, A. K. Geim, and K. S. Novoselov, "Control of graphene's properties by reversible hydrogenation: Evidence for graphane," *Science*, vol. 323, p. 5914, 2009.

[73] S. Choubak, M. Biron, P. L. Levesque, R. Martel, and P. Desjardins, "No graphene etching in purified hydrogen," *J. Phys. Chem. Lett.*, vol. 4, p. 1100, 2013.

[74] N. Reckinger, A. Felten, C. N. Santos, B. Hackens, and J.-F. Colomer, "The influence of residual oxygen on the synthesis of graphene by atmospheric pressure chemical vapor deposition," *arXiv:1303.3951*.

[75] M. C. Schabel and J. L. Martins, "Energetics of interplanar binding in graphite," *Physics Review B*, vol. 46, p. 7185, 1992.

[76] L. Xie, L. Jiao, and H. Dai, "Selective etching of graphene edges by hydrogen plasma," *J. Am. Chem. Soc.*, vol. 132, p. 14751, 2010.

[77] Y. Zhang, Z. Li, P. Kim, L. Y. Zhang, and C. W. Zhou, "Anisotropic hydrogen etching of chemical vapor deposited graphene," *ACSnano*, vol. 6, pp. 126–132, 2012.

[78] D. Geng, B. Wu, Y. Guo, B. Luo, Y. Xue, J. Chen, G. Yu, and Y. Liu*, "Fractal etching of graphene," *JACS*, vol. dx.doi.org/10.1021/ja402224h, 2013.

[79] P. Nemes-Incze, G. Magda, K. Kamarás, and L. P. Biró, "Crystallographically selective nanopatterning of graphene on sio2," *Nano Res.*, vol. 3, p. 110, 2010.

[80] K. Kim, V. I. Artyukhov, W. Regan, Y. Liu, M. F. Crommie, B. I. Yakobson, and A. Zettl, "Ripping graphene: Preferred directions," *NanoLett*, vol. 12, p. 293, 2011.

[81] L. Gao, W. Ren, H. Xu, L. Jin, Z. Wang, T. Ma, L.-P. Ma, Z. Zhang, Q. Fu, L.-M. Peng, X. Bao, and H.-M. Cheng, "Repeated growth and bubbling transfer of graphene with millimetre-size single-crystal grains using platinum," *Nature Communications*, vol. 3, p. 699, 2012.

[82] J. Coraux, A. T. N'Diaye1, M. Engler1, C. Busse, D. Wall, N. Buckanie, F.-J. M. zu Heringdorf, R. van Gastel, B. Poelsema, and T. Michely, "Growth of graphene on ir(111)," *New J. Phys.*, vol. 11, p. 023006, 2009.

[83] T. Oznuluer, E. Pince, E. O. Polat, O. Balci, O. Salihoglu, and C. Kocabas, "Synthesis of graphene on gold," *Appl. Phys. Lett.*, vol. 98, p. 183101, 2011.

[84] M. Wang, S. K. Jang, W. J. Jang, M. Kim, S. Y. Park, S.-W. Kim, S.-J. Kahng, J.-Y. Choi, R. S. Ruoff, Y. J. Song, and S. Lee, "A platform for large-scale graphene electronics cvd growth of single-layer graphene on cvd-grown hexagonal boron nitride," *Adv. Mater.*, vol. 25, p. 2746, 2013.

[85] H. Kim, I. Song, C. Park, M. Son, M. Hong, Y. Kim, J. S. Kim, H.-J. Shin, J. Baik, and H. C. Choi, "Copper-vapor-assisted chemical vapor deposition for high-quality and metal-free single-layer graphene on amorphous $sio_2$ substrate," *ACS Nano*, vol. 7, p. 6575, 2013.

[86] J. Chen, Y. Guo, Y. Wen, L. Huang, Y. Xue, D. Geng, B. Wu, B. Luo, G. Yu, and Y. Liu, "Two-stage metal-catalyst-free growth of high-quality polycrystalline graphene films on silicon nitride substrates," *Advanced Materials*, vol. 25, p. 992, 2013.

[87] S. C. Xu, B. Y. Man, S. Z. Jiang, C. S. Chen, C. Yang, M. Liu, X. G. Gao, Z. C. Suna, and C. Zhang, "Direct synthesis of graphene on sio2 substrates by chemical vapor deposition," *CrystEngComm*, vol. 15, p. 1840, 2013.

[88] H. Medina, Y.-C. Lin, C. Jin, C.-C. Lu, C.-H. Yeh, K.-P. Huang, K. Suenaga, J. Robertson, and P.-W. Chiu, "Metal-free growth of nanographene on silicon oxides for transparent conducting applications," *Advanced Functional Materials*, vol. 22, p. 2123, 2012.

[89] C. S. Lee, C. S. Cojocaru, W. Moujahid, B. Lebental, M. Chaigneau, a. L. N. Marc Chatelet, and J.-L. Maurice, "Synthesis of conducting transparentfew-layer graphene directly on glass at 450°c," *Nanotechnology*, vol. 23, p. 265603, 2012.

[90] M. A. Fanton, J. A. Robinson, C. Puls, Y. Liu, M. J. Hollander, B. E. Weiland, M. LaBella, K. Trumbull, R. Kasarda, C. Howsare, J. Stitt, and D. W. Snyder,

"Characterization of graphene films and transistors grown on sapphire by metal-free chemical vapor deposition," *ACSnano*, vol. 5, p. 8062, 2011.

[91] H. J. Song, M. Son, C. Park, H. Lim, M. P. Levendorf, A. W. Tsen, J. Park, and H. C. Choi, "Large scale metal-free synthesis of graphene on sapphire and transfer-free device fabrication," *Nanoscale*, vol. 4, p. 3050, 2012.

[92] Z. Yan, Z. Peng, Z. Sun, J. Yao, Y. Zhu, Z. Liu, P. M. Ajayan, and J. M. Tour, "Growth of bilayer graphene on insulating substrates," *ACSnano*, vol. 10, p. 8187, 2011.

[93] W. Yang, G. Chen, Z. Shi, C.-C. Liu, L. Zhang, G. Xie, M. Cheng, D. Wang, R. Yang, D. Shi, K. Watanabe, T. Taniguchi, Y. Yao, Y. Zhang, and G. Zhang, "Epitaxial growth of single-domain graphene on hexagonal boron nitride," *Natiure Materials*, vol. doi:10.1038/nmat3695, 2013.

[94] W. Zhu, T. Low, V. Perebeinos, A. A. Bol, Y. Zhu, H. Yan, J. Tersoff, and P. Avouris, "Structure and electronic transport in graphene wrinkles," *Nano Letter*, vol. 12, p. 3431, 2012.

[95] V. E. Calado, G. F. Schneider, A. M. M. G. Theulings, C. Dekker, and L. M. K. Vandersypen *Appl. Phys. Lett*, vol. 101, p. 103116, 2012.

[96] K. Yan, H. L. Peng, H. Zhou, H. Li, and Z. F. Liu *Nano Letter*, vol. 11, pp. 1106–1110, 2011.

[97] H.-Y. Chiu, V. Perebeinos, Y.-M. Lin, and P. Avouris *Nano Letter*, vol. 10, p. 4634, 2010.

[98] Y. Kim, H. Yun, S.-G. Nam, M. Son, D. S. Lee, D. C. Kim, S. Seo, H. C. Choi, H.-J. Lee, S. W. Lee, and J. S. Kim *arXiv*, p. 1206.3410, 2012.

[99] B. Wang and M.-L. Bocquet, "Interfacial coupling in rotational monolayer and bilayer graphene on ru(0001) from first principles," *Nanoscale*, vol. 4, p. 4687, 2012.

[100] O. Taisuke, A. Bostwick, J. L. McChesney, T. Seyller, and e. E. R. Karsten Horn *Physics Review Letter*, vol. 98, p. 206802, 2007.

[101] J. Hass, F. Varchon, J. E. Millan-Otoya, M. Sprinkle, N. Sharma, W. A. de Heer, C. Berger, P. N. First, L. Magaud, and E. H. Conrad, "Why multilayer graphene on 4h-sic(0001̀ ) behaves like a single sheet of graphene," *Physics Review Letter*, vol. 100, p. 125504, 2008.

[102] E. J. Mele, "Interlayer coupling in rotationally faulted multilayer graphenes," *J. Phys. D: Appl. Phys.*, vol. 45, p. 154004, 2012.

[103] P. Venezuela, M. Lazzeri, and F. Mauri *Phys. Rev. B*, vol. 84, p. 035433, 2011.

[104] F. Han, G. H.; Gunes, J. J. Bae, E. S. Kim, S. J. Chae, H.-J. Shin, J.-Y. Choi, D. Pribat, and Y. H. Lee *Nano Lett*, vol. 11, pp. 4144–4148, 2011.

[105] I. Khrapach, F. Withers, T. H. Bointon, D. K. Polyushkin, W. L. Barnes, S. Russo, and M. F. Craciun, "Novel highly conductive and transparent graphene-based conductors," *Adv. Mat.*, vol. 24, p. 2844, 2012.

[106] K. S. Novoselov, A. K. Geim1, S. V. Morozov, D. Jiang, Y. Zhang, S. V. Dubonos, I. V. Grigorieva, and A. A. Firsov, "Electric field effect in atomically thin carbon films," *Science*, vol. 306, p. 666, 2004.

[107] C. Lee, X. Wei, J. W. Kysar, and J. Hone, "Measurement of the elastic properties and intrinsic strength of monolayer graphene," *Science*, vol. 321, p. 385, 2008.

[108] A. M. van der Zande, R. A. Barton, J. S. Alden, C. S. Ruiz-Vargas, W. S. Whitney, P. H. Q. Pham, J. Park, J. M. Parpia, H. G. Craighead, and P. L. McEuen, "Large-scale arrays of single-layer graphene resonators," *Nano Lett.*, vol. 10, p. 4869, 2010.

[109] M. Liu, X. Yin, E. Ulin-Avila, B. Geng, T. Zentgraf, L. Ju, F. Wang, and X. Zhang, "A graphene-based broadband optical modulator," *Nature*, vol. 474, p. 64, 2011.

[110] A. Reserbat-Plantey, L. Marty, O. Arcizet, N. Bendiab, and V. Bouchiat, "A local optical probe for measuring motion and stress in a nanoelectromechanical system," *Nature Nano.*, vol. 7, p. 151, 2012.

[111] M. Lopes, A. Candini, M. Urdampilleta, A. Reserbat-Plantey, V. Bellini, S. Klyatskaya, L. Marty, M. Ruben, M. Affronte, W. Wernsdorfer, and N. Bendiabâ *ACSNano*, vol. 4, 2010.

[112] C. Chung, Y.-K. Kim, D. Shin, S.-R. Ryoo, B. H. Hong, and D.-H. Min, "Biomedical applications of graphene and graphene oxide," *Acc. Chem. Res.*, vol. DOI: 10.1021/ar300159f, 2013.

[113] P. Nguyen and V. Berry, "Graphene interfaced with biological cells: Opportunities and challenges," *J. Phys. Chem. Lett.*, vol. 3, p. 1024, 2012.

[114] S. Garaj, W. Hubbard, A. Reina, J. Kong, D. Branton, and J. A. Golovchenko, "Graphene as a sub-nanometer trans-electrode membrane," *Nature*, vol. 467, p. 190, 2010.

[115] D. Prasai, J. C. Tuberquia, R. R. Harl, G. K. Jennings, and K. I. Bolotin, "Graphene: Corrosion-inhibiting coating," *ACS Nano*, vol. 6, p. 1102, 2012.

[116] C. R. Dean, A.F.Young, I.Meric, C.Lee, L.Wang, S.Sorgenfrei, K.Watanabe, T.Taniguchi, P. Kim, K.L.Shepard, and J. Hone *Nature Nano.*, vol. 5, p. 722, 2010.

[117] C. R. Dean, L. Wang, P. Maher, C. Forsythe, F. Ghahari, Y. Gao, J. Katoch, M. Ishigami, P. Moon, M. Koshino, T. Taniguchi, K. Watanabe, K. L. Shepard, J. Hone, and P. Kim, "Hofstadter butterfly and the fractal quantum hall effect in moire superlattices," *Nature*, vol. 497, p. 598, 2013.

[118] R. V. Gorbachev, A. K. Geim, M. I. Katsnelson, K. S. Novoselov, T. Tudorovskiy, I. V. Grigorieva, A. H. MacDonald, S. V. Morozov, K. Watanabe, T. Taniguchi, and L. A. Ponomarenko, "Strong coulomb drag and broken symmetry in double-layer graphene," *Nature Physics*, vol. 8, p. 896, 2012.

[119] V. P. Gusynin, S. G. Sharapov, and J. P. Carbotte, "Unusual microwave response of dirac quasiparticles in graphene," *Phys. Rev. Lett.*, vol. 96, p. 256802, 2006.

[120] T. Stauber, N. M. R. Peres, and A. K. Geim, "Optical conductivity of graphene in the visible region of the spectrum," *Phys. Rev. B*, vol. 78, p. 085432, 2008.

[121] K. F. Mak, M. Y. Sfeir, Y. Wu, C. H. Lui, J. A. Misewich, and T. F. Heinz, "Measurement of the optical conductivity of graphene," *Phys. Rev. Lett.*, vol. 101, p. 196405, 2008.

[122] P. Blake, E. W. Hill1, A. H. C. Neto, K. S. Novoselov, D. Jiang, R. Yang, T. J. Booth, and A. K. Geim, "Making graphene visible," *Appl. Phys. Lett.*, vol. 91, p. 063124, 2007.

[123] F. Wang, Y. Zhang, C. Tian, C. Girit, A. Zettl, M. Crommie, and Y. R. Shen, "Gate-variable optical transitions in graphene," *Science*, vol. 320, p. 206, 2008.

[124] E. H. Lock, M. Baraket, M.Laskoski, S. P. Mulvaney, W. K. Lee, P. E. Sheehan, D. R. Hines, J. T. Robinson, J. Tosado, M. S. Fuhrer, S. C. Hernandez, and S. G. Walton, "High-quality uniform dry transfer of graphene to polymers.," *NanoLett.*, vol. 12, p. 102, 2011.

[125] H. Cao, Q. Yu, L. A. Jauregui, J. Tian, W. Wu, Z. Liu, R. Jalilian, D. K. Benjamin, Z. Jiang, J. Bao, S. S. Pei, and Y. P. Chen *Appl. Phys. Lett.*, vol. 96, p. 25, 2010.

[126] K. Kim, S. C. L. Tan, W. Regan, J. Yuk, E. Chatterjee, M. Crommie, M. Cohen, S. Louie, and A. Zettl, "Raman spectroscopy study of rotated double-layer graphene: misorientation-angle dependence of electronic structure," *Phys. Rev. Lett.*, vol. 108, p. 246103, 2012.

[127] L. Malard, M. Pimentaa, G. Dresselhausb, and M. Dresselhaus, "Raman spectroscopy in graphene," *Physics Reports*, vol. 473, p. 51, 2009.

[128] A. C. Ferrari and D. M. Basko, "Raman spectroscopy as a versatile tool for studying the properties of graphene," *Nature Nanotechnology*, vol. 8, p. 235, 2013.

[129] G. G. Samsonidze, E. B. Barros, R. Saito, J. Jiang, G. Dresselhaus, and M. S. Dresselhaus. *Phys. Rev. B*, vol. 75, p. 155420, 2007.

[130] L. M. Moreira, "Raman spectroscopy of graphene: probing phonons, electrons and electron-phonon interactions," *PhD Thesis*, 2009.

[131] A. Das, S. Pisana, B. Chakraborty, S. Piscanec, S. K. Saha, U. V. Waghmare, K. S. Novoselov, H. R. Krishnamurthy, A. K. Geim, A. C. Ferrari, and A. K. Sood, "Monitoring dopants by raman scattering in an electrochemically top-gated graphene transistor," *Nature Nano.*, vol. 3, p. 210, 2008.

[132] A. Das, B. Chakraborty, S. Piscanec, S. Pisana, A. K. Sood, and A. C. Ferrari, "Phonon renormalisation in doped bilayer graphene," *Phys. Rev. B*, vol. 79, p. 155417, 2009.

[133] C. Casiraghi, S. Pisana, K. S. Novoselov, A. K. Geim, and A. C. Ferrari, "Raman fingerprint of charged impurities in graphene," *Appl. Phys. Lett.*, vol. 91, p. 233108, 2007.

[134] J. Yan, Y. Zhang, P. Kim, and A. Pinczuk, "Electric field effect tuning of electron-phonon coupling in graphene," *Phys. Rev. Lett.*, vol. 98, p. 166802, 2007.

[135] D. Yoon, Y. W. Son, and H. Cheong, "Strain-dependent splitting of double resonance raman scattering band in graphene," *Phys. Rev. Lett.*, vol. 106, p. 155502, 2011.

[136] M. Huang, Y. Hugen, T. F. Heinz, and J. Hone, "Probing strain induced electronic structure change in graphene by raman spectroscopy.," *Nano Lett.*, vol. 10, p. 4074, 2010.

[137] C. H. Lui, Z. Li, Z. Chen, P. V. Klimov, L. E. Brus, and T. F. Heinz *Nano Letter*, vol. 11, 2011.

[138] M. Kalbac, H. Farhat, J. Kong, P. Janda, L. Kavan, and M. S. Dresselhaus, "Raman spectroscopy and in situ raman spectroelectrochemistry of bilayer 12c/13c graphene," *NanoLett.*, vol. 11, p. 1957, 2011.

[139] S. J. Haigh, A. Gholinia, R. Jalil, S. Romani, L. Britnell, D. C. Elias, K. S. Novoselov, L. A. Ponomarenko, A. K. Geim, and R. Gorbachev, "Cross-sectional imaging of individual layers and buried interfaces of graphene-based heterostructures and superlattices," *Nature Materials*, vol. 11, p. 764, 2012.

[140] Z. Liu, L. Ma, G. Shi, W. Zhou, Y. Gong, S. Lei, X. Yang, J. Zhang, J. Yu, K. P. Hackenberg, A. Babakhani, J.-C. Idrobo, R. Vajtai, J. Lou, and P. M. Ajayan, "In-plane heterostructures of graphene and hexagonal boron nitride with controlled domain sizes," *Nature Nanotechnology*, vol. 8, p. 119, 2013.

[141] M. P. Levendorf, Cheol-JooKim, L. Brown, P. Y.Huang, R. Havener, D. A. Muller, and JiwoongPark, "Graphene and boron nitride lateral heterostructures for atomically thin circuitry," *Nature*, vol. 488, p. 627, 2012.

[142] J. M. Yuk, K. Kim, B. Aleman, W. Regan, J. H. Ryu, J. Park, P. Ercius, H. M. Lee, A. P. Alivisatos, M. F. Crommie, J. Y. Lee, and A. Zettl, "Graphene veils and sandwiches," *Nano Lett.*, vol. 11, p. 3290, 2011.

[143] D.-H. Chae, D. Zhang, X. Huang, and K. von Klitzing, "Electronic transport in two stacked graphene monolayers," *Nano Lett.*, vol. 12, p. 3905, 2012.

[144] R. W. Havener, H. Zhuang, L. Brown, R. G. Hennig, and J. Park, "Angle-resolved raman imaging of interlayer rotations and interactions in twisted bilayer graphene," *Nano Lett.*, vol. 12, p. 3162, 2012.

[145] M. S. Dresselhaus and G. Dresselhaus, "Intercalation compounds of graphite," *Advances in Physics*, vol. 51, p. 1, 2002.

[146] R. Heyrovska, "Atomic structures of graphene, benzene and methane with bond lengths as sums of the single, double and resonance bond radii of carbon," *arXiv:0804.4086*, 2008.

[147] P. R. Wallace, "The band theory of graphite," *Phys. Rev.*, vol. 71, p. 622, 1947.

[148] D. R. Cooper, B. D'Anjou, N. Ghattamaneni, B. Harack, M. Hilke, A. Horth, N. Majlis, M. Massicotte, L. Vandsburger, E. Whiteway, and V. Yu *ISRN Condensed Matter Physics*, vol. 2012, p. 501686, 2012.

[149] F. D. M. Haldane, "Model for a quantum hall effect without landau levels: Condensed-matter realization of the "parity anomaly"," *Phys. Rev. Lett.*, vol. 61, p. 2015, 1988.

[150] J. W. McClure, "Diamagnetism of graphite," *Phys. Rev.*, vol. 104, p. 666, 1956.

[151] J. C. Slonczewski and P. R. Weiss, "Band structure of graphite," *Phys. Rev.*, vol. 109, p. 272, 1958.

[152] M. I. Katsnelson, "Graphene: carbon in two dimensions," *Materials Today*, vol. 10, p. 20, 2007.

[153] "Band structure of graphene, massless dirac fermions as low-energy quasiparticles, berry phase, and all that," *https://wiki.physics.udel.edu*.

[154] M. Pashangpour and V. Ghaffari, "Investigation of structural and electronic transport properties of graphene and graphane using maximally localized wannier functions," *J. Theor. Appl. Phys.*, vol. 7, p. 1, 2013.

[155] Y. Gaoa and Z. Yuan, "Anisotropic low-energy plasmon excitations in doped graphene: An ab initio study," *Solid State Communications*, vol. 151, p. 1009, 2011.

[156] K. S. Novoselov, S. V. Morozov, T. M. G. Mohinddin, L. A. Ponomarenko, D. C. Elias, R. Yang, I. I. Barbolina, P. Blake, T. J. Booth, D. Jiang, J. Giesbers, E. W. Hill, and A. K. Geim, "Electronic properties of graphene," *phys. stat. sol. (b)*, vol. 11, p. 4106, 2007.

[157] Website *http://phelafel.technion.ac.il/ tzipora/theory.html*.

[158] D. Berdebes, T. Low, and M. Lundstrom, "Lecture notes on low bias transport in graphene: An introduction," *NCN@Purdue Summer School: Electronics from the Bottom Up*, 2009.

[159] G. Zebrev, "Graphene field effect transistors: Diffusion-drift theory," *Physics and Applications of Graphene - Theory, Edited by Dr. Sergey Mikhailov*, vol. Chapter 23, p. 478, 2011.

[160] E. H. Hwang, S. Adam, and S. D. Sarma, "Carrier transport in two-dimensional graphene layers," *Phys. Rev. Lett.*, vol. 98, p. 186806, 2007.

[161] J. Martin, N. Akerman, G. Ulbricht, T. Lohmann, J. H. Smet, K. von Klitzing, and A. Yacoby, "Observation of electronâhole puddles in graphene using a scanning single-electron transistor," *Nature Physics*, vol. 4, p. 144, 2008.

[162] S. D. Sarma, S. Adam, E. H. Hwang, and E. Rossi, "Electronic transport in two dimensional graphene," *arxiv:1003.4731v2*, 2010.

[163] Y. Wu, V. Perebeinos, Y. ming Lin, T. Low, F. Xia, and P. Avouris, "Quantum behavior of graphene transistors near the scaling limit," *NanoLett*, vol. 12, p. 1417, 2012.

[164] J. Wang and L. M *IEEE Trans. Elec. Dev.*, vol. 50, p. 1604, 2003.

[165] M. S. Shur *IEEE EDL*, vol. 23, p. 511, 2002.

[166] F. Xia, V. Perebeinos, Y.-M. Lin, Y. Wu, and P. Avouris, "The origins and limits of metal graphene junction resistance," *Nature Nano*, vol. 6, p. 179, 2011.

[167] M. Lee, J. R. Williams, S. Zhang, C. D. Frisbie, and D. Goldhaber-Gordon *Phys. Rev. Lett.*, vol. 107, p. 256601, 2011.

[168] U. et al, "Electric-field-induced superconductivity in an insulator," *Nature mat.*, vol. 7, p. 855, 2008.

[169] K. Ueno, S. Nakamura, H. Shimotani, H. T. Yuan, N. Kimura, T. Nojima, H. Aoki, Y. Iwasa, and M. Kawasaki, "Discovery of superconductivity in ktao3 by electrostatic carrier doping," *Nature Nanotech.*, vol. 6, p. 408, 2011.

[170] A. T. Bollinger, G. Dubuis, J. Yoon, D. Pavuna, J. Misewich, and I. Bozovic, "Superconductorâinsulator transition in la2âxsrxcuo4 at the pair quantum resistance," *Nature*, vol. 472, p. 458, 2011.

[171] X. Shi, G. Logvenov, A. T. Bollinger, I. Bozovic, C. Panagopoulos, and D. Popovic, "Emergence of superconductivity from the dynamically heterogeneous insulating state in la2âxsrxcuo4," *Nature mat.*, vol. 12, p. 47, 2013.

[172] J. T. Ye, S. Inoue, K. Kobayashi, Y. Kasahara, H. T. Yuan, H. Shimotani, and Y. Iwasa, "Liquid-gated interface superconductivity on an atomically flat film," *Nature Mat.*, vol. 9, p. 125, 2010.

[173] J. T. Ye, Y. J. Zhang, R. Akashi, M. S. Bahramy, R. Arita1, and Y. Iwasa, "Superconducting dome in a gate-tuned band insulator," *Science*, vol. 338, p. 1193, 2012.

[174] K. Taniguchi, A. Matsumoto, H. Shimotani, and H. Takagi, "Electric-field-induced superconductivity at 9.4âk in a layered transition metal disulphide mos2," *Appl. Phys. Lett.*, vol. 101, p. 042603, 2012.

[175] R. Nandkishore, L. S. Levitov, and A. V. Chubukov, "Chiral superconductivity from repulsive interactions in doped graphene," *Nature Physics*, vol. 8, p. 158, 2012.

[176] D. K. Efetov and P. Kim *Phys. Rev. Lett.*, vol. 105, p. 256805, 2010.

[177] J. Yea, M. F. Craciunc, M. Koshinod, S. Russoe, S. Inouea, H. Yuana, H. Shimotania, A. F. Morpurgof, and Y. Iwasa, "Accessing the transport properties of graphene and its multilayers at high carrier density," *PNAS*, vol. 108, p. 13002, 2010.

[178] A. Newaz, Y. S. Puzyrev, B. Wang, S. T. Pantelides, and K. I. Bolotin, "Probing charge scattering mechanisms in suspended graphene by varying its dielectric environment," *Nature Communications*, vol. 3, p. 734, 2012.

[179] E. Uesugi, H. Goto, R. Eguchi, A. Fujiwara, and Y. Kubozono, "Electric double-layer capacitance between an ionic liquid and few-layer graphene," *Scientific Reports*, vol. 3, p. 1595, 2013.

[180] D. D. M. Tortello, A. Sola, K. Sharda, M. Brunam, J. R. Nair, C. Gerbaldi, and R. S. GOnnelli, "Large control of surface carrier density by electrochemical gating with a novel polymer electrolyte solution," *Conference Abstract*, 2013.

[181] E. Hall, "On a new action of the magnet on electric currents," *American Journal of Mathematics*, vol. 2, p. 287, 1879.

[182] D. Tsui, H. Stormer, and A. Gossard, "Two-dimensional magnetotransport in the extreme quantum limit," *Phys. Rev. Lett.*, vol. 48, p. 1559, 1982.

[183] S. Oh, "The complete quantum hall trio," *Science*, vol. 340, p. 153, 2013.

[184] J. E. Avron, D. Osadchy, and R. Seiler, "A topological look at the quantum hall effect," *Physics Today*, p. 38, 2003.

[185] M. Buttiker, "Absence of backscattering in the quantum hall effect in multiprobe conductors," *Phys. Rev. B*, vol. 38, p. 9375, 1988.

[186] M. O. Goerbig, "Quantum hall effects," *Book Chapter*, vol. Chpt. 3, p. 44, 2009.

[187] D. Yoshioka, "The quantum hall effect," *Springer*, 2002.

[188] H. A. Fertig, "Viewpoint: A view from the edge," *Physics*, vol. 2, p. 15, 2009.

[189] *http://www.sciencegl.com/3dsurf/shots/e3dmap/SPMelectronmap.html.*

[190] G. Finkelstein, P. I. Glicofridis, R. C. Ashoori, and M. Shayegan, "Topographic mapping of the quantum hall liquid using a few-electron bubble," *Science*, vol. 289, p. 90, 2000.

[191] M. I. Katsnelson, "Graphene: Carbon in two dimensions,"

[192] K. S. Novoselov, E. McCann, S. V. Morozov, V. I. Fal'ko, M. I. Katsnelson, U. Zeitler, D. Jiang, F. Schedin, and A. K. Geim, "Unconventional quantum hall effect and berryâs phase of 2Ï in bilayer graphene," *Nature Physics*, vol. 2, p. 177, 2006.

[193] E. Y. Andrei, G. Li, and X. Du, "Electronic properties of graphene: a perspective from scanning tunneling microscopy and magnetotransport," *Rep. Prog. Phys.*, vol. 75, p. 056501, 2012.

[194] K. I. Bolotin, F. Ghahari, M. D. Shulman, H. L. Stormer, and P. Kim, "Observation of the fractional quantum hall effect in graphene," *Nature*, vol. 462, p. 199, 2009.

[195] C. R. Dean, A. F. Young, P. Cadden-Zimansky, L. Wang, H. Ren, K. Watanabe, T. Taniguchi, P. Kim, J. Hone, and K. L. Shepard, "Multicomponent fractional quantum hall effect in graphene," *Nature Physics*, vol. 7, p. 693, 2011.

[196] K. S. Novoselov, Z. Jiang, Y. Zhang, S. V. Morozov, H. L. Stormer, U. Zeitler, J. C. Maan, G. S. Boebinger, P. Kim, and A. K. Geim, "Room-temperature quantum hall effect in graphene," *Science*, vol. 315, p. 1379, 2007.

[197] A. Tzalenchuk, S. Lara-Avila, A. Kalaboukhov, S. Paolillo, M. Syvajarvi, R. Yakimova, O. Kazakova, T. J. B. M. Janssen, V. Fal'ko, and S. Kubatkin, "Towards a quantum resistance standard based on epitaxial graphene," *Nature Nanotechnology*, vol. 5, p. 186, 2010.

[198] T. Shen1, W. Wu, Q. Yu, C. A. Richter, R. Elmquist, D. Newell, and Y. P. Chen, "Quantum hall effect on centimeter scale chemical vapor deposited graphene films," *Appl. Phys. Lett.*, vol. 99, p. 232110, 2011.

[199] M. O. Goerbig, J.-N. Fuchs, K. Kechedzhi, and V. I. Fal'ko *Phys. Rev. Lett.*, vol. 99, p. 087402, 2007.

[200] S. Piscanec, M. Lazzeri, F. Mauri, A. C. Ferrari, and J. Robertson, "Kohn anomalies and electron-phonon interactions in graphite," *Phys. Rev. Lett.*, vol. 93, p. 185503, 2004.

[201] V. Popov, "Non-adiabatic phonon dispersion of graphene," *Bulg. J. Phys.*, vol. 38, p. 72, 2011.

[202] J. Yan, Y. Zhang, P. Kim, and A. Pinczuk, "Electric
field effect tuning of electronphonon coupling in graphene.," *Phys. Rev. Lett.*, vol. 98, p. 166802, 2007.

[203] T. Ando, "Magnetic oscillation of optical phonon in graphene," *J. Phys. Soc. Jpn.*, vol. 76, p. 024712, 2007.

[204] P. Kossacki, C. Faugeras, M. Kuhne, M. Olita, A. Mahmood, E. Dujardin, R. R. Nair, A. K. Geim, and M. Potemski, "Circular dichroism of magnetophonon resonance in doped graphene," *Phys. Rev. B*, vol. 86, p. 205431, 2012.

[205] O. Kashuba and V. I. Fal'ko *Phys. Rev. B*, vol. 80, p. 241404(R), 2009.

[206] C. Faugeras, M. Amado, P. Kossacki, M. Orlita, M. Kuhne, A. A. L. Nicolet, Y. I. Latyshev, and M. Potemski, "Magneto-raman scattering of graphene on graphite: Electronic and phonon excitations," *Phys. Rev. Lett.*, vol. 107, p. 036807, 2011.

[207] J. Yan, S. Goler, T. D. Rhone, M. Han, R. He, P. Kim, V. Pellegrini, and A. Pinczuk, "Observation of magnetophonon resonance of dirac fermions in graphite," *Phys. Rev. Lett.*, vol. 105, p. 227401, 2010.

[208] A. M. Goossens, V. E. Calado, A. Barreiro, K. Watanabe, T. Taniguchi, and L. M. K. Vandersypen *Appl. Phys. Lett.*, vol. 100, p. 073110, 2012.

[209] N. Lindvall, A. Kalabukhov, and A. Yurgens *J. Appl. Phys.*, vol. 111, p. 064904, 2012.

[210] Y.-C. Lin, C.-C. Lu, C.-H. Yeh, C. Jin, K. Suenaga, and P.-W. Chiu, "Graphene annealing: How clean can it be?," *Nano Lett.*, vol. 12, p. 414, 2012.

[211] J. Moser, A. Barreiro, and A. Bachtold, "Current-induced cleaning of graphene," *Appl. Phys. Lett.*, vol. 94, p. 163513, 2007.

[212] X. L. Liang, B. A. Sperling, I. Calizo, G. J. Cheng, C. A. Hacker, Q. Zhang, Y. Obweng, K. Yan, H. L. Peng, Q. L. Li, X. X. Zhu, A. R. H. Yuan, Walker, Z. F. Liu, L. M. Peng, and C. A. Richter *ACSnano*, vol. 5, pp. 9144–9153, 2011.

[213] L. Britnell, R. V. Gorbachev, R. Jalil, B. D. Belle, F. Schedin, A. Mishchenko, T. Georgiou, M. I. Katsnelson, L. Eaves, S. V. Morozov, N. M. R. Peres, J. Leist, A. K. Geim, K. S. Novoselov, and L. A. Ponomarenko *Science*, vol. 335, p. 6071, 2012.

[214] A. S. Mayorov, R. V. Gorbachev, S. V. Morozov, L. Britnell, R. Jalil, L. A. Ponomarenko, P. Blake, K. S. Novoselov, K. Watanabe, T. Taniguchi, and A. K. Geim, "Micrometer-scale ballistic transport in encapsulated graphene at room temperature," *Nano Lett.*, vol. 11, p. 2396, 2011.

[215] X. Du, I. Skachko, A. Barker, and E. Y. Andrei, "Approaching ballistic transport in suspended graphene," *Nature Nano.*, vol. 3, p. 491, 2008.

[216] X. Du, I. Skachko, and E. Y. Andrei, "Towards ballistic transport in graphene," *International Journal of Modern Physics B*, vol. 22, p. 4579, 2008.

[217] H. Sojoudi, J. Baltazar, C. Henderson, and S. Graham *J. Vac. Sci. Technol. B*, vol. 30, p. 041213, 2012.

[218] A. Pirkle, J. Chan, A. Venugopa, D. Hinojos, C. W. Magnuson, S. McDonnell, L. Colombo, E. M. Vogel, R. S. Ruoff, and R. M. Wallace, "The effect of chemical residues on the physical and electrical properties of chemical vapor deposited graphene transferred to $sio_2$," *Appl. Phys. Lett.*, vol. 99, p. 122108, 2011.

[219] Z. H. Ni, H. Wang, Z. Q. Luo, Y. Y. Wang, T. Yu, Y. H. Wu, and Z. X. Shen, "The effect of vacuum annealing on graphene," *J. Raman Spectrosc.*, vol. 41, p. 479, 2010.

[220] S. Berciaud, M. Y. Han, K. F. Mak, L. E. Brus, P. Kim, and T. F. Heinz, "Electron and optical phonon temperatures in electrically biased graphene," *Phys. Rev. Lett.*, vol. 104, p. 227401, 2010.

[221] M. Freitag, M. Steiner, Y. Martin, V. Perebeinos, Z. Chen, J. C. Tsang, and P. Avouris, "Energy dissipation in graphene field-effect transistors," *Nano Lett.*, vol. 9, p. 1883, 2009.

[222] Z. Liu, L. Ma, G. Shi, W. Zhou, Y. Gong, S. Lei, X. Yang, J. Zhang, J. Yu, K. P. Hackenberg, A. Babakhani, J.-C. Idrobo, R. Vajtai, J. Lou, and P. M. Ajayan *Nature Nanotechnology*, vol. 8, p. 119, 2013.

[223] N. Peltekis, S. Kumar, N. McEvoy, K. Lee, A. Weidlich, and G. S. Duesberg, "The effect of downstream plasma treatments on graphene surfaces," *Carbon*, vol. 50, p. 395, 2012.

[224] P. Esquinazi, D. Spemann, R. Hohne, A. Setzer, K.-H. Han, and T. Butz, "Induced magnetic ordering by proton irradiation in graphite," *Phys. Rev. Lett.*, vol. 91, p. 227201, 2003.

[225] J. Hong, E. Bekyarova, P. Liang, W. A. de Heer, R. C. Haddon, and S. Khizroev, "Room-temperature magnetic ordering in functionalized graphene," *Scientific Reports*, vol. 2, p. 624, 2012.

[226] O. V. Yazyev and L. Helm, "Defect-induced magnetism in graphene," *Phys. Rev. B*, vol. 75, p. 125408, 2007.

[227] R. R. Nair, M. Sepioni, I.-L. Tsai, O. Lehtinen, J. Keinonen, A. V. Krasheninnikov, T. Thomson, A. K. Geim, and I. V. Grigorieva, "Spin-half paramagnetism in graphene induced by point defects," *Nat. Phys.*, vol. 8, p. 199, 2012.

[228] J. Bai, X. Zhong, S. Jiang, Y. Huang, and X. Duan, "Graphene nanomesh," *Nature Nanotechnology*, vol. 5, p. 190, 2010.

[229] X. Liang, Y.-S. Jung, S. Wu, A. Ismach, D. L. Olynick, S. Cabrini, and J. Bokor, "Formation of bandgap and subbands in graphene nanomeshes with sub-10 nm ribbon width fabricated via nanoimprint lithography," *Nano Lett.*, vol. 10, p. 2454, 2010.

[230] V. H. Nguyen, M. C. Nguyen, H.-V. Nguyen, and P. Dollfus, "Disorder effects on electronic bandgap and transport in graphene-nanomesh-based structures," *J. Appl. Phys.*, vol. 113, p. 013702, 2013.

[231] P. Lee and T. Ramakrishnan, "Disordered electronic systems," *Rev. Mod. Phys.*, vol. 57, p. 287, 1985.

[232] A. Miller and E. Abrahams, "Impurity conduction at low concentrations," *Physical Review*, vol. 120, p. 745, 1960.

[233] N. F. Mott, "Localized states in a pseudogap and near extremities of conduction and valence bands," *Philosophical Magazine*, vol. 19, p. 835, 1969.

[234] B. I. Shklovskii and A. L. Efros, "Electronic properties of doped semiconductors," *Springer-Verlag, Berlin*, 1984.

[235] Abrahams, Anderson, Licciardello, and Ramakrishnan, "Scaling theory of localization: Absence of quantum diffusion in two dimensions," *Phys. Rev. Lett.*, vol. 42, p. 673, 1979.

[236] P. A. Lee, "Real-space scaling studies of localization," *Phys. Rev. Lett.*, vol. 42, p. 1492, 1979.

[237] B. L. Altshuler, A. G. Aronov, and P. A. Lee, "Interaction effects in disordered fermi systems in two dimensions," *Phys. Rev. Lett.*, vol. 44, p. 1288, 1980.

[238] K. E. J. Goh, M. Y. Simmons, and A. R. Hamilton, "Electron-electron interactions in highly disordered two-dimensional systems," *Phys. Rev. B*, vol. 77, p. 235410, 2008.

[239] F. Tikhonenko, A. A. Kozikov, A. K. Savchenko, and R. Gorbachev, "Transition between electron localization and antilocalization in graphene," *Phys. Rev. Lett.*, vol. 103, p. 226801, 2009.

[240] H. Suzuura and T. Ando, "Crossover from symplectic to orthogonal class in a two-dimensional honeycomb lattice," *Phys. Rev. Lett.*, vol. 89, p. 266603, 2002.

[241] E. McCann, K. Kechedzhi, V. I. Falâko, H. Suzuura, T. Ando, and B. L. Altshuler, "Weak-localization magnetoresistance and valley symmetry in graphene," *Phys. Rev. Lett.*, vol. 97, p. 146805, 2006.

[242] A. F. Morpurgo and F. Guinea, "Intervalley scattering, long-range disorder, and effective time-reversal symmetry breaking in graphene," *Phys. Rev. Lett.*, vol. 97, p. 196804, 2006.

[243] J.-H. Chen, W. G. Cullen, C. Jang, M. S. Fuhrer, and E. D. Williams *Phys. Rev. Lett.*, vol. 102, p. 236805, 2009.

[244] C. Gomez-Navarro, R. T. Weitz, A. M. Bittner, M. Scolari, A. Mews, M. Burghard, and K. Kern, "Electronic transport properties of individual chemically reduced graphene oxide sheets," *Nano Lett.*, vol. 7, p. 3499, 2007.

[245] A. B. Kaiser, C. Gomez-Navarro, R. S. Sundaram, M. Burghard, and K. Kern, "Electrical conduction mechanism in chemically derived graphene monolayers," *Nano Lett.*, vol. 9, p. 1787, 2009.

[246] S. Stankovich, D. A. Dikin, R. D. Piner, K. A. Kohlhaas, A. Kleinhammes, Y. Jia, Y. Wu, S. T. Nguyen, and R. S. Ruoff, "Synthesis of graphene-based nanosheets via chemical reduction of exfoliated graphite oxide," *Carbon*, vol. 45, p. 1558, 2007.

[247] A. Allain, "Superconductivity induced in the graphene doped with metallic nanoparticles," *http://perso.neel.cnrs.fr/vincent.bouchiat/page_personnelle_de_Vincent_Bouchiat/Theses_files/these_adrien_allain.pdf*, 2012.

[248] F. V. Tikhonenko, D. W. Horsell, R. V. Gorbachev, and A. K. Savchenko, "Weak localization in graphene flakes," *Phys. Rev. Lett.*, vol. 100, p. 056802, 2008.

[249] B. D. Josephson, "Possible new effects in superconductive tunnelling," *Physics Letters*, vol. 1, p. 251, 1962.

[250] R. Fazio and G. Schon, "Charge and vortex dynamics in arrays of tunnel junctions," *Phys. Rev. B*, vol. 43, p. 5307, 1991.

[251] V. Ambegaokar, B. I. Halperin, and J. S. Langer, "Hopping conductivity in disordered systems," *Phys. Rev. B*, vol. 4, p. 2612, 1971.

[252] H. M. Jaeger, D. B. Haviland, B. Orr, and A. M. Goldman, "Onset of superconductivity in ultrathin granular metal films," *Phys. Rev. B*, vol. 40, p. 182, 1989.

[253] C. B.Winkelmann, N. Roch, W. Wernsdorfer, V. Bouchiat, and F. Balestro, "Superconductivity in a singleâc60 transistor," *Nature Physics*, vol. 5, p. 876, 2009.

[254] J.-P. Cleuziou, W. Wernsdorfer, V. Bouchiat, T. OndarÃ§uhu, and M. Monthioux, "Carbon nanotube superconducting quantum interference device," *Nature Nanotechnology*, vol. 1, p. 53, 2006.

[255] B. Kessler, "Hybrid two-dimensional electronic systems and other applications of sp-2 bonded light elements," *https://docs.google.com/file/d/oB8PwugczX-MbXpPOTZlaoctaEE/edit?usp=sharing*, 2010.

[256] M. Tinkham, "Introduction to superconductivity," *Second Edition. New York, NY: McGraw-Hill*, 1996.

[257] S. L. Sondhi, S. M. Girvin, J. P. Carini, and D. Shahar, "Continuous quantum phase transitions," *Rev. Mod. Phys.*, vol. 69, p. 315, 1997.

[258] V. Gantmakher and V. Dolgopolov, "Superconductor-insulator quantum phase transition," *Physics-Uspekhi*, vol. 53, p. 3, 2010.

[259] N. Markovic, C. Christiansen, A. M. Mack, W. H. Huber, and A. M. Goldman, "Superconductor-insulator transition in two dimensions," *Phys. Rev. B*, vol. 60, p. 4320, 1999.

[260] T. I. Baturina, D. R. Islamov, J. Bentner, C. Strunk, M. R. Baklanov, and A. Satta, "Superconductivity on the localization threshold and magnetic-field-tuned superconductorâinsulator transition in tin films," *JETP Lett.*, vol. 79, p. 337, 2004.

[261] H. S. J. van der Zant, W. J. Elion, L. J. Geerligs, and J. E. Mooij, "Quantum phase transitions in two dimensions: Experiments in josephson-junction arrays," *Phys. Rev. B*, vol. 54, p. 10081, 1996.

[262] J. E. Mooij, B. J. van Wees, L. J. Geerligs, M. Peters, R. Fazio, and G. Schon, "Unbinding of charge-anticharge pairs in two-dimensional arrays of small tunnel junctions," *Phys. Rev. Lett.*, vol. 65, p. 645, 1990.

[263] J. M. Kosterlitz and D. Thouless, "Ordering, metastability and phase transitions in two-dimensional systems," *J. Phys. C*, vol. 6, p. 1181, 1973.

[264] T. Zhang, P. Cheng, W.-J. Li, Y.-J. Sun, G. Wang, X.-G. Zhu, K. He, L. Wang, X. Ma, X. Chen, Y. Wang, Y. Liu, H.-Q. Lin, J.-F. Jia, and Q.-K. Xue, "Superconductivity in one-atomic-layer metal films grown on si(111)," *Nature Physics*, vol. 6, p. 104, 2010.

[265] S. Qin, J. Kim, Q. Niu, and C. K. Shih, "Superconductivity at the two-dimensional limit," *Science*, vol. 324, p. 1314, 2009.

[266] K. Clark, A. Hassanien, S. Khan, K.-F. Braun, H. Tanaka, and S. W. Hla, "Superconductivity in just four pairs of (bets)2gacl4 molecules," *Nature Nanotechnology*, vol. 5, p. 261, 2010.

[267] D. B. Haviland, Y. Liu, and A. M. Goldman, "Onset of superconductivity in the tvvo-dimensional limit," *Phys. Rev. Lett.*, vol. 62, p. 2180, 1989.

[268] H. Jager, D. B. Haviland, A. M. Goldman, and B. G. Orr, "Threshold for superconductivity in ultras thin amorphous gallium films," *Phys. Rev. B*, vol. 34, p. 4920, 1986.

[269] S. Chakravarty, S. Kivelson, G. T. Zimanyi, and B. I. Halperin, "Effect of quasiparticle tunneling on quantum-phase fluctuations and the onset of superconductivity in granular films," *Phys. Rev. B*, vol. 35, p. 7265, 1987.

[270] T. Pang, "Universal critical normal sheet resistance in ultrathin films," *Phys. Rev. Lett.*, vol. 62, p. 2176, 1989.

[271] L. Geerligs and J. Mooij, "Charge quantization and dissipation in arrays of small josephson junctions," *Physica B: Condensed Matter*, vol. 152, p. 212, 1988.

[272] B. G. Orr, H. M. Jaeger, A. M. Goldman, and C. G. Kuper, "Global phase coherence in two-dimensional granular superconductors," *Phys. Rev. Lett.*, vol. 56, p. 378, 1986.

[273] R. Fazio and G. Schon, "Quantum phase transitions in josephson junction arrays," *Lectures given at the School on "Superconductivity in Networks and Mesoscopic Structures", Certosa di Pontignano - Siena*, 1997.

[274] E. Simanek and R. Brown, "Effect of dissipation on the phase transition in granular superconductors," *Phys. Rev. B*, vol. 34, p. 3495, 1986.

[275] M. P. A. Fisher, "Dissipation and quantum actuations in granular superconductivity," *Phys. Rev. B*, vol. 36, p. 1917, 1987.

[276] K.-H. Wagenblast, A. van Otterlo, G. Schon, and G. T. Zimanyi, "New universality class at the superconductor-insulator transition," *Phys. Rev. Lett.*, vol. 78, p. 1779, 1997.

[277] A. J. Rimberg, T. R. Ho, C. Kurdak, and J. Clarke, "Dissipation-driven superconductor-insulator transition in a two-dimensional josephson-junction array," *Phys. Rev. Lett.*, vol. 78, p. 2632, 1997.

[278] Y. Takahide, R. Yagi, A. Kanda, Y. Ootuka, and S. ichi Kobayashi, "Superconductor-insulator transition in a two-dimensional array of resistively shunted small josephson junctions," *Phys. Rev. Lett.*, vol. 85, p. 1974, 2000.

[279] L. J. Geerligs, M. Peters, L. E. M. de Groot, A. Verbruggen, and J. E. Mooij, "Charging effects and quantum coherence in regular josephson junction arrays," *Phys. Rev. Lett.*, vol. 63, p. 326, 1989.

[280] M.P.A.Fisher, "Quantum phase transitions in disordered two-dimensional superconductors," *Phys.Rev.Lett*, vol. 65, p. 923, 1990.

[281] M. P. A. Fisher and G. Grinstein, "Quantum critical phenomena in charged superconductors," *Phys. Rev. Lett.*, vol. 60, p. 208, 1988.

[282] A.M.Finkelstein, "Superconducting transition temperature in amorphous films," *JETP Lett.*, vol. 45, p. 46, 1987.

[283] A. M. Finkel'stein, "Suppression of superconductivity in homogeneously disordered systems," *Physica B*, vol. 197, p. 636, 1994.

[284] K. Efetov, "Phase transition in granulated superconductors," *Sov. Phys. JETP*, vol. 51, p. 1015, 1980.

[285] R. Fazioa and H. van der Zant, "Quantum phase transitions and vortex dynamics in superconducting networks," *Physics Reports*, vol. 355, p. 235, 2001.

[286] T. I. Baturina, A. Y. Mironov, V. M. Vinokur, M. R. Baklanov, and C. Strunk, "Localized superconductivity in the quantum-critical region of the disorder-driven superconductor-insulator transition in tin thin films," *Phys. Rev. Lett.*, vol. 99, p. 257003, 2007.

[287] A. F. Hebard and M. A. Paalanen, "Pair-breaking model for disorder in two-dimensional superconductors," *Phys. Rev. B*, vol. 30, p. 4063, 1984.

[288] A. Yazdani and A. Kapitulnik, "Superconducting-insulating transition in two-dimensional a-moge thin films," *Phys. Rev. Lett.*, vol. 74, p. 3037, 1995.

[289] N. Mason and A. Kapitulnik, "Dissipation effects on the superconductor-insulator transition in 2d superconductors," *Phys. Rev. Lett.*, vol. 82, p. 5341, 1999.

[290] P. Phillips, S. Sachdev, S. Kravchenko, and A. Yazdani, "Quantum conductors in a plane," *Proc. Natl. Acad. Sci. USA*, vol. 96, p. 9983, 1999.

[291] E. Abrahams, S. V. Krachenko, and M. P. Sarachik, "Colloquium: Metallic behavior and related phenomena in two dimensions," *Rev. Mod. Phys*, vol. 73, p. 251, 2001.

[292] D. Ephron, A. Yazdani, A. Kapitulnik, and M. R. Beasley, "Observation of quantum dissipation in the vortex state of a highly disordered superconducting thin film," *Phys. Rev. Lett.*, vol. 76, p. 1529, 1996.

[293] D. Dalidovich and P. Phillips, "Fluctuation conductivity in insulator-superconductor transitions with dissipation," *Phys. Rev. Lett.*, vol. 84, p. 737, 2000.

[294] D. Dalidovich and P. Phillips, "Interaction-induced bose metal in two dimensions," *Phys. Rev. B*, vol. 64, p. 052507, 2001.

[295] A. Kapitulnik, N. Mason, S. A. Kivelson, and S. Chakravarty, "Effects of dissipation on quantum phase transitions," *Phys. Rev. B*, vol. 63, p. 125322, 2001.

[296] D. Das and S. Doniach, "Existence of a bose metal at t50," *Phys. Rev. B*, vol. 60, p. 1261, 1999.

[297] D. Das and S. Doniach, "Bose metal: Gauge-field fluctuations and scaling for field-tuned quantum phase transitions," *Phys. Rev. B*, vol. 64, p. 134511, 2001.

[298] P. G. D. Gennes, "Superconductivity of metals and alloys," *Benjamin, New York*, 1966.

[299] G. E. Blonder, M. Tinkham, and T. M. Klapwijk, "Transition from metallic to tunneling regimes in superconducting microconstrictions: Excess current, charge imbalance, and supercurrent conversion," *Phys. Rev. B*, vol. 25, p. 4515, 1982.

[300] V. Lukic, "Conductance of superconductor-normal metal contact junction beyond quasiclassical approximation," *PhD thesis, unpublished*, 1997.

[301] A. Kastalsky, A. W. Kleinsasser, L. H. Greene, R. Bhat, F. P. Milliken, and J. P. Harbison, "Observation of pair currents in superconductor-semiconductor contacts," *Phys. Rev. Lett.*, vol. 67, p. 3026, 1991.

[302] C. D. Usadel, "Generalized diffusion equation for superconducting alloys," *Phys. Rev. Lett.*, vol. 25, p. 507, 1970.

[303] Y. V. Nazarov, "Circuit theory of andreev conductance," *Phys. Rev. Lett.*, vol. 73, p. 1420, 1994.

[304] T. M. Klapwijk, "Proximity effect from an adreev perspective," *J. Super. Inco. Nov. Magn.*, vol. 17, p. 593, 2004.

[305] Proefschrift, "Proximity effects in superconducting spin-valve structures," *PhD thesis, Universiteit Leiden*, 2010.

[306] S. Gueron, "Quasiparticles in a diffusive conductor: Interaction and pairing," *PhD Thesis.*, 1997.

[307] H. Courtois, P. Charlat, P. Gandit, D. Mailly, and B. Pannetier, "The spectral conductance of a mesoscopic proximity superconductor and the reentrance effect," *Journal of Low Temperature Physics*, vol. 116, p. 187, 1999.

[308] V. G. Kogan, "Coherence length of a normal metal in a proximity system," *Phys. Rev. B*, vol. 26, p. 88, 1982.

[309] B. L. Alâtshuler, A. G. Aronov, and D. E. Khmelnitsky, "Effects of electron-electron collisions with small energy transfers on quantum localisation," *J. Phys. C*, vol. 15, p. 7367, 1982.

[310] S. Gueron, H. Pothier, N. O. Birge, D. Esteve, and M. H. Devoret, "Superconducting proximity effect probed on a mesoscopic length scale," *Phys. Rev. Lett.*, vol. 77, p. 3025, 1996.

[311] J. Rammer and H. Smith, "Quantum field-theoretical methods in transport theory of metals," *Rev. Mod. Phys.*, vol. 58, p. 323, 1986.

[312] W. Belzig, C. Bruder, and G. Schon, "Local density of states in a dirty normal metal connected to a superconductor," *Phys. Rev. B*, vol. 54, p. 9443, 1996.

[313] S. Pilgram and a. C. B. W. Belzig, "Excitation spectrum of mesoscopic proximity structures," *Phys. Rev. B*, vol. 62, p. 12462, 2001.

[314] A. Volkov, P. H. C. Magnee, B. J. van Wees, and T. M. Klapwijk, "Proximity and josephson effects in superconductor-two-dimensional electron gas planar junctions," *Physica C*, vol. 242, p. 261, 1995.

[315] M. Y. Kupriyanov and V. F. Lukichev *Zh. Eksp. Teor. Fiz.*, vol. 94, p. 139, 1987.

[316] W. Y. Shih and D. Stroud, "Two-dimensional superconducting arrays in a magnetic field: Effects of lattice structures," *Phys. Rev. B*, vol. 32, p. 158, 1985.

[317] K. K. Likharev, "Superconducting weak links," *Rev. Mod. Phys.*, vol. 51, p. 101, 1979.

[318] L. Aslamazov, A. Larkin, and Y. Ovchinnikov, "Josephson effect in superconductors separated by a normal metal," *ZhETF*, vol. 55, p. 323, 1968.

[319] M. V. Feigel'man, A. Kamenev, A. I. Larkin, and M. A. Skvortsov, "Weak charge quantization on a superconducting island," *Phys. Rev. B*, vol. 66, p. 054502, 2002.

[320] C. Bruder, R. Fazio, and G. Schoen *Physica B*, vol. 203, p. 246, 1994.

[321] A. Schmid, "Diffusion and localization in a dissipative quantum system," *Phys. Rev. Lett.*, vol. 51, p. 1506, 1983.

[322] L. P. Gor'kov and G. Teitel'baum, "Dual role of d electrons in iron pnictides," *Zh. Eksp. Teor. Fiz*, vol. 37, p. 833, 1959.

[323] W. Wu and P. W. Adams, "Avalanches and slow relaxation: Dynamics of ultrathin granular superconducting films in a parallel magnetic field," *Phys. Rev. Lett.*, vol. 74, p. 610, 1995.

[324] H. B. Heersche, P. Jarillo-Herrero, J. B. Oostinga, L. M. K. Vandersypen, and A. F. Morpurgo, "Bipolar supercurrent in graphene," *Nature*, vol. 446, p. 56, 2007.

[325] X. Du, "Josephson current and multiple andreev reflections in graphene sns junctions," *PRB*, vol. 77, p. 184507, 2008.

[326] F. Miao, S. Wijeratne, Y. Zhang, U. C. Coskun, W. Bao, and C. N. Lau, "Phase-coherent transport in graphene quantum billiards," *Science*, vol. 317, p. 1530, 2007.

[327] U. C. Coskun, M. Brenner, T. Hymel, V. Vakaryuk, A. Levchenko, and A. Bezryadin, "Distribution of supercurrent switching in graphene under the proximity effect," *Phys. Rev. Lett.*, vol. 108, p. 097003, 2012.

[328] A. M. Black-Schaffer and J. Linder, "Strongly anharmonic current-phase relation in ballistic graphene josephson junctions," *Phys. Rev. B*, vol. 82, p. 184522, 2010.

[329] D. Jeong, J.-H. Choi, G.-H. Lee, S. Jo, Y.-J. Doh, and H.-J. Lee, "Observation of supercurrent in pbin-graphene-pbin josephson junction," *Phys. Rev. B*, vol. 83, p. 094503, 2011.

[330] I. Borzenets, U. C. Coskun, S. J. Jones, and G. Finkelstein, "Phase diffusion in graphene-based josephson junctions," *Phys. Rev. B*, vol. 107, p. 137005, 2011.

[331] T. Dirks, T. L. Hughes, S. Lal, B. Uchoa, Y.-F. Chen, C. Chialvo, P. M. Goldbart, and N. Mason, "Transport through andreev bound states in a graphene quantum dot," *Nature physics*, vol. 7, p. 386, 2011.

[332] C. Girit, V. Bouchiat, O. Naaman, Y. Zhang, M. F. Crommie, A. Zettl, and I. Siddiqi, "Tunable graphene dc superconducting quantum interference device," *Nano Lett.*, vol. 9, p. 198, 2009.

[333] K. Komatsu, C. Li, S. Autier-Laurent, H. Bouchiat, and S. Gueron, "Superconducting proximity effect in long superconductor/graphene/superconductor junctions: From specular andreev reflection at zero field to the quantum hall regime," *Phys. Rev. B*, vol. 86, p. 115412, 2012.

[334] P. Rickhaus, M. Weiss, L. Marot, and C. Schonenberger, "Quantum hall effect in graphene with superconducting electrodes," *Nano Lett.*, vol. 12, p. 1942, 2012.

[335] R. A. Jishi, D. M. Guzman, and H. M. Alyahyaei, "Theoretical investigation of two-dimensional superconductivity in intercalated graphene layers," *Adv. Studies Theor. Phys.*, vol. 5, p. 703, 2011.

[336] G. Profeta, M. Calandra, and F. Mauri, "Phonon-mediated superconductivity in graphene by lithium deposition," *Nature Physics*, vol. 8, p. 131, 2012.

[337] K. Kanetania, K. Sugawarab, T. Satoa, R. Shimizub, K. Iwayab, T. Hitosugib, and T. Takahashia, "Ca intercalated bilayer graphene as a thinnest limit of superconducting c6ca," *Proc. Natl. Acad. Sci. USA*, vol. 27, p. 109, 2012.

[338] M. Xue, G. Chen, H. Yang, Y. Zhu, D. Wang, J. He, and T. Cao, "Superconductivity in potassium-doped few-layer graphene," *J. Am. Chem. Soc.*, vol. 134, p. 6536, 2012.

[339] J. Biscaras, N. Bergeal, S. Hurand, C. Feuillet-Palma, A. Rastogi, R. C. Budhani, M. Grilli, S. Caprara, and J. Lesueur, "Multiple quantum criticality in a two-dimensional superconductor," *Nature Materials*, vol. 12, p. 542, 2013.

[340] T. Cren, L. Serrier-Garcia, F. Debontridder, and D. Roditchev, "Vortex fusion and giant vortex states in confined superconducting condensates," *Phys. Rev. Lett.*, vol. 107, p. 097202, 2011.

[341] M. R. Beasley, J. E. Mooij, and T. P. Orlando, "Possibility of vortex-antivortex pair dissociation in two-dimensional superconductors," *Phys. Rev. Lett.*, vol. 42, p. 1165, 1979.

[342] H. Courtois, M. Meschke, J. T. Peltonen, and J. P. Pekola, "Origin of hysteresis in a proximity josephson junction," *Phys. Rev. Lett.*, vol. 101, p. 067002, 2008.

[343] L. G. Aslamazov and A. I. Larkin, "Effect of fluctuations on the properties of a superconductor above the critical temperature," *Fiz. Tv. Tela*, vol. 10, p. 1104, 1968.

[344] K. S. Tikhonov, G. Schwiete, and A. M. Finkelstein, "Fluctuation conductivity in disordered superconducting films," *Phys. Rev. B*, vol. 85, p. 174527, 2012.

[345] K. S. Tikhonov, M. V. Feigel'man, and M. A. Skvortsov *paper in preparation*, 2013.

[346] F. K. Wilhelm, A. D. Zaikin, and G. Schon, "Superconducting current in narrow proximity wires," *Czech. J. Phys.*, vol. 46, p. 3295, 1996.

[347] D. J. Resnick, J. C. Garland, J. T. Boyd, S. Shoemaker, and R. S. Newrock, "Kosterlitz-thouless transition in proximity-coupled superconducting arrays," *Phys. Rev. Lett.*, vol. 47, p. 1542, 1981.

[348] N. Reyren, S. Thiel, A. D. Caviglia, L. F. Kourkoutis, G. Hammerl, C. Richter, C. W. Schneider, T. Kopp, A. S. Retschi, D. Jaccard, M. Gabay, D. A. Muller, J. M. Triscone, and J. Mannhart, "Superconducting interfaces between insulating oxides," *Science*, vol. 317, p. 1196, 2007.

[349] V. M. Galitski and A. I. Larkin, "Disorder and quantum fluctuations in superconducting films in strong magnetic fields," *Phys. Rev. Lett.*, vol. 87, p. 087001, 2001.

[350] M. V. Feigelman and L. B. Ioffe, "Theory of diamagnetism in granular superconductors," *Phys. Rev. Lett.*, vol. 74, p. 344, 1995.

[351] D. M. Kagan, L. B. Ioffe, and M. V. Feigelman, "Quantum glass transition in a periodic long-range josephson array," *ZhETH*, vol. 116, p. 1450, 1999.

# ACKNOWLEDGEMENTS

Luckily, I could travel to France for my PhD and to start the whole new page of my life. During the past three years, I enjoyed very much not only the wonderful French culture, but also the fabulous research activities here in Grenoble. Here I would like to thank all the people who have helped me with this thesis.

I wish to thank my supervisor Dr. Vincent Bouchiat, whom I met in a north-east Chinese town three years ago. I was assigned by my previous institute to guide him to sightseeing. Shortly after, he didn't mind my being an ignorant dumb guy, and became my guide to scientific research – all happened like yesterday! Equal thanks to Dr. Irina Ionica. As a co-supervisor of my thesis, she is so patient in teaching me and always helpful at needs. I really enjoyed the time I worked with her.

Many thanks to my group members: Adrien Allain who taught me every single detail of the experimental setup. He also helped me a lot of my life in Grenoble; Laëtitia Marty who is always super nice and patiently helped me a lot; Nedjma Bendiab who is truly kind from both inside and outside, I learnt a lot from her besides the Raman knowledge; Johann Coraux who is absolutely a charming person, rigorous in science and easy-going in daily life.

I wish to give my deepest appreciation to Amina Kimouche, Antoine Reserbat-plantey, Alexandre Artaud, Cornellia Schwarz, Dipankar Kalitar, Fabien Jean, Haid Arjmandi-Tash, Jinxing Liu, John Landers, Mitsuki Ito, Shelender Kumar, Sergio Vlaic, Yani Chen, Zoltan Osvath. They are wonderful team mates, who helped me a lot during my thesis. Also thanks to the colleagues outside my group: Christoph Blanc, Farida Veliev, Hanno Flentje, Johanna Seidemann, Katrin Zimmerman, Przemyslaw Lesczynski, Sayanti Sammadar. I was lucky to be able to work with them.

Thanks to all those who I collaborated during the last few years: Benjamin Piot, Cécile Naud, Claude Chapelier, Clément Faugeras, Clemens Winkleman, Greta Dellea, Gilles Cunge, Hanako Okuno, Jean-Yves Veuillen, Milan Orlita, Pierre Mallet, Pierre Strobel, Shimpei Ohno, Violetta Sessi.

A lot of thanks to the NanoSpin group: Christophe Thirion, Edgar Bonet, Franck Balestro, Jarno Jarvinen, Jean-Pierre Cleuziou, Matias Urdampilleta, Ngoc-Viet Nguyen, Oksana Gaier, Raoul Piquerel, Romain Vincent, Romain Maurand, Stefan Thiele, Wolfgang Wernsdorfer. And thanks to Christophe Guttin, David Jeguso, Julien Jarreau, Richard Haettel, Sébastien Pairis, Valérie Reita, for their technical help. Also thanks to the NanoFab team: Bruno Fernandez, Gwénaëlle Julie, Jean-francois Motte, Thierry Crozes, Sébastien Dufresnes, Thierry Fournier.

Without their help I could not carry out a single experiment.

Special thanks to Benjamin Sacépé and Misha Feigel'man for their great help in analysing my experiment and strong supports in theory. And special thanks to the CIBLE program from the Région Rhône-Alpes for their funding my PhD studies.

At the end, I would like to thank my family for their supports. Especially, thanks to my wife Deffe, she surely deserves it. It is she who makes me realize that marriage is so beautiful, beautiful because it is always happy to be next to the right person, beautiful because it is never to give up.